

University of Denver

Digital Commons @ DU

Electronic Theses and Dissertations

Graduate Studies

1-1-2016

Galvanic Corrosion of Aluminum/Carbon Composite Systems

Eva Håkansson
University of Denver

Follow this and additional works at: <https://digitalcommons.du.edu/etd>



Part of the [Mechanical Engineering Commons](#)

Recommended Citation

Håkansson, Eva, "Galvanic Corrosion of Aluminum/Carbon Composite Systems" (2016). *Electronic Theses and Dissertations*. 1120.

<https://digitalcommons.du.edu/etd/1120>

This Dissertation is brought to you for free and open access by the Graduate Studies at Digital Commons @ DU. It has been accepted for inclusion in Electronic Theses and Dissertations by an authorized administrator of Digital Commons @ DU. For more information, please contact jennifer.cox@du.edu, dig-commons@du.edu.

GALVANIC CORROSION OF ALUMINUM/CARBON COMPOSITE SYSTEMS

A Dissertation

Presented to

The Faculty of the Daniel Felix Ritchie School of Engineering and Computer Science

University of Denver

In Partial Fulfillment

of the Requirements for the Degree

Doctor of Philosophy

by

Eva Håkansson

June 2016

Advisor: Dr. Maciej Kumosa

© Copyright by Eva Håkansson 2016

All Rights Reserved

Author: Eva Håkansson
Title: GALVANIC CORROSION OF ALUMINUM/CARBON COMPOSITE SYSTEMS
Advisor: Dr. Maciej Kumosa
Degree Date: June 2016

ABSTRACT

Aluminum/carbon composite systems can have outstanding mechanical properties. Aluminum and carbon fiber reinforced polymer matrix composites (CFRP) are typically considered corrosion resistant when used alone, but can develop severe galvanic corrosion when in physical contact in the same component or structure.

General engineering practice is to avoid contact between aluminum and CFRP in any application where moisture may be present, but it is still of great importance to understand the consequences if the two materials accidentally become in contact. There may also be applications where a low rate of galvanic corrosion is acceptable.

This dissertation contributes unique experimental and numerical approaches to improve the fundamental understanding of galvanic corrosion in aluminum/carbon composite systems, with particular focus on rate limiting control mechanisms in a high-temperature low-sag bare overhead transmission line conductor utilizing a CFRP load bearing core.

The improved understanding was accomplished partially by the development of a novel assessment method for the in-situ galvanic corrosion testing of bare overhead conductors of various designs. The method allows for real-time measurements of galvanic corrosion currents while retaining the original geometry of the conductors.

One of the most important findings is that the galvanic corrosion is under *cathodic control*, which means that the total galvanic corrosion rate is determined by the

exposed carbon area, and independent of the exposed aluminum area. Another important finding is that the galvanic corrosion process is under *diffusion control*, which means that the total galvanic corrosion rate is mainly controlled by the rate at which oxygen arrives at the carbon surface. The implication of these findings is that the geometry of the component or structure can affect the galvanic corrosion rate by orders of magnitude.

The dissertation work has also included the development of a structural health monitoring method for CFRP supported overhead conductors using Time Domain Reflectometry (TDR).

This comprehensive research has significantly contributed to the increased acceptance of CFRP supported bare overhead conductors in both the United States and worldwide. The knowledge gained in this study is already aiding the evaluation of existing conductor designs and the development of future ones.

ACKNOWLEDGEMENTS

A PhD dissertation is always a team effort. This study would never have been possible without help from other people. I would like to acknowledge the following:

Dr. Maciej Kumosa – my academic supervisor – for making the dream about a National Science Foundation research center come true, and for making my PhD dream come true as well. • Dr. Paul Predecki, professor emeritus at DU, for also having been invaluable in the work. • For the members of the NSF Center for Novel High Voltage/ Temperature Materials and Structures and the NSF (GOALI) for financing this study. • Dr. Richard E. Ricker at NIST, Gaithersburg for providing knowledge and a very sound perspective on corrosion. • Dr. Davor Balzar, Dr. Margareta Stefanovic, Dr. Ali Azadani, Dr. Yun-Bo Yi, and Dr. Eric Bosze for serving on my graduate committee. • Dr. Corinne Lengsfeld for lending me equipment • Roy Noble, Tim Hosking, and Andrew Renton at Transpower NZ for their hospitality • Dr. Jim Roberts and Steve Cicoria at NOAA Boulder • Dr. Joe Hoffman, Dr. Euripides Solis-Ramos, Chrissy Henderson, Daniel Waters, Tianyi Lu, Edward Clark, James Schwab, Justin Hughes, Bruce Allen, Monika Bleszynski, Jon Buckley, Clayton Pankey, and Amani Alfaifi at DU for great collaboration and camaraderie. Joe deserves particular acknowledgement for reviewing this *entire* dissertation. • My parents Lena and Sven Håkansson for laying the foundation for my love of science. • Bill Dubé for being my husband and the love of my life, and convincing me to attend engineering school in the first place, and my dear friends Prof. Dr. Wolfgang and Monika Schürer for making it possible. And everybody else that I have forgotten to mention....

TABLE OF CONTENTS

Chapter One: Introduction	1
1.1 Applications of aluminum/carbon composite systems in high voltage engineering.....	2
1.1.1 The transmission line service environment.....	6
1.1.2 Results from previous galvanic corrosion research	11
1.2 Applications of aluminum/carbon composite systems in aerospace.....	12
1.3 Research objective	14
1.4 Research sponsors.....	15
Chapter Two: Fundamentals of galvanic corrosion	16
2.1 Thermodynamics of galvanic corrosion.....	20
2.1.1 Electrode potential and Nernst equation	21
2.1.2 Galvanic series	23
2.1.3 Corrosion reactions in aluminum/carbon galvanic couples	27
2.2 Kinetics of galvanic corrosion	37
2.2.1 Polarization and electrode efficiency.....	38
2.2.2 Polarization curves and Tafel behavior.....	39
2.2.3 Faraday's Law – mass loss calculations from galvanic current.....	45
2.3 Environmental factors	46
2.3.1 Temperature	46
2.3.2 Conductivity of the electrolyte.....	47
2.3.3 Dissolved oxygen.....	50
2.3.4 Effect of pH.....	51
2.4 Geometry and area ratio.....	51
2.5 Atmospheric galvanic corrosion	52
2.5.1 Presence of salt and its effect on the electrolyte layer thickness	53
Chapter Three: Development of a new in-situ method for evaluation of galvanic corrosion in bare overhead transmission line conductors	55
3.1 The importance of new transmission conductor designs	55
3.2 Traditional galvanic testing of bare conductors.....	58
3.3 Development of the proposed method	60
3.3.1 Basic principles behind the proposed method	60
3.3.2 Electrical connections	64
3.3.3 Measurements circuits	82
3.3.4 Importance of retaining the original geometry	85
3.4 Application of proposed method to galvanic testing of conductors	88
3.5 Results and discussion	89
Chapter Four: Evaluation of critical factors affecting galvanic corrosion.....	93
4.1 Input data for numerical modeling.....	93
4.1.1 Equilibrium potentials and galvanic series	93
4.1.2 Tafel slopes and exchange current density	96
4.1.3 Electrolyte oxygen content	102

4.2 Investigation of control mechanisms	103
4.2.1 Experimental setup.....	103
4.2.2 Results.....	110
4.2.3 Discussion and conclusions about control mechanisms	125
4.3 Summary of input data for numerical modeling	131
 Chapter Five: Evaluation of electrolyte layer formation and oxygen transport in atmospheric conditions	132
5.1 Oxygen consumption by the cathodic reaction	132
5.2 Presence of salt and its effect on the electrolyte layer thickness	134
5.2.1 Hygroscopic properties of different salts – experimental procedure	136
5.2.2 Electrolyte layer thickness as a function of relative humidity and salt load density	140
5.2.3 Salinity as a function of relative humidity.....	159
 Chapter Six: Numerical Modeling of galvanic corrosion – immersed conditions.....	166
6.1 Basic procedure for Finite Element Modeling of galvanic corrosion.....	167
6.1.1 Common assumptions.....	167
6.2 Fundamental mathematical relations	169
6.2.1 Differential equation for conductivity of the electrolyte	169
6.2.2 Boundary conditions	174
6.3 Comsol Multiphysics Corrosion Module.....	175
6.3.1 Comsol electrochemistry modules.....	175
6.3.2 Current distribution.....	178
6.3.3 Study type	179
6.3.4 Step-by-step procedure	181
6.4 Immersed model: Parallel electrodes, resistance dominated	183
6.4.1 Input data	184
6.4.2 Analytical solution.....	187
6.4.3 Finite Element model.....	197
6.4.4 Experimental validation models	200
6.5 Chapter conclusions	210
 Chapter Seven: Numerical modeling of atmospheric galvanic corrosion	211
7.1 Steady-state finite element modeling of atmospheric galvanic corrosion	214
7.1.1 Model geometry and reactions.....	214
7.1.2 Comsol model geometry and boundary conditions	218
7.1.3 Electrolyte	220
7.1.4 Current distribution.....	220
7.1.5 Global definitions and parameters	220
7.1.6 Average and maximum operators	221
7.1.7 Initial values.....	221
7.1.8 Meshing.....	222
7.1.9 Parametric sweeps.....	222
7.1.10 Results: Comparison of 10 mm and 98 mm anode	223

7.1.11 Discussion	229
7.1.12 Comparison with experimental measurements	232
7.2 Time-dependent numerical model of atmospheric galvanic corrosion.....	235
7.2.1 Galvanic corrosion knee-point and formation of Al(OH) ₃ gel	237
7.2.2 Assumptions for numerical model	240
7.2.3 Model geometry	241
7.2.4 Diffusion of oxygen through the corrosion products.....	243
7.2.5 Mathematical expression for galvanic corrosion rate	244
7.2.6 Solving technique.....	246
7.2.7 Initial condition.....	247
7.2.8 Results and discussion	249
7.2.9 Conclusions regarding this model.....	252
7.3 Discussion and chapter conclusions.....	253
Chapter Eight: Monitoring for galvanic corrosion in carbon fiber composite core overhead conductors using time domain reflectometry	259
8.1 Circuit theory for TDR and application in ACCC	262
8.1.1 Transmission line theory.....	262
8.1.2 Characteristic impedance	266
8.1.3 Coefficient of reflection.....	268
8.1.4 Attenuation.....	270
8.2 Experimental work.....	274
8.2.1 Characteristic impedance	276
8.2.2 VOP and attenuation	277
8.2.3 Detection of galvanic corrosion and other faults	281
8.3. Discussion.....	285
8.3.1 Applications of TDR on ACCC and similar cables	286
8.4 Chapter conclusions	289
Chapter Nine: General discussion and final conclusions.....	290
References	314
Appendix A: Acronyms, terminology and symbols	323
Appendix B: Error analysis.....	325
B.1 Effect of temperature and temperature control, and errors in temperature measurements.....	325
B.2 Errors in humidity measurements	330
B.3 Errors caused by reference electrodes	331
B.4 Calibration of potentiostat.....	333
B.5 Errors in mass measurements.....	333
B.6 Errors in galvanic corrosion current measurements.....	334
B.7 Conclusions about measurement errors.....	334

LIST OF FIGURES

Figure 1: ACCC vs. ACSR.....	3
Figure 2: Laboratory induced damage through low-velocity impact.....	4
Figure 3: Cracks in the ACCC conductor corrosion barrier caused by Aeolian vibrations (high cycle fatigue).	5
Figure 4: Transmission line structure in New Zealand.	6
Figure 5: Schematic of the generation, transmission and distribution system.....	7
Figure 6: The author standing on the foundation (circled) shows the scale of a typical transmission line tower located in New Zealand.	7
Figure 7: Bulging of ACSR conductor due to build-up of corrosion products.....	8
Figure 8: Severe corrosion damage on ACSR conductor after 35 years in service in New Zealand.....	9
Figure 9: Sectioning of the conductor in previous figures.....	9
Figure 10: Close-up of the steel strands in previous figure.	10
Figure 11: Close-up of pitting corrosion of the aluminum strands in Figure 9.	10
Figure 12: Anodic galvanic corrosion current density in 3 mass % NaCl solution.....	11
Figure 13: Materials used in the Boeing 787 Dreamliner.....	13
Figure 14: Traditional distribution of materials in airplanes.	13
Figure 15: Rating of material from a galvanic corrosion perspective.	14
Figure 16: Trailer license plate lost due to galvanic corrosion between the steel screws and the Al plate.	17
Figure 17: Forms of corrosion.	18
Figure 18: Requirements for galvanic corrosion to occur.	19
Figure 19: Schematic illustration of the galvanic corrosion between CFRP and Al.	21
Figure 20: Galvanic series in seawater.	25
Figure 21: Galvanic series of interest in this study in 0.6 M NaCl at room temperature, vs. Ag/AgCl reference electrode.	26
Figure 22: Splitting of water during corrosion of aluminum.....	29
Figure 23: Reduction of oxygen during corrosion of aluminum.	30
Figure 24: Formation of Al(OH) ₃ on the aluminum strands in a transmission line conductor sample.	31
Figure 25: Graphite-Al galvanic corrosion couple embedded in 3.5 mass % NaCl agar gel with added pH indicator.....	33
Figure 26: Mechanism of pitting corrosion.	35
Figure 27: Typical pitting corrosion of aluminum.....	36
Figure 28: Overpotential η as a function of $\log i$	41
Figure 29: Tafel slopes and equilibrium potential (dotted lines) for aluminum and CFRP in the ACCC conductor.....	42
Figure 30: Exchange current density for aluminum and CFRP in the ACCC conductor.	43
Figure 31: Schematic illustration of the potentiodynamic polarization curves for 4 different control types:.....	44
Figure 32: Schematic illustration of atmospheric galvanic corrosion.	53

Figure 33: Common designs for bare overhead transmission line conductors.	57
Figure 34: Wire-on-bolt test ASTM G116-99.	59
Figure 35: Demonstration samples of the two different conductor designs showing the internal features.	64
Figure 36: Simple electrical connections for short-term corrosion testing.	65
Figure 37: Corrosion of electrical connection.	66
Figure 38: Pre-heating the core.	67
Figure 39: Ends dipped in fast-curing epoxy.	67
Figure 40: The core partially covered with the polyester mesh.	68
Figure 41: The re-assembled conductor sample with the steel core off-set.	68
Figure 42: The conductor ends are potted in fast-curing epoxy.	69
Figure 43: The ends are sanded on a belt sander until the metal is exposed.	69
Figure 44: Holes are drilled and tapped.	70
Figure 45: Procedure for making the electrical connection on the “aluminum end”	71
Figure 46: The electrical connection on the “steel” end.	72
Figure 47: Sectioned view of the electrical connection to the steel core.	72
Figure 48: Sectioned view of the electrical connection to the aluminum strands.	73
Figure 49: The finished sample with the electrical connections covered in epoxy.	73
Figure 50: Control of continuity.	74
Figure 51: Cleaning of hardware using a polishing wheel.	74
Figure 52: Splitting of the ACCC core to simulate damage.	75
Figure 53: The split core (right) and the surrounding aluminum strands (left)	76
Figure 54: The conductor ends are potted in fast-curing epoxy.	77
Figure 55: The ACCC sample removed from the mold.	77
Figure 56: Holes are drilled and tapped.	78
Figure 57: Demo-sample with only half of the end covered with RTV.	78
Figure 58: ACCC samples ready for the electrical connection to the core.	79
Figure 59: Close-up of the core before the electrical connection is made.	79
Figure 60: Electrical connection covered in silicone RTV.	80
Figure 61: The finished ACCC sample.	80
Figure 62: ACCC and ACSR samples with additional mesh sleeves.	81
Figure 63: Varieties of the ACCC samples.	82
Figure 64: Measurement using precision shunt array with 10 channels.	83
Figure 65: A reference electrode can be used in an immersed environment.	83
Figure 66: Schematic of multiple channel measurement circuit using shunt resistors and a multi-zone sample.	84
Figure 67: Finished ACCC samples in the humidity chamber.	84
Figure 68: Four different samples prepared to quantify the geometry effect.	86
Figure 69: Predicted time to loss of 20 % of aluminum cross-section based on different testing methods.	88
Figure 70: Galvanic corrosion current density of corroding aluminum strands as a function of relative humidity for three different conductor designs.	92

Figure 71: Galvanic series for materials of interest in this study in 0.6 M NaCl at room temperature, vs. Ag/AgCl reference electrode.....	94
Figure 72: Potentiodynamic polarization scan with stainless steel mesh counter electrode (reference electrode barely visible in the background).....	96
Figure 73: Tafel slopes and equilibrium potential for aluminum and CFRP in the ACCC conductor.....	97
Figure 74: Exchange current density for aluminum and CFRP in the ACCC.....	98
Figure 75: Tafel slopes and equilibrium potential for aluminum and graphite.	99
Figure 76: Exchange current density for aluminum 6061-T6 and graphite.....	100
Figure 77: Zoomed in: exchange current density for aluminum 6061-T6 and graphite.	100
Figure 78: Illustration of tests.	104
Figure 79: ACCC samples with simulated damage.	105
Figure 80: Applying vacuum to ensure complete electrolyte penetration of the conductor sample.	109
Figure 81: The atmospheric conditions were created in a humidity chamber.	109
Figure 82: Polarization scans of CFRP and Al in agitated, stagnant, and oxygen-deprived 0.6 M NaCl.....	110
Figure 83: Galvanic corrosion current as a function of area ratio (CFRP:Al), NaCl concentration, and agitation level of separated materials immersed in bulk solution.	113
Figure 84: Galvanic corrosion rate for separated and fully assembled conductor samples with 1:28 CFRP/Al area ratios in different environments.	115
Figure 85: Galvanic corrosion potential vs. Ag/AgCl RE. Main bars represent the average value and error bars show the spread within each group of three or more samples.	116
Figure 86: Reaction products.	118
Figure 87: Galvanic corrosion rate vs. mass loss during drying of an ACCC sample with compromised corrosion barrier after immersion in 0.6 M NaCl solution.....	119
Figure 88: Cathodic galvanic corrosion current density for fully assembled samples in different environments and with different surface preparation.....	121
Figure 89: Mass gain [g/m] in addition to the salt load of ~100 mm long ACCC samples with and without galvanic corrosion.....	122
Figure 90: The pathway for oxygen to reach the cathodic reaction on the CFRP.	125
Figure 91: Summary of measured anodic galvanic corrosion current densities, mA/m ² .128	
Figure 92: Summary of measured galvanic corrosion rates, mm/year.	129
Figure 93: Summary of measured galvanic corrosion rates translated into time-to-failure for an overhead transmission line conductor.	130
Figure 94: Deliquescence of different salts in free air.....	138
Figure 95: Mass gain due to deliquescence of different salts in free air as a function of relative humidity.	139
Figure 96: Average electrolyte layer thickness as a function of salt load (NaCl) and relative humidity.	141
Figure 97: Electrolyte layer thickness gain slope as a function of relative humidity.	142
Figure 98: Electrolyte layer thickness – comparison of expression obtained from experimental data and from literature.	145

Figure 99: Electrolyte layer thickness – comparison of expression obtained from experimental data and from literature (zoomed in).....	145
Figure 100: Mass gain for NaCl in free air and on conductor sample.....	146
Figure 101: The pathway for oxygen to reach the cathodic reaction.....	148
Figure 102: i_{lim} as a function of oxygen diffusion through the air in the gaps between the strands.....	157
Figure 103: Electrolyte layer thickness as a function of relative humidity and salt load density.....	158
Figure 104: i_{lim} as a function of oxygen diffusion through the electrolyte layer on the cathode.....	158
Figure 105: Salinity of the electrolyte as a function of salt load density and relative humidity.....	160
Figure 106: Salinity of the electrolyte as a function of salt load density and relative humidity.....	162
Figure 107: Conductivity as a function of RH for non-saturated electrolytes.....	163
Figure 108: Data from the literature (Chen, Cui et al. 2008) for a) NaCl concentration, b) density, c) oxygen solubility, and d) conductivity.....	165
Figure 109: Infinitesimal element of the electrolyte.....	170
Figure 110: The Comsol electrochemistry modules.....	176
Figure 111: Comsol example problem: corrosion prevention.....	176
Figure 112: Comsol example problem: crevice corrosion.....	177
Figure 113: Comsol example problem: corrosion with deformed geometry.....	177
Figure 114: The available ‘physics’ types in the Comsol Corrosion module interface..	178
Figure 115: Applications for the different current distribution alternatives in the Comsol corrosion module.....	179
Figure 116: The available ‘study’ types in the Comsol Corrosion module interface.....	180
Figure 117: Step-by-step procedure for FE modeling of galvanic corrosion in Comsol.....	182
Figure 118: Illustration of the finite element model geometry.....	183
Figure 119: Validation experiment for parallel electrode model.....	184
Figure 120: Illustration of the IR drop.....	193
Figure 121: Analytical solution for parallel electrode model for four different electrolytes and four different electrode distances.....	196
Figure 122: Finite element solution for parallel electrode model for four different electrolytes and four different electrode distances.....	199
Figure 123: Potential gradient through the electrolyte for the parallel electrode model with 100 mm electrode distance.....	200
Figure 124: Validation experiment for parallel electrode model with enclosed electrolyte volume.....	202
Figure 125: Setup for physical validation model (case A).....	203
Figure 126: Comparison of analytical solution, finite element model, and experimental measurements.....	204
Figure 127: Comparison of analytical solution, finite element model, and experimental measurements.....	205

Figure 128: Comparison of analytical solution, finite element model, and experimental measurements for each NaCl concentration.	206
Figure 129: Open electrolyte volume vs. enclosed electrolyte volume.	208
Figure 130: Comparison of analytical solution, finite element model, and experimental measurements for each NaCl concentration.	209
Figure 131: Two ways of creating a 2D model from a 3D structure.	215
Figure 132: Model geometry.	216
Figure 133: Illustrations of the chemical reactions taking place on anode and cathode.	216
Figure 134: The finished geometry for the 1:28 area ratio (98 mm anode) as displayed in the Comsol user interface.	219
Figure 135: The finished geometry with boundaries (in red) and domains (in black). ..	220
Figure 136: Mesh at the domain boundaries.	222
Figure 137: Potential distribution with different anode size, humidity, and salt load density.	224
Figure 138: Local current density.	225
Figure 139: Current density with the 98 mm anode.	225
Figure 140: Maximum cathodic current density.	226
Figure 141: Maximum anodic current density.	226
Figure 142: Average cathodic current density.	227
Figure 143: Average anodic current density.	228
Figure 144: Local corrosion current density for a salt load density of 0.5 g NaCl/m ² ...	229
Figure 145: Average anodic and cathodic galvanic corrosion current densities (model b, 98 mm anode). Note that LD represents as D _{NaCl} (salt load density) in the Comsol interface.	230
Figure 146: Average anodic corrosion current density as a function of salt load density at 100 % RH.	230
Figure 147: Validation samples in the humidity chamber.	232
Figure 148: Averages for anodic galvanic corrosion current densities for days 0 to 5. ..	233
Figure 149: Comparison of experimental data and steady-state numerical model.	234
Figure 150: Average galvanic corrosion current for two sets of five samples in 100 % RH.	235
Figure 151: Average galvanic corrosion current for two sets of five samples in 100 % RH and the cumulative galvanic corrosion charge per meter of conductor.	237
Figure 152: Al(OH) ₃ gel formation on a coplanar aluminum-graphite couple.	239
Figure 153: Al(OH) ₃ gel protruding from the crevices during corrosion testing.	239
Figure 154: Model geometry.	243
Figure 155: Experimentally measured galvanic corrosion rates.	248
Figure 156: Average anodic galvanic corrosion current densities as a function of time.	250
Figure 157: Average anodic galvanic corrosion current densities and thickness Δx, for the first 14 days.	251
Figure 158: Comparison of the steady-state FE model with experimental values.	255
Figure 159: Comparison of the steady-state FE model with experimental values.	256
Figure 160: Typical coaxial cable vs. ACCC.	261

Figure 161: Reflection caused by change in conductor spacing.....	263
Figure 162: Examples of common TDR reflections in coaxial cables.	264
Figure 163: Lumped transmission line parameters:.....	265
Figure 164: Attenuation in ACCC as a function of frequency	272
Figure 165: Reflections from a short pulse and a long pulse for the same two faults. ...	274
Figure 166: Connection between metallic coaxial cable and ACCC cable.	275
Figure 167: Experimental setup.....	276
Figure 168: Waveforms for sub-nanosecond, 10 ns, and 100 ns pulse lengths.....	278
Figure 169: Reflections from open and shorted end of ACCC cable.	280
Figure 170: Reflection from open and shorted end of ACCC cable with 1 nanosecond pulse length.	280
Figure 171: Predicted vs. Experimental attenuation, extrapolated to 2000 m of travel distance through an ACCC cable.....	281
Figure 172: Metal probe inserted to make electrical contact between the Al and the CFRP.....	282
Figure 173: Paper rod soaked in NaCl solution inserted to make electrical contact between the Al and the CFRP.....	282
Figure 174: Reflections from different introduced faults.	283
Figure 175: Reflections from different introduced faults.	284
Figure 176: Potential applications of TDR on ACCC.	288
Figure 177: Summary of measured galvanic corrosion rates, mA/m ²	298
Figure 178: Summary of measured galvanic corrosion rates, mm/year.	299
Figure 179: Summary of measured galvanic corrosion rates translated into time-to-failure for an overhead transmission line conductor.	300
Figure 180: Specified accuracy in the temperature loggers.....	325
Figure 181: Temperature, relative humidity, and dew point fluctuations in the laboratory from May 22, 2014 to January 3, 2015.....	327
Figure 182: Example of ambient temperature and fluctuations in the galvanic corrosion current registered from July 11 to July 14 2014.	327
Figure 183: Noise from heaters in METC.	329
Figure 184: High degree of electrical noise in test series with low corrosion currents. .	329
Figure 185: Specified accuracy in the humidity loggers	330
Figure 186: Calibration of humidity meter and humidity controller.	331
Figure 187: Crystals forming in the Ag/AgCl reference electrode.....	332
Figure 188: Salt bridge.....	333

List of Tables

Table 1: Materials potentially active in the corrosion of the ACCC conductor	5
Table 2: Positions of some metals in order of energy required to convert their oxides to produce 1 kg of metal.	17
Table 3: Conversion of corrosion rates for aluminum.	46
Table 4: Molar conductivity of some common ions at 25°C	48
Table 5: Conductivity and resistivity of select electrolytes	50
Table 6: Anodic galvanic corrosion current density in ACCC samples	87
Table 7: Input values for numerical modeling	101
Table 8: Conductivity, resistivity, and dissolved oxygen concentration of the electrolytes	102
Table 9: Input values for parallel electrode model in 0.6 M NaCl at RT	131
Table 10: Salts included in the test of hygroscopic properties, their Deliquescence Relative Humidity (DHR) at 25°C, and common uses	135
Table 11: Electrolyte concentrations and resulting salt load densities	141
Table 12: Diffusion coefficients for oxygen at 20°C.....	148
Table 13: Maximum theoretical cathodic current density vs. measured cathodic current density.....	153
Table 14: Conductive heat transfer vs. Ionic conduction – the same mathematical base	173
Table 15: Input values for parallel electrode model in 0.6 M NaCl at RT	184
Table 16: Resistance of selected electrolytes.....	189
Table 17: Iterations to solve galvanic corrosion current, parallel electrode model in 0.6 M NaCl with 25 mm electrode distance	194
Table 18: Input values and functions for COMSOL.....	221
Table 19: Data for the ACCC cable of the size “Drake”	266
Table 20: Predicted attenuation in ACCC as function of frequency (expressed as loss of voltage)	273
Table 21: Measured characteristic impedance	277
Table 22: Measured vs. Predicted attenuation (expressed as loss in voltage)	281

CHAPTER ONE: INTRODUCTION

Corrosion is like the red-headed step child; it is often ignored until the will is to be settled, or in the engineering case, until the component is already in service and problems are discovered. Galvanic corrosion is a particularly problematic form of corrosion. Two materials that are considered corrosion resistant while used alone - such as aluminum and carbon fiber reinforced polymer matrix composite (CFRP) - can develop severe galvanic corrosion when in physical contact in the same component or structure. The carbon fibers in CFRP are often not fully embedded in the polymer matrix, and fracture, wear or aging can also expose the carbon fibers. A high fiber volume fraction is common in high-performance composites, which typically makes the entire composite component sufficiently conductive to participate in galvanic corrosion. The result can be severely accelerated corrosion of the less noble material, which in this case would be the aluminum.

General engineering practice is to avoid contact between aluminum and CFRP or similar carbon-containing materials in any application where moisture may be present. This includes structures used outdoors such as transmission line conductors and airplane fuselages. Although the general solution is to insulate the CFRP from the aluminum with a layer of glass fiber reinforced composite or a polymer coating, it is of great importance

to understand the consequences if the two materials accidentally get in contact. There may also be applications where a low rate of galvanic corrosion is acceptable.

The cost of corrosion is also visible on the bottom line; the annual cost of corrosion in the world is estimated to \$2.2 trillion. In the United States alone, the cost of corrosion is estimated to \$276 billion, of which the cost for the electrical utilities is \$6.9 billion (NACE 2002).

1.1 Applications of aluminum/carbon composite systems in high voltage engineering

Aluminum/carbon composite systems are found in many different applications. The material combination is typically used where high mechanical performance is required, such as in airplanes, race cars, and high-end bicycles. One specific application of CFRP together with aluminum in the same component has been used as the example in this study: the *High-Temperature Low-Sag (HTLS) conductor design Aluminum Conductor Composite Core (ACCC ®)*¹ manufactured by CTC Global. Although this dissertation is largely focused on this application, the findings are applicable to many other applications utilizing aluminum/carbon composite systems.

This next generation bare overhead transmission line conductor utilizes a Polymer Matrix Composite (PMC) core that carries the mechanical load. The core is surrounded by helically wound aluminum strands, which carry the electrical current. The core is composed of CFRP with an outer layer of unidirectional fiberglass composite that serves as a galvanic corrosion barrier. This hybrid composite with a high temperature epoxy

¹ The generic name *Aluminum Conductor Composite Supported (ACCS)* has been suggested because “ACCC” is a registered trademark. Reference (Håkansson E. et al., In Review) uses the acronym ACCS, while this dissertation will use ACCC consistently.

matrix is manufactured through simultaneous pultrusion. The final core is a straight, solid, and stiff but bendable rod, very similar to a composite fishing rod or golf club shaft.

The ACCC design differs from traditional bi-metallic transmission line conductors such as *Aluminum Conductor Steel Reinforced* (ACSR), which feature galvanized steel wires surrounded by hard-drawn 1350 alloy aluminum strands (Figure 1). Due to the higher mechanical strength and lower mass of the PMC core, the ACCC conductor can have a larger aluminum cross-sectional area. Because the PMC core carries all the mechanical load, the aluminum can be fully annealed which has lower strength but higher conductivity. Combined with the low thermal expansion of the PMC and the higher allowed operating temperature compared to ACSR, an ACCC conductor has up to twice the current-carrying capacity compared to an ACSR conductor with the same outer diameter without exceeding the amount of allowed sag (EPRI 2002), (Clairmont 2008), (Chan, Clairmont et al. 2008).



Figure 1: ACCC vs. ACSR.

Left) ACCC conductor with a hybrid composite core with fully annealed aluminum strands.

Right) Conventional conductor with galvanized steel wires surrounded by hard drawn aluminum strands.

Bare overhead transmission line conductors are exposed to the surrounding environmental conditions without any additional protective covers or coatings.

Traditional conductor designs have a known inherent problem with galvanic corrosion between the galvanized steel and the aluminium that may drastically reduce the service-life in corrosive environments, whereas the ACCC conductor design has no inherent galvanic corrosion problem (Håkansson 2013), (Håkansson, Predecki et al. 2015).

However, galvanic corrosion can develop in the ACCC conductor if the fiberglass barrier is compromised and CFRP-to-metal contact is present anywhere in the conductor. The fiberglass barrier can be damaged by over-bending (Burks, Armentrout et al. 2009), impact (see Figure 2), fatigue (Burks, Armentrout et al. 2011) (see Figure 3), or aging (Burks, Armentrout et al. 2011), (Hoffman, Middleton et al. 2015). With a high fiber volume fraction, the entire composite component is sufficiently conductive to participate in galvanic corrosion.



Figure 2: Laboratory induced damage through low-velocity impact. The composite core fails in shear resulting in a long crack extending into the conductor. Photo courtesy of Daniel Waters.



Figure 3: Cracks in the ACCC conductor corrosion barrier caused by Aeolian vibrations (high cycle fatigue).

Photo from (Burks, Armentrout et al. 2011).

Table 1: Materials potentially active in the corrosion of the ACCC conductor			
Component:	Active material:	Chemical composition:	Comment:
Aluminum strands	Al 1350-O	Aluminum ($\geq 99.5\%$) Iron ($\leq 0.40\%$) Silicon ($\leq 0.10\%$) (Matweb 2013)	Only components $\geq 0.10\%$ listed here.
CFRP core	Carbon fibers	Carbon (approx. 65 % volume fraction of the composite)	

Galvanic corrosion is both a power transmission problem and a safety problem. Significant loss of aluminum cross-section due to localized corrosion as well as corrosion of splices and joints can increase the resistance, resulting in a local elevation of the temperature. The increased temperature represents both a loss of power and potential problem of overheating of the conductor. Overheating can cause breakdown of the epoxy matrix in the core, which eventually can lead to catastrophic failure of the conductor.

Failure of the conductor presents a risk for people and property, as well as a risk for power blackouts (Brennan 2004).

1.1.1 The transmission line service environment

Transmission line refers in this case to the part of the electrical grid that is designed to transmit large quantities of electricity from power plants to substations (not to be confused *with transmission line theory* that will be presented in chapter 8).

Transmission lines can be placed underground or in the air. Overhead transmission lines consist of large metallic conductors hung from tall towers. In contrast to underground cables and wiring used in buildings that has a continuous outer layer of an insulating polymer, the overhead conductors are typically *bare*. The conductors are insulated from the towers with large insulators made of fiberglass composite, porcelain, or glass, while the air insulates the conductor from the surrounding environment. The system voltages are typically from 96 000 V up to 765 000 V, but can be even higher.



Figure 4: Transmission line structure in New Zealand. The salt laden ocean winds cause large problems with corrosion.

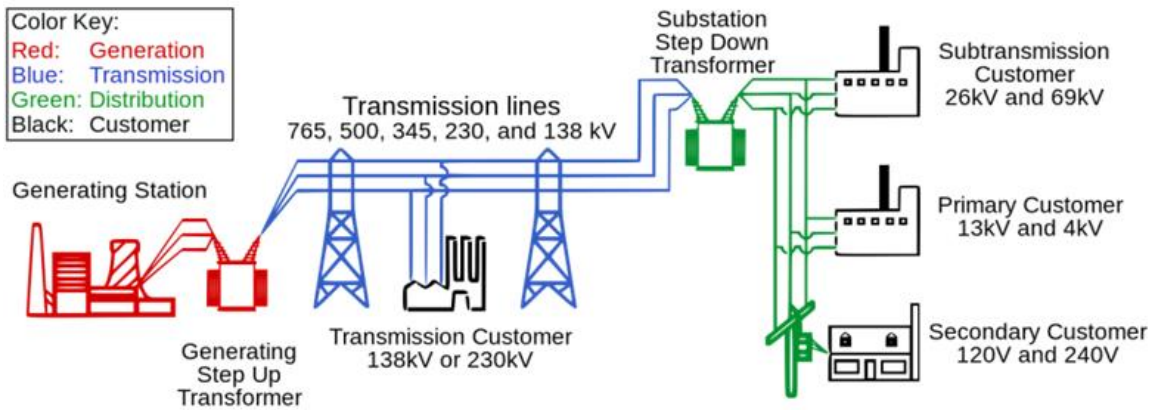


Figure 5: Schematic of the generation, transmission and distribution system.
 Source: Public domain Creative Commons 3.0, DOE, J J Messerly.



Figure 6: The author standing on the foundation (circled) shows the scale of a typical transmission line tower located in New Zealand.

One of the most corrosive environments in the world for transmission lines is New Zealand due to the salt laden ocean winds (Renton 2013). Figure 7 through Figure 11 show the corrosion damage to ACSR conductors after 35 years in service. The aluminum strands exhibit severe pitting corrosion and the conductor has started to bulge in places due to build-up of corrosion products between the strands. The steel strands in the bulges have lost a large fraction of the aluminum cladding.



*Figure 7: Bulging of ACSR conductor due to build-up of corrosion products.
From (Renton 2013)*



*Figure 8: Severe corrosion damage on ACSR conductor after 35 years in service in New Zealand.
From (Renton 2013)*

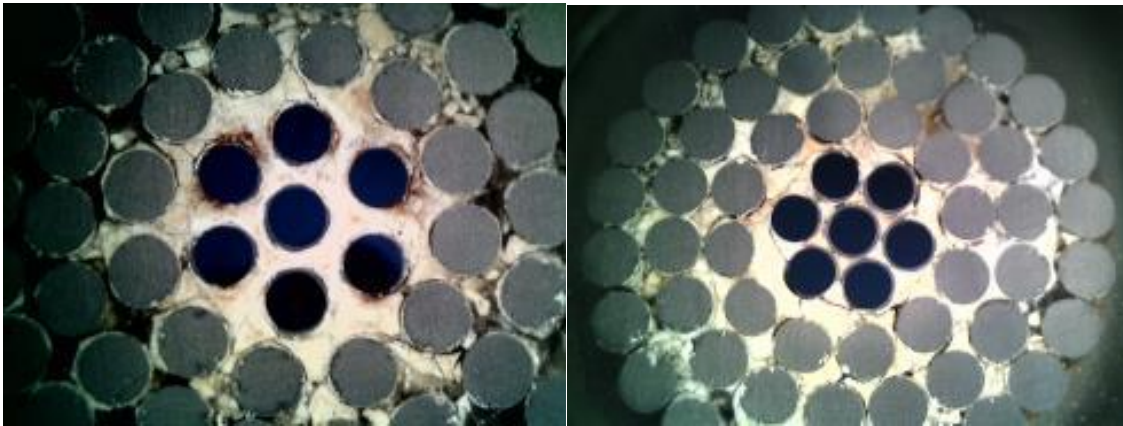


*Figure 9: Sectioning of the conductor in previous figures.
Left: Sectioning in a bulge. Right: Sectioning of a much less bulging section.*

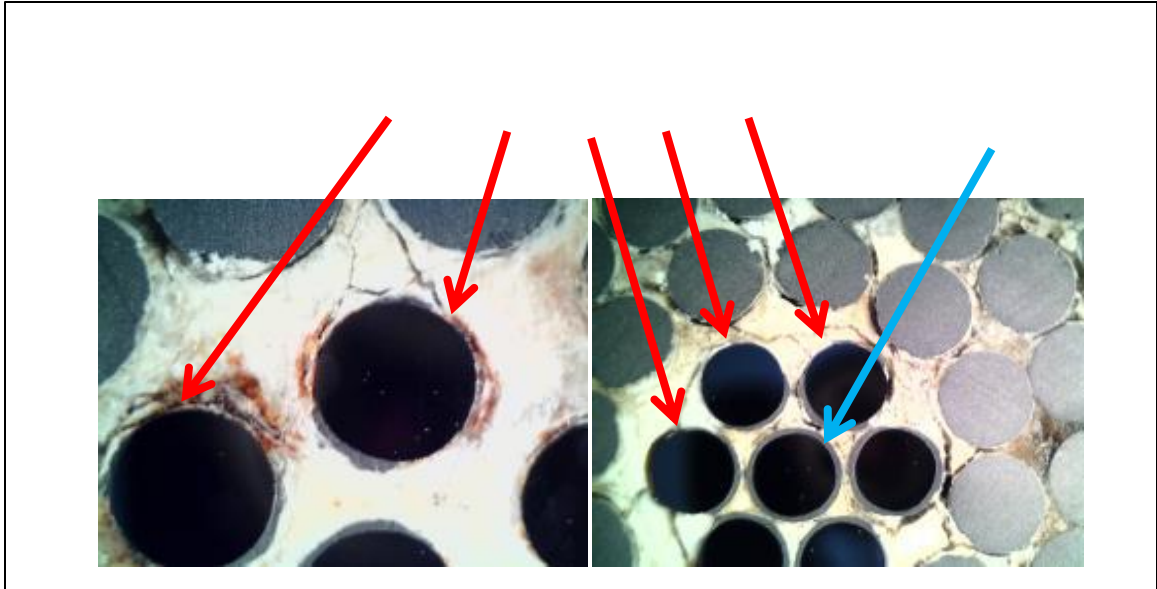


Figure 10: Close-up of the steel strands in previous figure. A large fraction of the aluminum cladding on the steel strands is lost. The red arrows point out areas where the loss is particularly large.

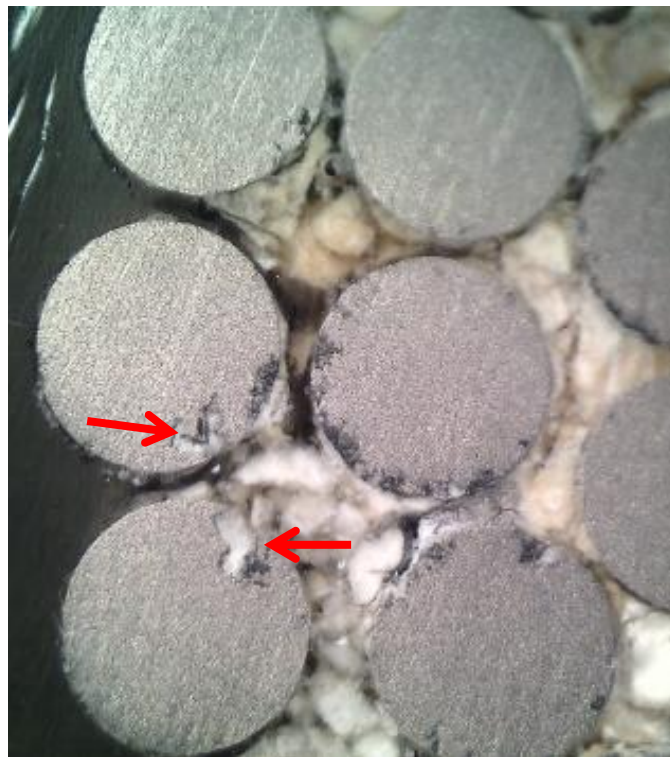


Figure 11: Close-up of pitting corrosion of the aluminum strands in Figure 9. The red arrows point out two particularly deep pits.

1.1.2 Results from previous galvanic corrosion research

This dissertation is a continuation from the author's master's thesis (Håkansson 2013), which was a comparative study of the galvanic corrosion performance of several different bare overhead transmission line conductors. One of the conductors was ACCC, and this section will summarize the findings regarding the ACCC and how it compares with other conductor designs, namely ACSR, ACSS (Aluminum Conductor Steel Supported) and ACCR (Aluminum Conductor Composite Reinforced). ACSS can be considered an improved version of ACSR, which was presented above. ACCR has a core of unidirectional metal matrix composite consisting of aluminum oxide (Al_2O_3) fibers embedded in an aluminum matrix. The surrounding strands are made from Al-Zr alloy. Figure 12 summarizes the galvanic corrosion rate in 3 mass % NaCl solution at room temperature and 85°C.

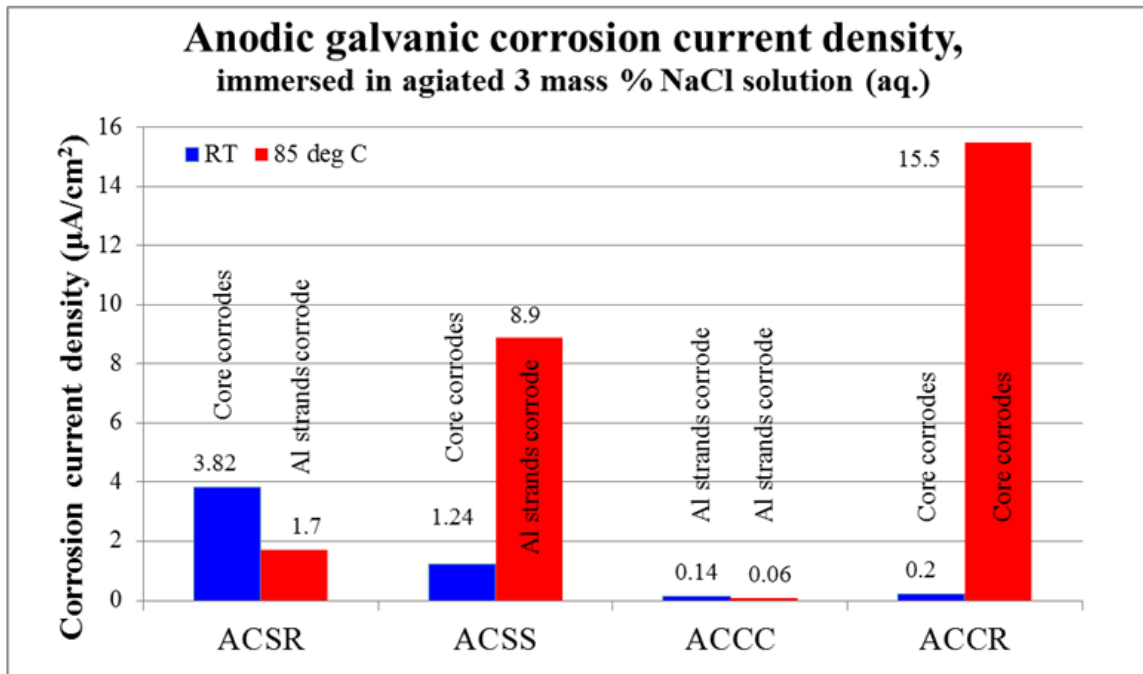


Figure 12: Anodic galvanic corrosion current density in 3 mass % NaCl solution. From (Håkansson 2013).

The galvanic corrosion rates were measured using an early version of the unique sample design presented in chapter 3. The extremely low galvanic corrosion rate exhibited by the ACCC was both intriguing and a reason for concern. It was a pleasant surprise that the galvanic corrosion rate was so low, but there was also a concern that the immersed testing was not giving an accurate prediction of the performance in the atmospheric service environment. The extremely high galvanic corrosion rate of the ACCR at 85°C also indicated that the testing methodology was neither fair nor generating accurate predictions for the real service environment. These results prompted a deeper analysis of the corrosion mechanisms in ACCC, and the result of this study is presented in this dissertation.

1.2 Applications of aluminum/carbon composite systems in aerospace

The combination of CFRP and lightweight metals such as aluminum is attractive for aerospace use due to its excellent mechanical properties. The amount of composite material in commercial aircraft is increasing, with Boeing 787 as a prime example where composites are used extensively in the airframe and primary structures (see Figure 13) (Hale 2006). However, the attitude towards galvanic corrosion appears to be quite different in the aerospace industry than in the power transmission industry. While galvanic corrosion is undesirable but accepted in power transmission, galvanic corrosion is rarely tolerated in aerospace. CFRPs present a particularly challenging situation due to the high conductivity of the carbon fibers and large potential difference between the carbon fibers and the aluminum alloys used in aircraft structures. The only practical

method to prevent galvanic corrosion is to keep moisture from bridging the two materials by use of coatings, sealants, and proper drainage (Banis, Marceau et al. 1999).

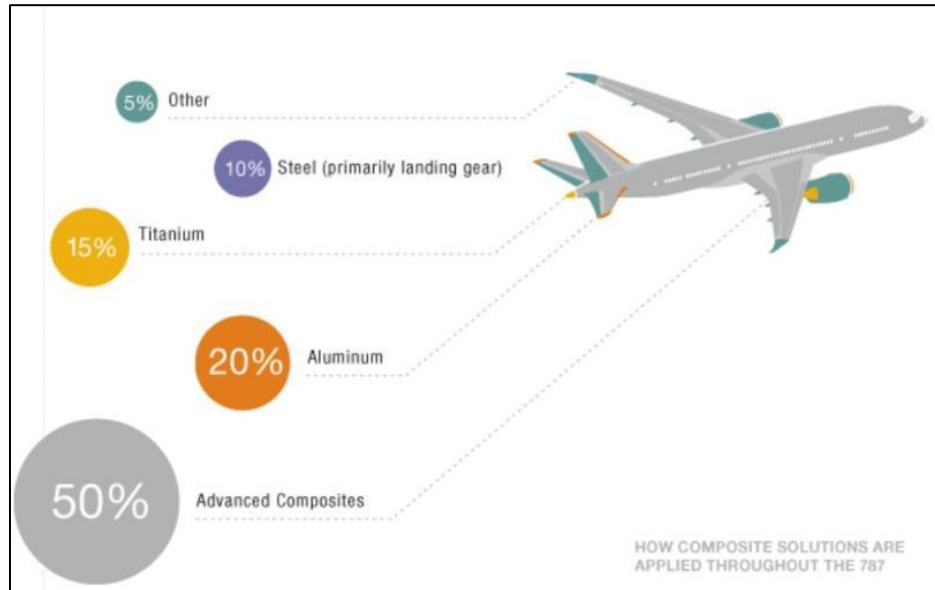


Figure 13: Materials used in the Boeing 787 Dreamliner.
From (Hale 2006)

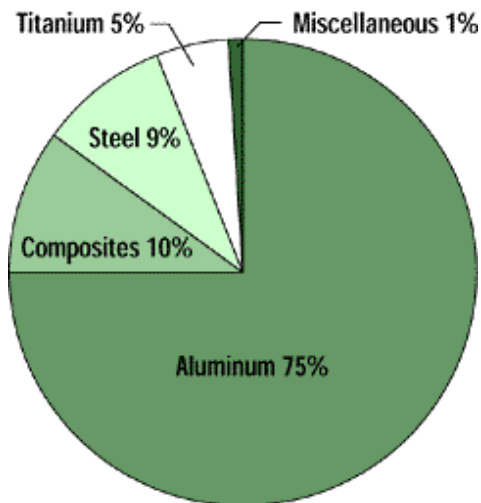


Figure 14: Traditional distribution of materials in airplanes.
From (Banis, Marceau et al. 1999)

The aircraft manufacturer, Boeing, groups materials into four categories based on the galvanic properties (Figure 15). Unless considered necessary from a cost or weight

perspective, Boeing’s objective is to avoid coupling materials from different groups. If coupling cannot be avoided; finishing and sealants are used to prevent corrosion (Banis, Marceau et al. 1999). Aluminum is found in group 2 while CFRP (with a graphite base) is in group 4, indicating that this is a material combination that should be avoided


Reactive end (anodic)  Passive end (cathodic)	1	Magnesium and magnesium alloys.
	2	Cadmium-titanium plate and cadmium, zinc, aluminum, and their alloys.
	3	Iron, steels (except the corrosion-resistant steels), lead, tin, and their alloys.
	4	Copper, brass, bronze, copper-beryllium, copper-nickel, chromium, nickel and nickel-base alloys, cobalt-base alloys, corrosion-resistant steels (200, 300, 400 series PH steels), graphite, titanium, and titanium alloys.

Figure 15: Rating of material from a galvanic corrosion perspective.
From (Banis, Marceau et al. 1999)

Because the tolerance for galvanic corrosion in aerospace applications is very low, the research presented in this dissertation is more applicable to areas where a low level of galvanic corrosion may be tolerated, such as in power transmission. However, some of the findings may be useful for the aerospace sector anyway.

1.3 Research objective

The objective of this research was to improve the fundamental understanding of galvanic corrosion in aluminum/carbon composite systems through experimental work and numerical modeling. The objective was also to develop a method to quantify the galvanic corrosion in a specific application of aluminum/carbon composites, namely a high-temperature low-sag bare overhead transmission line conductor utilizing a carbon fiber reinforced composite core. In addition, the objective was to develop a monitoring

method for the named conductor. The galvanic corrosion has been studied from a mechanical engineering perspective, with the motivation to develop methods to predict and prevent this threat to the mechanical integrity of the system.

1.4 Research sponsors

This research was funded by the NSF I/UCRC Center for Novel High Voltage Materials and Structures under #IIP 1362135 and by the NSF Grant Opportunities for Academic Liaison with Industry program under #CMMI-123252. The work was performed at the University of Denver over the period 2011-2016. This dissertation is a continuation of the author's master's thesis (Håkansson 2013) that was completed in June 2013.

CHAPTER TWO: FUNDAMENTALS OF GALVANIC CORROSION

Corrosion is a natural phenomenon. Most metals occur in nature as minerals and ores, which are more favorable forms from an energy perspective because of their lower energy states. Large amounts of energy are needed to convert, for example, aluminum ore to aluminum. The high energy state in the metallic form is the driving force of corrosion. The energy used in the production of the metal is returned when the metal corrodes and reverts back to its original state in which it was found or another low-energy state. The energy stored in the metal is relatively large for metals such as aluminum and iron, and relatively low for metals such as gold, silver, and copper (see Table 2). The higher the energy, the higher is the metal's tendency to release this energy by corrosion (Roberge 2008).

A metal's tendency to corrode can be determined from the perspective of the Gibbs free energy change as the material goes from reactants to reaction products. Only when the change in Gibbs free energy is negative ($\Delta G^{\circ}_T < 0$), can the corrosion reaction happen spontaneously. However, the negative value of the Gibbs energy change only points out the *possibility* of the reaction, not its probability or *rate*. Kinetic restrictions typically prevail over thermodynamic possibilities (Groisman 2010).

Table 2: Positions of some metals in order of energy required to convert their oxides to produce 1 kg of metal.			
Source: (Roberge 2008)			
	Metal	Oxide	Energy (MJ/kg)
Highest Energy	Li	Li ₂ O	40.94
	Al	Al ₂ O ₃	29.44
	Mg	MgO	23.52
	Ti	TiO ₂	18.66
	Cr	Cr ₂ O ₃	10.24
	Na	Na ₂ O	8.32
	Fe	Fe ₂ O ₃	6.71
	Zn	ZnO	4.93
	K	K ₂ O	4.17
	Ni	NiO	3.65
	Cu	Cu ₂ O	1.18
	Pb	PbO	0.92
	Pt	PtO ₂	0.44
	Ag	Ag ₂ O	0.06
Lowest Energy	Au	Au ₂ O ₃	-0.18



Figure 16: Trailer license plate lost due to galvanic corrosion between the steel screws and the Al plate. The corrosion was caused by exposure to NaCl, MgCl₂ and other salts during several trips to the Bonneville Salt Flats, Utah. The original green paint from the license plate can still be seen on top of the aluminum corrosion products.

Galvanic corrosion may occur when two metals or other conductive materials of a different nature are in contact with each other and an electrolyte such as rain, ocean spray or moisture is present and bridges the two materials. The galvanic corrosion is caused by

the difference in the susceptibility of two metals to corrode (Roberge 2008). Galvanic corrosion can also occur between a metal and a nonmetallic conductor such as graphite, CFRP, or other carbon-filled polymer that is sufficiently conductive.

Galvanic corrosion is named after Luigi Galvani, who discovered the effect in the 1700s (Roberge 2008). The word “corrosion” comes from the Latin’s “corrodere”, which means “to eat away”(Groysman 2010).

Forms of corrosion

Galvanic corrosion is often listed as a form of corrosion - Figure 17 from Davis (Davis 1999) is no exception - but it is more accurate to describe it as a mechanism that accelerates other forms of corrosion, rather than a form of corrosion itself. The galvanic action simply accelerates the corrosion rate, making an existing corrosion problem even worse, but does not otherwise change the type of corrosion (Davis 1999).

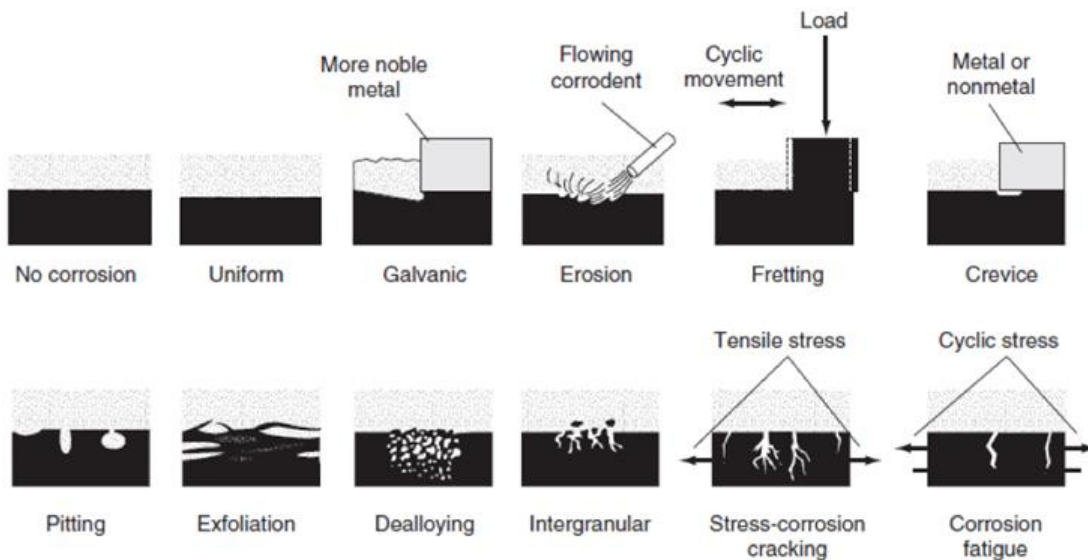


Figure 17: Forms of corrosion.
Source: (Davis 1999).

During galvanic corrosion, the rate of corrosion of one member of the galvanic couple is increased above that which would occur if the material were exposed to the same environment but without galvanic coupling. The rate of corrosion of the other member will be reduced or even cease completely. The change in corrosion rates when the two materials are galvanically coupled is the *galvanic corrosion*. The effect of galvanic corrosion is often localized to the joint of the two materials. The severity of the galvanic corrosion may vary significantly from a negligible increase in corrosion rate for one of the materials to a large increase in corrosion, causing rapid failure (Francis 2000).

Galvanic corrosion can be compared to the function of a battery with its two electrodes and the electrolyte. Three conditions must be met simultaneously for galvanic corrosion to take place (Vargel 2004):

- 1) two metals of different nature, or one metal and a conductive non-metal,
- 2) presence of an electrolyte,
- 3) electrical continuity.

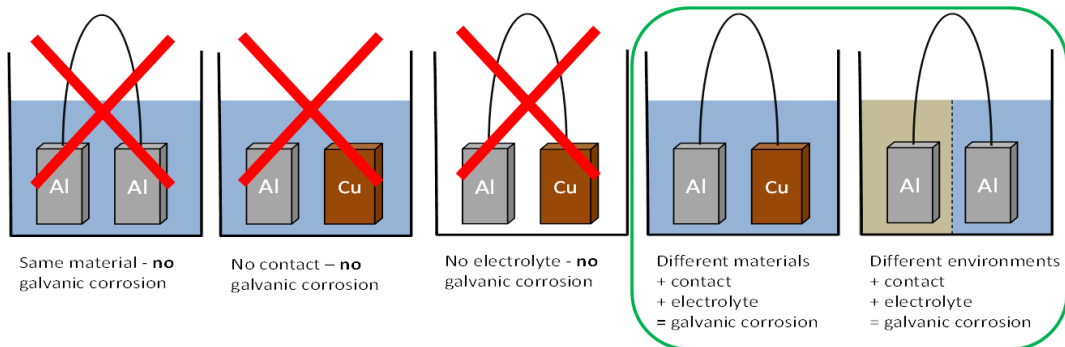


Figure 18: Requirements for galvanic corrosion to occur.

If even one of these three conditions is not met, galvanic corrosion will not occur.

Figure 18 illustrates scenarios where galvanic corrosion will and will not take place. For

example, if the two metals are not in direct electrical contact with each other, no electrons can flow and no anodic or cathodic reaction will take place. If there is no electrolyte present, no ions can flow and no reaction will take place.

Galvanic corrosion is typically associated with dissimilar metals or materials, but galvanic corrosion can under certain conditions also occur on the *same* metal.

Acceleration of corrosion can be caused by the phenomena known as *differential aeration cells* and *concentration cells*. The difference in concentration of some component in the electrolyte leads to discrete cathodic and anodic regions on the same metal, which accelerates the corrosion (NACE/ASTM 2012, Goch 2013). Pitting and crevice corrosion can be seen as galvanic corrosion on a micro scale where the difference between the environment in the deep pit or crevice and the surroundings drives the corrosion.

2.1 Thermodynamics of galvanic corrosion

Galvanic corrosion is a redox-reaction where at least one reduction reaction and at least one oxidation reaction occur simultaneously. The reactions are spatially separated with reduction occurring on the cathode and oxidation on the anode. For galvanic corrosion to occur, the galvanic circuit has to be complete with both a direct metallic connection, and an ionic contact through the electrolyte bridging both materials, as illustrated in Figure 19 (Roberge 2008), (Delmonte 1981), (Francis 2000).

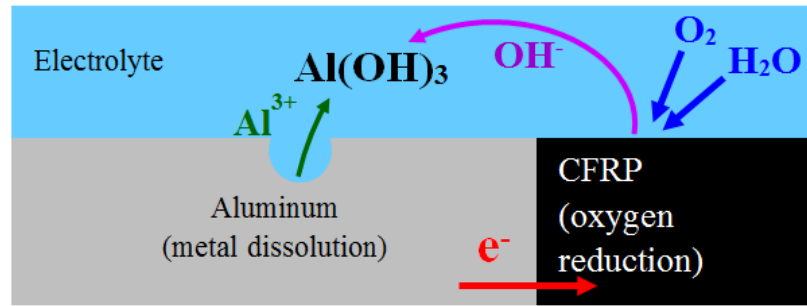


Figure 19: Schematic illustration of the galvanic corrosion between CFRP and Al.

2.1.1 Electrode potential and Nernst equation

In the absence of a galvanic coupling, a metal immersed in an electrolyte will take up an electric potential, known as its *corrosion potential*. The potential is determined by the equilibrium between anodic and cathodic corrosion reactions occurring on the surface of the metal, which are dependent on the material and the nature of the electrolyte that is present (Francis 2000). The dilemma is that the absolute value of this potential cannot be measured. Only potential differences across spatial separations can be measured. Hence, the corrosion potential must be measured against a standard reference electrode, which has been chosen for its stable potential (Munn and Devereux 1991).

When two metals with different corrosion potentials are in electrical contact while immersed in an electrolyte, galvanic corrosion will occur. The metal with the most negative potential will become the *anode*, while the metal with the most positive potential will become the *cathode*. Because of the potential difference, a current will flow from the cathode to the anode to equalize the potentials. The current flow will increase the corrosion on the anodic material. The additional corrosion caused by the coupling is the *galvanic corrosion*, while the corrosion that would occur in the same environment in

absence of the galvanic coupling is often called *self-corrosion* (Francis 2000):

$$\text{Self-corrosion} + \text{Galvanic corrosion} = \text{Total corrosion} \quad (2.1.1-1)$$

At the same time as the corrosion of the anode increases, the corrosion of the cathode decreases. Hence, a material can be protected by coupling to a more anodic material. The anodic material is then called a *sacrificial anode* and is the principle of *cathodic protection* (Francis 2000). Cathodic protection is often used on ships by mounting sacrificial anodes of aluminum or magnesium on the steel hull. The zinc coating on galvanized steel does both serve as a water-tight barrier as well as a sacrificial anode.

The corrosion potential is sometimes also called electromotive force. It is symbolized either with E or ΔU . The potential is related to Gibbs free energy by the Nernst equation (Groisman 2010):

$$\Delta G = - n * F * E \quad (2.1.1-2)$$

where

ΔG = the change of Gibbs free energy [J/mol],

n = valency [e^- /ion] (3 for aluminum),

F = Faraday's constant [C/mol] (9.6483399×10^4 C/mol), and

E = the potential [V].

It is easy to see that the potential is a measure of a metal's susceptibility to corrode; the larger the energy differences between the reactants and the reaction products, the larger the potential.

It should be noted that the potential is affected by many factors and does not have a fixed value even in a specific electrolyte. The potential can vary with changes in the temperature, aeration, and flow rate.

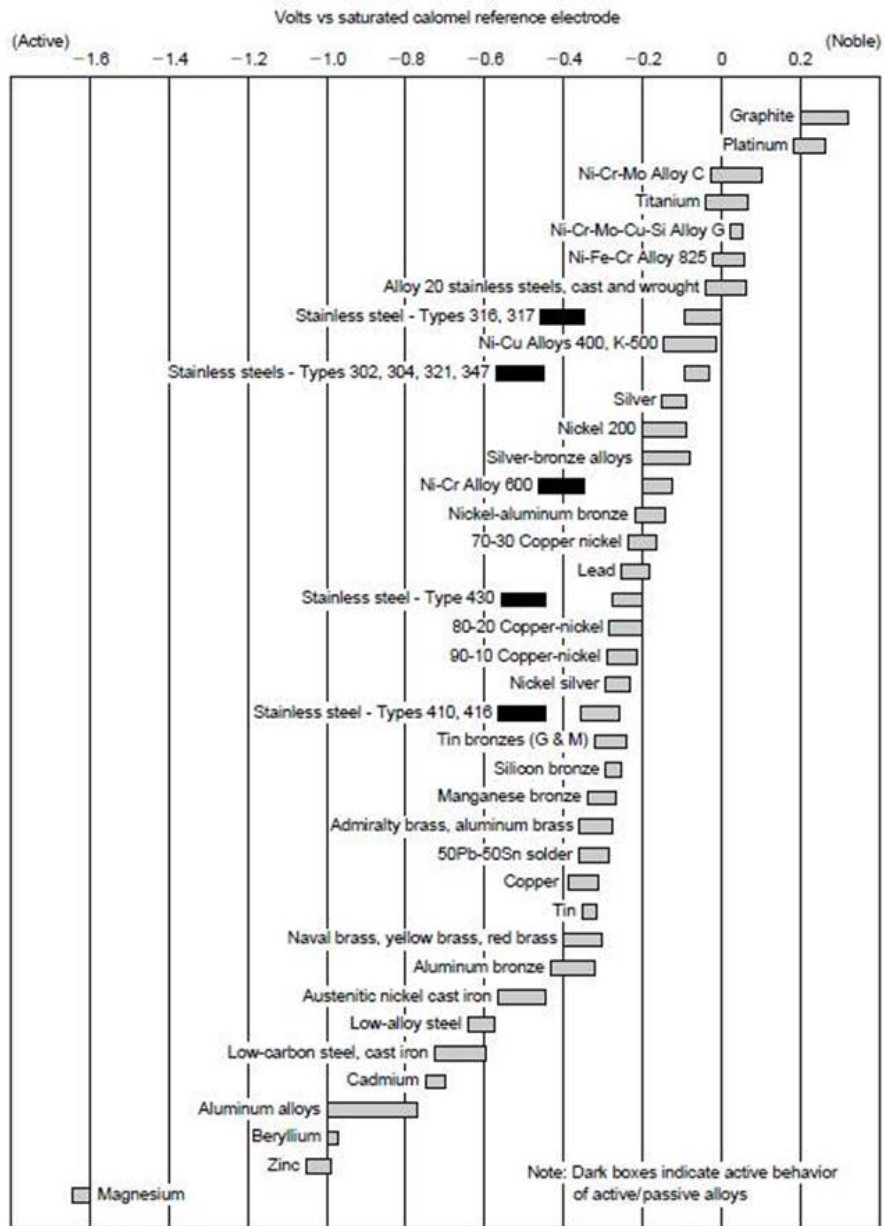
2.1.2 Galvanic series

A galvanic series is created by listing the potentials of metals in a specific environment in decreasing order (Figure 20 and Figure 21). If two of the metals are galvanically coupled, the material further down in the galvanic series will be the anode and the material further up will be the cathode. It is important to note that the galvanic series can only be used to predict the *possible direction* of galvanic corrosion. The potential difference is grossly inadequate for predicting the magnitude of galvanic corrosion since it does not take into account factors such as polarization and area ratio effects (Roberge 2008). However, experience shows that galvanic corrosion may be a problem if two metals in direct contact have a difference in corrosion potential (ΔU) of more than 100-250 mV (Groisman 2010), (Vargel 2004). The difference between CFRP and aluminum in Figure 21 is 800 mV, which is well above these rule-of-thumb values.

Seawater is the most extensively studied electrolyte in galvanic corrosion systems. Figure 20 shows a typical galvanic series for common engineering materials in seawater. Figure 21 shows a galvanic series created in this study of conductor materials

in 3.5 mass % (0.6 M) NaCl solution (the process of generating the galvanic series is presented in chapter 4). The absolute values of the potentials are slightly different since the two series were created using different types of reference electrodes (Saturated calomel vs. Silver/Silver Chloride), but the relative rankings are identical.

As illustrated by their position in the galvanic series, the CFRP takes the role as the cathode and the aluminum as the anode. Coupling may cause accelerated corrosion of the aluminum, while the carbon fibers are inert and will not be affected. The role of the CFRP can be compared with a catalyst; it increases the reaction rate without being consumed. (There is a concern that the corrosion products may affect the polymer matrix, but that is outside the scope of this dissertation.)



Galvanic series for metals and alloys in seawater. Flowing seawater at 2.4 to 4.0 m/s; immersion for 5 to 15 days at 5 to 30°C. (Source: ASTM.)

Figure 20: Galvanic series in seawater. Electromotive force series for metals and alloys in seawater at 5-30°C (dark boxes indicate active behavior of active-passive alloys). Source: (Groisman 2010)

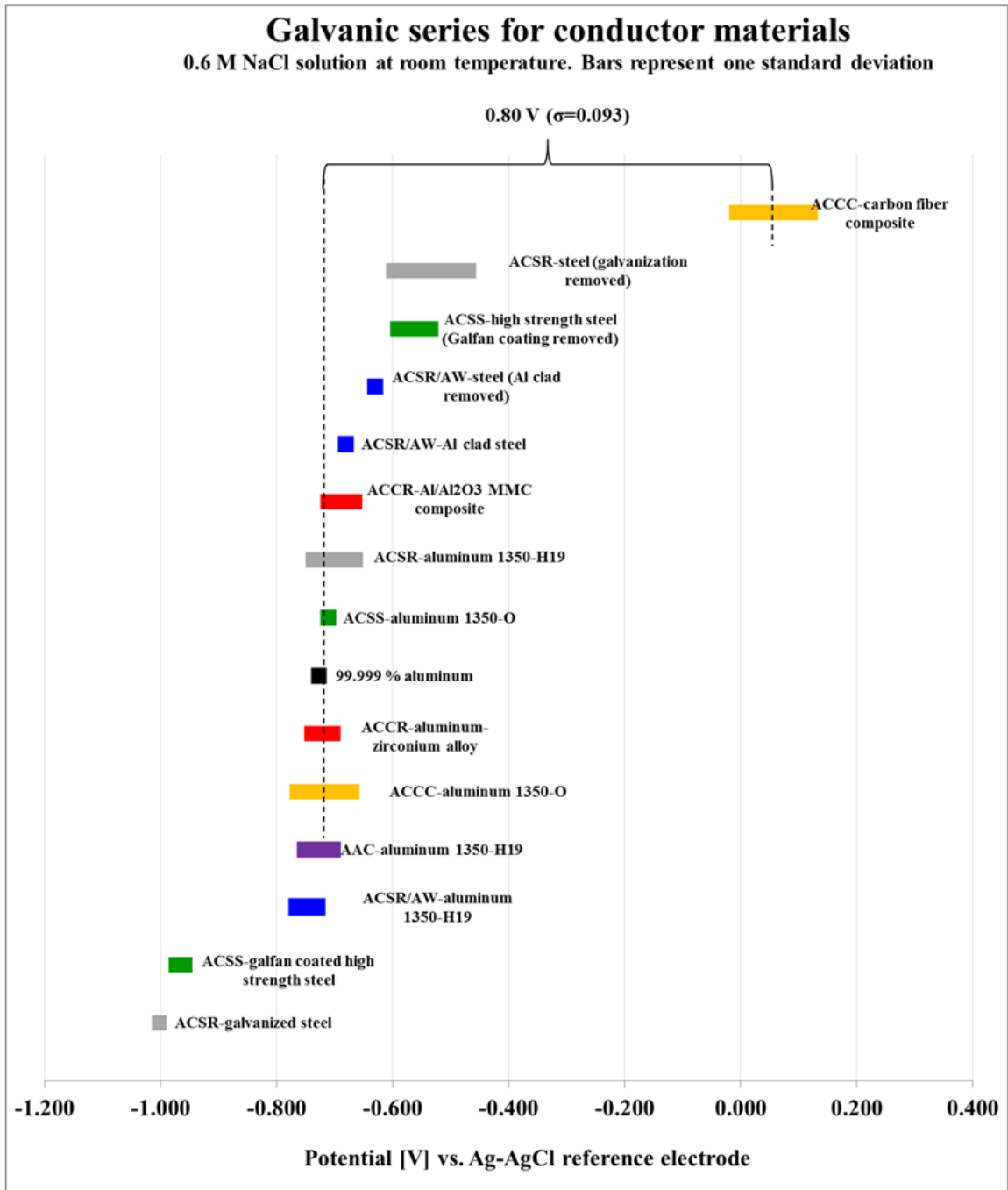


Figure 21: Galvanic series of interest in this study in 0.6 M NaCl at room temperature, vs. Ag/AgCl reference electrode.

The process of generating the galvanic series is presented in chapter 4. (Acronyms refer to common conductor types and are explained in Appendix A.) The difference in corrosion potential between the CFRP and aluminum in the ACCC conductor is highlighted.

2.1.3 Corrosion reactions in aluminum/carbon galvanic couples

The focus of this study is galvanic corrosion in the presence of aqueous electrolytes containing NaCl and with a pH close to neutral, but corrosion can also occur in the presence of non-aqueous electrolytes such as jet fuel, O₂, Cl₂, or acetone (Groysman 2010).

Galvanic corrosion is a redox reaction, which means that oxidation and reduction occur simultaneously. The oxidation reaction occurs mostly, or totally, on the anode and the reduction reaction occurs mostly, or totally, on the cathode. There can be multiple cathodic reactions, as well as multiple anodic reactions occurring simultaneously (Roberge 2008). This section will present the most common reactions in the studied aluminum/carbon galvanic couples.

Anodic reaction

The general anodic reaction during corrosion is the dissolution of metal where the corroding material is transformed into ions:



where the value of n depends on the nature of the metal (it is always 3 for aluminum, while the valence can vary for other metals) (Vargel 2004), (Roberge 2008), (Francis 2000).

For aluminum, the anodic reaction is:



Cathodic reactions

The anodic reaction must be balanced by the cathodic reaction(s). There are a number of different possible cathodic reactions. All the cathodic reactions have one thing in common – they consume the electrons released in the anodic reaction(s). The reaction depends both on the metals involved and environmental factors such as pH and dissolved oxygen. The anodic corrosion of aluminum in neutral electrolytes sometimes develops enough energy to split water directly on the cathodic site. Figure 22 illustrates this process. *Water splitting* cathodic reaction (Roberge 2008), (Francis 2000):



Another very common cathodic reaction in neutral or basic solutions exposed to the atmosphere is *oxygen reduction* (Roberge 2008), (Francis 2000), which is illustrated in Figure 23:



The cathodic reaction in *acidic* electrolytes is often the reduction of hydrogen ions to hydrogen gas (Roberge 2008), (Francis 2000):



It is important to note that the cathodic reactions take place on the cathode in an aluminum/carbon galvanic couple, but may take place on the aluminum surface if no other cathode is present. This is the case in pitting corrosion that will be described later.

The difference is that carbon is a much more efficient cathode, and the contact with it will increase the total corrosion rate.

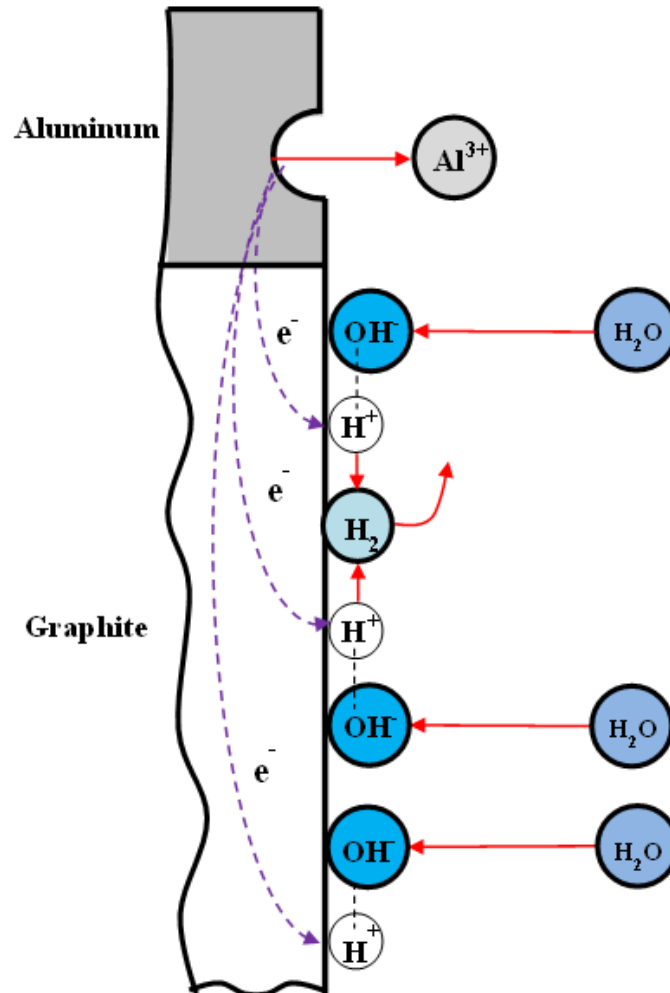


Figure 22: Splitting of water during corrosion of aluminum.
Note: the reaction is not balanced.

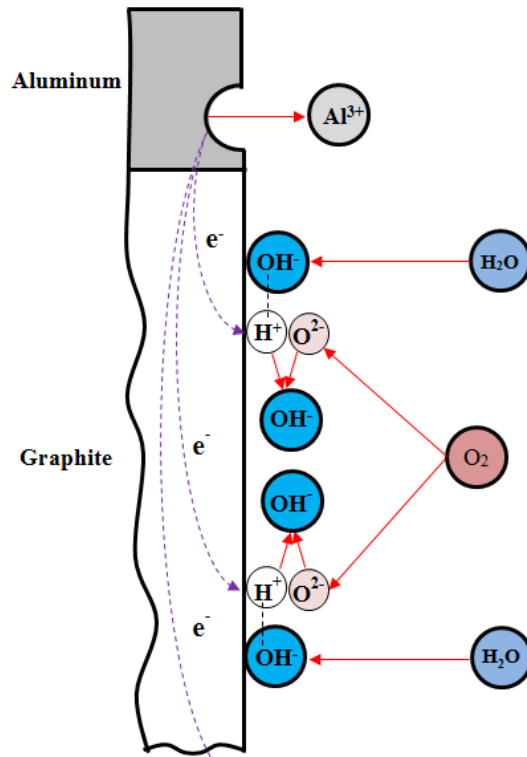
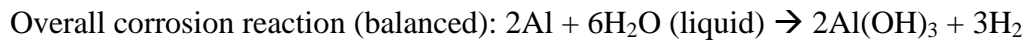
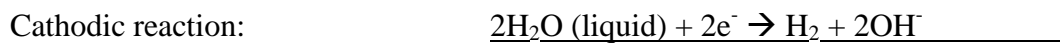


Figure 23: Reduction of oxygen during corrosion of aluminum.
 Note: the reaction is not balanced.

Combined reactions

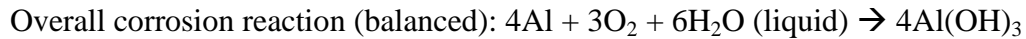
On a global level, the corrosion reaction is the sum of the anodic and cathodic reactions (Vargel 2004). The two most likely combined reactions for corrosion of the aluminum components studied in this work are the following:

Splitting of water: (2.1.3-6)



Reduction of oxygen:

(2.1.3-7)



Both reactions result in the formation of aluminum hydroxide Al(OH)_3 , which is the most likely corrosion product in the corrosion of aluminum (Vargel 2004), (Francis 2000). Newly formed Al(OH)_3 precipitates as a gelatinous substance on the surface of the corroding material (Vargel 2004). The Al(OH)_3 may eventually crystallize and dry to a white solid, which can be seen in Figure 24. Powder X-ray Diffraction (XRD) of dried corrosion products from testing of high voltage conductors in this study supports the suggested reactions. The pattern displayed matches for gibbsite, boehmite and bayerite, which are all forms of aluminum hydroxide. However, the XRD pattern was somewhat inconclusive since there was also a large amorphous phase present. There could therefore have been other corrosion products present that could not be identified with XRD.



Figure 24: Formation of Al(OH)_3 on the aluminum strands in a transmission line conductor sample. Left) Sample that is still wet; Right) Dried sample.

Local change in pH in the galvanic corrosion of aluminum and graphite

The anodic and cathodic reactions can result in local changes of the pH. The cathodic reactions presented above create hydroxyl ions (OH⁻) which can drastically increase the pH. The anodic reactions can cause a local decrease of the pH because of hydrolysis. Al³⁺ ions cannot exist in water, they form complex ions with water and become [Al(H₂O)₆]³⁺. This aluminum complex acts like an acid and donates an H⁺ (Vargel 2004):



The Al³⁺ ions soon react with the OH⁻ ions generated by the cathodic reactions, but until then they will cause a local decrease in pH. In the same way, the generation of OH⁻ ions at the cathode causes a local increase in pH.

The experiment shown in Figure 25 illustrates the local change in pH. The aluminum and graphite are connected to each other by drilling and tapping a hole in each piece. A screw joins the two pieces and ensures good electrical connection. The galvanic couple is then embedded in agar gel with 3.5 mass % NaCl and an added pH indicator. The pH is 3-4 around the anode and 9-10 around the cathode, with a sharp interface between the two areas.

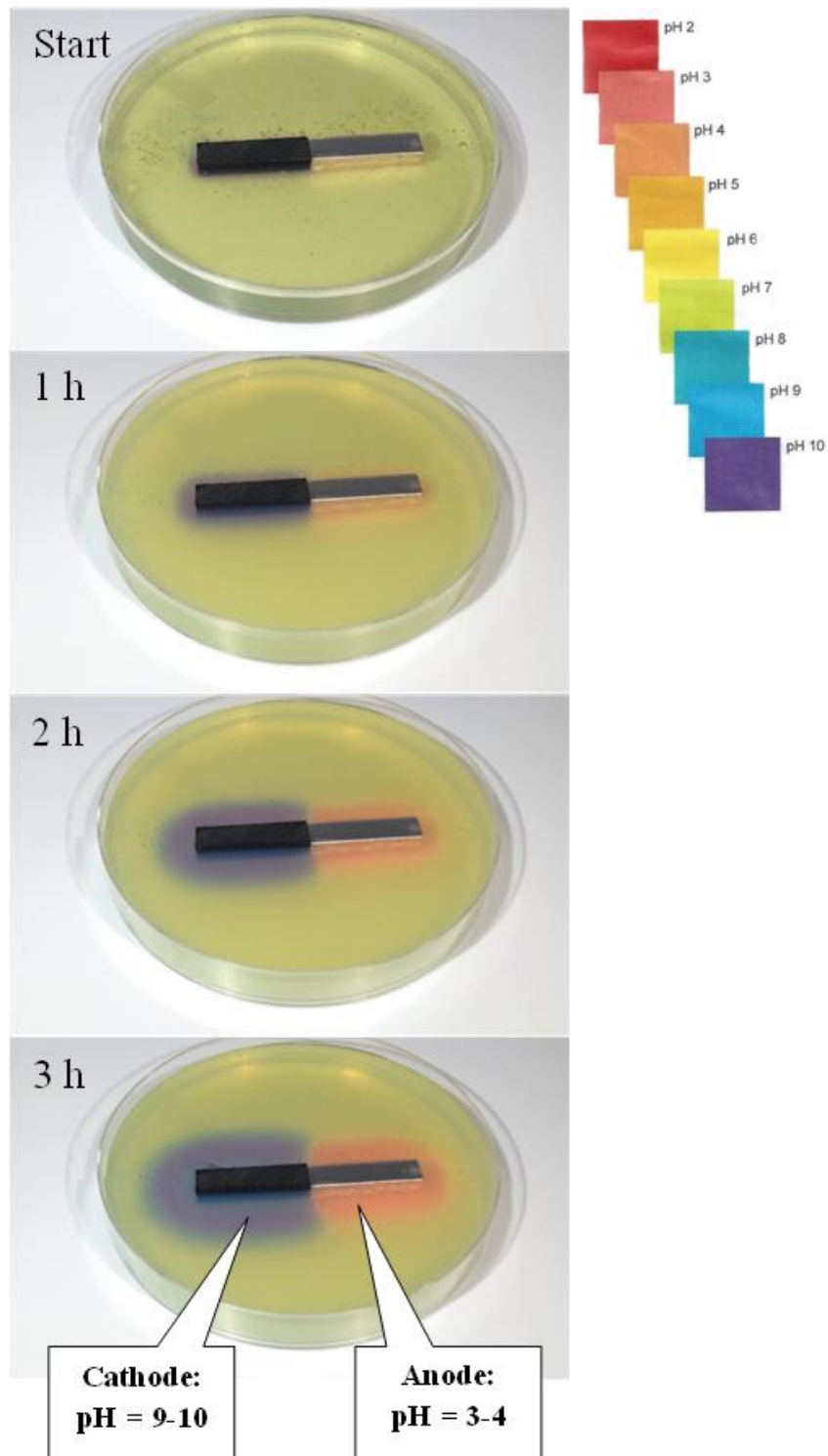


Figure 25: Graphite-Al galvanic corrosion couple embedded in 3.5 mass % NaCl agar gel with added pH indicator.

Color key to the right in the picture.

Autocatalytic reactions and active-passive cells

Pitting corrosion can be envisioned as galvanic corrosion on a micro-scale, and can be transformed to a macro-scale and severely accelerated if a cathode in the form of a conductive carbon containing material is present. When no external electrode such as carbon is present, pitting corrosion is an example of an active-passive cell, in which the anode is the metal in the active state and the cathode is the same metal in the passive state (typically in the form of Al_2O_3) (NACE/ASTM 2012). The cathodic material can also present as inclusions or other microscopic contaminants. When this is the case, the reaction is a galvanic action on a micro-scale, but would still be called pitting corrosion and not galvanic corrosion. Figure 26 illustrates pitting corrosion with two different cathodic reactions caused by microscopic inclusions and Figure 27 shows typical pitting corrosion damage. Pitting corrosion accelerated by galvanic coupling will have the same characteristic pattern.

A similar phenomenon can also occur on a more global level between two similar or identical aluminum alloys. If one of the materials has a problem maintaining its passivity for some reason, the difference in corrosion potential (E_{corr}) between the two metals can result in an electromotive force that accelerates the corrosion. The result will be more severe corrosion of the active material, which will work as a sacrificial anode and protect the more passive material. This was observed in the master's work (Håkansson 2013) preceding this study, where the ACCR conductor with an aluminum matrix composite core was galvanically attacked by the surrounding aluminum alloy strands. This did only occur at 85°C , and did not occur at room temperature. This is an

example of a test procedure that changed the corrosion mechanism in a way that was not representative for the real service environment.

The decrease in pH, as explained above, can sometimes cause localized breakdown of the passive film resulting in accelerated corrosion of the underlying material. This mechanism is called *autocatalytic* and is the cause of pitting and crevice corrosion. Once the passive film is broken and the pit starts to grow, the local environment is altered in such a way that further pit growth is promoted. The pit growth rate is often limited by the mass-transport of metal ions from the pit (Frankel G.S. 2003).

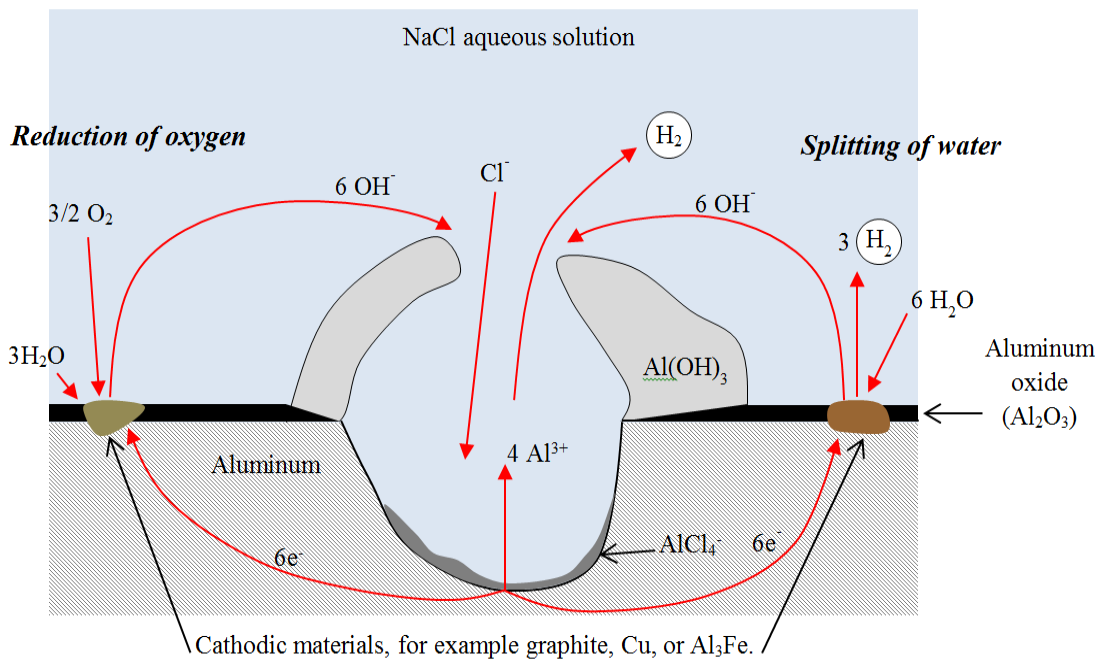


Figure 26: Mechanism of pitting corrosion.
Based on (Vargel 2004)



*Figure 27: Typical pitting corrosion of aluminum.
The strands of an ACCC conductor after 3 months submersion in 85°C, 3 mass % NaCl aqueous solution.*

Aluminum is prone to pitting and crevice corrosion in aqueous electrolytes with neutral or close to neutral pH (4.0 to 8.5) (Davis 1999), which basically includes all natural environments such as seawater, surface water, and moist air (Vargel 2004). The passive layer of Al_2O_3 is stable in pH between 4.0 and 8.5, but becomes unstable and breaks down when the pH locally goes below 4.0 (Frankel G.S. 2003).

In the case of galvanic corrosion of an aluminum/carbon galvanic couple in a neutral electrolyte, the total corrosion rate will be a combination of corrosion damage where the carbon acts as a cathode and where the aluminum itself, or inclusions in the aluminum, acts as a cathode. This will be shown in chapter 4.

Passivation and effect of microstructure

The formation of a stable aluminum oxide (mostly Al_2O_3) film on the aluminum surface is called passivation. The oxide film prevents further corrosion, and this naturally forming layer is the reason for aluminum being considered a corrosion resistant material.

The phenomenon of passivation can cause the galvanic corrosion current to change by six orders of magnitude during a corrosion experiment, as will be shown later. If the oxide layer breaks locally, significant corrosion can occur in a small area. This is the mechanisms behind pitting corrosion, that was described in the previous section (Vargel 2004).

The alloying and microstructure can strongly affect the breakdown of the passive film. Physical or chemical inhomogeneities on the surface form initiation sites for corrosion pits. The same is the case for scratches, inclusions, second-phase particles, intermetallic particles, and grain boundaries (Vargel 2004), (Frankel G.S. 2003). An aluminum alloy or component that is susceptible to pitting corrosion is of course also susceptible to galvanic corrosion in contact with carbon containing materials, as the galvanic coupling provides an even better cathode. The inclusions in aluminum-matrix composites make these materials highly susceptible to corrosion (Davis 1999).

2.2 Kinetics of galvanic corrosion

The thermodynamics determine if a corrosion process can occur, but the *kinetics* controls the rate of the corrosion process. The kinetics often prevail over thermodynamics. Corrosion mechanisms are also often quite complex, and a comprehensive understanding of both the thermodynamics and the kinetics is necessary to predict the corrosion rate in the real service environment (Roberge 2008), (Delmonte 1981), (Francis 2000), (Ricker 1995).

Corrosion processes are not equilibrium reactions; instead, competing processes are common and the corrosion system is typically stochastic and small perturbations can cause large changes in the galvanic corrosion rate. This section will present the kinetics of galvanic corrosion with a focus on the galvanic coupling between aluminum and carbon.

2.2.1 Polarization and electrode efficiency

The rate of the anodic and cathodic reactions in a galvanic couple varies from metal to metal. The faster the reaction rate, the higher the *electrode efficiency* (Francis 2000). The electrode efficiency can also be illustrated by the shift in the potential of the two metals when they are galvanically coupled. The two potentials want to equilibrate and this is what drives the current flow. The anode will shift to a more electropositive value while the cathode will shift to a more electronegative value. This shift is called *polarization*, and is one of the most important phenomena in corrosion kinetics (Francis 2000). As the two metals approach the same potential, the final potential difference between them will be equal to the product of the current and the resistance through the electrolyte. The potential difference is called the *IR drop* after Ohm's law $U=I \cdot R$, (where U is the potential, I is the current and R is the resistance) (Francis 2000).

The extent of the polarization depends both on the metals and the electrolyte, but the cathode is almost always much more polarized than the anode in neutral electrolytes. The efficiency of the cathodic reaction usually has a more significant impact on the galvanic corrosion rate than the efficiency of the anodic reaction. This is also the case in aluminum/carbon galvanic couples studied in this research, and will be discussed in depth

in chapter 4. The more a particular metal (or other conductive material such as CFRP) is polarized, the more effective it is as a cathode to drive the corrosion of the anode (Francis 2000).

2.2.2 Polarization curves and Tafel behavior

The polarization behavior of a metal can be investigated using common electrochemical testing methods such as the *potentiodynamic polarization scan*. The metal is immersed in the electrolyte of interest and a potential is applied. The potential is slowly changed (1-5 mV/sec) and the change in current between the sample and a counter electrode is measured (the method will be used in chapter 4). The result is also called a *polarization curve* (Monk 2001).

The polarization curve for a material in an electrochemical system is somewhat analogous to the stress-strain curve for a mechanical material. The polarization curve represents how the corrosion kinetics responds to a change in the potential, in a similar way to the stress-strain curve describing how the material strain changes with applied stress. The polarization curve is, however, more complicated than the stress-strain curve since the system consists of both a metal and an electrolyte, with a distinct interface between the two. The polarization curve is affected by the properties of the material and the electrolyte, but also by, for example, agitation of the electrolyte. The polarization curve is a necessary part of the input data for most forms of galvanic corrosion modeling. Figure 29 shows the polarization curves for the CFRP and aluminum from an ACCC conductor.

Equilibrium potential, Tafel slope, and exchange current density

The *equilibrium potential* E_{eq} (also known as the *rest potential*), is the potential where the current response is zero. This is the potential the material would have if there were no applied current or potential. It can easily be found in the polarization scan. The equilibrium potentials are marked with dotted lines in Figure 29.

The Tafel equation, named after the Swiss chemist Julius Tafel, describes how the corrosion current on an electrode depends on the electrode potential, and is one of the most fundamental relationships in corrosion kinetics (Monk 2001). The Tafel equation is often stated in the following form:

$$\Delta V = A \cdot \ln\left(\frac{i}{i_0}\right) \quad (2.2.2-1)$$

where

ΔV = over-potential [V] (note that the graph in Figure 28 uses η),

A = is the “Tafel slope” [V/decade],

i = current density [A/m^2],

i_0 = exchange current density [A/m^2].

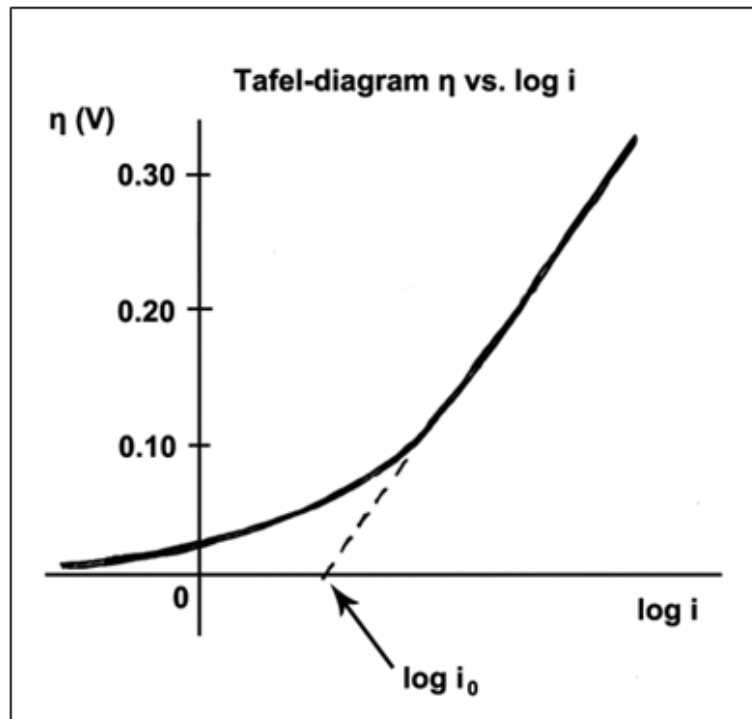


Figure 28: Overpotential η as a function of $\log i$.
Source: Dr Rob CM Jakobs, Eindhoven Technical University, Creative Commons 3.0.

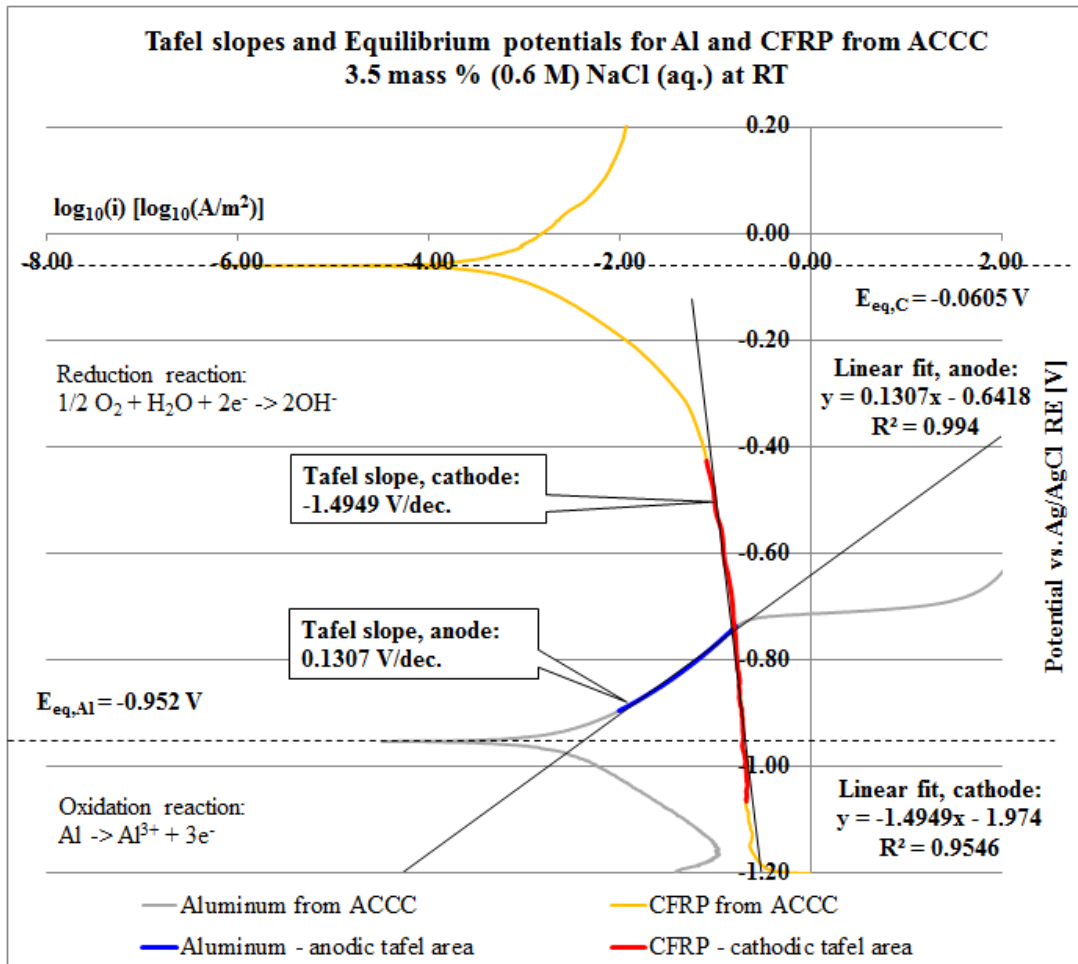


Figure 29: Tafel slopes and equilibrium potential (dotted lines) for aluminum and CFRP in the ACCC conductor.

Figure 29 shows the potentiodynamic polarization curves for the aluminum and CFRP from an ACCC conductor. Note that the independent variable is the applied potential that is plotted on the y-axis, while the dependent variable is the resulting current which is plotted on the x-axis. This is opposite to the standard convention for plotting mathematical relations, but follows the convention commonly used in corrosion science.

The Tafel slopes were extracted from the polarization curves by fitting linear trendlines to the selected regions of the curves. The selected region for the cathode is marked in red, while the selected region for the anode is marked in blue.

Figure 30 illustrates how the *exchange current density* is determined by the intercept of the Tafel slope line with a horizontal axis going through the equilibrium potential. This is most easily accommodated by plotting the lower half of the polarization curve for cathodic material and the upper half of the curve for the anodic material on the same axis as in Figure 30.

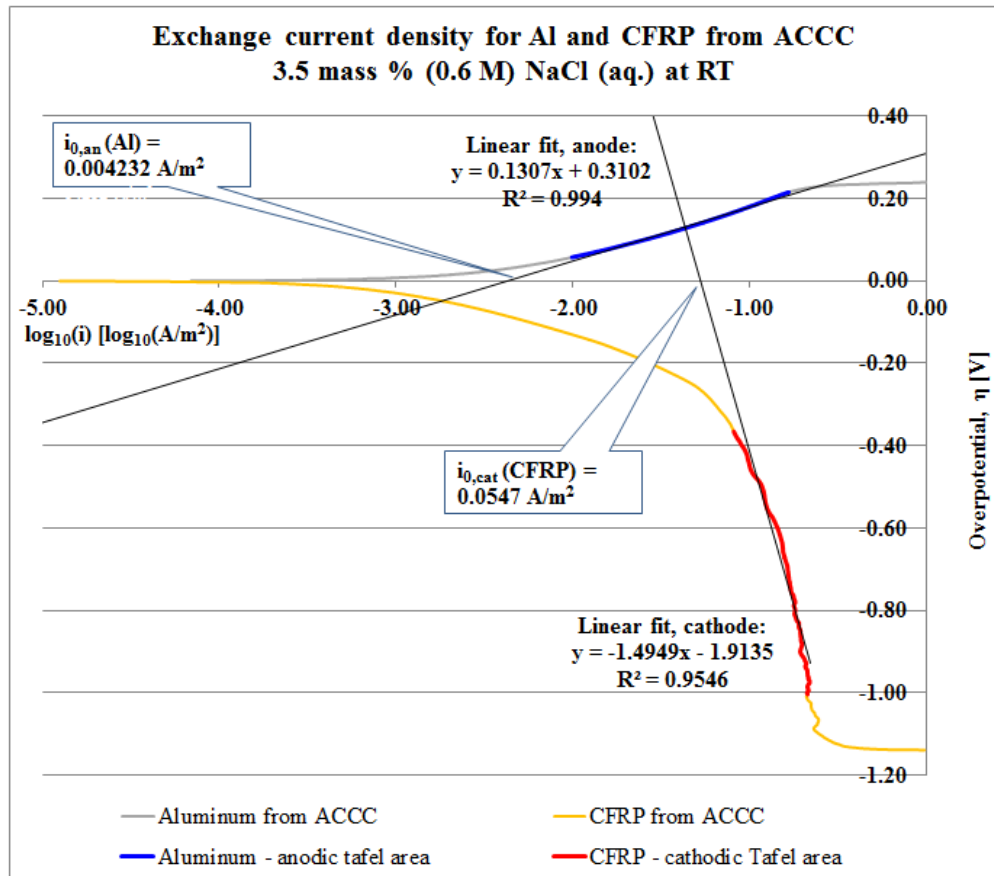


Figure 30: Exchange current density for aluminum and CFRP in the ACCC conductor.

2.2.3 Control type

The polarization behavior and the shape of the polarization curves are highly influenced by the control type of the specific galvanic couple.

1. **Diffusion control** means that the rate of the reaction is controlled by the rate at which reactants arrive at the reacting surface(s). The diffusion of oxygen at the cathode is often not fast enough to sustain the highest possible rate of corrosion. In that case, the corrosion rate is diffusion limited and the reaction is under so called *cathodic control*. If the anodic reaction is the rate limiting reaction, the process is said to be under *anodic control*.
2. **Oxide formation or Resistance controlled.** The formation of an oxide layer on the aluminum, which may or may not lead to passivation, can introduce a high electrical resistance which limits the rate of the corrosion.
3. A **mixed process** where more than one cathodic or anodic reaction occurs at the same time might complicate the model and the interpretation. One example is the simultaneous reduction of oxygen and hydrogen ions (Zhang 2011).

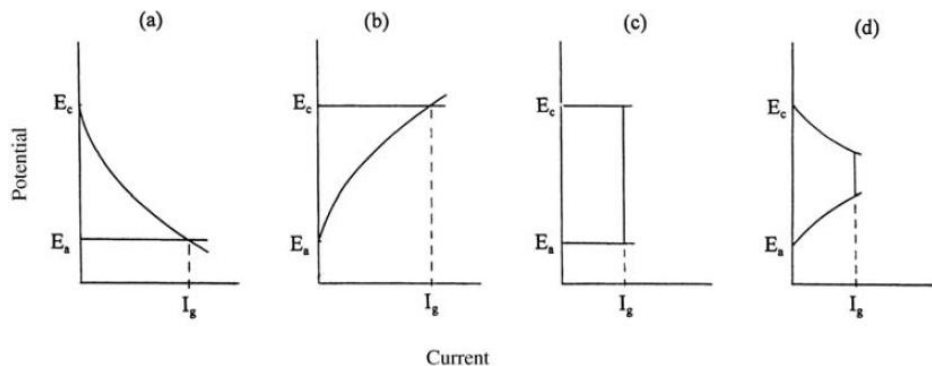


Figure 31: Schematic illustration of the potentiodynamic polarization curves for 4 different control types: a) cathodic control, b) anodic control, c) resistance control, and d) mixed control. The current is the responding corrosion current when a potential is applied. Source: (Revie 2000)

As it will be shown in subsequent chapters, the corrosion of ACCC and aluminum/carbon couples in general appears to be under cathodic control.

2.2.3 Faraday's Law – mass loss calculations from galvanic current

The mass loss due to galvanic corrosion can be calculated using Faraday's law (2.2.3-1), which supplies a direct relation between the corrosion current and the mass loss due to corrosion (Vargel 2004):

$$m = \frac{1}{F} \cdot \frac{W}{n} \cdot I \cdot t \quad (2.2.3-1)$$

where

m = mass lost [g],

W = atomic mass of the metal [g/mol] (27 g/mol for aluminum),

n = valency [e⁻/ion] (3 for aluminum),

I = current [A],

t = time [s],

F = Faraday constant [C/mol] (96 485 C/mol).

To use Faraday's law to calculate loss of thickness due to corrosion, the corrosion has to be uniform. This is typically not the case for aluminum in neutral saltwater.

Faraday's law can still be used to calculate the loss of mass, but the results have to be interpreted with caution and one must keep in mind that the law may dramatically underestimate the problem when localized corrosion occurs (Vargel 2004), (GamryInstruments 2011).

The corrosion current is also often translated into loss of thickness per unit time.

Table 3 contains common units for corrosion of aluminum. The table should be read from left to right, i.e.: $1 \text{ mA/m}^2 = 0.00109 \text{ mm/year}$.

Table 3: Conversion of corrosion rates for aluminum.				
Source: (CorrosionDoctors 2014)				
	A/m ²	mA/m ²	mm/year	g/(m ² *day)
A/m ²	1	1000	1.09	8.05
mA/m ²	0.001	1	0.00109	0.00805
mm/year	0.917	917	1	7.40
g/(m ² *day)	0.124	124.2	0.135	1

2.3 Environmental factors

2.3.1 Temperature

The effect of temperature on galvanic corrosion is complex. In general, all metals become more electronegative in saltwater with increased temperature (Schumacher 1979). An increase in temperature is often expected to increase the galvanic corrosion rate. However, an increase in temperature decreases the solubility of oxygen, which will decrease the corrosion of steel and other metals. Increased temperature can also promote the formation of the natural oxide layer. Extended periods of high temperature can also change the microstructure and thereby also the corrosion behavior (Vargel 2004).

While an increase in temperature causes acceleration of most chemical reactions according to the Arrhenius equation, an increased temperature may also cause evaporation of the water. The effect of temperature on atmospheric galvanic corrosion is therefore even more complex than in immersed conditions. Increased evaporation of the electrolyte decreases the electrolyte thickness but increases the salt concentration.

Changes in ambient temperature also cause simultaneous changes in relative humidity. At high levels of relative humidity, a small decrease in temperature can result in exceeding the dew-point, causing condensation which promotes corrosion. This has been investigated by, for example, Van den Steen (Van den Steen, Simillion et al. 2016).

While the increased salt concentration may increase the conductivity of the electrolyte and potentially increase the corrosion rate, increased temperature and salt concentration limits the solubility of oxygen. The decreased presence of water may also inhibit corrosion. This may result in an overall reduced corrosion rate (Syed 2006). This is particularly true for transmission line conductors that may have a temperature increase due to high electrical loads without any changes in the ambient temperature. Experiments conducted in this study indicate that the galvanic corrosion ceases due to drying at a conductor temperature of approximate 45°C in an ambient condition of 100 % RH and 25°C. The corrosion rate is negligible at temperatures below the freezing point of the electrolyte (Syed 2006).

2.3.2 Conductivity of the electrolyte

The conductivity of the electrolyte is an important parameter in galvanic corrosion because the electrical resistance of the electrolyte may affect the corrosion rate. The corrosion current through the electrolyte is a flow of ions, not electrons. Therefore, the electrical conductance (the inverse of the resistance) in aqueous solutions is determined by the mobility of ions, not electrons. The higher the mobility of ions and the higher the valence, the higher the ability to carry the electric corrosion current between

the anodic and cathodic sites, and the greater the galvanic corrosion and the more aggressive the solution is towards the metals (Groysman 2010), (Vargel 2004), (RadiometerAnalytical 2004). Not all ions carry charge (conduct electricity) equally. H⁺ and OH⁻ have very high mobility and are very good charge carriers, while Na⁺ and Cl⁻ move at a slower rate and are not as good conductors. Table 4 shows the molar conductivity of some common ions.

Table 4: Molar conductivity of some common ions at 25°C		
Source: (Zoski 2007)		
Type of ion	Ion	Molar conductivity [S*L/(mol*m)]
Cations	H ⁺	34.982
	Na ⁺	5.011
	NH ₄ ⁺	7.35
	K ⁺	7.35
Anions	OH ⁻	19.86
	Cl ⁻	7.635
	CH ₃ COO ⁻	4.09
	Br ⁻	7.81

The conductivity can be measured with a conductivity meter, but no equipment of this kind was available during this study. The conductivity was instead calculated using Kohlrausch's law. The conductivity varies greatly with the ion concentration and the types of ions present. The molar conductivity is the sum of the conductivities for the cations and the anions (Boyes 2009), (Zoski 2007):

$$\kappa = z_+ \cdot n_+ \cdot \lambda_+^\circ + z_- \cdot n_- \cdot \lambda_-^\circ \quad (2.3.2-1)$$

where:

κ = limiting molar conductivity [S/m],

z_+ = the charge of each cation,

n_+ = number of moles of cations dissolved [mol/m³],

λ°_{+} = the limiting molar conductivity for the cations [$S \cdot m^2/mol$],

z^{-} = the charge of each anion,

n = number of moles of anions dissolved [mol/m^3],

λ°_{-} = the limiting molar conductivity for the anions [$S \cdot m^2/mol$].

The most common electrolyte used in this study is an aqueous solution with 3.5 mass % NaCl, which also can be expressed as 0.6 M NaCl. Assuming that the NaCl is fully dissociated, the conductivity of 0.6 M NaCl would be:

$$\kappa_{0.6 M NaCl} = 1 \cdot 600 \left[\frac{mol}{m^3} \right] \cdot 5.01E(-3) \left[\frac{S \cdot m^2}{mol} \right] + 1 \cdot 600 \left[\frac{mol}{m^3} \right] \cdot 7.64E(-3) \left[\frac{S \cdot m^2}{mol} \right] = 7.59 \left[\frac{S}{m} \right]$$

(2.3.2-2)

The conductivity of seawater is in the literature stated to be 5.4 S/m (RadiometerAnalytical 2004). Although the salinity of a 0.6 M NaCl solution is similar to that of seawater, the latter also contains other salts such as MgCl₂ and KCl, resulting in a slightly different conductivity. The high conductivity of seawater is a main reason for the corrosiveness of marine environments.

The conductivity of an electrolyte is also a function of temperature. The temperature correction can be estimated as a linear function in moderately and highly conductive solutions. The temperature coefficient Θ is often expressed as a conductivity variation in %/°C. The temperature coefficient of salt solutions generally fall into the range 2.2-3.0 %/°C, where the conductivity increases with temperature (RadiometerAnalytical 2004). Because the vast majority of the tests presented in this

dissertation were performed at room temperature, the effect of temperature has been neglected.

While 0.6 M NaCl has been the most common electrolyte in this study, several lower concentrations have also been used. Table 5 lists the calculated conductivities and resistivities for additional electrolyte concentrations used in this study. Note that the resistivity is the inverse of the conductivity.

NaCl concentration [mass %]	NaCl molarity [M]	Conductivity [S/m]	Resistivity [$\Omega \cdot m$]
3.5	0.6	7.59	0.132
1.0	0.17	2.17	0.461
0.1	0.017	0.217	4.61
0.01	0.0017	0.0217	46.1

The conductivity of the thin layer of electrolyte in atmospheric corrosion is discussed in detail in chapter 5.

2.3.3 Dissolved oxygen

Oxygen plays an important role in corrosion in general and in the galvanic corrosion in aluminum/carbon composite systems in particular. It will be shown in this study that the transport of oxygen to the cathode is the dominant rate controlling mechanism. The corrosion of other materials is also highly dependent on the presence of dissolved oxygen. For example, the corrosion of iron occurs only if dissolved oxygen is present (Vargel 2004), (Roberge 2008). The dissolved oxygen concentrations in the electrolytes used in this study are presented in chapter 4 and 5.

Although the thin layer of electrolyte often can be considered saturated with oxygen in atmospheric conditions, it will be shown in chapter 7 that the electrolyte film still may be a restriction for the oxygen transport. The deposition of corrosion products may have even greater influence on the oxygen transport, which also will be shown in chapter 7.

2.3.4 Effect of pH

The pH is a very important factor in corrosion. Steel has poor corrosion resistance in acidic aqueous solutions, while aluminum has poor corrosion resistance both in highly acidic and highly alkaline media (Vargel 2004). Unless otherwise stated, all experiments, analyses and discussions in this dissertation assumes the electrolyte pH to be close to neutral (approximately pH 6.0 to 8.0).

The corrosion process itself can also cause a local change in pH, even if the starting pH was neutral, which was discussed in section 2.1.3. The local change in pH will help promote the corrosion process.

2.4 Geometry and area ratio

The anodic and cathodic processes happen simultaneously, and the electrons released at the anodic site are immediately consumed at the cathodic site. There is no net accumulation of charges anywhere. The anodic current is always equal to the cathodic current. However, this does not mean that the current densities are equal. If the anodic

and cathodic surfaces have different areas, they will have different current densities (Roberge 2008).

The implications of the surface area ratio can be severe in certain corrosion situations. The effect of a certain amount of anodic current will be much greater when concentrated in a small area than spread over a much larger area. Another possible implication of a much smaller anodic area is less cathodic polarization, which will help maintain the voltage of the galvanic couple at a value close to the open circuit potential. The much smaller anodic area gives rise to a particularly vicious form of galvanic corrosion. A very large cathode area connected to a very small anode area is the most unfavorable ratio in most practical corrosion situations (Roberge 2008). The importance of area ratios and geometry will be investigated in chapter 4 and 5. Atmospheric corrosion is one of the most common forms of corrosion.

2.5 Atmospheric galvanic corrosion

Galvanic corrosion in atmospheric conditions follow the same fundamental principles as immersed conditions, but it is a special case because the galvanic corrosion processes take place in a thin layer of electrolyte on the surface of the materials. The layer thickness is often less than 100 μm . Atmospheric corrosion is often intermittent since it can only occur when water is present (Vargel 2004), (Linares 2006). The existence of a very limited amount of electrolyte makes the description of the kinetics particularly difficult. The formation, composition and destruction of the thin electrolyte layer are influenced by many different factors, making it difficult to understand the

kinetics of the individual processes. The kinetics can also change rapidly, for example a chemically controlled process may suddenly become mass-transport controlled due to buildup of corrosion products (Barton 1973, Cole, Ganther et al. 2004).

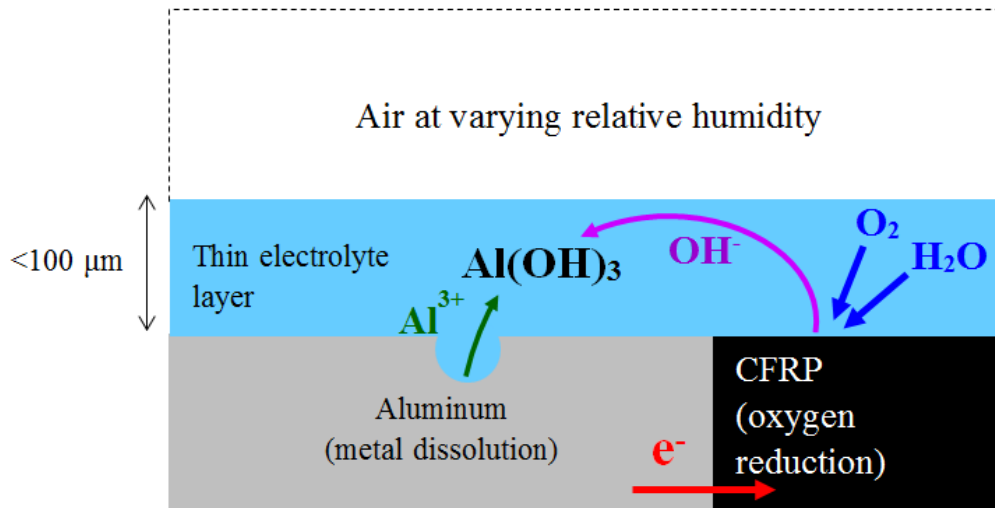


Figure 32: Schematic illustration of atmospheric galvanic corrosion.

2.5.1 Presence of salt and its effect on the electrolyte layer thickness

The electrolyte in atmospheric corrosion is typically neutral or slightly acidic. This chapter and the remaining dissertation will assume that the pH of the electrolyte is close to neutral. Although there likely can be low pH present on transmission lines due to nitric acid from corona discharges and from sulfur pollution, that would be the subject for another study.

Because of the limited amount of electrolyte, the solubility of reaction products is easily exceeded and the products are either precipitated as solids or given off as gases. Periodic renewal of the electrolyte layer due to rain can wash off the corrosion products and change the properties of the electrolyte drastically. Rain may promote corrosion by

providing water for the electrolyte, but may also inhibit the corrosion by washing away soluble stimulation species such as salt from the surface. Fog and high relative humidity may in some cases be more corrosive than rain, because they provide the necessary moisture without the cleaning effect (Barton 1973).

The common occurrence of NaCl and other salts on outdoor structures can result in the presence of an electrolyte layer if the relative humidity (RH) of the air is sufficiently high; precipitation is not needed. NaCl forms a liquid electrolyte when the RH exceeds 76 %, which is also known as the Deliquescence Relative Humidity (DRH) (Cole, Ganther et al. 2004, EncyclopediaBritannica 2014, OmegaInstruments 2014). NaCl and other salts are particularly common in coastal regions and near highways treated with de-icing salts (Barton 1973, EPRI 2000, Cole, Ganther et al. 2004, Vera, Delgado et al. 2006, Moreira 2008, Van den Steen, Simillion et al. 2016). The thickness of the electrolyte layer is a function of the type and amount of salt present, and the relative humidity. These relations have been described, for example, by Van den Steen et al. (Van den Steen, Simillion et al. 2016), Thébault et al. (Thébault, Vuillemin et al. 2011), and Chen et al. (Chen, Cui et al. 2008) and have been extensively investigated in this dissertation. The findings are presented in chapter 5.

CHAPTER THREE: DEVELOPMENT OF A NEW IN-SITU METHOD FOR EVALUATION OF GALVANIC CORROSION IN BARE OVERHEAD TRANSMISSION LINE CONDUCTORS

This chapter will present the development of a novel assessment method for the in-situ galvanic corrosion testing of bare overhead transmission line conductors of various designs, but with particular focus on impact damaged ACCC conductors. The assessment method was originally developed during the author's master's work (Håkansson 2013), but has been further improved as described in this chapter.

The method can be used for real-time measurements of galvanic corrosion currents while retaining the original geometry of the conductors. It will be shown that the original geometry of the conductors cannot be ignored when evaluating for galvanic corrosion performance.

3.1 The importance of new transmission conductor designs

The demand for more reliable electricity supply and the expansion of renewable energy sources are generating an increasing interest in *High-Temperature Low-Sag* (HTLS) overhead high voltage transmission line conductors. HTLS conductors offer several advantages compared with the standard designs, as briefly described in chapter 1. Higher operating temperatures, significantly less sag at high temperature, and reduced

resistance can result in up to twice the current-carrying capacity for the same diameter and weight conductor. The retained conductor diameter and conductor mass enables the use of the same right-of-ways (ROWs) and the same towers while increasing the power transmission capacity. The ability to use the same ROWs is of great importance to the power utilities due to the public opposition to new ROWs. Thus, HTLS conductors can enable an increase of the transmitted power by existing structures with minimal licensing requirements (EPRI 2002), (Chan, Clairmont et al. 2008).

Most HTLS conductors use materials that are relatively new to the power industry, such as PMC and Metal Matrix Composites (MMC). Even if these materials have a proven track record in other applications, there is a concern about the corrosion performance in the harsh service environment of power transmission conductors.

Of particular interest to the power utilities is an *Aluminum Conductor Composite Core* (ACCC) design with a mechanical load bearing core of a hybrid PMC, which also was presented in chapter 1. Potential forms of damage that could result in galvanic corrosion are found in Figure 2 and Figure 3. Other improved versions of more traditional conductor designs such as the *Aluminum Conductor Steel Supported* (ACSS) with a zinc-5 % aluminum-mischmetal coated high-strength steel core and the *Aluminum Conductor Composite Reinforced* (ACCR) with a core of MMC, are also of significant interest for the power utilities.

The standard conductor design - the *Aluminum Conductor Steel Reinforced* (ACSR) - has a core of galvanized steel wires surrounded by aluminum strands. This design has been in use for over one hundred years and completely dominates the existing

high voltage grid, while HTLS conductors have been in service for a much shorter time. ACSR has an inherent galvanic corrosion problem due to the direct contact of the dissimilar metals. However, the galvanic corrosion performance of the present ACSR design is considered acceptable for most applications. Mono-metallic *All Aluminum Conductors* (AAC) are sometimes used in highly corrosive environments, but they have lower strength which limits the span length. AAC will not be covered further in this work but is included in Figure 33.

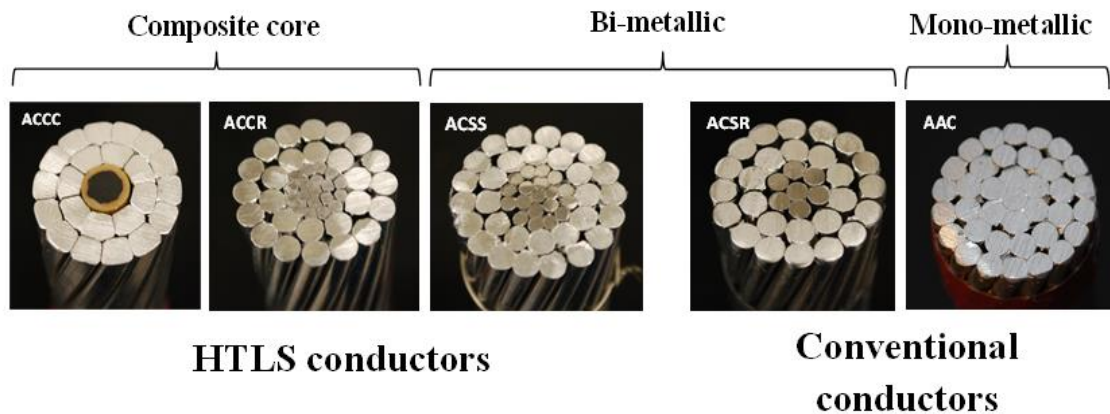


Figure 33: Common designs for bare overhead transmission line conductors.

In common for all these new designs is the largely unknown corrosion performance, particularly when it comes to ACCC with a compromised corrosion barrier. In order for the HTLS conductors to gain the confidence of the power utilities, a better understanding of the corrosion mechanisms and the corrosion performance is necessary. The first step is to develop a measurement method that can quantify the influence of environmental conditions on galvanic corrosion for a large number of environmental variables in a reasonable time frame. A method of this type could be used to directly

compare different conductor designs for their resistance to galvanic corrosion and to make service-life predictions. This chapter will describe the development of such a method.

3.2 Traditional galvanic testing of bare conductors

Atmospheric corrosion measurement techniques consist primarily of long-term exposure tests. The quantification of the corrosion damage is either measured gravimetrically or geometrically at the end of a pre-determined exposure period, or the time to failure is measured for a fixed set of exposure conditions (Ricker and Fink 1997). Long exposure times on the order of years are necessary to get a significant mass loss in a high voltage conductor in a non-accelerated environment. This is very time-consuming and often reveals little or no information regarding galvanic corrosion currents. The exposure time can be decreased by an accelerated environment such as high temperature or high salt concentrations, which is used in the popular standard test ASTM B117-11 "Standard Practice for Operating Salt Spray (Fog) Apparatus" (ASTM 2011). The drawback of the accelerated testing is that numerical interpretation of the results becomes uncertain. For example, changes in temperature, pH, or halide ion concentration may influence different materials differently and alter the galvanic relationships in ways that do not occur in service. These aspects make traditional exposure tests unsuitable for numerical service-life predictions (Ricker 1995).

The ASTM G116-99 "Standard Practice for Conducting Wire-on-Bolt Test for Atmospheric Galvanic Corrosion" (ASTM 2010) is a test designed to specifically

evaluate galvanic corrosion where the evaluation is based on mass loss. While it is quite popular, its very specific requirements for the cathodic material being in the shape of a threaded bolt and the anodic material being a wire (see Figure 34), makes it unsuitable for evaluation of PMCs and MMCs in conductor applications or to evaluate the effects of sample or crevice geometry.



*Figure 34: Wire-on-bolt test ASTM G116-99.
Left) Immediately after installation at the Kennedy Space Center beach corrosion test site.
Right) After 30 days. Source: (CorrosionDoctors 2014)*

There is a wide range of electrochemical techniques for estimating corrosion rates that can be performed using standard size samples immersed in electrolytes. These methods, however, require immersion in a conductive electrolyte and are difficult to apply to atmospheric conditions (Ricker and Fink 1997).

Galvanic corrosion can be estimated by measuring the galvanic corrosion current between two materials and assuming that it is directly proportional to the mass loss. To measure galvanic corrosion current, the materials must be in ionic contact through an electrolyte while the electric connection must be through an external measurement circuit. This is usually accomplished by separating the two materials and immersing them

in an electrolyte. ASTM G71-81 “Standard Guide for Conducting and Evaluating Galvanic Corrosion Tests in Electrolytes” (ASTM 2014) is an example of a standard practice for this kind of testing.

However, by disassembling a conductor specimen, the unique geometry of the conductor is lost. This means that the influence of the geometry and the influence of corrosion product hydrolysis on passivity and corrosion mechanisms in the crevices are also lost. The immersed environment may also be a poor simulation of the atmospheric conditions in the real service environment, as we will show in the next section. It is believed that a reliable evaluation of the galvanic corrosion performance of a bare overhead conductor has to be performed using a method that retains the original geometry of the conductor sample. The importance of retaining the geometry will be demonstrated in subsequent sections.

3.3 Development of the proposed method

3.3.1 Basic principles behind the proposed method

It was apparent early in this study that geometry was critical in the corrosion performance and should not be ignored (Håkansson 2013, Håkansson, Predecki et al. 2015). The influence of geometry on galvanic corrosion both in service and in testing is also well known from the literature, particularly if crevices are present (Barton 1973), (Hack 1993), (Revie 2000), (Francis 2000). The stranded geometry of bare overhead conductors forms a large number of crevices of varying size. Water and pollutants will collect in the crevices, promoting the corrosion. Liquid electrolyte may also form in

environments with high humidity due to the hygroscopic nature of commonly present salts such as NaCl (Ricker and Fink 1997). The trapped electrolyte combined with the two or more conductive materials in direct electrical contact will result in varying degrees of galvanic corrosion.

The development work started with long-term exposure tests by immersing ACCC (with a compromised galvanic corrosion barrier), ACSR, and ACCR conductor samples into an aerated aqueous solution of 3.0 mass % NaCl at 85°C. This is a highly aggressive environment and corrosion damage was evaluated using measurements of mass loss. It soon became evident, however, that the results were very difficult to interpret. It could not be determined if the galvanic corrosion was purely accelerated, or if the corrosion mechanisms had changed in a way that would not occur in real service. It was concluded that testing in a non-accelerated, or at least a much less accelerated environment, was needed for an accurate evaluation of galvanic corrosion performance. In order to measure the corrosion rate in a non-accelerated environment, a much more sensitive measurement method than mass loss was needed. Electrochemical measurement methods, such as direct measurement of galvanic corrosion current, offered the needed sensitivity.

The in-situ method presented in this chapter was originally developed for bi-metallic conductors such as ACSR (Håkansson 2013), (Håkansson, Predecki et al. 2015). Obviously, direct measurement of galvanic corrosion current is not possible in unaltered bi-metallic conductor samples because the different materials are in direct electrical contact. The objective was to enable the direct measurement of galvanic corrosion

currents while retaining the original geometry of the conductor. Because the development of the method for bi-metallic conductors laid the base for the measurement technique that later was used for the ACCC conductor, the principles for using the method for bi-metallic conductors will be presented here. The alternative sample design for ACCC is presented in the next section. The respective designs were used to compare the corrosion performance of ACCC (with a compromised galvanic corrosion barrier) to ACSR and ACSS. The comparison is presented later in this chapter.

Sample design for bi-metallic conductors

The key innovation in the proposed method is to insert a thin separator material that only allows ionic conduction between the materials that participate in the galvanic corrosion. The electrical connection that completes the galvanic circuit is then reestablished through an external measurement circuit. It was found that the separator material may be any thin, porous, non-conductive material such as filter paper, fabric, or a woven polymer mesh sleeve. The woven polyester mesh sleeve appeared to work best for the tested materials, but other materials may offer similar or improved performance. The chosen sleeve was originally manufactured as abrasion protection for electrical wire harnesses. Combined with the preparation process described in subsequent sections, the sleeve provides a physical separation of approximately 0.5 mm between the dissimilar materials in ACSR conductors.

To protect the electrical connections against corrosion, the ends of the sample are potted in epoxy or covered with room temperature vulcanizing (RTV) silicone, or both. This also encloses the ends and simulates a continuous conductor sample.

The finished sample is placed in a simulated representative environment such as wetting with NaCl solution or another electrolyte and being placed in humid air. It can also be placed in salt fog, using for example a testing chamber conforming to ASTM B117-11 (ASTM 2011). The interactions between the conductor materials can be now be studied by real-time measurements of the galvanic corrosion current in the external circuit. Other electrochemical measurements are also possible. If the sample is immersed, a reference electrode can be used.

It is believed that this method can also be used to evaluate samples in the actual service environment by placing the samples and the measurement equipment in the vicinity of a transmission line. This would expose the samples to an environment that is very close to real service conditions (perhaps with the exception of the conductor temperature in case that is higher than ambient).

Sample design for ACCC conductor samples

The ACCC conductor required a slightly modified approach. The unaltered conductor has a galvanic corrosion barrier of glass fiber reinforced PMC, serving both as a physical and electrical barrier between the aluminum and the CFRP. Therefore, the intact conductor should not have issues with galvanic corrosion. However, as described earlier, the galvanic barrier may be compromised by impact damage, fatigue, aging,

improper installation, or manufacturing flaws. Therefore, it is of importance to assess the galvanic corrosion performance with a compromised barrier.

To simulate damage from for example over-bending, the hybrid PMC core was split in half along the axial direction to simulate possible impact damage (see Figure 52). Loose carbon fibers were trimmed off to avoid direct electrical contact with the aluminum. With the split core, the fiberglass composite layer still provided a physical separation between the CFRP and the aluminum, making the woven polyester mesh redundant in this case. A more detailed description of the preparation of the ACCC samples can be found in the next section.

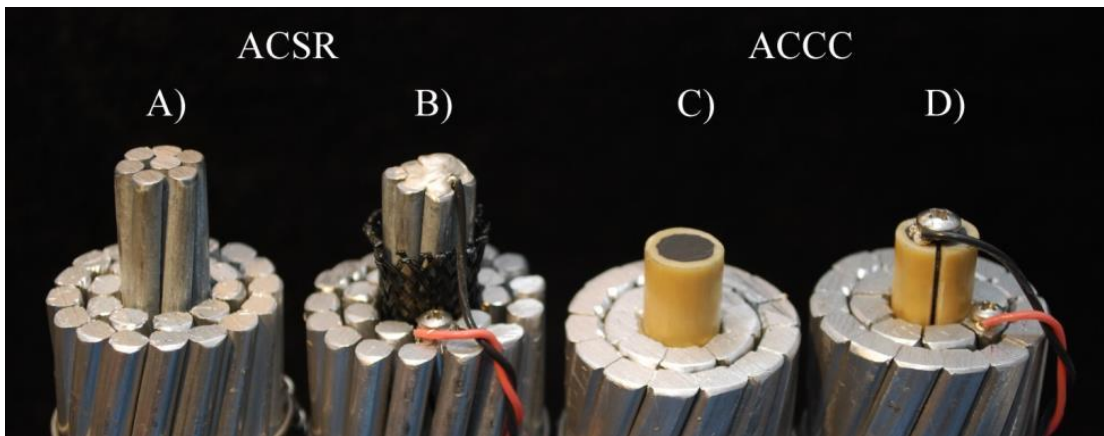


Figure 35: Demonstration samples of the two different conductor designs showing the internal features. A) Unaltered ACSR conductor; B) ACSR with separator mesh and electrical connections; C) Unaltered and undamaged ACCC conductor; D) ACCC conductor with induced damage and electrical connections.

3.3.2 Electrical connections

The electrical connections proved to be the greatest challenge in the development of the proposed method. Since the method is based on electrochemical measurements, good electrical connections are necessary for meaningful measurements. Electrical connections should be made without altering the properties of the tested materials, with a

minimum electrical resistance, and without applying additional galvanic potentials or currents that would influence the test results. The connections must also withstand the corrosive testing environment.

For short-term experiments, electrical connections can be bonded directly to the materials with silver-filled epoxy and covered with a layer of RTV silicone to prevent the silver from imposing galvanic currents or potentials (simple connections shown in Figure 36). However, this design proved to be insufficient for long-term testing. During long-term testing, the corrosion damaged the interface between the aluminum and the silver-filled epoxy. Because corrosion products usually have a greater volume than the metal they replace, the build-up of corrosion products lifted up the silver-filled epoxy which eventually resulted in a complete separation (Figure 37). The time-to-failure for these electrical connections depends on the severity of the testing environment and varied from days, for severely corrosive environments, to weeks for less corrosive conditions.



Figure 36: Simple electrical connections for short-term corrosion testing. The connections will be covered with silicone RTV before exposure to the corrosive environment.

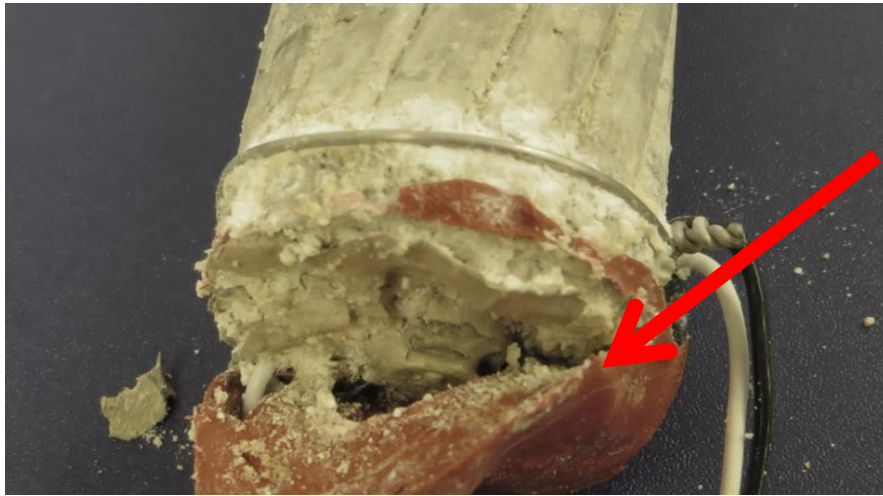


*Figure 37: Corrosion of electrical connection.
The corrosion has crept underneath the silver-filled epoxy and separated it from the aluminum.*

The solution to the above problems with electrical connections was to pot the ends of the sample in epoxy *before* making the electrical connections. The potting turned out to be a critical step where the epoxy created a protective barrier for the electrical connection. The electrolyte cannot move between the strands and attack the vulnerable interface between the tested material and the electrical connection. After several iterations, the sample preparation techniques described below were found to work well for even highly corrosive testing environments.

Electrical connections on bi-metallic conductors

- 1) The core is removed from the conductor and held together with hose clamps (tape can be used under the hose clamps to protect the coating on the steel strands). The core is pre-heated to approximately 60°C and the ends are dipped in fast curing epoxy to cover the exposed steel surface and prevent it from participating in

galvanic reactions. The pre-heating ensures fast curing and prevents the epoxy from wicking up between the strands. The ends are then wrapped with a thin polyimide tape to add an extra insulating barrier.



Figure 38: Pre-heating the core.



Figure 39: Ends dipped in fast-curing epoxy.

- 2) The core is covered with the polyester mesh and inserted back into the surrounding aluminum strands. The core is offset so it sticks out approximately 10 mm and allows access to only the steel on one side and aluminum on the other. The sample is held together with stainless steel wire or hose clamps. The

insulation is checked with an electric continuity meter to ensure there is no electrical connection between the core and the aluminum strands.



Figure 40: The core partially covered with the polyester mesh.



Figure 41: The re-assembled conductor sample with the steel core off-set.

- 3) The ends of the re-assembled conductor sample are potted in a fast-curing epoxy. The thickness is not critical; approximately 5 mm is enough. A 3-minute casting epoxy was used in this study. The samples were pre-heated to approximately 60°C to ensure fast and even curing. Fast curing is important to prevent the liquid from wicking up between the strands.



Figure 42: The conductor ends are potted in fast-curing epoxy.

- 4) The ends are sanded on a belt sander until the metal is exposed.

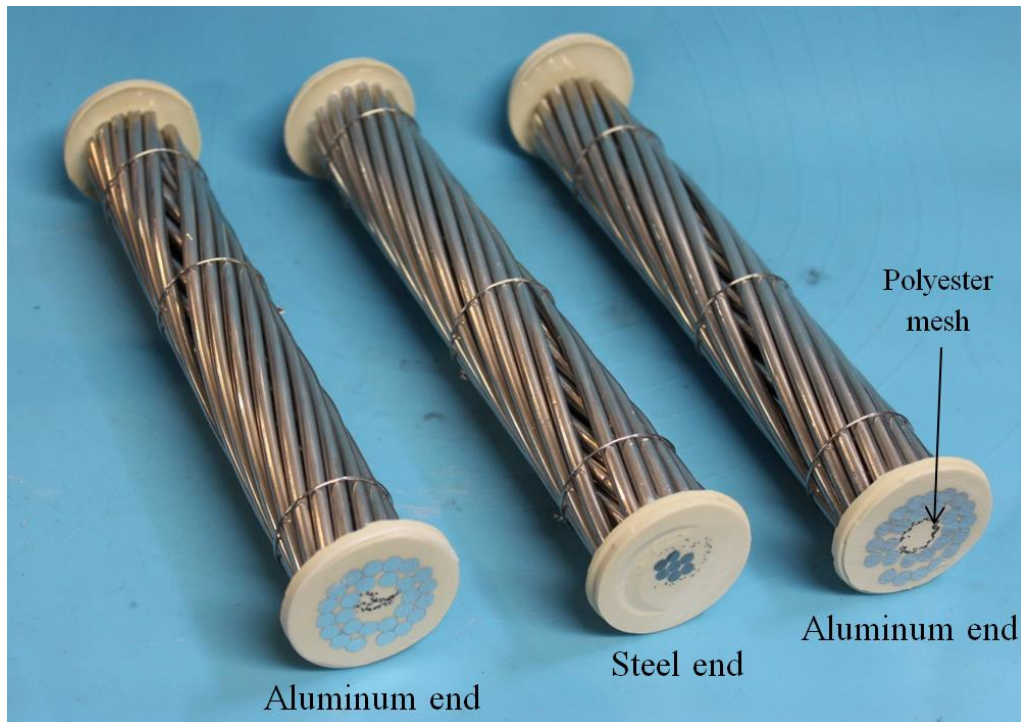


Figure 43: The ends are sanded on a belt sander until the metal is exposed.

- 5) A hole is drilled and tapped in the center of the “aluminum end” and next to the core on the “steel end”.



Figure 44: Holes are drilled and tapped.

- 6) A stainless steel washer is bonded to the ends of the exposed strands with silver-filled epoxy. The wire is wrapped around a screw which is threaded into the hole. More silver-filled epoxy is added to make contact between the washer, screw and wire. The screw is tightened to secure the electrical connection (see Figure 45).

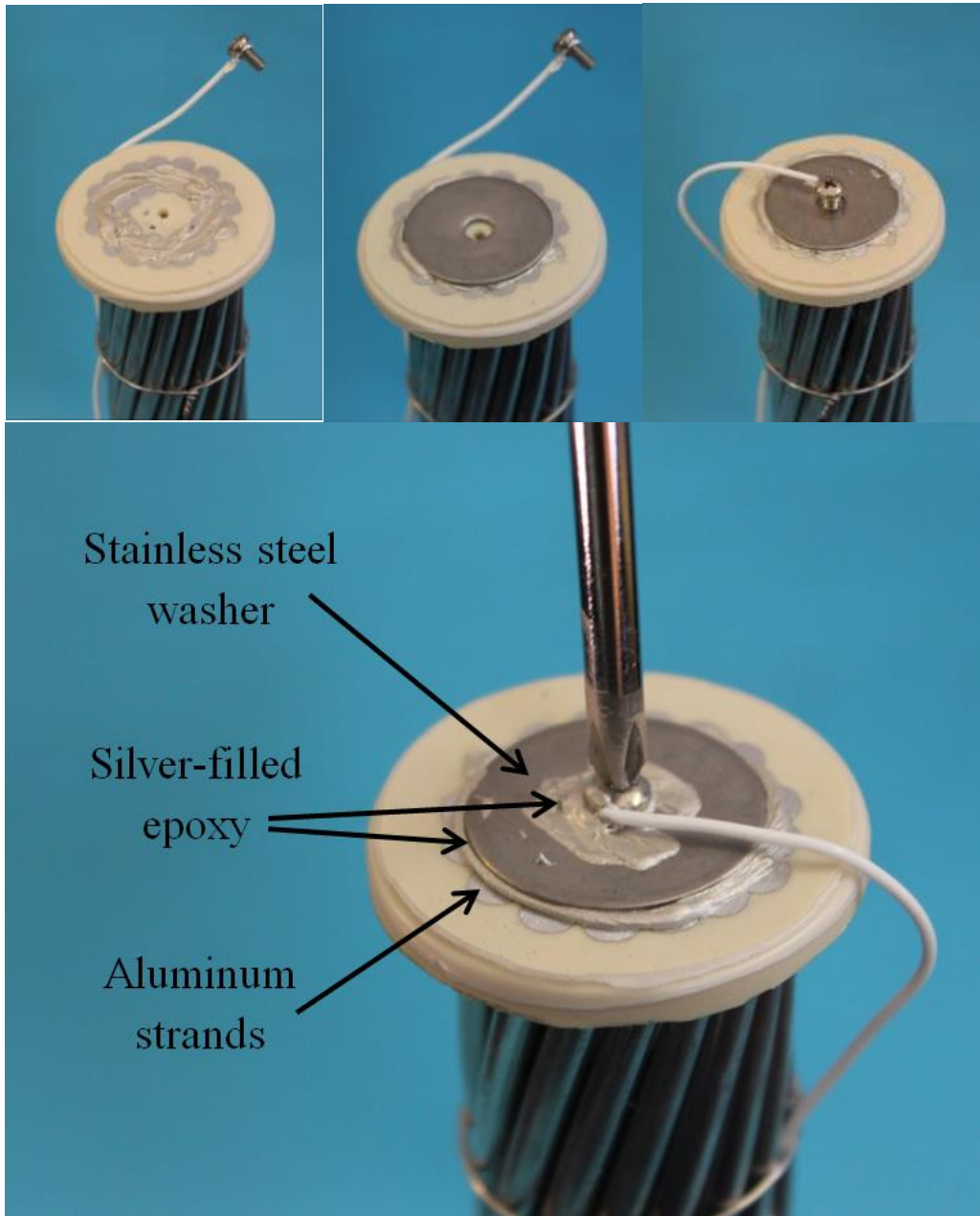


Figure 45: Procedure for making the electrical connection on the “aluminum end”.

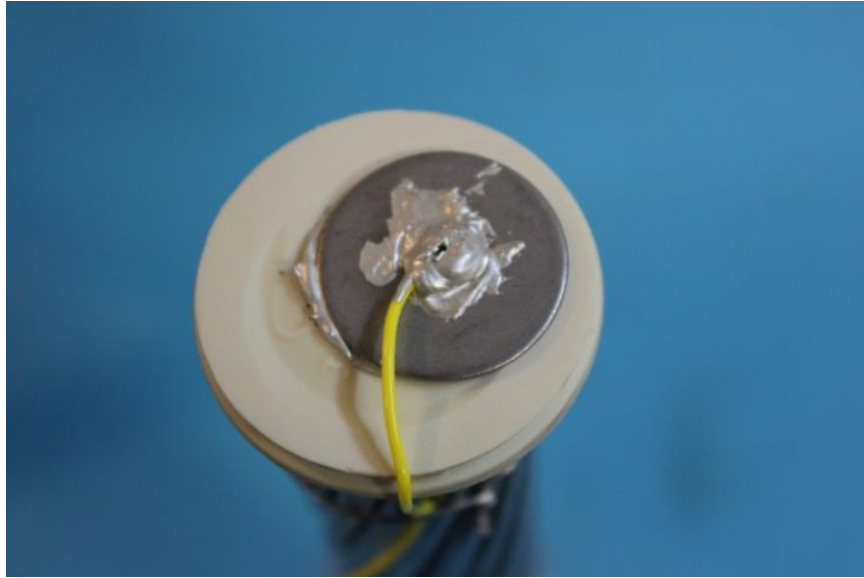


Figure 46: The electrical connection on the "steel" end.

- 7) The wire electrical connection is either covered with RTV silicone or potted in epoxy again.

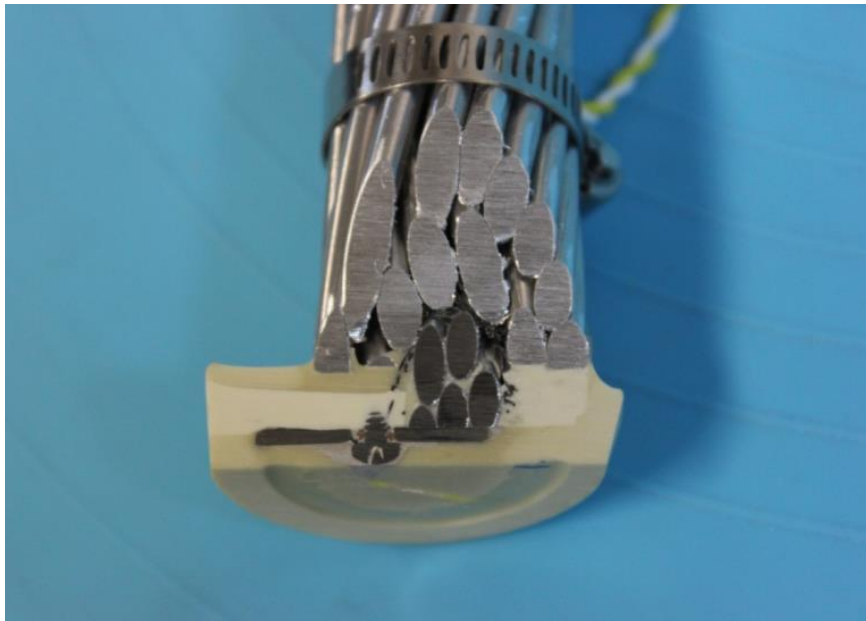


Figure 47: Sectioned view of the electrical connection to the steel core.



Figure 48: Sectioned view of the electrical connection to the aluminum strands.

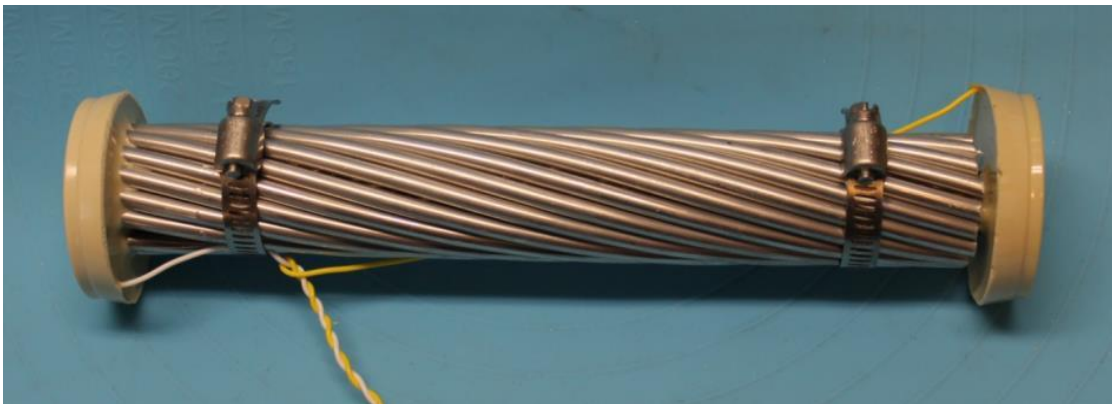


Figure 49: The finished sample with the electrical connections covered in epoxy.

It has been observed that it is very important to check the isolation between the two materials after each step with an electrical continuity meter. If an undesirable metallic connection is made between the two materials inside the sample, the sample will be rendered inadequate.



Figure 50: Control of continuity.

It is also recommended that all hardware should be clean, de-greased and preferably polished or sanded to remove oxide layers before assembly. Furthermore, corrosion resistant 316 stainless steel alloy is recommended for washers, wires, screws etc. High-quality electrical wire (tin or silver-coated copper) has been shown to increase the reliability and durability of the electrical connections. If special preparation of some materials is desired such as pickling of the aluminum, it should preferably be done before assembly since chemicals may damage the potting material or wires.



Figure 51: Cleaning of hardware using a polishing wheel.

Electrical connections on ACCC conductors

- 1) The sample is cut to desired length and held together with either stainless steel wire or stainless steel hose clamps.
- 2) The composite core is removed from the conductor sample. A hole is drilled axially into the center of the CFRP to a depth of approximately 5 mm (exact size and depth depends on the screw size to be used for the electrical connection). The core is split in half along the axial direction to simulate impact or over-bending damage. Loose carbon fibers are trimmed off to avoid direct electrical contact with the aluminum.



Figure 52: Splitting of the ACCC core to simulate damage.



Figure 53: The split core (right) and the surrounding aluminum strands (left)

- 3) The core is inserted back into the aluminum strands. The core is off-set approximately 10 mm, with the end with the hole in the CFRP protruding.
- 4) The “aluminum end” of the ACCC sample is potted in fast-curing epoxy (a 3-minute casting epoxy was used in this study). The thickness is not critical; approximately 5 mm is enough. The samples were pre-heated to approximately 60°C to ensure fast and even curing. Fast curing is important to prevent the liquid from wicking up between the strands.



Figure 54: The conductor ends are potted in fast-curing epoxy. The uncured epoxy is a brown translucent liquid, while the cured epoxy is opaque beige.

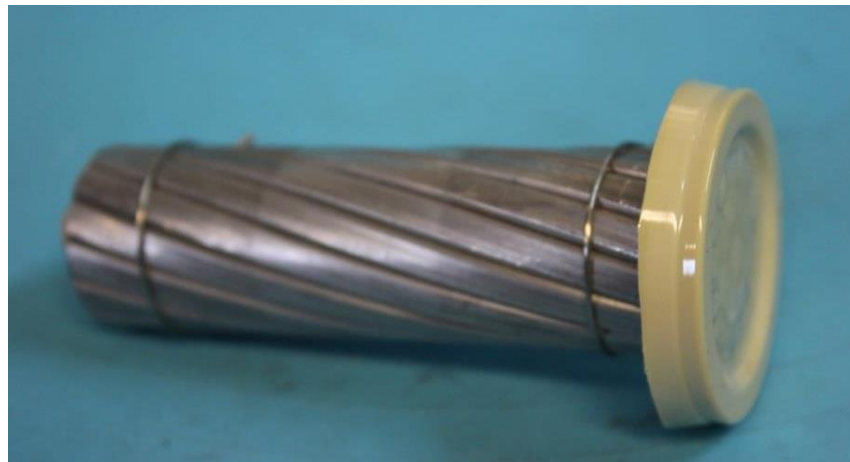


Figure 55: The ACCC sample removed from the mold.

- 5) The “aluminum end” is sanded on a belt sander until the metal is exposed.
- 6) A hole is drilled and tapped in the center of the “aluminum end”.



Figure 56: Holes are drilled and tapped.

- 7) A stainless steel washer is bonded to the ends of the exposed strands with silver-filled epoxy. A wire is wrapped around a screw and threaded into the hole. More silver-filled epoxy is added to make contact between the washer, screw and wire. The screw is tightened to secure the electrical connection.
- 8) The wire electrical connection is either covered with RTV silicone or potted in epoxy again.

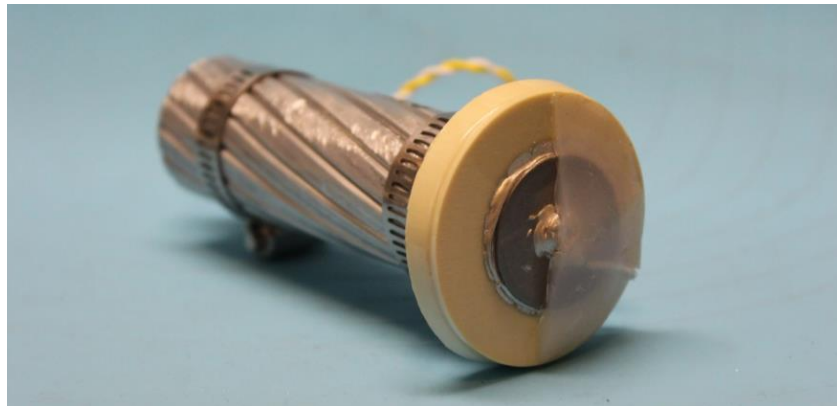


Figure 57: Demo-sample with only half of the end covered with RTV.

- 9) On the CFRP side, a stainless steel screw is bonded to the core by dipping it silver-filled epoxy and threaded into the pre-drilled hole. More silver-filled epoxy is used to cover the screw head and ensure a good connection.

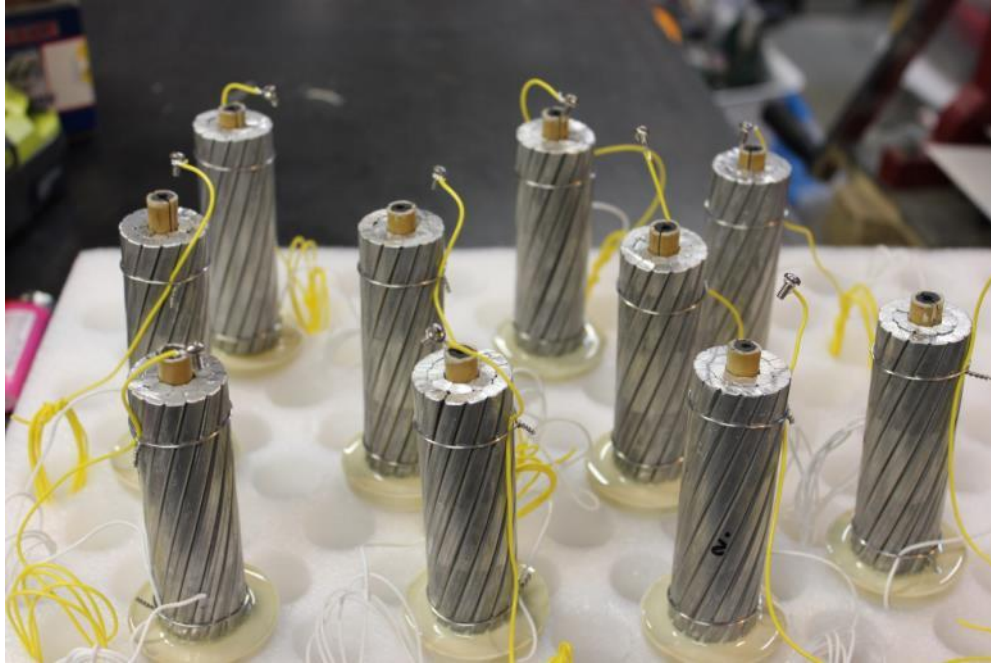


Figure 58: ACCC samples ready for the electrical connection to the core.

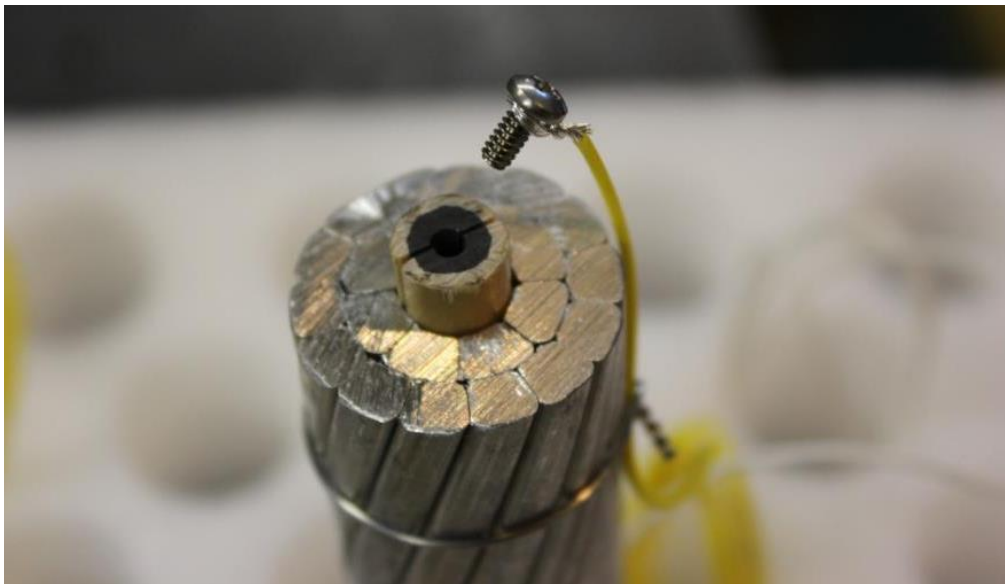


Figure 59: Close-up of the core before the electrical connection is made.

10) The electrical connection is either covered with RTV silicone or potted in epoxy again.

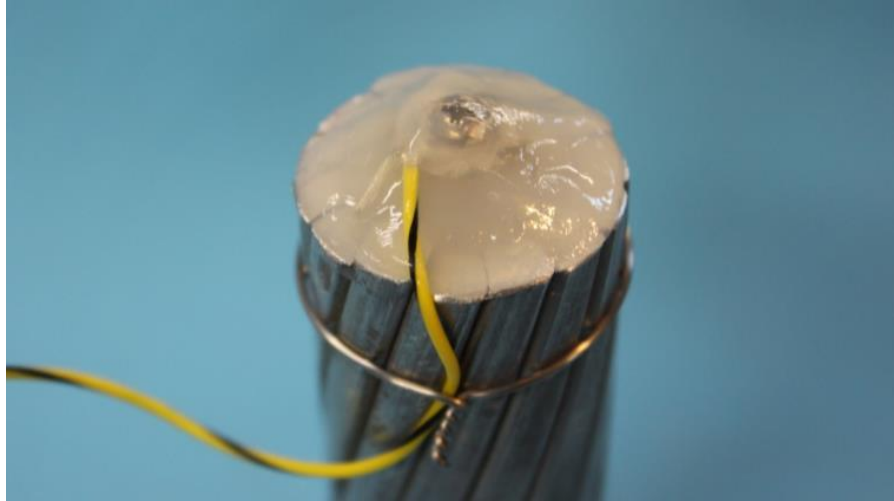


Figure 60: Electrical connection covered in silicone RTV.

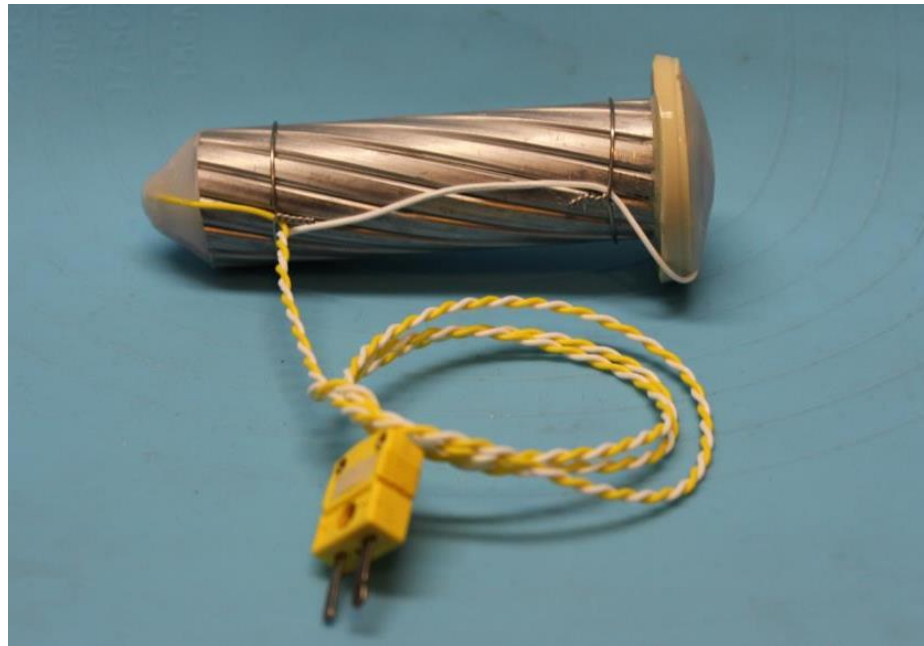


Figure 61: The finished ACCC sample.

Note: the connected wire is not a thermo-couple, it is a regular copper wire with a mono-metallic connector of thermo-couple style which offered a convenient system.

Varieties of sample designs

Additional mesh sleeves can be added to conductors that have several layers of strands to provide further information about the corrosion mechanisms. This concept is illustrated in Figure 62 for both ACCC and ACSR.

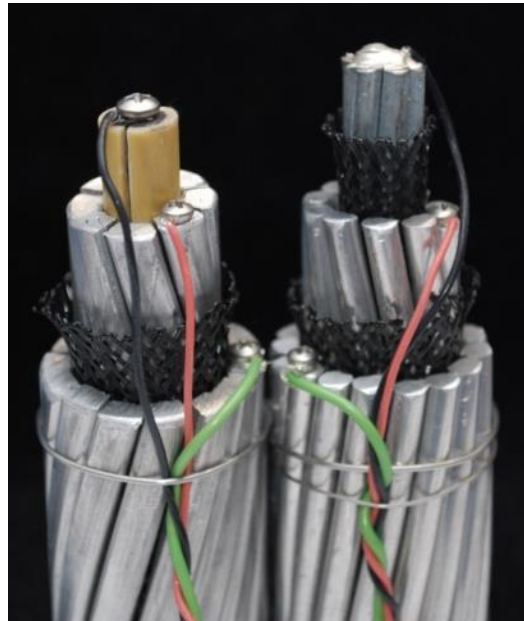


Figure 62: ACCC and ACSR samples with additional mesh sleeves.

A variety of ACCC samples were prepared for different purposes. Figure 63 shows the manufacturing of three different varieties: Left) ACCC with sampling tube for measurement of pH in the center during immersion; Middle) ACCC sample with only $\frac{1}{2}$ core; Right) ACCC with extra mesh to pin-point the anodic reaction.

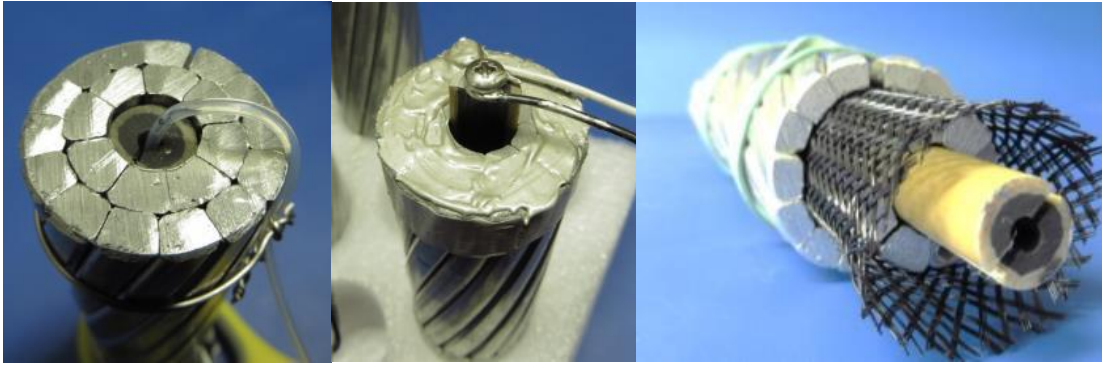


Figure 63: Varieties of the ACCC samples.

Left) With a thin tube connected to the center for sampling and/or modification of the environment inside the core during testing, Middle) With only half of a core to study the effect of anode-to-cathode area ratios, Right) With the aluminum strands separated into two zones to provide additional information about the details of the corrosion mechanism.

3.3.3 Measurements circuits

The most straightforward measurement is the direct measurement of galvanic corrosion currents. This can be done very accurately with a Zero Resistance Ammeter (ZRA). However, ZRAs are costly and have typically only one channel. A much less expensive alternative, but still accurate enough for many applications, is to measure the galvanic current using a high-quality voltmeter and a precision shunt resistor (1 % tolerance or better). This approach is described by Francis (Francis 2000). If a 1.0 Ω resistor is chosen, the magnitude of the measured current is the same as the magnitude of the voltage measured over the resistor. This method introduces a small resistance in the measurement circuit, but experiments performed in this study have shown that the effect of a 1 Ω resistor is well within the normal scatter of the measurements and can be considered negligible. The 1 Ω added by the shunt resistor should be compared to wires and electrical connections in the measurement instrument that can have several ohms of resistance. A shunt resistor array was built in order to exploit this capability in a common

data acquisition and switch unit and resulted in a 19 channel instrument with minimal additional cost. This setup was used to generate the data presented below.

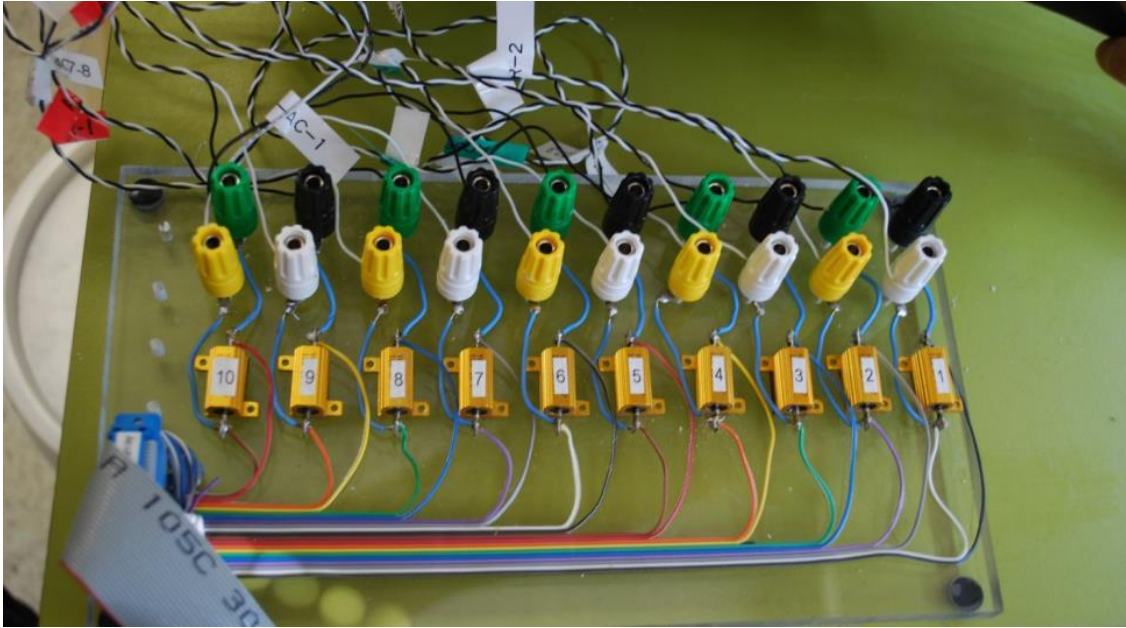


Figure 64: Measurement using precision shunt array with 10 channels.

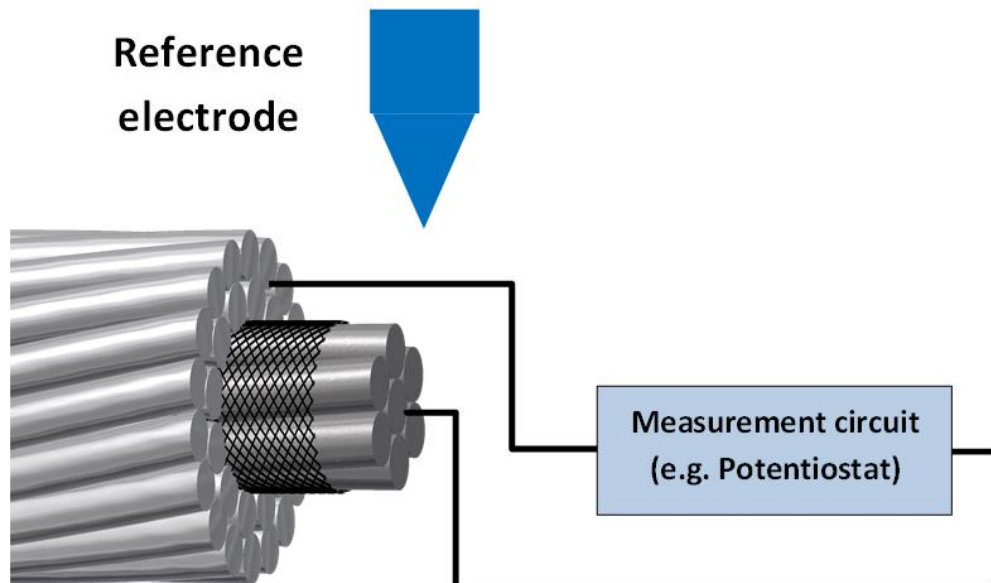


Figure 65: A reference electrode can be used in an immersed environment.

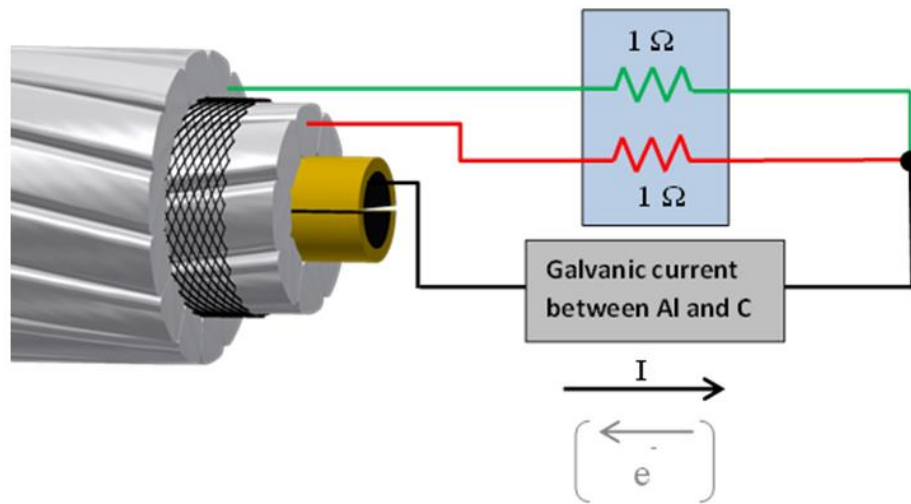


Figure 66: Schematic of multiple channel measurement circuit using shunt resistors and a multi-zone sample.



Figure 67: Finished ACCC samples in the humidity chamber.

3.3.4 Importance of retaining the original geometry

The author's previous research (Håkansson 2013, Håkansson, Predecki et al. 2015) had indicated that the geometry of the sample highly affected the measured corrosion rate during immersion testing. To illustrate the importance of retaining the original geometry, ACCC samples were used to demonstrate the effect of a complete separation of the different materials in the conductor during immersion testing. An ACCC conductor specimen was disassembled and the following samples were prepared from the materials (Figure 68):

i) a 100 mm long sample prepared as described above with impact damage simulated by splitting the core along the centerline while retaining the original geometry

ii) a 100 mm long sample, as above, but with a woven polyester sleeve placed, over the aluminum and the two halves of the core placed on the *outside* of the sleeve with the exposed CFRP facing the aluminum (instead of inside the aluminum strands as it would be in its original geometry),

iii) a 100 mm long sample with the split core (prepared as described above) but with the two core halves completely separated from the aluminum,

iv) a pair of aluminum and CFRP samples with an 1:1 exposed surface area (each area was 700 mm²).

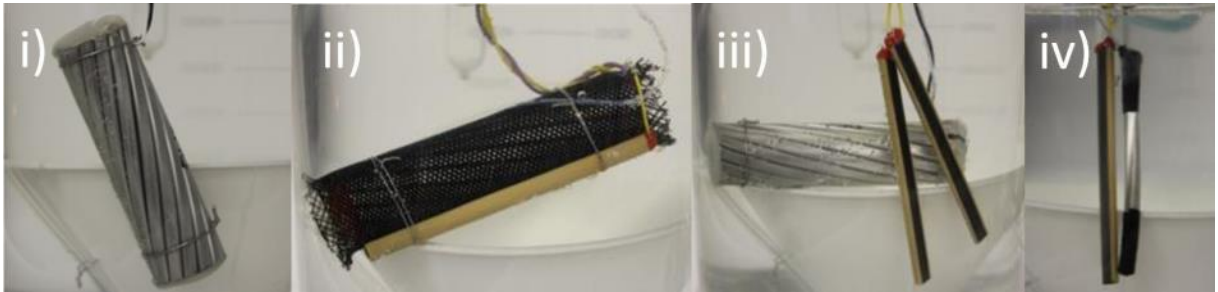


Figure 68: Four different samples prepared to quantify the geometry effect.

The galvanic corrosion current between the CFRP and the aluminum was measured with a potentiostat in ZRA mode during immersion in an aqueous 0.6 M NaCl solution at room temperature (22°C). The duration of each test was 2 hours, and an average of the corrosion current was calculated for the last 0.5 hours. The tests were performed in both agitated (aerated, 15 ml/s) and stagnant electrolyte. The stagnant tests were conducted immediately after agitation ceased to ensure presence of dissolved oxygen. The electrolyte volume was 1800 ml.

The anodic corrosion current densities for the four different configurations are presented in Table 6. The corroding material was in all cases the aluminum. The anodic current density in the agitated electrolyte was almost 1500 times higher for the completely separated 1:1 area ratio couple than for the conductor sample with the original geometry and simulated impact damage. The difference was 200 times in the stagnant electrolyte. This test illustrates the importance of retaining the original geometry. A complete separation of the materials would in this case have caused a severe overestimation of the corrosion rate.

Figure 69 illustrates the consequences of such over-estimation by using a failure criterion of 20 % loss of aluminum cross-section and the assumption that the corrosion rate will remain constant. Depending on the area ratio, geometry and the testing environment, the time to failure when the samples are tested in *immersed* conditions is predicted to be 0.039 years (2 weeks) to 66 years. The atmospheric data is from chapter 7. The large difference in corrosion rate in different geometries is believed to be due to the different mass transport of oxygen. An in-depth analysis of the oxygen transport through the ACCC conductor in immersed and atmospheric conditions can be found in chapters 5-7. The two green bars to the right represent the same sample design but in *atmospheric* conditions. The data is from chapter 7 and illustrates that it is not only important that a sample design should represent the actual component, but that the surface preparation and test duration also need to reflect the real service environment.

Configuration # (see figure 3)	Configuration of galvanic couple/sample	Anodic corrosion current density, mA/m ² (uncertainty)	
		Stagnant	Agitated
i)	Complete ACCC conductor with simulated impact damage	0.63 (0.020)	0.73 (0.083)
ii)	ACCC conductor sample with composite core halves on outside, facing the aluminum	1.9 (0.017)	14.9 (0.25)
iii)	ACCC conductor sample with composite core halves completely separated from the Al	7.2 (0.012)	42 (0.91)
iv)	Pair of aluminum and CFRP samples with an 1:1 area ratio	130 (12)	1064 (28)

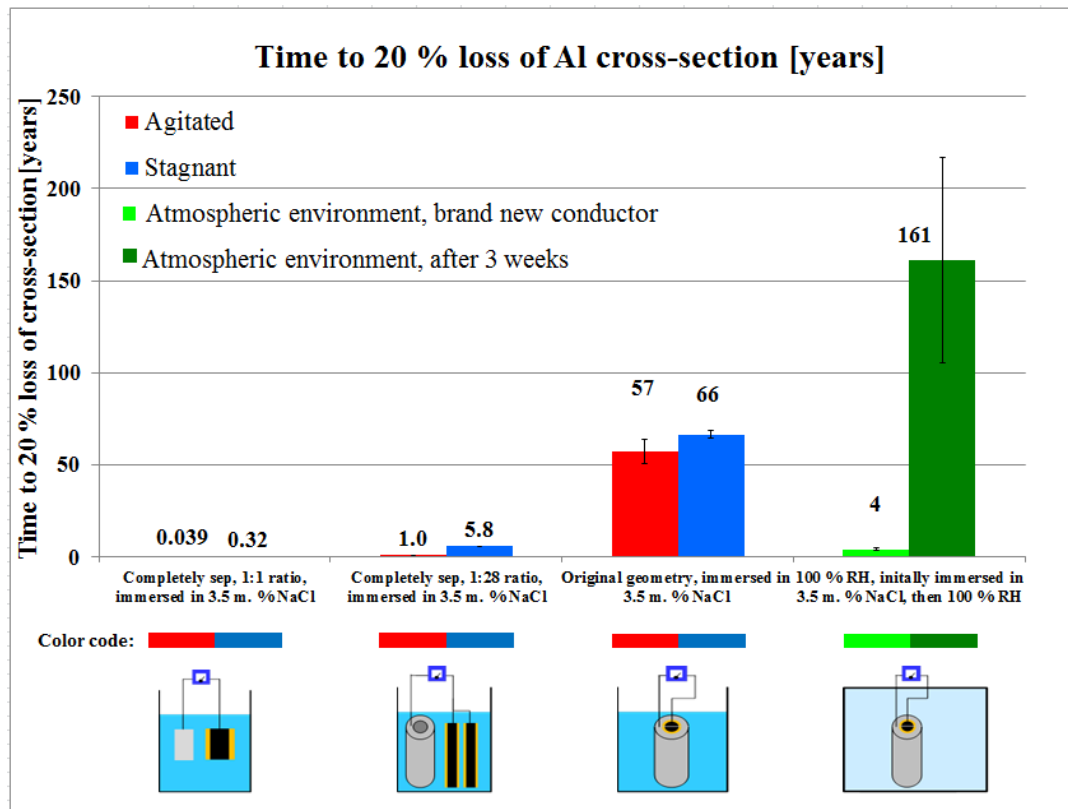


Figure 69: Predicted time to loss of 20 % of aluminum cross-section based on different testing methods.

3.4 Application of proposed method to galvanic testing of conductors

The suitability of the proposed assessment method to quantify changes in the galvanic corrosion rate in an atmospheric environment was evaluated by subjecting salt-loaded conductor specimens to varying RH. Three different conductor types were tested: ACCC, ACSR, and ACSS. All specimens were of the conductor specifications known as “Drake” (EPRI 2002) and had an outer diameter of approximately 28.5 mm. The supplied specimens of ACCC had trapezoidal aluminum strands, while the strands in the ACSR and ACSS specimens were round. All three conductor types had strands of aluminum alloy 1350. To eliminate potential undesirable effects of different strand geometries, the ACSS and ACSR samples were re-stranded in this research using trapezoidal strands

from the ACCC. Eleven samples were tested: including three samples of ACSR, three of ACSS, and five of ACCC. All samples had a length of 100 mm. The samples were prepared as described in previous sections.

The samples were immersed in a 3.5 mass % NaCl aqueous solution for approximately 10 minutes to allow penetration of the electrolyte into the crevices. Excessive electrolyte was wiped off from the outer surface and the mass of each of the wet samples was registered. The samples were left to dry in room air overnight (RH 31.5 % ($\sigma = 2.4$ %), temperature 26.1 °C ($\sigma = 1.0$ °C, elevation 1609 m above sea level). The salt load density (the mass of salt per unit surface area of the entire sample) was on average 3.1 g/m² ($\sigma=0.85$ g).

The dry samples were placed in a controlled humidity chamber at room temperature and exposed to increasing levels of RH over the next 8 days. The samples were held at each humidity level for 20-25 hours. Starting at 50 % RH, the RH was increased in increments of 10 %. The room temperature was on average 25.9 °C ($\sigma = 1.2$ °C). The RH levels were controlled to within ± 2 %. The samples were given 12 hours to stabilize at each level of RH. The averages of the anodic corrosion current densities were calculated for the remaining 8-13 hours of each humidity level period.

3.5 Results and discussion

Aluminum was found to be the anodic material in all cases and was thus the material that experienced accelerated corrosion due to the presence of galvanic corrosion. This was unexpected for ACSR and ACSS because published galvanic series for these metals in NaCl aqueous solutions identify Zn and Zn alloys as being anodic to Al and Al

alloys (Cramer and B. S. Covino 2005). While the corrosion behavior of these alloys during plain exposure without crevices in aerated environments agrees with the galvanic series, the electrochemical series indicates that bare Al can be anodic to Zn and its alloys under certain conditions (Pourbaix 1974). The ability of Al alloys to assume more active potentials when the passive film is damaged has been confirmed by measuring potential transients during scratching (Stoudt, Vasudevan et al. 1992). During plain exposure, Al alloys form a continuous passive film that insulates the underlying metal from the environment. This passive film makes Al the cathode in the galvanic corrosion reaction between Al and Zn. However, in a heterogeneous assembly, the passive film may be locally attacked by chemical or physical means and this can reverse the galvanic relationship between these metals. A reversed relationship would explain why the aluminum was the material that experienced galvanic corrosion. This illustrates the importance of an in-situ technique, such as the one developed here, in understanding galvanic corrosion in heterogeneous assemblies. In the ACCC sample, the CFRP was - as expected - the more noble material and caused accelerated corrosion of the aluminum.

Figure 70 illustrates the galvanic corrosion current density of the corroding aluminum strands as a function of RH. The data points are based on an average for 3-5 samples. Error bars present one standard deviation in the average values over the 8-13 hour measurement period. In general, the corrosion current displays an exponential dependency on the RH, a behavior that also has been reported in the literature (Ricker 2008). The galvanic corrosion rate rapidly increases at RH levels approximately 80 %. A RH of at least 80 % and an ambient temperature above 0°C are the fundamental

requirements for the *Time of Wetness* (TOW) parameter used to estimate atmospheric corrosion rates. The higher the TOW, the more corrosive an environment is considered to be. The rule-of-thumb is that the atmospheric corrosion is typically negligible at relative humidity levels below 80 % (Francis 2000, Roberge 2008). As mentioned in chapter 3, the Deliquescence Relative Humidity (DRH), which is the limit for a salt to form a liquid electrolyte by absorbing moisture from the surrounding air, is 76 % for NaCl at room temperature (EncyclopediaBritannica 2014, OmegaInstruments 2014). The correlation of the DRH for NaCl and the rule-of-thumb limit for atmospheric corrosion is likely no coincidence as NaCl is often present in outdoor atmospheric environments. The rapid increase in galvanic corrosion current density in Figure 70 shows that the rule-of-thumb of 80 % RH is indeed a good indicator of a critical level where the galvanic corrosion becomes significant under the tested conditions.

The data also suggest that the galvanic corrosion in impact damaged ACCC is lower than the inherent galvanic corrosion in ACSR and ACSS. This is good news for the ACCC conductor and illustrates that retaining the geometry is very important in the evaluation of aluminum/carbon composite systems. If the geometry is not retained, the testing can severely over-estimate or under-estimate the corrosion rate. In the first case a superior component may not be used due to fear of corrosion. In the latter case catastrophic failure may occur. In either case, retaining the geometry is critical for a fair evaluation.

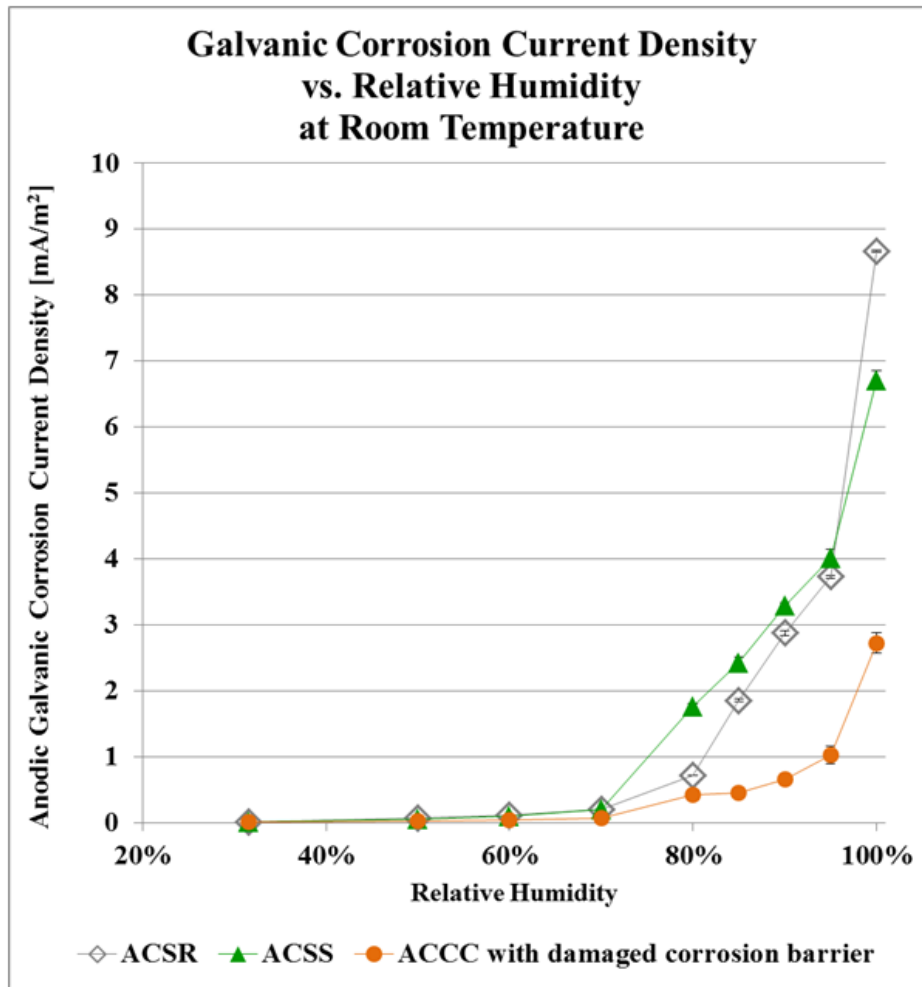


Figure 70: Galvanic corrosion current density of corroding aluminum strands as a function of relative humidity for three different conductor designs.

CHAPTER FOUR: EVALUATION OF CRITICAL FACTORS AFFECTING GALVANIC CORROSION

Numerical modeling of galvanic corrosion requires a larger number of input variables than a typical mechanical system, even for a simple model. This chapter describes the input data and how the data was collected for the modeling presented in subsequent chapters. In addition, the chapter also presents experimental investigations of the control mechanisms in both atmospheric and immersed conditions. Most of the work on control mechanisms was prompted by observations during the experimental characterization of the studied materials, of which some were presented in the previous chapter. The observed control mechanisms will be further discussed in the numerical modeling chapters 6-7. A discussion about possible measurement errors can be found in Appendix B.

4.1 Input data for numerical modeling

4.1.1 Equilibrium potentials and galvanic series

A galvanic series was generated for materials of interest to this study. The galvanic series (described in chapter 2) lists the equilibrium potentials for different materials in a specific electrolyte in decreasing order. A combination of potentiodynamic polarization scans (also described in chapter 2) and measurements of free corrosion

potential was used. The electrolyte was 0.6 M NaCl at room temperature. Figure 71 displays the results of all tested samples, while the bars in Figure 21 (repeated below) represent the average potential +/- one standard deviation. The difference in corrosion potential between CRFP and aluminum from the ACCC conductor is highlighted. From the CFRP's relative placement in the galvanic series, it can be determined that it is cathodic to aluminum, steel, and zinc, and may cause accelerated corrosion of these materials.

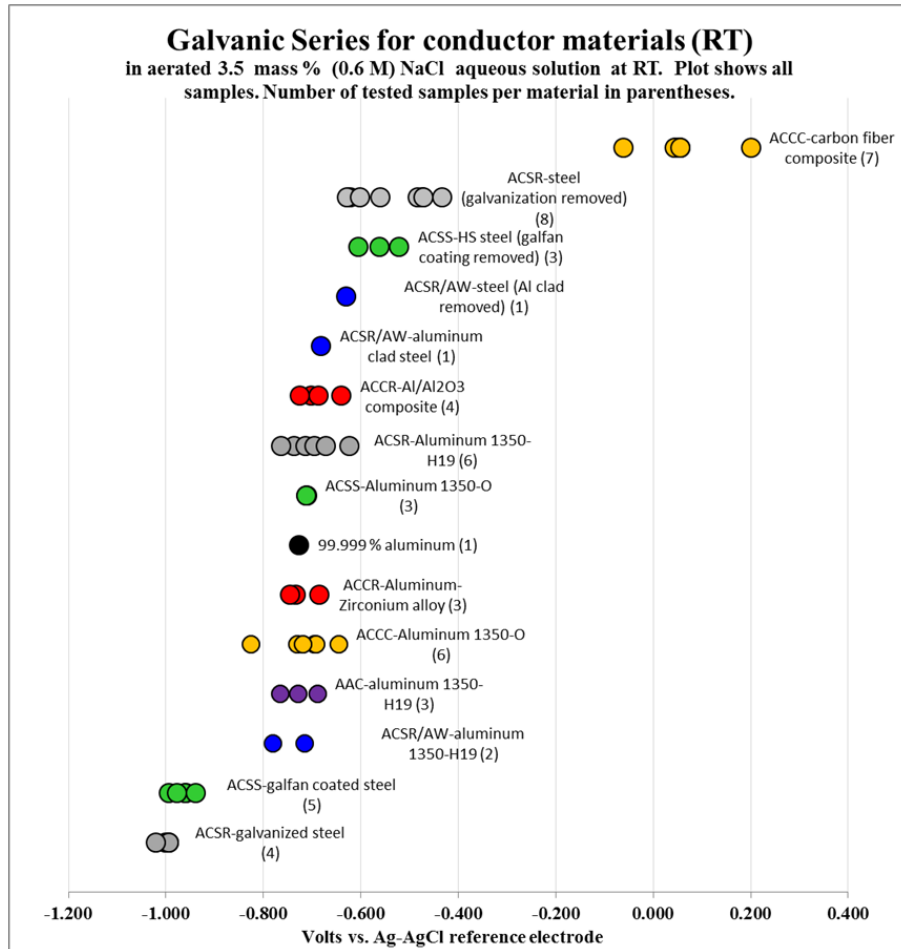


Figure 71: Galvanic series for materials of interest in this study in 0.6 M NaCl at room temperature, vs. Ag/AgCl reference electrode. Acronyms refer to common conductor types and are explained in Appendix A.

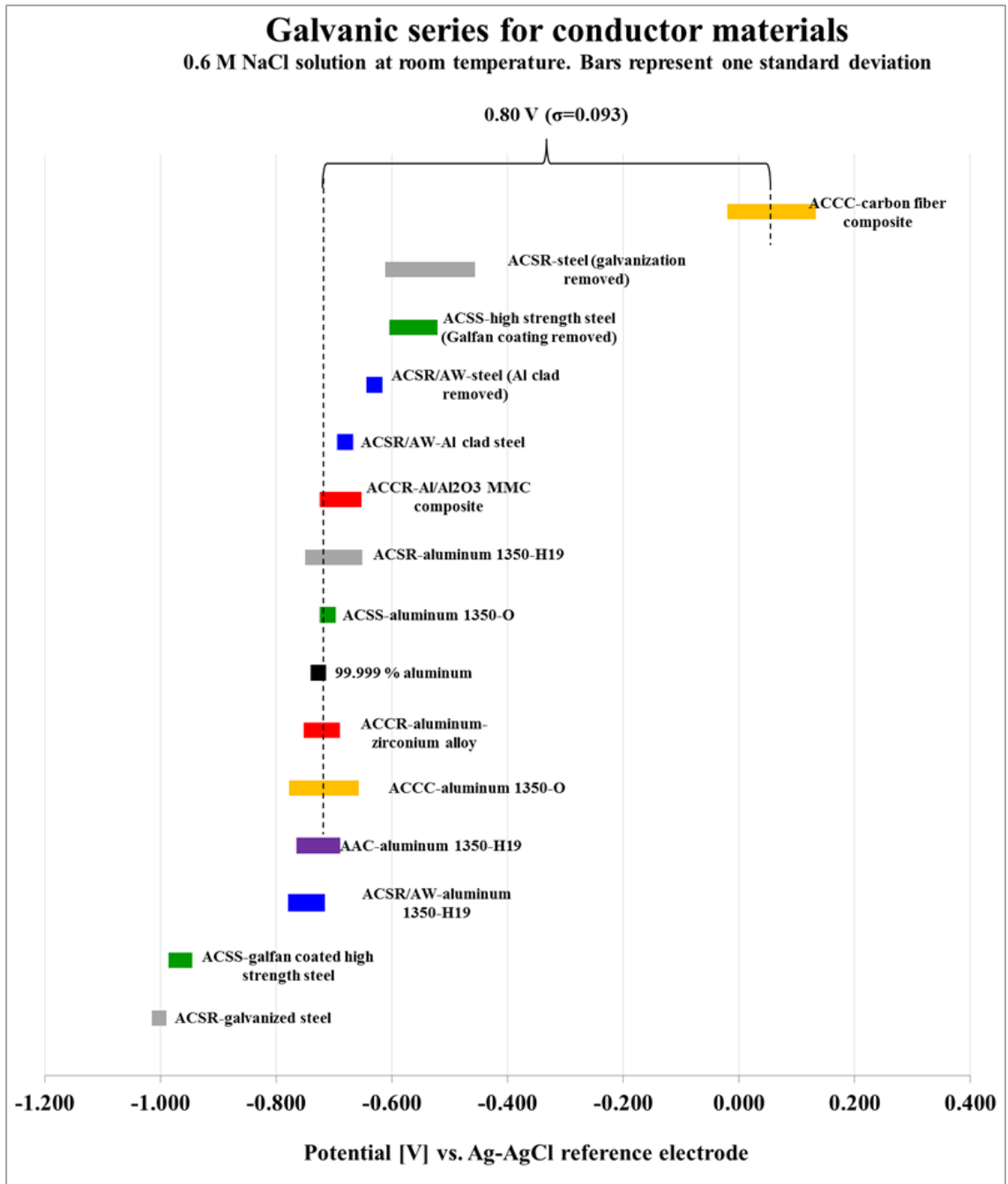


Figure 21 (repeated): Galvanic series of interest in this study in 0.6 M NaCl at room temperature, vs. Ag/AgCl reference electrode.

The difference in corrosion potential between CRFP and aluminum from the ACCC conductor is highlighted. Acronyms refer to common conductor types and are explained in Appendix A.

4.1.2 Tafel slopes and exchange current density

Tafel slopes and exchange current densities are used to describe the kinetics of a corrosion process and are necessary in the numerical modeling of galvanic corrosion. The process of extracting Tafel slopes and exchange current densities from potentiodynamic polarization curves was explained in section 2.2.2.

Figure 73 through Figure 77 show the polarization scans for CFRP and aluminum from ACCC, as well as solid graphite and aluminum alloy 6061-T6. Table 7 summarizes the Tafel slopes and exchange current densities extracted from these polarization curves. The curves were acquired by using potentiodynamic polarization scans of individual samples immersed in 0.6 M (3.5 mass %) NaCl aerated aqueous solution at room temperature. A stainless steel mesh surrounding the sample was used as the counter electrode as shown in Figure 72.

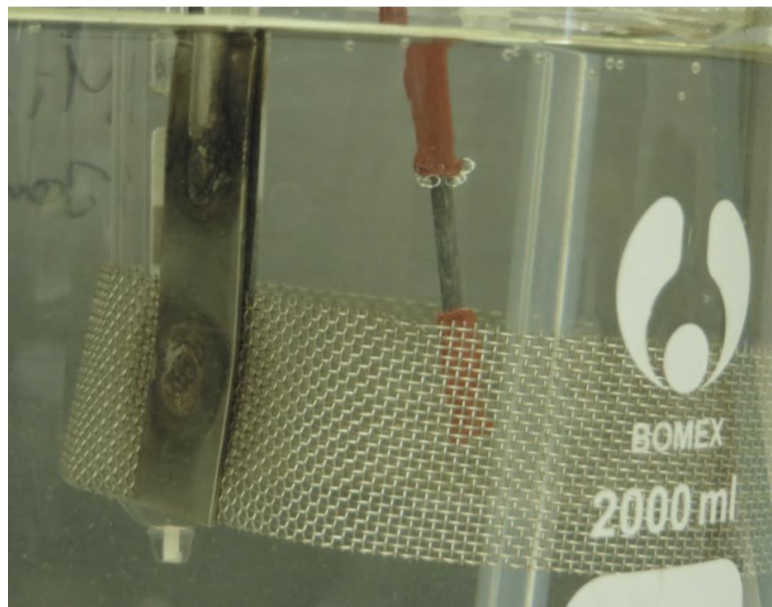


Figure 72: Potentiodynamic polarization scan with stainless steel mesh counter electrode (reference electrode barely visible in the background).

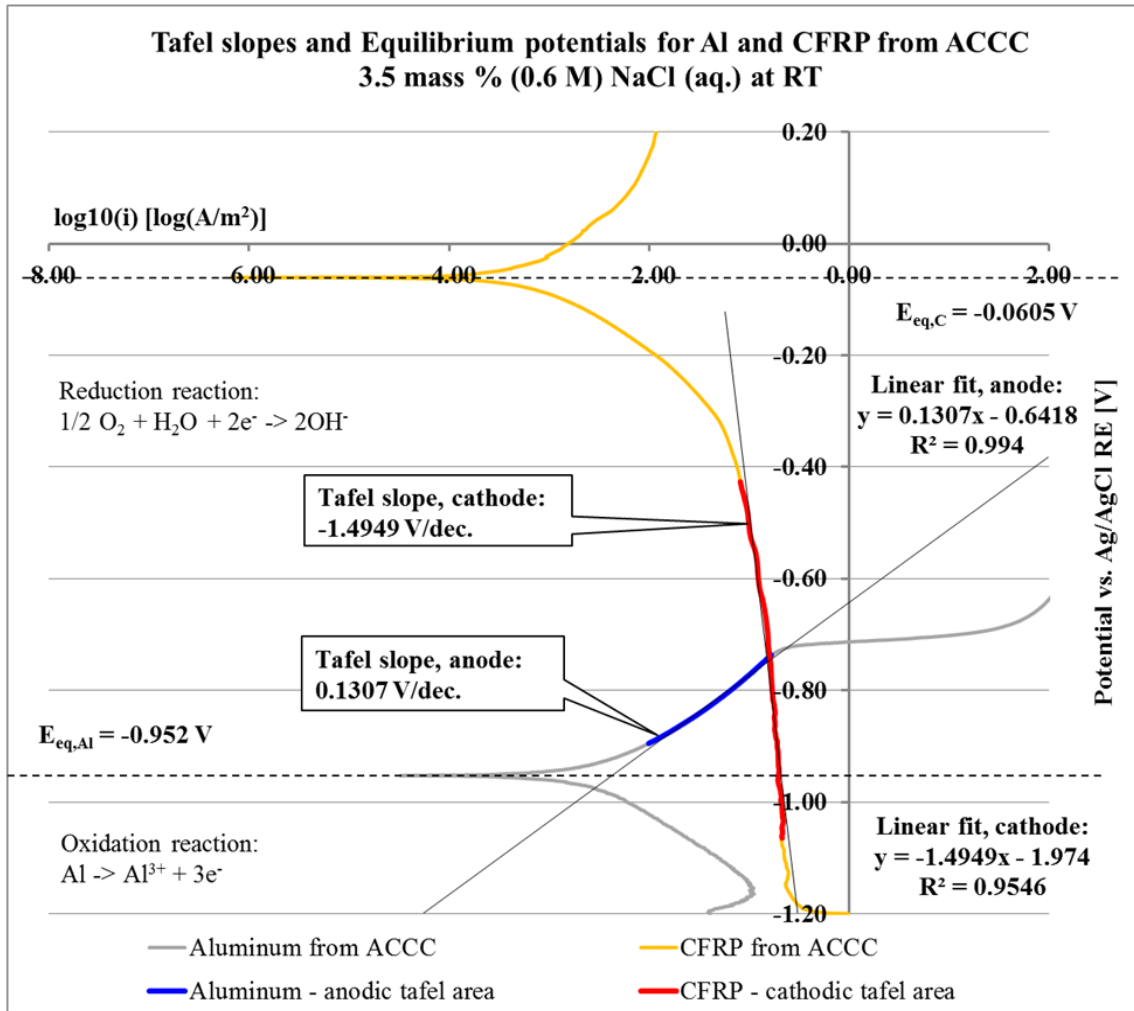


Figure 73: Tafel slopes and equilibrium potential for aluminum and CFRP in the ACCC conductor.

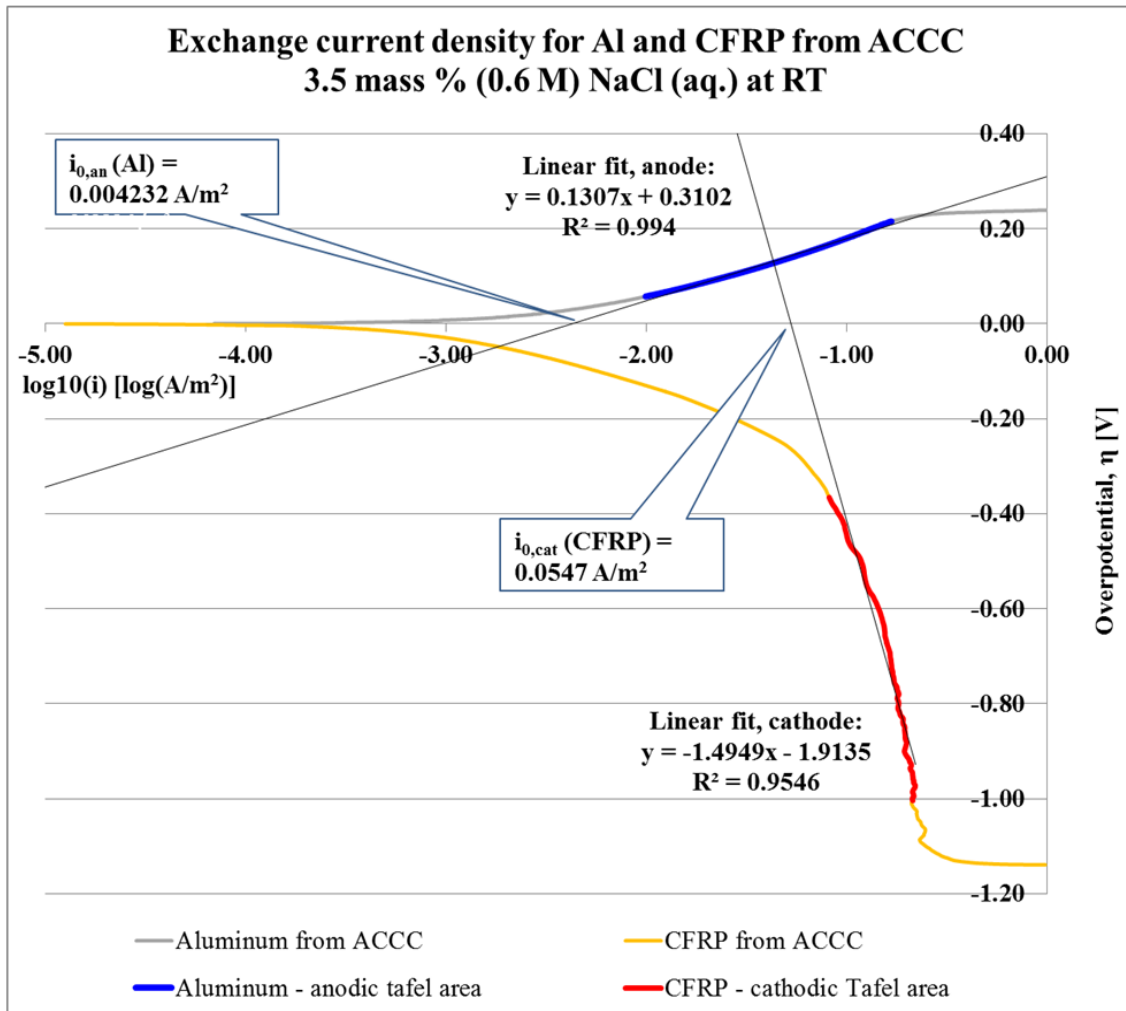


Figure 74: Exchange current density for aluminum and CFRP in the ACCC.

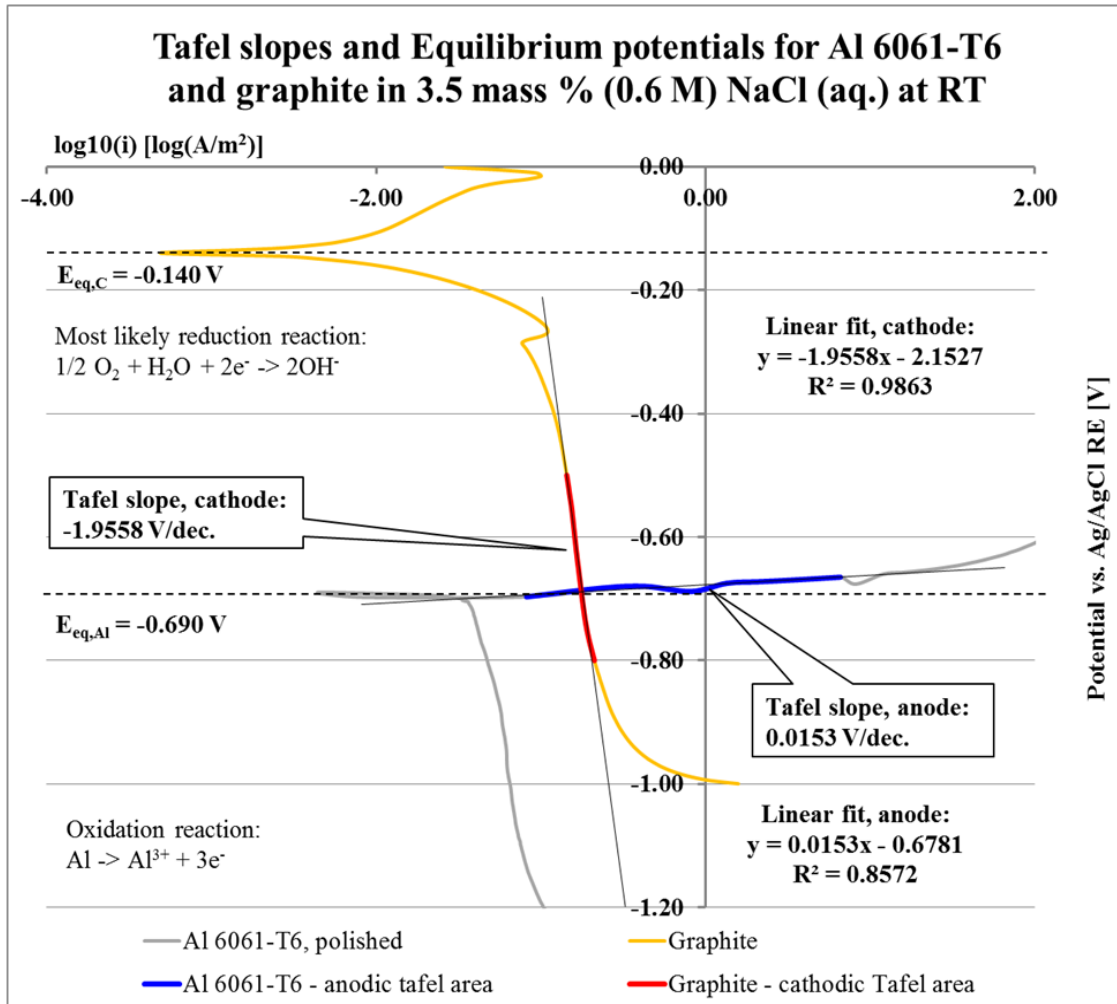


Figure 75: Tafel slopes and equilibrium potential for aluminum and graphite.

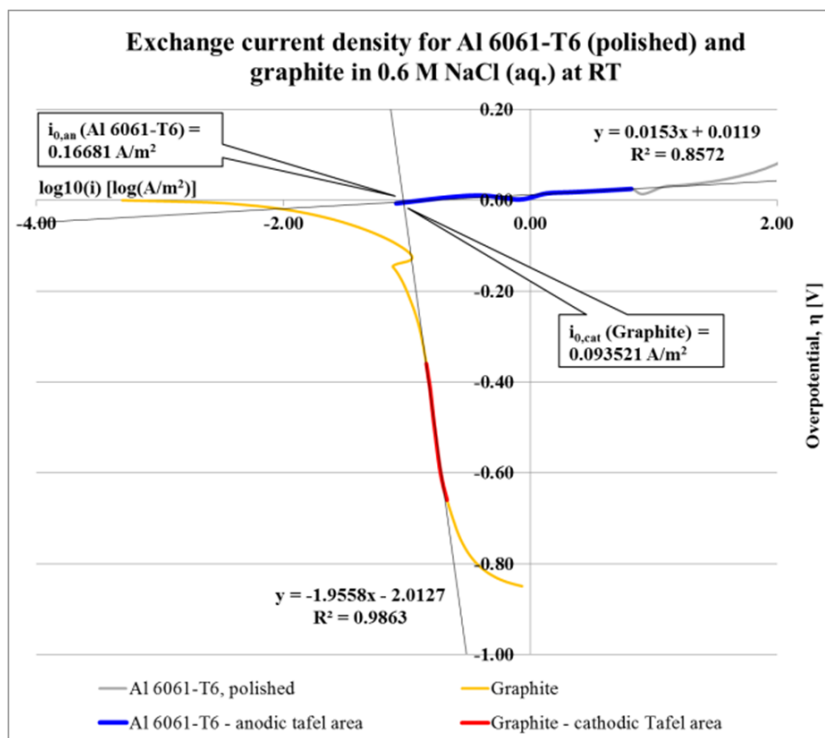


Figure 76: Exchange current density for aluminum 6061-T6 and graphite.

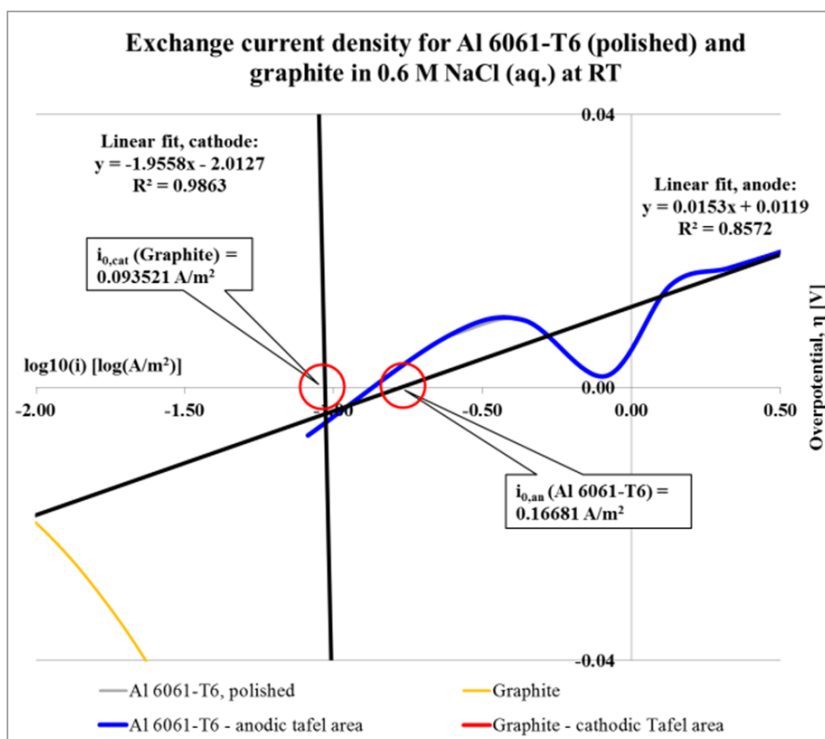


Figure 77: Zoomed in: exchange current density for aluminum 6061-T6 and graphite.

Table 7: Input values for numerical modeling (obtained experimentally from polarization curves in 0.6 M NaCl at RT)			
Variable name	Variable	Value	Unit
<u>Values for grahite/Al-6061 galvanic couple</u>			
$E_{eq,graphite}$	Equilibrium potential, graphite	-0.140	V
$E_{eq,Al-6061}$	Equilibrium potential, aluminum 6061-T6	-0.690	V
$A_{c,grahite}$	Tafel slope, graphite	-1.9558	V
$A_{a,Al-6061}$	Tafel slope, aluminum 6061-T6	0.0153	V
$i_{0,graphite}$	Exchange current density, graphite	0.09351	A/m ²
$i_{0,Al-6061}$	Exchange current density, Al 6061-T6	0.1668	A/m ²
<u>Values for the ACCC conductor</u>			
$E_{eq,C-ACCC}$	Equilibrium potential, CFRP	-0.0605	V
$E_{eq,Al-ACCC}$	Equilibrium potential, Al	-0.952	V
$A_{c,C-ACCC}$	Tafel slope, CFRP	-1.4949	V
$A_{a,Al-ACCC}$	Tafel slope, aluminum	0.1307	V
$i_{0,C-ACCC}$	Exchange current density, CFRP	0.0547	A/m ²
$i_{0,Al-ACCC}$	Exchange current density, aluminum	0.004232	A/m ²

4.1.3 Electrolyte oxygen content

The dissolved oxygen concentration in the electrolytes used for both the experimental characterizations presented in this chapter and the validation models presented in subsequent chapters was measured with a Milwaukee MW600 hand-held dissolved oxygen meter. All tests were performed at room temperature. The dissolved oxygen concentrations and the oxygen saturation limits were corrected for altitude and salinity per instructions in the meter manual (Milwaukee 2010). The values can be found in Table 8 below. The table also includes the conductivity and resistivity values, which were calculated using Kohlrausch’s law as described in chapter 2.

The increased NaCl concentration limits the solubility of oxygen, a phenomenon sometimes called “salting out” (Syed 2006). This pattern can be seen in the table below.

Table 8: Conductivity, resistivity, and dissolved oxygen concentration of the electrolytes						
Molarity [M]	NaCl conc. [% mass fraction]	Conductivity [S/m]	Resistivity [Ω*m]	Measured dissolved oxygen concentration (altitude and salinity corrected) [mg/liter]	Oxygen saturation limit (altitude and salinity corrected) [mg/liter] (Milwaukee 2010)	% of oxygen saturation limit
0.0017	0.01	0.0217	46.1	6.4	6.9	93 %
0.017	0.1	0.217	4.61	6.4	6.9	93 %
0.17	1.0	2.17	0.461	6.3	6.6	95 %
0.6	3.5	7.59	0.132	5.1	5.6	91 %

4.2 Investigation of control mechanisms

As illustrated in the previous chapter, the galvanic corrosion rate in an ACCC conductor with a compromised fiberglass barrier is highly dependent on the geometry when evaluated in immersed conditions. This raised a question about the corrosion control mechanisms and how predictions from immersed testing would translate to an atmospheric service environment. When no satisfying answers were found in the literature, this study was initiated to investigate the control mechanisms. Fundamental understanding of the control mechanisms is a first step towards prediction of the galvanic corrosion performance.

4.2.1 Experimental setup

Multiple experiments were conducted to identify the control mechanisms in the galvanic corrosion of Al/CFRP in general, and of the ACCC conductor with a compromised corrosion barrier in particular. Five different tests were conducted to study the individual characteristics of the galvanic corrosion process during immersed and atmospheric conditions (illustrated in Figure 78):

- I. Potentiodynamic polarization scans of the individual materials
- II. Galvanic corrosion current measurement in bulk solution of the separated materials with different area ratios
- III. Galvanic corrosion current and potential measurements of the representative area ratios (1:28) in different geometries in immersed conditions

- IV. Galvanic corrosion current measurements of the fully assembled conductor samples in immersed and in simulated atmospheric conditions
- V. Mass gain/loss of fully assembled conductors with and without galvanic corrosion in simulated atmospheric conditions.

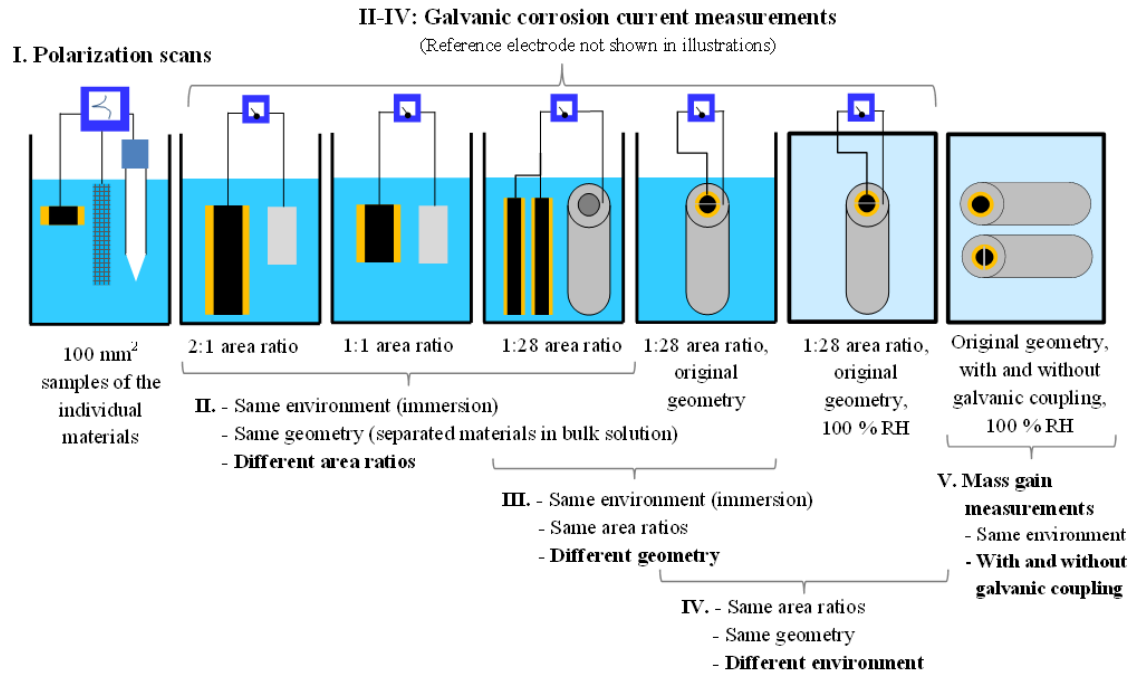
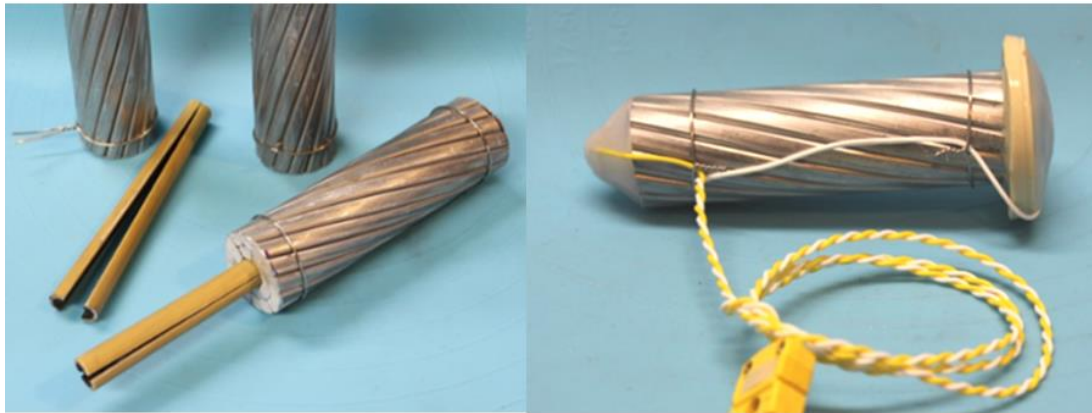


Figure 78: Illustration of tests.

Sample design

Two different sample designs were used: samples made from the individual materials and samples consisting of fully assembled ACCC conductors with a compromised galvanic corrosion barrier. The fully assembled conductor samples were prepared as described in chapter 3. This sample design results in a CFRP-to-aluminum surface area ratio of 1:28 (total surface area of exposed CFRP to total surface area of aluminum conductor strands). The lengths of the samples were ~100 mm.



*Figure 79: ACCC samples with simulated damage.
Left) Damage introduced by splitting the composite core along the centerline.
Right) Finished sample of ACCC with simulated damage.*

Potentiodynamic polarization scans were conducted using samples of the individual materials with an exposed surface area of 100 mm^2 . Galvanic corrosion measurements of the fully separated materials used samples of the different materials ranging from 0.0007 m^2 to 0.039 m^2 . An Ag/AgCl reference electrode was used for all measurements.

With exception of nine samples tested at atmospheric conditions in test group IV and all 10 samples in test group V, the aluminum material in all samples was either sanded or treated with phosphoric acid to remove grease, scale, and thick oxide layers originating from the manufacturing of the aluminum strands. The nine samples not treated this way were only degreased with isopropyl alcohol. The fully assembled samples where the aluminum was treated with phosphoric acid are called “Acid Prep” in the subsequent sections. The fully assembled samples where the aluminum was only degreased with isopropyl alcohol are called “As Received”.

Electrolytes

All immersed tests were performed in 0.6 M NaCl aqueous solution unless otherwise stated. The pH of the electrolyte was approximately 6.5. Three levels of agitation/aeration of the electrolyte were used: heavily agitated and aerated, stagnant (but still oxygen-rich), and stagnant and oxygen-deprived. An additional fourth level was added for certain tests: a jet of electrolyte was directed onto the sample surface to create the highest possible transport of reactants and reaction products. The agitation/aeration levels were accomplished using the following methods:

- 1) **Heavily agitated and aerated** electrolyte: Forcing air through the electrolyte (0.8 liter/min through a volume of 4500 ml).
- 2) **Stagnant and oxygen-rich** electrolyte: Forcing air through the electrolyte as above and turning off the air-flow just before the measurement was started.
- 3) **Oxygen-deprived** electrolyte: Boiling the electrolyte and sealing the container before cool down, and keeping the test cell free from air during the tests. Small cell volume (<1000 ml electrolyte) and long test duration (>20 hours) ensured that remaining dissolved oxygen was consumed before measurements were taken.
- 4) **Electrolyte jet**: A submerged pump was used to create a jet of electrolyte that was directed onto the sample surface. The volumetric flow was 70 ml/second, which generated a flow velocity of 1 m/s at the sample surface.

Tests were also conducted in atmospheric conditions where the samples were first immersed in the electrolyte, dried, and then subjected to different levels of relative humidity. All experiments were conducted at room temperature (average 25.2°C, $\sigma=2.1^\circ\text{C}$).

Testing protocol and number of samples

Previous test series have shown a much larger scatter in the galvanic corrosion rate in simulated atmospheric conditions than in immersed conditions. A test set of 18 samples was used for the galvanic corrosion measurements in atmospheric conditions in test group IV. Two sets of 5 samples each were used for test group V. Experience has shown that polarization scans give very consistent results, so one sample per material per environment was measured. All other test series used at least 3 samples for each condition.

Due to the dynamic nature of the corrosion process, the corrosion potential of the galvanic couple can fluctuate drastically over time without any obvious perturbations of the environment. A strict testing protocol was followed to obtain the corrosion potentials and corrosion currents in test group III. For every environment and sample type, the potential was first measured in agitated electrolyte, and subsequently in stagnant electrolyte using the same samples. Measurements were taken every 10 seconds for 1 hour. The average and spread was calculated for the last 30 minutes. The tests were repeated three times. For the oxygen-deprived electrolyte, measurements were taken every 5 minutes for 20 hours with averages and spreads calculated for the last 5 hours.

The longer test duration for the oxygen-deprived environment was chosen to ensure that any remaining oxygen would be consumed before the measurements were made that would be used to calculate the averages.

Test cycle for Groups IV and V

A test cycle including both atmospheric and immersed conditions was used in test Group IV and V. The samples were immersed in the electrolyte and complete penetration was ensured by applying a small under-pressure with a handheld vacuum pump during immersion Figure 80. Excessive electrolyte was wiped off the outside of the samples. After drying for 48 hours in ~20 % relative humidity (RH), the samples were subjected to a test cycle at room temperature consisting of 30 days at 85 % RH, 14 days at 100 %, 3 days of drying (15-20 % RH), 4 days of immersion (0.6 M NaCl), 2 days of drying (15-20 % RH), and finally back to 100 % RH for 15 days, making the total duration of the test cycle 70 days. The methods used for calculating averages and errors vary for different phases and are described in the results section.

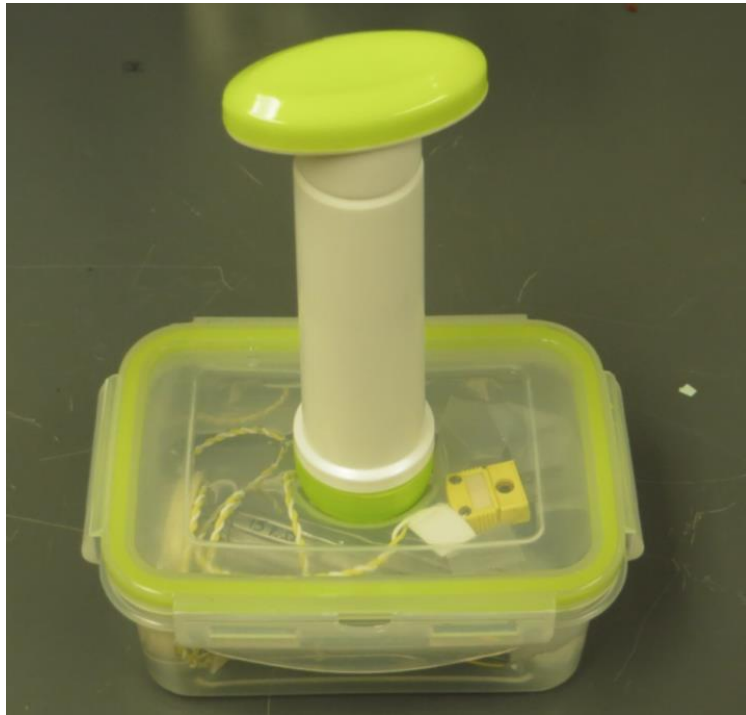


Figure 80: Applying vacuum to ensure complete electrolyte penetration of the conductor sample.



Figure 81: The atmospheric conditions were created in a humidity chamber.

4.2.2 Results

Test Group I: Polarization scans

Overlaying of the polarization curves for aluminum and CFRP (Figure 82) provides evidence that the galvanic corrosion is under cathodic control in all three environments (agitated, stagnant, and oxygen-deprived electrolyte) included in this test series. The steep slope of the cathodic curves (red lines) where they intersect the anodic curves (blue lines) is characteristic of cathodic control, which is obvious when Figure 82 is compared with Figure 31 (repeated below) (Hack 2005), (Revie 2000). This means that the corrosion rate on the cathodic site will set the total galvanic corrosion rate.

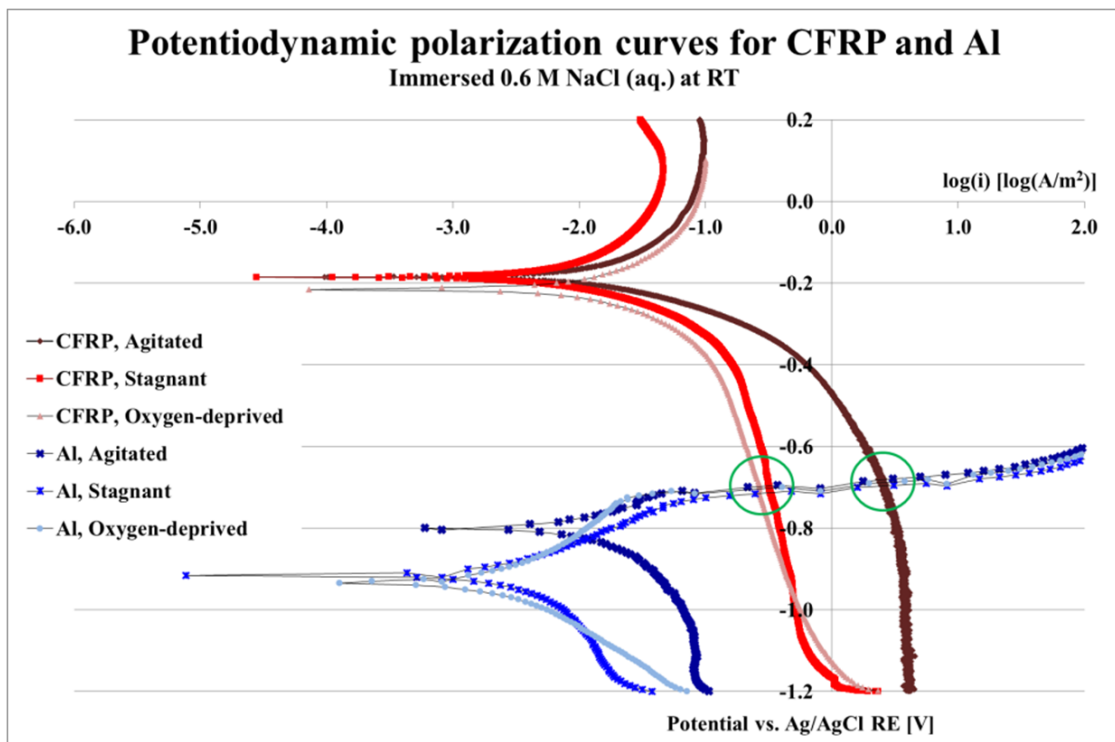


Figure 82: Polarization scans of CFRP and Al in agitated, stagnant, and oxygen-deprived 0.6 M NaCl.

The intersection between the polarization curve for the cathodic material and for the anodic material provides a rough estimate of the galvanic corrosion rate. There is an eight- or nine-fold difference in this estimate (marked with green circles) between the agitated electrolyte and the stagnant or oxygen-deprived electrolyte (2,470 mA/m² compared to 320 and 270 mA/m² respectively). This dramatic shift indicates that the cathodic reaction is dependent on transport of oxygen to the electrode-electrolyte interface, or transport of reaction products from the interface, or both.

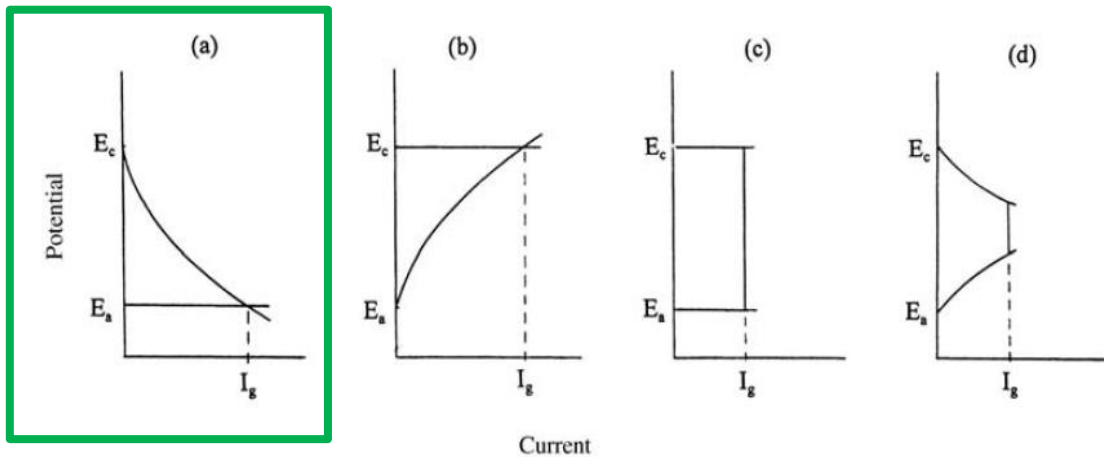


Figure 31 (repeated): Schematic illustration of polarization curves for four different control types. a) cathodic control, b) anodic control, c) resistance control, and d) mixed control. Source: (Revie 2000)

A small shift in the rest potential for the CFRP was noticed between the aerated and oxygen-deprived conditions. The rest potential shifted from -0.186 V for agitated and stagnant to -0.215 V in the oxygen-deprived environment. The aluminum displayed a larger shift from -0.800 V in the agitated to -0.915 V in stagnant and -0.935 V in oxygen-deprived environments. In general, it can be observed that a lower concentration of

dissolved oxygen and less agitation of the electrolyte results in a shift of the rest potential to more negative levels for both materials.

Test Group II: Galvanic corrosion current measurement in bulk solution of the separated materials with different area ratios

The eight- to nine-fold difference in predicted galvanic corrosion rate between agitated and stagnant electrolyte observed in the polarization scans is also apparent in galvanic corrosion current measurements of the separated materials immersed in bulk solution. Figure 83 illustrates how the area ratio, NaCl concentration, and level of agitation of the electrolyte affect the galvanic corrosion current density. The dependency on agitation points to mass transport of reactants, or corrosion products, or both, as the dominating control mechanism for separated materials immersed in bulk solution.

The figure also illustrates that the total corrosion rate is dominated by the exposed CFRP area, and is essentially independent of the Al area. The salt concentration also influences the total corrosion rate because a decrease in concentration will result in an increase in the resistance of the electrolyte. However, the effect is relatively weak, as demonstrated by the corrosion rates measured in 0.6 M NaCl and 0.017 M (0.1 mass %) NaCl.

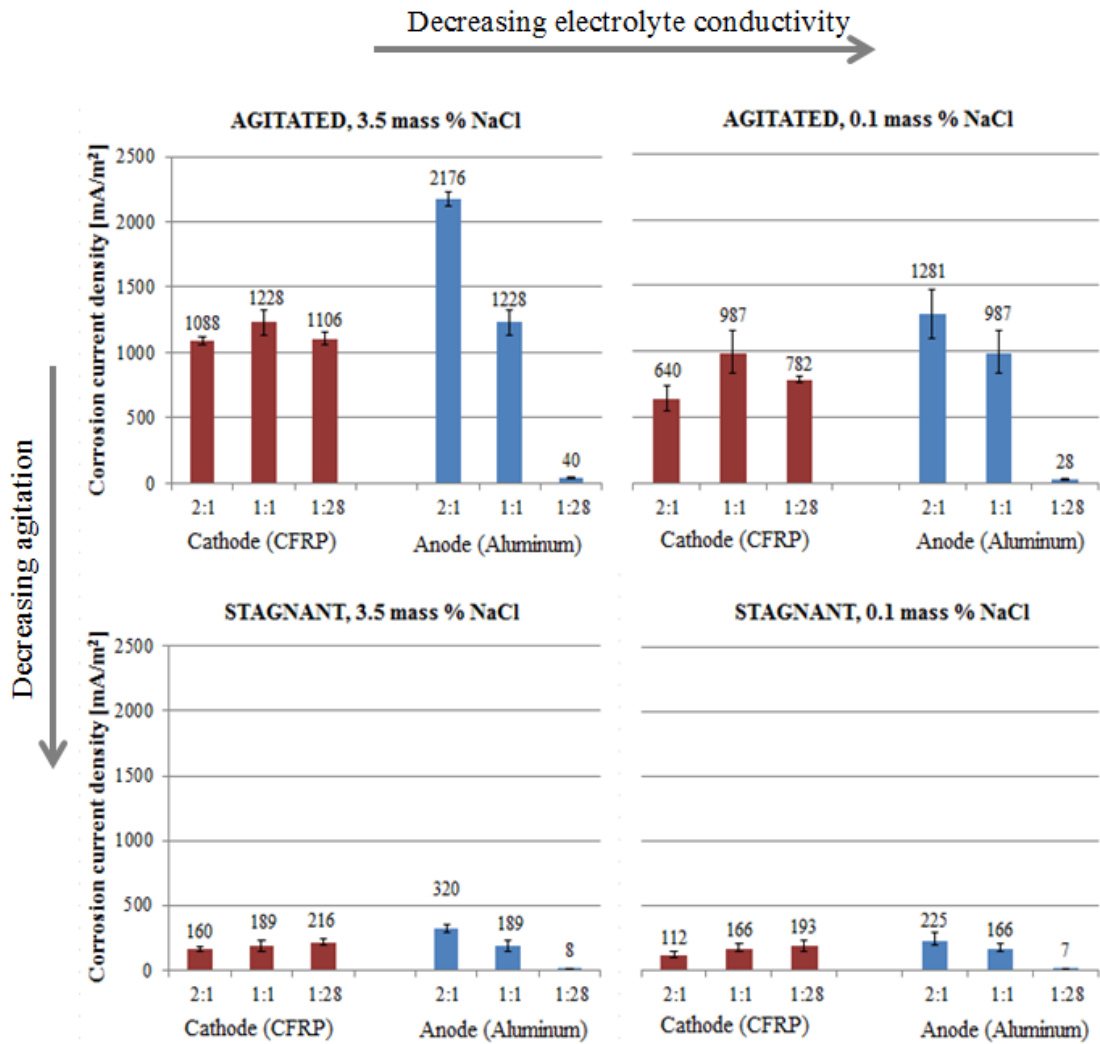


Figure 83: Galvanic corrosion current as a function of area ratio (CFRP:Al), NaCl concentration, and agitation level of separated materials immersed in bulk solution. Main bars represent the average value and error bars show the spread within each group of three or more samples.

Test Group III:

Galvanic corrosion current and potential, 1:28 area ratio, different geometries

Corrosion current

Figure 84 adds additional support for the mass transport of as the main limiting mechanisms. In the fully assembled conductor samples, the mass transport is largely limited by the narrow gaps between the aluminum strands (average gap width is 180 μm). The two bars to the very left in Figure 84 represent the galvanic corrosion rate for two samples in the same environment and with the same area ratio. The only difference is that the second bar represents a sample where the split composite core is on the *inside* of the aluminum strands, as it would be in-service. The move of the core from the *inside* of the sample to the *outside* resulted in a 32-fold increase in galvanic corrosion rate in agitated bulk solution. The difference was nine-fold in the stagnant solution and five-fold in the oxygen-deprived electrolyte.

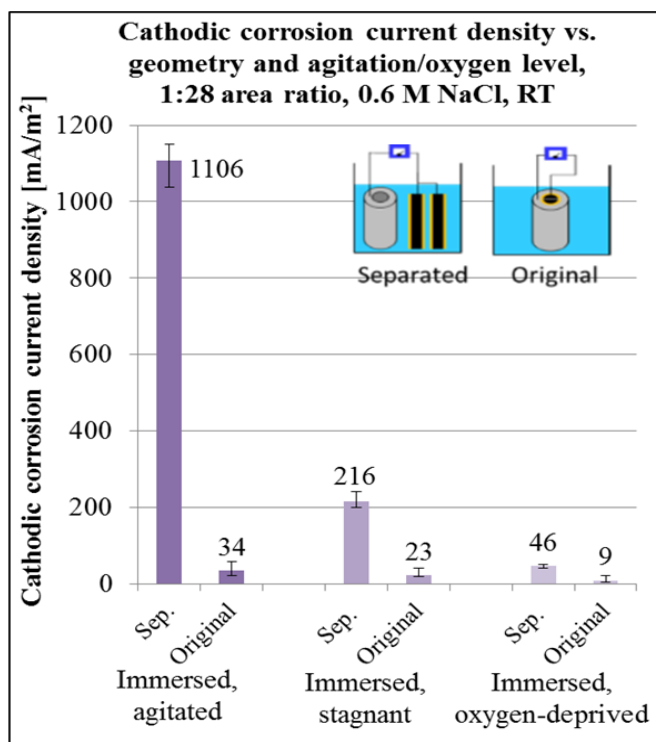


Figure 84: Galvanic corrosion rate for separated and fully assembled conductor samples with 1:28 CFRP/Al area ratios in different environments.

All of the four bars to the right in Figure 85 represent stagnant electrolytes. The large difference between the oxygen-rich electrolyte and the oxygen-deprived electrolyte provides strong evidence that the oxygen reduction reaction is the dominant cathodic reaction.

The non-zero galvanic corrosion rate and the evolution of gas bubbles (believed to be H₂) in the oxygen-deprived electrolyte provides support for the presence of the water splitting reaction on the cathode. The difference in galvanic corrosion rate between the original and separated sample designs could indicate two things: 1) the electrolyte was not completely oxygen free, or 2) the accumulation of corrosion products such as H₂ at the cathode decreases the galvanic corrosion rate, or both.

Corrosion potential

The corrosion potential (measured with respect to a reference electrode (RE)) of the galvanic couple will always lie between the equilibrium potentials of the anodic and cathodic half-reactions. If there is more than one cathodic reaction taking place, the potential will depend on both of them (Landolt 1995).

Figure 85 reveals that less agitation, lower levels of dissolved oxygen, and more restriction in the mass transport cause a shift in the corrosion potential towards a more negative level.

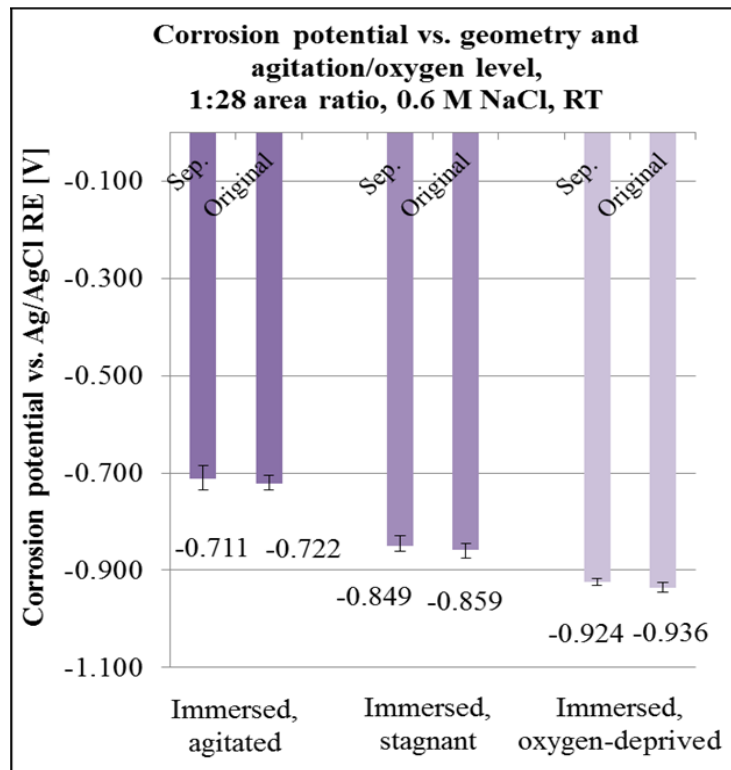
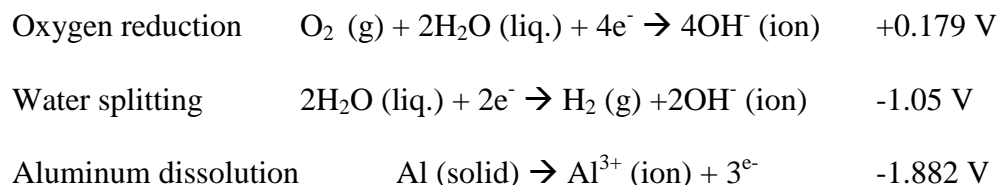


Figure 85: Galvanic corrosion potential vs. Ag/AgCl RE. Main bars represent the average value and error bars show the spread within each group of three or more samples.

The two probable cathodic reactions and the anodic aluminum dissolution reaction have the following corrosion potentials under standard conditions (with reference to Ag/AgCl RE) (Roberge 2008), (Vargel 2004):



Although these potentials may not translate directly to the testing environment, the shift of the corrosion potential of the galvanic couple towards more negative levels indicate that the water-splitting cathodic reaction is becoming more dominant.

The formation of gas bubbles - believed to be H_2 - emerging from the gaps between the aluminum wires supports the suggestion that the water splitting reaction is taking place on the cathode (see Figure 86). The volume of the gas was too small to analyze with available equipment. The gas formation was much more prominent under the oxygen-deprived conditions than under stagnant conditions. The presence of gas evolution could not be determined during agitated conditions. The tube-like structures in Figure 86 had grown on a sample subjected to a long-term immersion test in 0.5 M NaCl at 85°C performed in the master's thesis work preceding this dissertation work (Håkansson 2013). The openings of the tubes are all pointing upwards, indicating that the structures of deposited $Al(OH)_3$ were influenced by escaping hydrogen gas bubbles.

Although the data presented in and the gas bubbles in Figure 86 suggest that water-splitting takes place, the galvanic corrosion rate in the oxygen-starved environment was very low, as can be seen in Figure 84. The tunnels of $\text{Al}(\text{OH})_3$ in Figure 86 were created in a high-temperature environment (85°C). It is completely possible that the dominant cathodic reaction is dependent on the temperature, but that has not been investigated in this study. Because of the low galvanic corrosion rates measured in the oxygen-starved environment, the galvanic corrosion caused by the water-splitting reaction will be considered negligible from here on, unless otherwise stated.

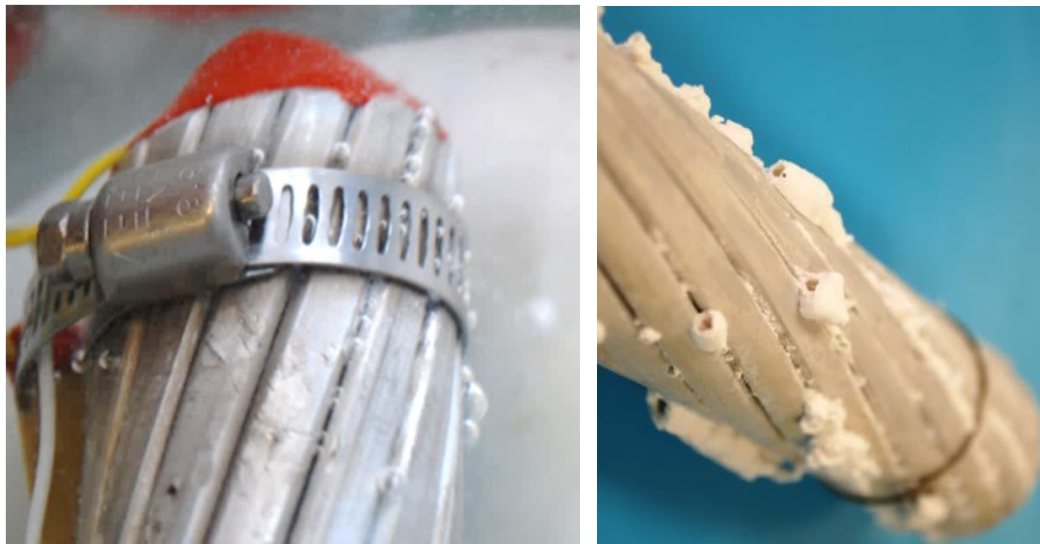


Figure 86: Reaction products.

Left) Gas evolution under oxygen-deprived conditions.

Right) Tube-like structures of corrosion products on a sample subjected to a long-term immersion test at 85°C in 0.5 M NaCl .

Test Group IV: Original geometry, different environments

Figure 87 compares the galvanic corrosion rate to the water evaporation during drying after being immersed in 0.6 M NaCl . The galvanic corrosion rate was measured in the 18 fully assembled conductor samples (nine of them “Acid Prep” and nine of them

“As Received”), while the mass loss was measured in an additional five samples subjected to the same conditions. The galvanic corrosion rate increased rapidly as the samples were drying. A hypothesis is that as soon as any continuous air path from the outside of the sample to the carbon surface is established (which may occur as soon as the sample is removed from the bulk solution), the cathodic reaction rate increases rapidly as transport of oxygen to the surface is no longer restricted by the electrolyte. As the sample dries further, the galvanic corrosion rate decreases with the decreasing electrolyte layer thickness. When the amount of electrolyte is no longer sufficient to bridge the two materials, the galvanic corrosion ceases completely.

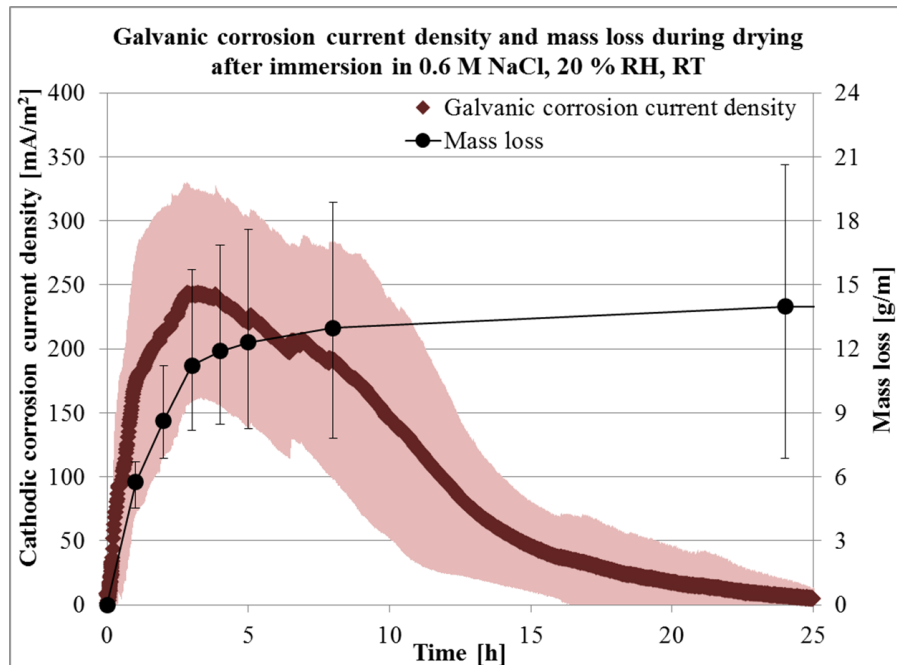


Figure 87: Galvanic corrosion rate vs. mass loss during drying of an ACCC sample with compromised corrosion barrier after immersion in 0.6 M NaCl solution. Average for corrosion rate is for 18 samples and shaded region indicates one standard deviation. Average for mass loss is for five samples and error bars display the spread within the group.

The drying experiment pointed to mass transport as being the dominant control mechanism. Figure 88 compares the galvanic corrosion rates measured in immersed and

atmospheric conditions (atmospheric corrosion rates were recorded during the last phase of the 70 day cycle). The drastically higher galvanic corrosion rates under atmospheric conditions support the hypothesis that mass transport of oxygen may be a major limiting mechanism. During immersion, the gaps between the aluminum strands are filled with electrolyte. The diffusion coefficient for oxygen is 10 800 times higher in air than it is in water (Giambattista, Richardson et al. 2004), which could explain the lower corrosion rate when the gaps are filled with electrolyte.

The figure also indicates another limiting mechanism under certain conditions: the scale and oxide layer on the as-received conductors originating from the manufacturing process and over 10 years of storage outdoors appears to drastically limit the galvanic corrosion rate during steady humid conditions. The presence of this passive layer also decreases the scatter. During constant humidity conditions, the scatter is very large for the acid treated samples, indicating a much more active-passive behavior for these samples. The atmospheric galvanic corrosion will be re-visited in chapter 7, where it will be shown that the deposition of $\text{Al}(\text{OH})_3$ can drastically affect the galvanic corrosion rate. Because the data presented here comes from a long-term test, the scatter may have been caused by deposition of corrosion products, causing different corrosion rates in different samples.

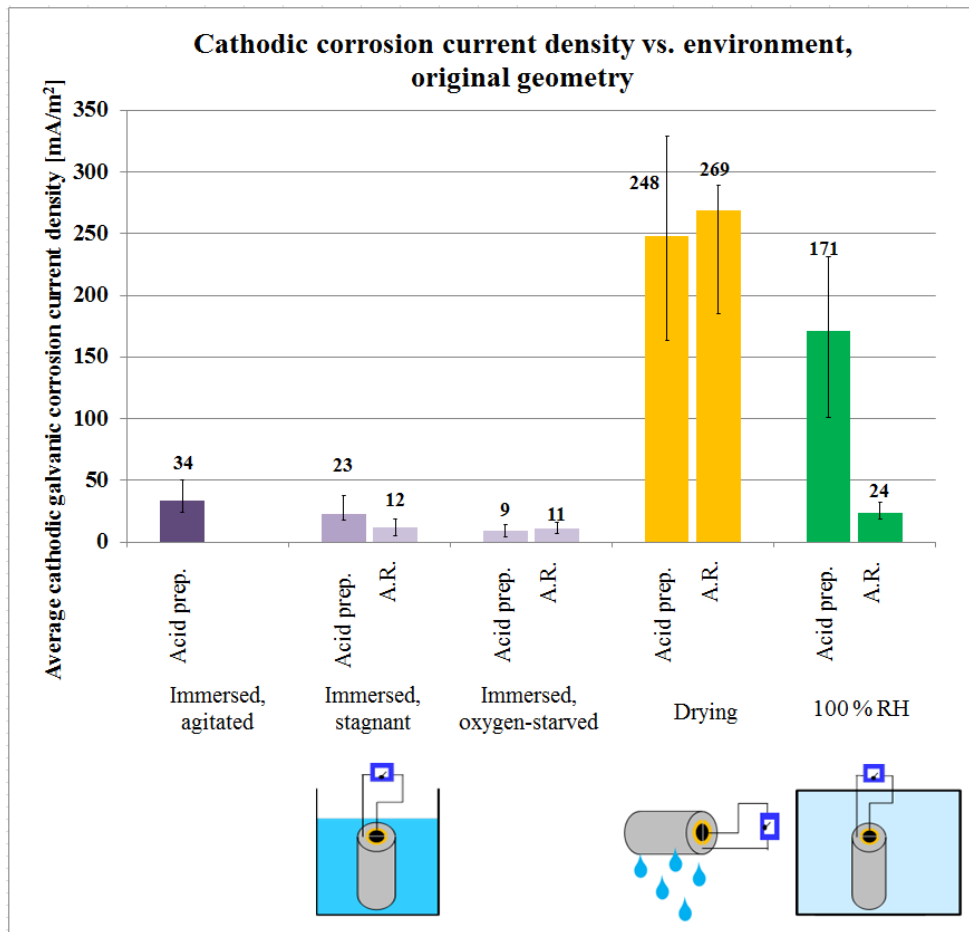


Figure 88: Cathodic galvanic corrosion current density for fully assembled samples in different environments and with different surface preparation.

Test Group V: Mass gain in presence and absence of galvanic corrosion

Figure 89 displays the mass change of ten “As Received” ACCC conductor samples during 44 days of atmospheric conditions and 8 days of drying. Five of the samples have a compromised galvanic corrosion barrier and five of them are intact. The mass gain does not include the salt load resulting from the initial exposure to 0.6 M NaCl solution (salt load density 2.7 g/m² ($\sigma=0.65$)). The corrosion products are trapped inside the conductor sample, resulting in an overall mass gain despite aluminum being lost due to corrosion.

The mass increased rapidly in the beginning as the salt present on the surface of the strands and core absorbed moisture from the atmosphere forming a liquid electrolyte. The mass also changed rapidly when the humidity was increased. The higher mass gain for the samples without galvanic corrosion during the 100 % RH phase is believed to be an artifact of their placement in the humidity chamber. The humidity was generated with ultrasonic humidifiers, and samples nearby the humidifiers may have had some water particles landing on them. Due to the small values measured, a thin layer of water on the surface would have likely skewed the values during the 100 % RH phase.

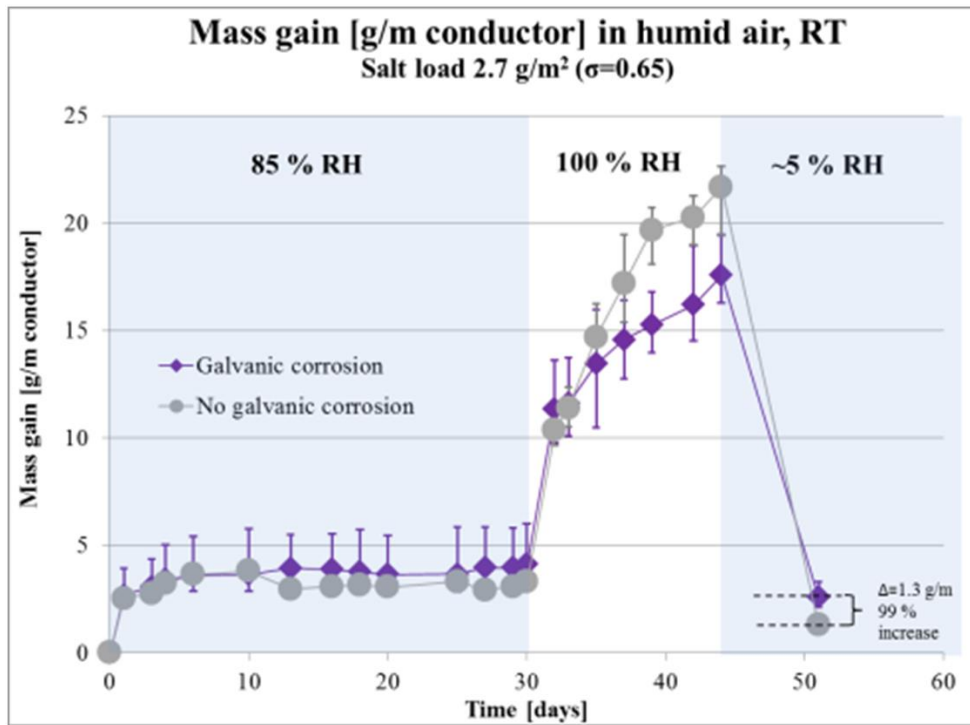


Figure 89: Mass gain [g/m] in addition to the salt load of ~100 mm long ACCC samples with and without galvanic corrosion.

Initially exposed to 0.6 M NaCl solution resulting in a salt load density of 2.7 g NaCl/m² ($\sigma=0.65$). Five samples of each kind. Error bars display max and min values within each group.

When the samples were thoroughly dried, only salt and corrosion products remained. The samples with galvanic corrosion had twice the mass gain compared to the samples without galvanic corrosion. The corrosion product is mainly aluminum hydroxide ($\text{Al}(\text{OH})_3$), confirmed by X-ray diffraction in previous studies. The difference in mass gain demonstrates that the presence of galvanic corrosion had doubled the corrosion rate of the aluminum under these conditions.

Assuming that the increase in mass is due to a build-up of aluminum hydroxide only, the average galvanic corrosion current density needed to generate the difference between the two sets can be calculated.

The difference in mass gain is 1.3 g per meter of conductor during a period of 44 days. The molecular weight is 27 g/mol for Al and 78 g/mol for $\text{Al}(\text{OH})_3$. That is a mass increase of 2.89 times, which means that 0.45 g of Al was lost to corrosion to create 1.3 g of $\text{Al}(\text{OH})_3$. Knowing that every Al atom will release 3 electrons, 0.45 g of Al lost to galvanic corrosion will equal 1608 C (coulombs). 1 A equals 1 C/s, and 44 days is $3.801\text{E}6$ seconds, so the average current would be 0.000423 A. The trapezoidally stranded ACCC conductor used in this study has an exposed aluminum area of 0.389 m^2 per meter of conductor. The current calculated from the mass gain would result in an average anodic galvanic corrosion current density of 1.1 mA/m^2 .

During the same period, the nine As Received samples placed in the same environment had an average measured anodic corrosion current density of 0.85 mA/m^2 (shown as 24 mA/m^2 cathodic current density in Figure 88; dividing by 28 gives the

anodic current density). The current density calculated from the mass gain is a bit higher than the current density that was measured directly, but it is within the measured range.

The corrosion in the absence of galvanic corrosion is also known as the *self-corrosion*. Assuming a uniform corrosion of the aluminum, the calculated self-corrosion corrosion rate is equal to a penetration rate of 0.007 mm/year or 7 $\mu\text{m}/\text{year}$. At this rate, it would take 40 years to lose 20 % of the aluminum cross-section due to the galvanic corrosion. The presence of the galvanic corrosion resulted in a doubling of the total corrosion rate of the aluminum from approximately 7 $\mu\text{m}/\text{year}$ to 14 $\mu\text{m}/\text{year}$.

Francis (Francis 2000) states that a typical penetration rate for self-corrosion of aluminum in marine atmospheres is 0.6 $\mu\text{m}/\text{year}$. The average self-corrosion rate calculated from the mass gain is one order of magnitude higher. This means that the testing environment can be considered a severely corrosive - and likely an accelerated - environment. In order to use laboratory evaluation to predict service life, this large discrepancy between typical corrosion rates and measured rates in the laboratory has to be addressed. The testing environment likely needs to be adjusted, but this is outside the scope of this dissertation.

The twice as high mass gain of the samples with a galvanic coupling provides strong evidence that the galvanic coupling accelerates the total corrosion of the aluminum, and does not merely move the cathodic processes from the aluminum to the CFRP.

4.2.3 Discussion and conclusions about control mechanisms

Control mechanisms in immersed conditions

The study has confirmed that the galvanic corrosion is under *cathodic control* in immersed conditions (Hack 2005) and that the dominating cathodic reaction is the reduction of oxygen. The total galvanic corrosion rate is primarily dominated by the cathodic half-reaction, which is common for corrosion in immersed environments. Because of the cathodic control, the cathodic reaction rate controls the total galvanic corrosion rate, independent of the area ratio of cathode and anode. The galvanic corrosion rate is weakly dependent on the NaCl concentration, but highly dependent on the oxygen content and agitation.

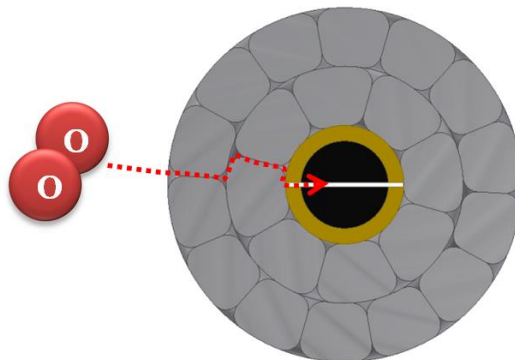


Figure 90: The pathway for oxygen to reach the cathodic reaction on the CFRP. The hydrogen gas will travel the same path, but in the opposite direction, when the water splitting reaction takes place.

The strong effect of agitation indicates a *concentration polarization* control type, also known as *diffusion control*, where the rate of the reaction is controlled by the rate at which reactants arrive at the CFRP surface. In stagnant electrolyte, the diffusion of

oxygen to the cathode is not fast enough to sustain the highest possible rate of corrosion, which makes the corrosion rate diffusion limited. The drastically lower galvanic corrosion rate in the fully assembled conductor samples compared to the separated samples with identical area ratio also supports this conclusion.

Control mechanisms in atmospheric conditions

The control mechanisms are much more complex in atmospheric galvanic corrosion. As shown in chapter 3 (and will be discussed further in chapter 5), the galvanic corrosion rate is highly dependent on electrolyte layer thickness, which is a function of salt load density and relative humidity.

The literature (Barton 1973) states that because the electrolyte layer is so thin, the transport rate of oxygen to the cathode surface is so fast that the corrosion rate is in no way controlled by the cathodic oxygen reduction process. However, the ACCC conductor with introduced damage is a special case because the cathode is buried deep inside the component with only thin gaps for the oxygen transport, which is quite different from typical structures subjected to atmospheric corrosion such as bridges and roofs. High humidity and high salt load density can result in enough electrolyte to completely fill the crevices. The buildup of corrosion products also appears to limit the corrosion rate over time, perhaps due to restrictions in mass transport. This observation will be re-visited in chapter 7.

The scale and oxide layer on the as-received conductor samples that had been stored outdoors for over a decade drastically limited the corrosion rate under steady,

humid conditions in some of the test series. The difference between conductor sample with a thick oxide layer originating from the manufacturing and samples where this layer has been removed will be re-visited in chapter 7. It will be shown that this layer has less of an effect if the test is run over a long time period. It is known that the formation of an oxide film, which can be formed during dry conditions, can change the course of corrosion under other conditions (Barton 1973). This is the principle behind anodizing of aluminum components. The protective layer on the aluminum would not affect the kinetics of the cathodic reaction, which means the decrease in total galvanic corrosion rate would be due to resistance control caused by the insulating oxide layer.

Galvanic corrosion rates and time-to-failure

The effect of the control mechanisms identified above can be seen in Figure 91. The galvanic corrosion rates are expressed in average *anodic* galvanic corrosion current density for area ratios, geometries, and electrolyte properties that were of particular interest. Compared to the situation where an electrolyte jet was directed onto the sample surface, the corrosion rates in all other conditions are extremely low.

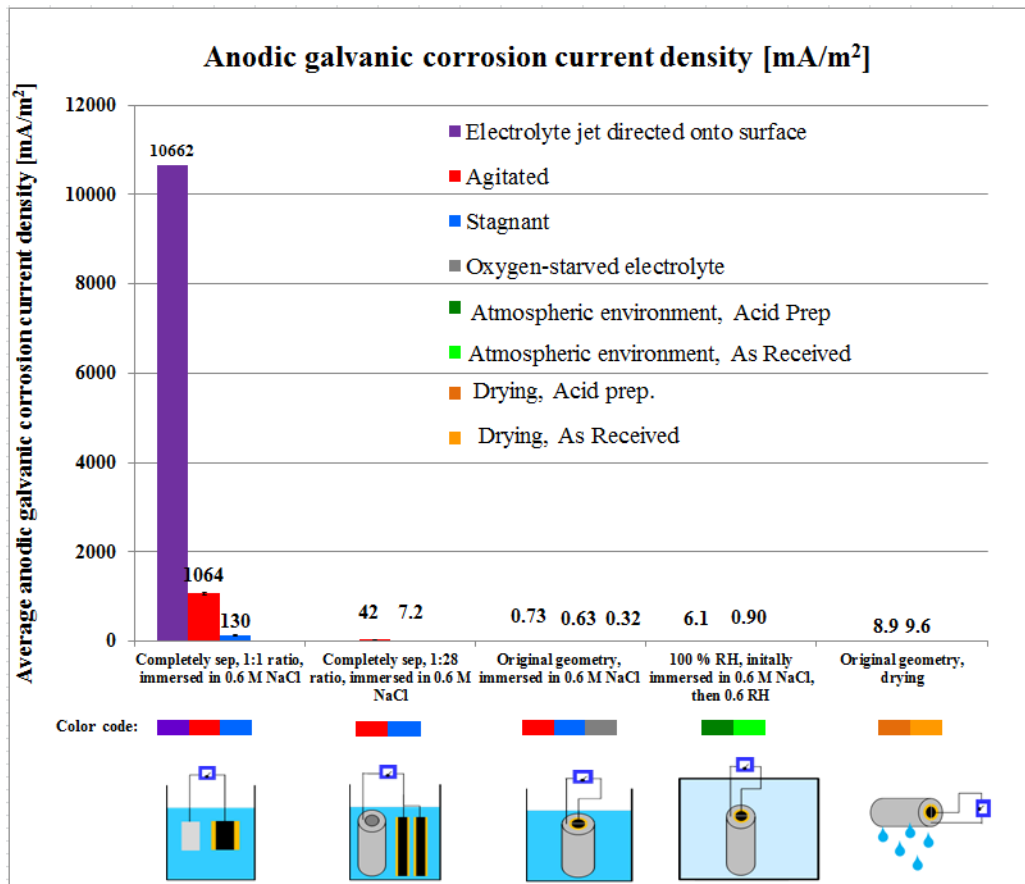


Figure 91: Summary of measured anodic galvanic corrosion current densities, mA/m².

In Figure 92, the galvanic corrosion rates are translated into average corrosion penetration rate of the aluminum. This assumes that the corrosion is uniform. Aluminum in neutral electrolytes develops pitting corrosion, which means that the corrosion is localized. The local corrosion penetration can therefore be much deeper than the plot indicates, but the average corrosion rates still represent the total mass loss of the aluminum.

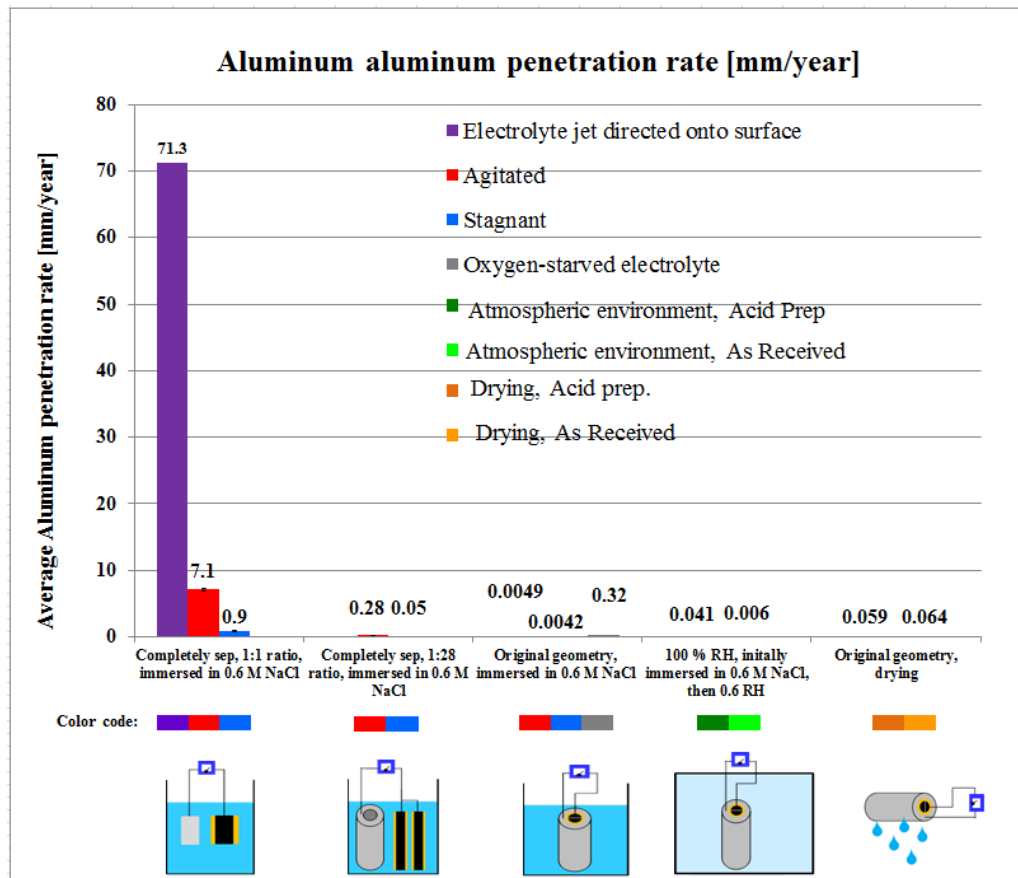


Figure 92: Summary of measured galvanic corrosion rates, mm/year.

It may be hard to comprehend what these rates would mean to a transmission line conductor. Using a failure criterion that assumes that a transmission line conductor is considered failed when it has lost 20 % of its aluminum cross-section, we can translate the above corrosion rates into time-to-failure. Figure 93 illustrates the time-to-failure using this criterion. The importance of a suitable testing method is obvious in the plot. Just by changing the area ratio, geometry, electrolyte agitation, surface preparation, and level of dissolved oxygen, the same materials in the same electrolyte will have a predicted time-to-failure of 35 hours to 130 years. That is a difference of 32,500 times, or more than three orders of magnitude! The difference in atmospheric conditions is also

more than an order of magnitude depending on the surface preparation. The atmospheric corrosion will be discussed in detail in the next section.

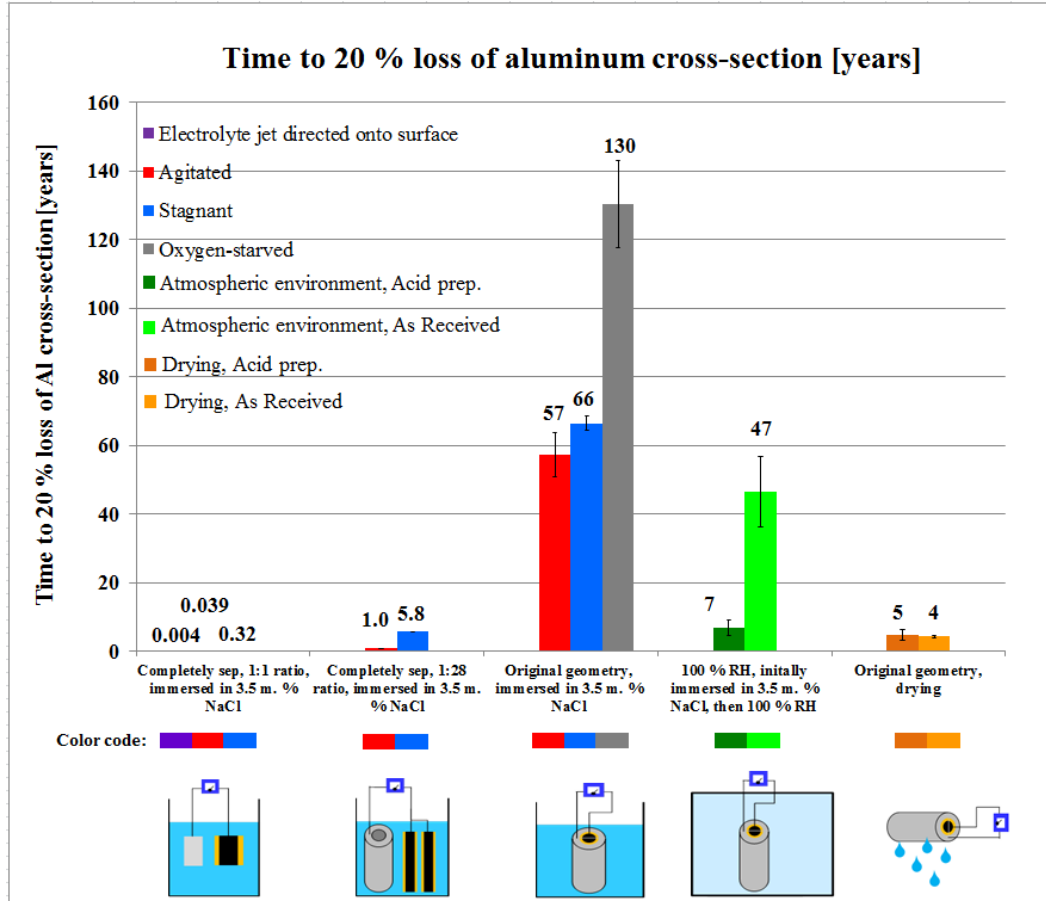


Figure 93: Summary of measured galvanic corrosion rates translated into time-to-failure for an overhead transmission line conductor.

The prediction assumes that the galvanic corrosion rate remains unchanged.

4.3 Summary of input data for numerical modeling

Table 9 summarizes the input data obtained in this chapter that will be used for the numerical modeling in chapters 6 and 7.

Table 9: Input values for parallel electrode model in 0.6 M NaCl at RT (obtained experimentally)			
Input data for parallel plate model in chapter 6 with Al 6061-T6 and graphite			
Variable name	Variable	Value	Unit
$E_{eq,graphite}$	Equilibrium potential, graphite	-0.140	V
$E_{eq,Al-6061}$	Equilibrium potential, aluminum 6061-T6	-0.690	V
$A_{c,graphite}$	Tafel slope, graphite	-1.9558	V
$A_{a,Al-6061}$	Tafel slope, aluminum 6061-T6	0.0153	V
$i_{0,graphite}$	Exchange current density, graphite	0.09351	A/m ²
$i_{0,Al-6061}$	Exchange current density, Al 6061-T6	0.1668	A/m ²
Input data for parallel plate model in chapter 7, steady-state atmospheric model of the ACCC conductor			
$E_{eq,C-ACCC}$	Equilibrium potential, CFRP from ACCC	-0.0605	V
$E_{eq,Al-ACCC}$	Equilibrium potential, 1350-O Al from ACCC	-0.952	V
$A_{c,C-ACCC}$	Tafel slope, CFRP from ACCC	-1.4949	V
$A_{a,Al-ACCC}$	Tafel slope, 1350-O Al from ACCC	0.1307	V
$i_{0,C-ACCC}$	Exchange current density, CFRP from ACCC	0.0547	A/m ²
$i_{0,Al-ACCC}$	Exchange current density, 1350-O Al from ACCC	0.004232	A/m ²
E_{cond}	Electrolyte conductivity	24.4	S/m
d_{film}	Electrolyte layer thickness (formatted for Comsol)	$D_{NaCl} * 2.15E-11 * \exp(6.03E-4 * RH)$	m
$O_{2,solubility}$	Oxygen solubility in water	$3.0E-4 * e^{(6.59 * RH)}$	mol/m ³
i_{lim}	Limiting current density based on oxygen diffusion through the electrolyte layer (formatted for Comsol)	$D_{O2} * (O_{2,solubility}) / (d_{film} * 2.59E-6)$	A/m ²

CHAPTER FIVE: EVALUATION OF ELECTROLYTE LAYER FORMATION AND OXYGEN TRANSPORT IN ATMOSPHERIC CONDITIONS

The necessity of retaining the original geometry during galvanic corrosion testing of the ACCC conductor was shown in chapter 3, and it was concluded in section 4.2 that the geometry affects the transport of oxygen to the cathode which in turn affects the total galvanic corrosion rate. In an atmospheric environment, the galvanic corrosion reactions take place in a very thin layer of electrolyte bridging the anode and the cathode. This section will analyze how the electrolyte layer thickness and composition is dependent on the salt load density and relative humidity, and how the layer thickness affects the oxygen transport to the reacting CFRP surface.

5.1 Oxygen consumption by the cathodic reaction

If we know the cathodic reaction(s), the oxygen consumption for a certain corrosion current can be calculated. It was shown in previous sections that the reduction of oxygen appears to be the dominant cathodic reaction. There was also evidence of the water splitting reaction taking place, but at a rate that is orders of magnitude lower. The work presented in this section will therefore be based on the assumption that reduction of oxygen is the only cathodic reaction.

Reduction of oxygen:



For every 4 electrons consumed at the cathode, one oxygen molecule is reduced. 1 A is equal to 1 C/s (coulomb per second) which is the same as 6.241×10^{18} electrons per second. With one oxygen molecule reduced per 4 electrons, 1.560×10^{18} oxygen molecules will be reduced per second. This is equivalent to 2.59×10^{-6} moles of O_2 or 82.9 μg per second. The oxygen consumption can thus be expressed as $82.9 \times 10^{-6} \text{ [(g/s)/(C/s)]} = 82.9 \times 10^{-6} \text{ [g/(A*s)]} = \mathbf{2.59 \times 10^{-6} \text{ [mol/(A*s)]}$.

If we know the limits of the diffusion, we can also calculate a theoretical maximum corrosion current density, also known as the *diffusion-limited oxygen reduction current density*, i_{lim} (Chen, Cui et al. 2008). The following section will present the development of an expression for the electrolyte layer thickness as a function of salt-load density and relative humidity (RH), which in turn will be used to generate an expression for the diffusion-limited oxygen reduction current density. These expressions will be used for the numerical modeling of atmospheric galvanic corrosion in chapter 7.

5.2 Presence of salt and its effect on the electrolyte layer thickness

A fundamental requirement for galvanic corrosion to occur is the presence of a liquid electrolyte. The amount of electrolyte on a surface subjected to atmospheric air is strongly dependent on the presence of salt on the surface. While the amount of salt matters, the type of salt may be even more important, particularly in drier conditions.

Hygroscopy is a substance's ability to attract and hold water molecules through absorption or adsorption from the surrounding environment. Many salts are hygroscopic, but the level of hygroscopy differs significantly. Some salts are so hygroscopic that they dissolve in the water they absorb in their crystal lattice and form a solution; a property called *deliquescence* (EncyclopediaBritannica 2014). This property is often exploited in products used to control humidity and in dust control.

In a closed container with sufficient amount of salt to keep the solution saturated, the vapor pressure of water above the saturated solution will have a unique value that is dependent on the type of salt (and weakly dependent on the temperature). This results in a relative humidity in the closed container of a certain value, which is often used to calibrate humidity sensors (the calibration application is discussed more in Error Analysis in Appendix B). As described in earlier chapters, this relative humidity level is known as *Deliquescence Relative Humidity* (DRH) (EncyclopediaBritannica 2014). This means that at ambient relative humidity levels above DRH, liquid electrolyte may be present on a salt-loaded conductor.

Although NaCl and MgCl₂ are chemically similar substances and are both used for deicing of highways, they have drastically different DRH. They are both deliquescent,

but the vapor pressure of an $MgCl_2$ solution is much lower than the vapor pressure of a $NaCl$ solution. The result of this difference is that $MgCl_2$ deliquesces at room temperature at RH of 33 %, while $NaCl$ requires 76 % RH to deliquesce (OmegaInstruments 2014), (QuantifoilInstruments 2014).

Table 10: Salts included in the test of hygroscopic properties, their Deliquescence Relative Humidity (DHR) at 25°C, and common uses				
Sources: (OmegaInstruments 2014), (QuantifoilInstruments 2014), (ASTM 2008),				
Compound	Full name	DHR	Common use/common presence	Chemical form used in experimental work (according to supplier)
LiCl	Lithium Chloride	11 %	Feedstock for manufacturing of lithium	Not specified
$CaCl_2$	Calcium Chloride	32 %	Dust control, deicing	Anhydrous
$MgCl_2$	Magnesium Chloride	33 %	Deicing, dust control / major compound in seawater	Hexahydrate
NaCl	Sodium Chloride	76 %	Deicing / major compound in seawater	Anhydrous
KCl	Potassium Chloride	85 %	Feedstock in process industry / major compound in the Utah Salt Flats	Anhydrous
Mixture of NaCl, $MgCl_2$, Na_2SO_4 , $CaCl_2$, KCl, $NaHCO_3$, KBr, H_3BO_3 , $SrCl_2$, NaF	ASTM D1141 Artificial Seasalt	N/A	Used for corrosion testing	Not specified

Because atmospheric galvanic corrosion only can occur if there is a liquid electrolyte present, the difference in deliquescence between the common deicing salts $MgCl_2$ and $NaCl$ may have large implications for the corrosion of transmission line conductors in the proximity of highways treated with de-icing salts or that are exposed to these salts for other reasons.

The DRH for common salts can be found in the literature (see Table 10), but it was also of interest to know the water absorption at levels below and above DRH. Experiments were performed both with pure salts in free air, and with salt-loaded conductor samples. For the test in free air, five different salts were used: CaCl_2 , MgCl_2 , NaCl , KCl and ASTM D1141 artificial seasalt². Only NaCl was used in the tests with salt-loaded conductor samples.

5.2.1 Hygroscopic properties of different salts – experimental procedure

The salts were dried and then exposed to increasing humidity levels, staying at each level for a minimum of 24 hours. Figure 95 shows how the MgCl_2 and CaCl_2 samples are completely liquid already at 44 % RH (blue and red circles), while it takes 80 % RH for the NaCl sample to almost completely dissolve (green circle). KCl is starting to dissolve at 90 % (purple circle), but did not fully dissolve before the test was completed. The ASTM D1141 artificial seawater started to dissolve at 44 % RH, but was not completely dissolved until 100 % relative humidity was reached. The observed DRHs agree well with the table values.

After the test was finished, the samples were left in room air at 50 % RH for 10 days. As expected, the NaCl and KCl samples had dried again while MgCl_2 and CaCl_2 were still completely liquid. The ASTM seasalt had large crystals in the electrolyte, likely

² ASTM D1141 Artificial Seasalt is sea salt mix containing elements found in natural seawaters in quantities greater than 0.0004 %: 58.490 % NaCl , 26.460 % $\text{MgCl}_2 \cdot 6\text{H}_2\text{O}$, 9.750 % Na_2SO_4 , 2.765 % CaCl_2 , 1.645 % KCl , 0.477 % NaHCO_3 , 0.238 % KBr , 0.071 % H_3BO_3 , 0.095 % $\text{SrCl}_2 \cdot 6\text{H}_2\text{O}$, and 0.007 % NaF .

of NaCl (no chemical analysis was performed, but their appearance indicated that they were likely NaCl).

Detailed procedure for investigation of hygroscopic properties of different salts

1. 10-20 g of each salt was placed in a glass container. The mass of the container and the salt respectively was recorded.
2. The open glass containers with salts were placed in $\sim 100^{\circ}\text{C}$ atmosphere for 2 hours to ensure dryness (the MgCl_2 arrived moist from the supplier). The containers were sealed to keep the salts dry.
3. The mass of each sample was recorded.
4. 1 g of each salt was placed in a black bowls. The black bowls were chosen to give a good contrast to the white salt. A photo was taken of the dry salts.
5. The salts were subjected to increasing levels of relative humidity in room air at room temperature. Due to the difficulties to achieve steady control at a humidity level below room air humidity, the test was started at room air humidity (44 % RH). The humidity was kept at each level for 48 hours. The humidity levels and temperature were logged. A new photo was taken at the end of each humidity level.
6. Photos were taken and the mass of each sample was recorded at the end of each humidity level period.



Figure 94: Deliquescence of different salts in free air.

Figure 95 shows the mass gain of each salt as a function of the relative humidity. The dotted line marks the 80 % RH level that is generally considered the critical humidity level for atmospheric corrosion to take place (Roberge 2008), (Francis 2000), (CorrosionDoctors 2014). The mass gain of NaCl (green markers) is rapidly increasing above 80 % RH, which perhaps could be the original reason for the 80 % rule-of-thumb.

At 80 % relative humidity the CaCl₂, MgCl₂, and ASTM artificial seasalt had 6.3, 4.1 and 3.5 times higher mass gain than NaCl respectively. As a result, there would be drastically more electrolyte present for the same salt load density.

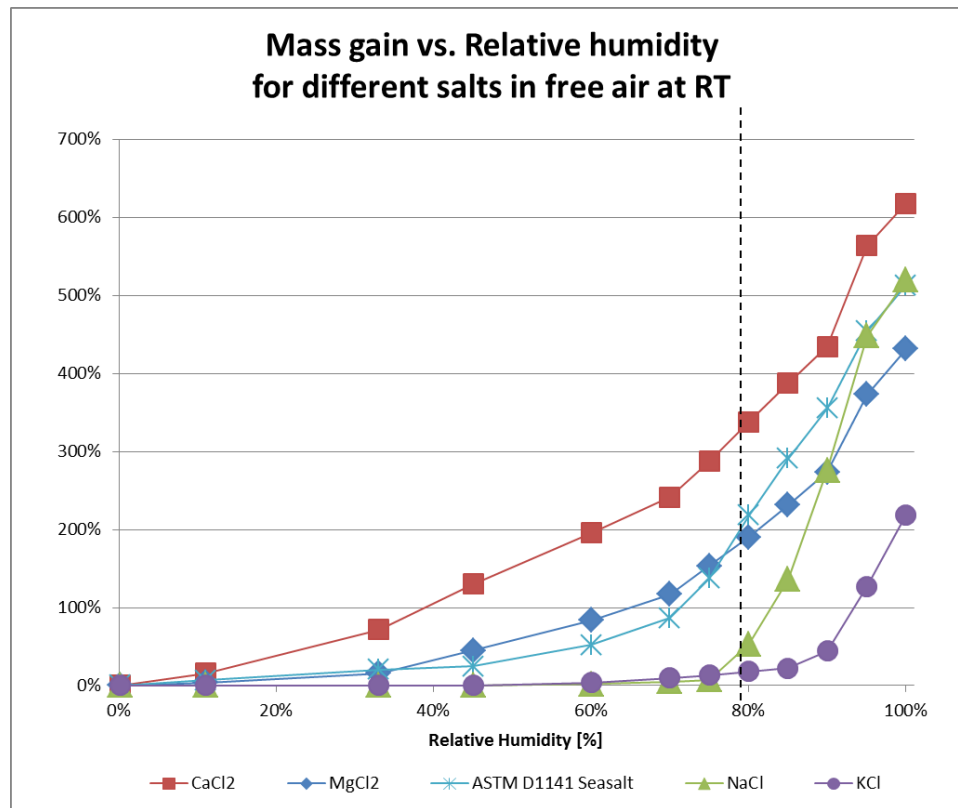


Figure 95: Mass gain due to deliquescence of different salts in free air as a function of relative humidity.

5.2.2 Electrolyte layer thickness as a function of relative humidity and salt load density

A function for the electrolyte layer thickness as a function of humidity and NaCl salt load density was generated through experiments using salt-loaded conductor samples. ACCC samples prepared according to the method described in chapter 3 were immersed in different concentration NaCl aqueous solutions. The amount of electrolyte trapped inside each sample was measured. Based on the known salt concentration of the electrolyte and the geometry of the sample, the average salt load density (the mass of salt per unit exposed surface area) was calculated. The samples were dried and then subjected to increasing levels of relative humidity at room temperature. The average electrolyte layer thickness was calculated from the mass gain. Note that this section is only valid for NaCl; if other salts are present the expressions may be different. It is also only valid at room temperature ($\sim 25^{\circ}\text{C}$).

The same sample was used for all but one test series to eliminate errors caused by the variation of gap sizes between the aluminum strands on different samples. The sample was new at the beginning of the test, and showed no apparent signs of corrosion at the end of the test. An additional sample with apparent corrosion damage was subjected only to the 0.6 M NaCl solution. Due to the corrosion products on the surface, this sample trapped a much greater amount of electrolyte which resulted in a much higher salt load density. The test procedure was the same as for the salt samples in free air: the sample was subjected to increasing levels of relative humidity, staying at each level for a minimum of 24 hours.

Table 11: Electrolyte concentrations and resulting salt load densities	
NaCl concentration in immersion electrolyte [wt. %]	Resulting salt load density on the sample surface [g/m²]
0.017 M (0.1 mass %)	0.0572
0.085 M (0.5 mass %)	0.273
0.17 M (1 mass %)	0.571
0.6 M (3.5 mass %)	1.80
	3.16*

* for sample with apparent corrosion damage

The average electrolyte layer thickness is plotted as a function of salt load density for each humidity level in Figure 96. Linear trendlines with 0,0 intercept were fitted to all plots and the R² values ranged from 0.97 to 0.99.

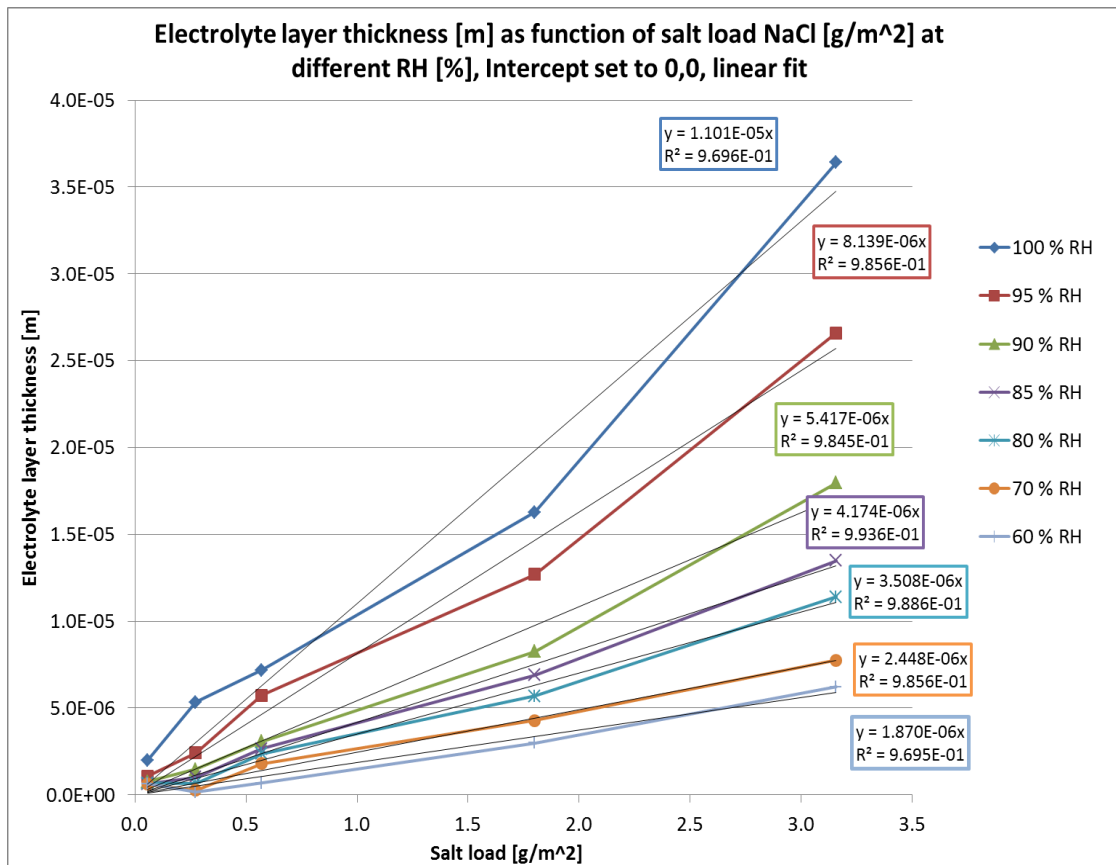


Figure 96: Average electrolyte layer thickness as a function of salt load (NaCl) and relative humidity.

The linear fits can be expressed as a general equation for the electrolyte layer thickness as:

$$t_L = S_L(RH) * D_{NaCl} \quad (5.2.2-1)$$

where

t_L = thickness of the electrolyte layer [m],

$S_L(RH)$ = slope for layer thickness gain as function of humidity [m/(g/m²)],

D_{NaCl} = salt load density of NaCl [g/m²].

The electrolyte layer thickness slopes for each humidity level were then plotted against the relative humidity in Figure 97. An exponential trendline was fitted with good agreement ($R^2 = 0.987$).

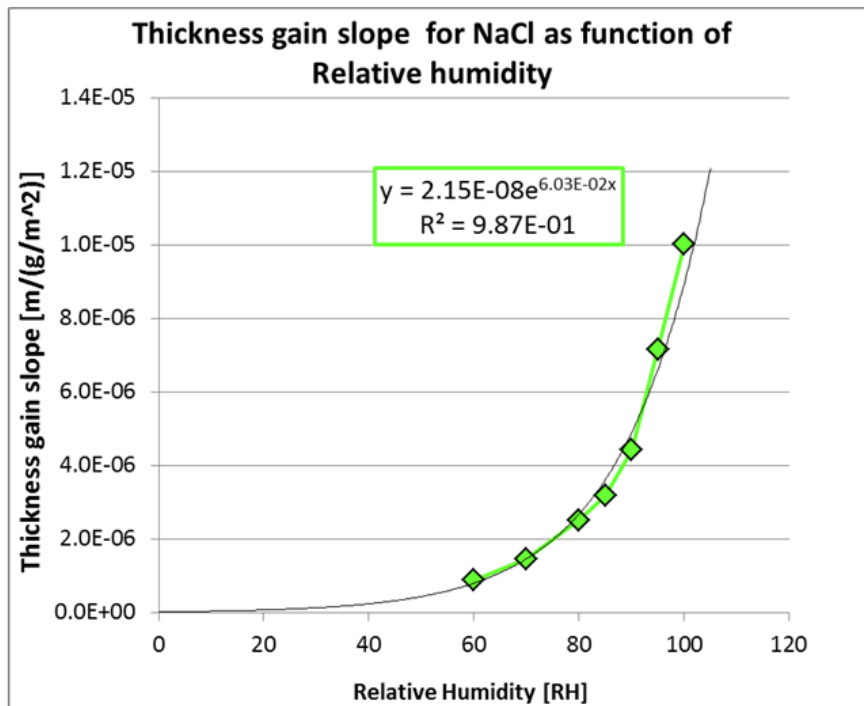


Figure 97: Electrolyte layer thickness gain slope as a function of relative humidity.

Thus, the exponential fit can be expressed as a general equation for the electrolyte layer thickness gain slope as:

$$S_L(RH) = 2.15E(-8) * e^{6.03E(-2)*RH} \quad (5.2.2-2)$$

where

S_L = slope for layer thickness gain as function of humidity [$m/(g/m^2)$],

RH = relative humidity [%].

By substituting equation (5.2.2-2) into (5.2.2-1), we get a general equation for the electrolyte layer thickness as a function of salt load density and relative humidity:

$$t_L = D_{NaCl} * 2.15E(-8) * e^{6.03E(-2)*RH} \quad (5.2.2-3)$$

where

t_L = thickness of the electrolyte layer [m],

D_{NaCl} = salt load density of NaCl [g/m^2],

RH = relative humidity [%].

Equation (5.2.2-3) will be used in the finite element modeling in chapter 7 as the expression for the electrolyte layer thickness, where D_{NaCl} and RH can be input as variables.

Comparison with literature data

The modeling software package Comsol Multiphysics (more about Comsol in chapter 6) uses data from reference Chen et al. (Chen, Cui et al. 2008) in its corrosion

module tutorials. This data is based on the documented deliquescence behavior of NaCl and presents the following function for the thickness of the electrolyte layer:

$$WL = \frac{DD(24.90+14.80RH-22.80RH^2)}{5811.94+23909.82RH-3291.21RH^2-57990.86RH^3+31576.80RH^4} \quad (5.2.2-4)$$

where

WL = thickness of the electrolyte layer [m],

DD = amount of deposited NaCl particles [kg/m²].

Figure 98 and Figure 99 show the plotting of equation (5.2.2-3) generated by experimental measurements performed in this study and equation (5.2.2-4) obtained from the literature.

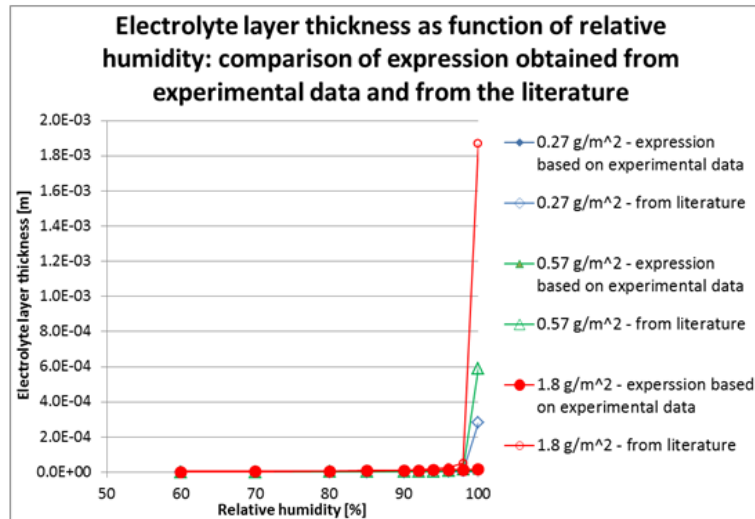


Figure 98: Electrolyte layer thickness – comparison of expression obtained from experimental data and from literature.

At a first glimpse, there appears to be very little agreement between equation (5.2.2-4) and the expression obtained in this study (5.2.2-3) in Figure 98. However, zooming in on the plots reveals that the agreement is fairly good to approximately 90 % RH, as can be seen in Figure 99.

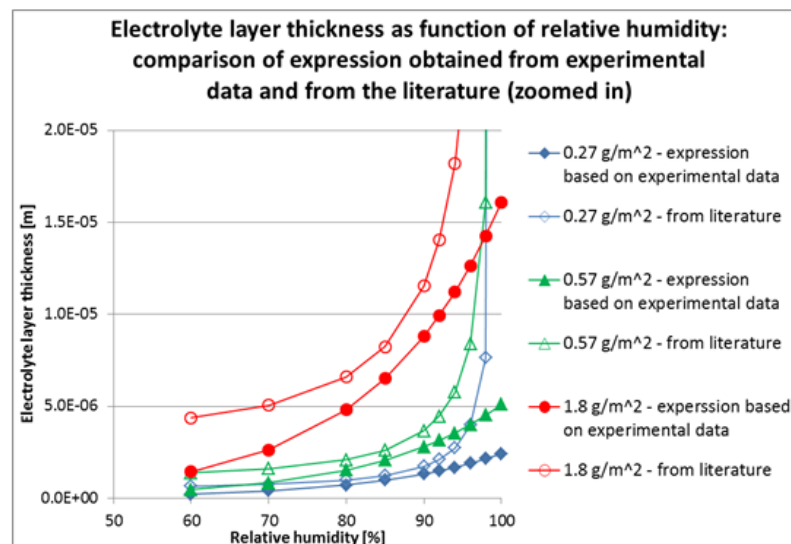


Figure 99: Electrolyte layer thickness – comparison of expression obtained from experimental data and from literature (zoomed in).

Above 90 % RH, the expression from Chen et al. (Chen, Cui et al. 2008) deviates severely from the expression obtained from experimental values. This could be caused by the difference in geometry; the experimental data is from a stranded conductor sample while the literature data is assumed to be for a flat surface in free air. To investigate if this is a possible explanation, the mass gain of the electrolyte in the conductor sample is compared to the mass gain of NaCl in free air in Figure 95. While comparing the two plots in Figure 100, it is clear that the mass gain of the electrolyte on the conductor sample follows a similar function as in free air. The expression obtained from the experimental data appears to be closer to the free air volume gain than the expression from the literature. From here on, the expression obtained from the experimental data will be used for the electrolyte layer thickness in the modeling.

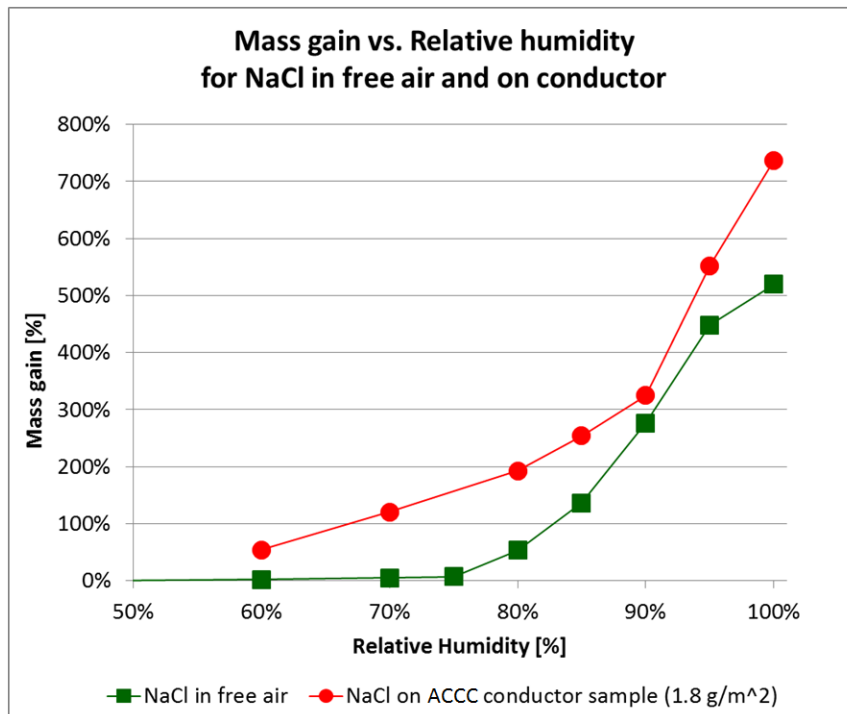


Figure 100: Mass gain for NaCl in free air and on conductor sample.

Salt concentration for maximum layer thickness

The average crevice width in an ACCC sample with damaged corrosion barrier prepared using the method described in chapter 3 was estimated to 180 μm . This value was found by measuring the maximum amount of liquid that could be trapped inside a sample and then calculating the average gap width based on the geometry.

Because the electrolyte layer is assumed to be uniform on all surfaces of the sample, the maximum theoretical electrolyte layer thickness would be half the crack width, which means 90 μm . Using equation (5.2.2-3), we can calculate that a salt load density of 10.1 g/m^2 NaCl at 100 % RH would generate the maximum layer thickness and completely fill the gaps with electrolyte. A higher salt load density would overflow the sample and cause the electrolyte to drip off.

Diffusion of oxygen through air versus electrolyte

The cathode area inside an ACCC sample with simulated impact damage is 0.014 m^2 per m length of conductor. Assuming that the average gap width is 180 μm , the total area of the openings between the 14 outer strands in the ACCC is 0.0032 m^2 per meter length of conductor. The cathode area is 4.4 times larger than the outer opening that the oxygen has to diffuse through. Due to the stranded nature, the opening for diffusion will get smaller deeper into the sample. The area of the openings between the inner 8 strands is only 0.0018 m^2 per meter length of conductor. The average of the two areas is 0.0025 m^2 per meter or 5.7 times smaller than the cathode area. The average path length for the oxygen to diffuse to cathode is 0.0147 m (illustrated in Figure 101) in this simplified model.

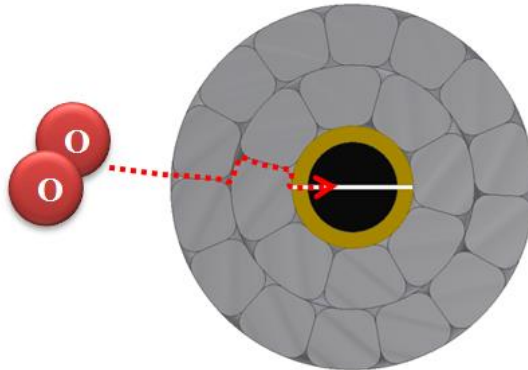


Figure 101: The pathway for oxygen to reach the cathodic reaction.

The diffusion of oxygen through air is 10,800 times faster than the diffusion of oxygen through water (see Table 12). There is some dependency on temperature and a very weak dependence on relative humidity, but the difference between air and water is so large that the effect of temperature and relative humidity will be neglected.

Table 12: Diffusion coefficients for oxygen at 20°C	
Source: (Giambattista, Richardson et al. 2004)	
Medium	Diffusion coefficient [m²/s]
Oxygen through air, 100 % RH (15 % O ₂ conc.)	2.14 E-05
Oxygen through water	1.97 E-09

Starting with the crevices filled with air, we can calculate the oxygen flux and thus also the maximum possible cathodic corrosion current density (assuming that the only cathodic reaction taking place is the reduction of oxygen). The molar concentration of oxygen at 20°C at atmospheric pressure is 8.714 mol/m³ (Denny 1993). Assuming a linear concentration gradient from ambient oxygen concentration at the opening to zero

of the ambient oxygen concentration at the cathode, the following equation for the maximum flux of oxygen through the conductor can be generated using Fick's first law:

$$J = -D_{O_2} * \frac{\Delta c}{\Delta x} \quad (5.2.2-5a)$$

With values for air:

$$J = -D_{O_{2,air}} * \frac{\Delta c}{\Delta x} = -(2.14E(-5)) \left[\frac{m^2}{s} \right] * \frac{-8.714 \left[\frac{mol}{m^3} \right]}{0.0147 [m]} = 0.0127 \left[\frac{mol}{s * m^2} \right] \quad (5.2.2-5b)$$

where

J = flux of oxygen in air [mol/(s*m²)],

D_{O_2} = diffusion coefficient for oxygen in water [m²/s],

$D_{O_{2,air}}$ = diffusion coefficient for oxygen in air [m²/s],

Δc = the change in concentration [mol/m³],

Δx = diffusion path length [m].

With the above assumptions, the total maximum oxygen diffusion through the air in the gaps would be 1.59×10^{-5} mol/s per meter of conductor. Divided by a cathode area of 0.014 m^2 per m length of conductor, the maximum oxygen supply would be 1.14×10^{-3} mol/(s*m²). Using the oxygen consumption per As (ampere second) calculated in the previous section, the maximum cathodic corrosion current density would be 440 A/m^2 .

The calculation was repeated for the crevices filled with a water-based electrolyte. The electrolyte was assumed to be saturated at the crevice openings, which equals an oxygen concentration of 0.40 mol/m^3 (U.S. Geological Survey 1998), and assumed to have zero oxygen content at the reacting CFRP surface. With a linear gradient, the maximum theoretical cathodic current density would be $0.0037 \text{ A/m}^2 = 3.7 \text{ mA/m}^2$ (0.13

mA/m^2 if expressed as anodic current density). The cathodic corrosion current densities measured in chapter 3 for an immersed environment were 17.6 to 20.4 mA/m^2 (0.63 to 0.73 mA/m^2 if expressed as anodic current densities, but this section will use cathodic corrosion current densities throughout).

The measured values are approximately five times higher than the calculated values. The discrepancy likely has two different causes. One is the simplified geometry. The other is the additional cathodic reaction – the water splitting – that does not depend on oxygen supply. The cathodic corrosion current density measured in oxygen-starved conditions was 9 mA/m^2 . Adding the calculated cathodic current density to the measured cathodic current density for oxygen-starved conditions, the resulting value is 12.7 mA/m^2 . This value is 28 to 38 % lower than the measured values in oxygen-rich electrolyte, which has to be considered a very good agreement for a very simple model. This provides additional support to the hypothesis that oxygen transport is the dominant control mechanism.

The theoretical maximum cathode current density with air in the gaps is 119,000 times higher than in immersed conditions. However, the calculated maximum cathodic corrosion current density of 440 A/m^2 when the diffusion of oxygen through the air is the only limiting mechanisms, is 1630 times higher than the highest measured cathodic current density in this study of 0.27 A/m^2 for a fully assembled ACCC sample (see Figure 88). The calculated maximum value is still 41 time higher than the all-time-high cathodic corrosion current density of 10.6 A/m^2 measured in this study when a jet of oxygen-rich

electrolyte was directed onto the surface (shown as anodic corrosion current density I in Figure 91, but the cathodic current density will be identical due to the 1:1 area ratio).

This indicates that there are additional limiting mechanisms. These will be discussed in the following sections.

Effective gap size as a function of electrolyte layer thickness

One reason for the difference between the calculated maximum cathodic current density and the measured result is that the calculated value assumed that the gaps in the conductor were completely filled with air. If this were the case, no corrosion could take place because there is no electrolyte present. As the electrolyte layer grows due to increased salt load density and/or humidity, the available cross-sectional area for oxygen diffusion will decrease. At a salt load density of 3.1 g/m^2 , the electrolyte layer thickness grows as a function of relative humidity. At 100 % RH, the average electrolyte layer thickness is $28 \text{ }\mu\text{m}$ thick. This would decrease the average gap width to $124 \text{ }\mu\text{m}$. Assuming that there still would be a continuous path of air from the conductor surface to the cathode, the maximum cathodic current density would decrease to 278 A/m^2 .

Oxygen diffusion through the electrolyte layer in atmospheric conditions

In reality, there cannot be an air path all the way to the reacting surface. The cathode is covered with an electrolyte layer where the reduction reaction is taking place. Due to the much lower diffusivity of oxygen through water, there may be a bottleneck in the oxygen's path to the cathode. Assuming that this electrolyte layer also is $28 \text{ }\mu\text{m}$ and

the concentration goes from the maximum solubility in fresh water at the surface of the electrolyte layer to zero at the surface of the cathode, the diffusion through the electrolyte layer would limit the cathode current density to 11 A/m².

There is, however, another error in this calculation. It is based on the solubility of oxygen in freshwater. The solubility of oxygen goes down as salt concentration goes up. As shown in previous sections, the salt concentration in the thin layer of electrolyte is quite high. The salt concentration at 100 % RH of the electrolyte in the samples in

Figure 70 was 10.3 mass % NaCl. This high salt concentration is outside the tables available for this study, but the saturation limit at 3.5 mass % NaCl is 0.18 mol/m³, compared to 0.4 mol/m³ for freshwater. It would be expected that this limit decreases further as the NaCl concentration goes up. The Comsol tutorial (COMSOL 2014) and Chen et al. (Chen, Cui et al. 2008) use the following equation for the oxygen solubility in the electrolyte layer as a function of relative humidity:

$$O_{2,solubility} = 0.0003 * e^{(6.95 * RH)} \quad (5.2.2-6)$$

Using equation (5.2.2-6), the maximum theoretical current density will instead be 6.0 A/m² at 100 % RH. This value is two orders of magnitude smaller than the first presented value based solely on the diffusion of oxygen through air, but it is still approximately one order of magnitude larger than the actually measured values for these conditions. There are obviously additional limiting mechanisms other than just the diffusion of oxygen. The values presented here will be used as the limiting cathodic current density i_{lim} , an important variable in modeling that sets the theoretical limit for the

current density. Table 13 compares the calculated maximum theoretical cathode current densities with measured values.

Table 13: Maximum theoretical cathodic current density vs. measured cathodic current density		
	Theoretical maximum based on diffusion of oxygen [A/m ²]	Measured (data from chapter 3)[A/m ²]
For assembled ACCC samples with compromised corrosion barrier (prepared as described in chapter 3)		
Immersed in liquid	0.0037	0.017 to 0.020
Gaps completely filled with air	440	-----
28 μm layer of electrolyte	6.0	0.076
Highest value measured in atmospheric conditions (see Figure 88)	-----	0.27
For CFRP sample immersed in electrolyte		
Highest value overall in immersed conditions (see Figure 91)	-----	10.7

Using the findings in this and previous sections, we can create a function for i_{lim} . Because the oxygen has to diffuse through both air and liquid under atmospheric conditions, we will actually get two functions.

Limiting current due to diffusion of oxygen through air:

$$i_{lim} \left[\frac{A}{m^2} \right] = J \left[\frac{mol}{s \cdot m^2} \right] * \frac{A_{opening} \left[\frac{m^2}{m} \right]}{2.59 \cdot 10^{-6} \left[\frac{mol}{A \cdot s} \right]} / A_{cathode} \left[\frac{m^2}{m} \right] \quad (5.2.2-7)$$

where

i_{lim} = theoretical maximum cathodic corrosion current [A/m²],

J = flux of oxygen based on Fick's first law [mol/(s*m²)],

A_{opening} = total area of the opening between the strands per meter of conductor [m²/m], and

A_{cathode} = area of the cathode per meter conductor [m²/m].

Knowing that J is a function of concentrations and diffusion path length, the opening is a function of the geometry and layer thickness, the equation can be expanded to include these variables:

$$i_{lim} \left[\frac{A}{m^2} \right] = -D_{O_2} \left[\frac{m^2}{s} \right] * \frac{\Delta c \left[\frac{mol}{m^3} \right]}{\Delta x [m]} * \frac{(W_{gap} - (2 * t_L)) [m] * \frac{(n_{s,i} + n_{s,o})}{2} * L_{gap} \left[\frac{m}{m} \right]}{2.59 * 10^{-6} \left[\frac{mol}{A * s} \right]} / A_{cathode} \left[\frac{m^2}{m} \right] \quad (5.2.2-8)$$

where

i_{lim} = theoretical maximum cathodic corrosion current [A/m²],

D_{O_2} = diffusion coefficient for oxygen in air [m²/s],

W_{gap} = the average width of the gaps between the aluminum strands [m],

Δc = the change in concentration [mol/m³],

Δx = diffusion path length [m],

t_L = thickness of electrolyte layer [m],

$n_{s,i}$ = number of inner strands,

$n_{s,o}$ = number of outer strands,

L_{gap} = the length of the strands per meter of conductor (takes into account the helical stranding) [m/m],

$A_{cathode}$ = area of the cathode per meter of conductor [m²/m].

Expression for diffusion of oxygen under atmospheric conditions

Assuming a linear concentration profile and using expression (5.2.2-3) for the electrolyte layer thickness as a function of RH and salt load density, the final expression for the *limiting current density due to diffusion of oxygen through the air and electrolyte layer to the cathode* will be the following:

$$i_{lim,air} \left[\frac{A}{m^2} \right] = \frac{-D_{O_2} \left[\frac{m^2}{s} \right] * \frac{c_{ambient} \left[\frac{mol}{m^3} \right]}{\Delta x [m]} * \frac{(W_{gap} - (2 * D_{NaCl} * 2.15E-08 * e^{6.03E-02 * RH})) [m] * \frac{(n_{s,i} + n_{s,o})}{2} * L_{gap} \left[\frac{m}{m} \right]}{2.59 * 10^{-6} \left[\frac{mol}{A * s} \right] * A_{cathode} \left[\frac{m^2}{m} \right]} \quad (5.2.2-9)$$

where

$i_{lim,air}$ = theoretical maximum cathodic corrosion current due to diffusion of oxygen through air [A/m²],

D_{O_2} = diffusion coefficient for oxygen in air [m²/s],

$C_{ambient}$ = concentration of oxygen in the ambient air [mol/m³],

W_{gap} = the average width of the gaps between the aluminum strands [m],

Δx = the total path length for the oxygen to reach the cathode [m],

D_{NaCl} = salt load density [g/m²],

RH = relative humidity of the surrounding air [%],

$n_{s,i}$ = number of inner strands,

$n_{s,o}$ = number of outer strands,

L_{gap} = the length of the strands per meter of conductor (takes into account the helical stranding) [m/m], and

A_{cathode} = area of the cathode per meter conductor [m²/m].

We can generate a similar expression for the *limiting current density due to the diffusion of oxygen through the electrolyte layer* when the oxygen reaches the cathode:

$$\begin{aligned}
 i_{\text{lim},e} \left[\frac{\text{A}}{\text{m}^2} \right] &= -D_{\text{H}_2\text{O}} \left[\frac{\text{m}^2}{\text{s}} \right] * \frac{S_{\text{O}_2} \left[\frac{\text{mol}}{\text{m}^3} \right]}{t_L [\text{m}] * 2.59 * 10^{-6} \left[\frac{\text{mol}}{\text{A} * \text{s}} \right]} = \\
 &= -D_{\text{H}_2\text{O}} \left[\frac{\text{m}^2}{\text{s}} \right] \\
 &\quad * \frac{0.0003 * e^{(6.59 * \frac{RH}{100})} \left[\frac{\text{mol}}{\text{m}^3} \right]}{(D_{\text{NaCl}} * 2.15E - 08 * e^{6.03E - 02 * RH}) [\text{m}] * 2.59 * 10^{-6} \left[\frac{\text{mol}}{\text{A} * \text{s}} \right]}
 \end{aligned}$$

(5.2.2-10)

$i_{\text{lim},e}$ = theoretical maximum cathodic corrosion current due to the diffusion of oxygen through the electrolyte [A/m²],

$D_{\text{H}_2\text{O}}$ = diffusion coefficient for oxygen in water [m²/s],

S_{O_2} = concentration (max solubility) of oxygen in the surface layer of the electrolyte [mol/m³] (function for S_{O_2} from (COMSOL 2014), (Chen, Cui et al. 2008)),

t_L = thickness of electrolyte layer [m],

D_{NaCl} = salt load density [g/m²],

RH = relative humidity of the surrounding air [%],

Depending on the thickness of the electrolyte layer, the diffusion of oxygen through the air or through the electrolyte layer may dominate. The lowest i_{lim} will be the theoretical limit for the cathode reaction due to oxygen diffusion. Figure 102 is a surface plot of equation (5.2.2-9) showing that the salt load density and the relative humidity both have to be high in order for the oxygen diffusion through air to really affect $i_{lim,air}$.

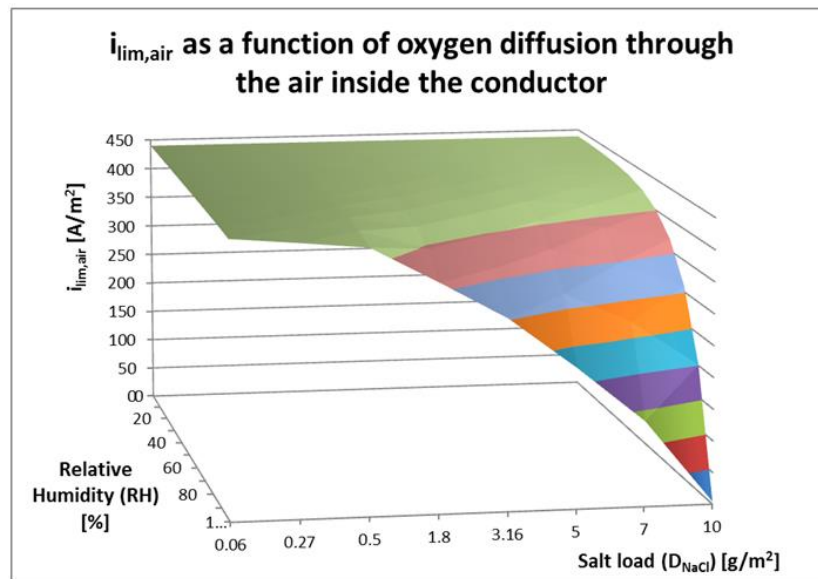


Figure 102: i_{lim} as a function of oxygen diffusion through the air in the gaps between the strands.

The reason for the drastic drop in $i_{lim,air}$ at a salt load density of approximately 10 g/m^2 is that the electrolyte layer grows so thick that there is no opening for the oxygen to diffuse into the conductor.

Figure 103 displays the electrolyte layer thickness as a function of humidity and salt load density. When the electrolyte layer exceeds $90 \text{ }\mu\text{m}$ (marked with the dashed red line), the gaps are full of liquid and equation (5.2.2-9) illustrated in Figure 102 would actually become negative. We can thus conclude that equation (5.2.2-9) for $i_{lim,air}$ is only valid when $t_L < 90 \text{ }\mu\text{m}$.

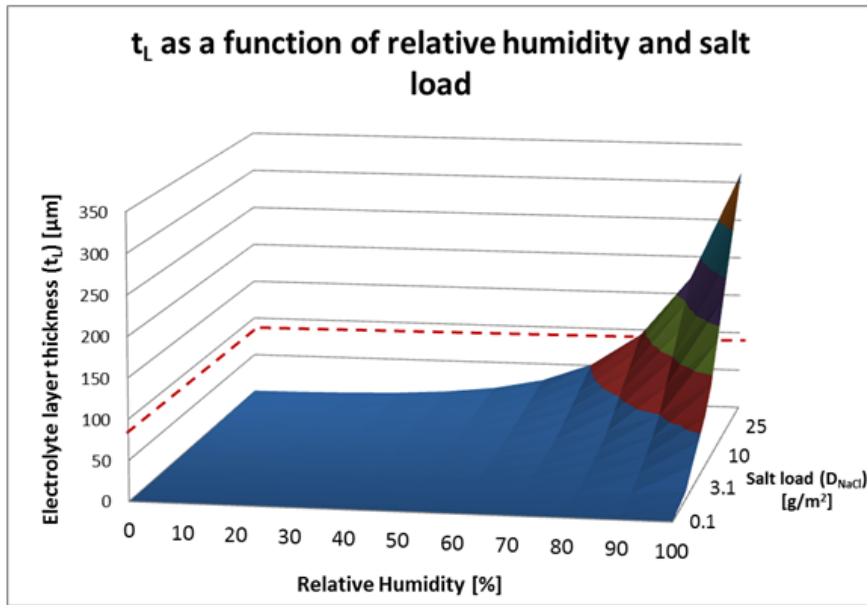


Figure 103: Electrolyte layer thickness as a function of relative humidity and salt load density.

Figure 104 is a surface plot of equation (5.2.2-10) for in $i_{lim,electrolyte}$ as a function of the diffusion of oxygen through the electrolyte layer under atmospheric conditions.

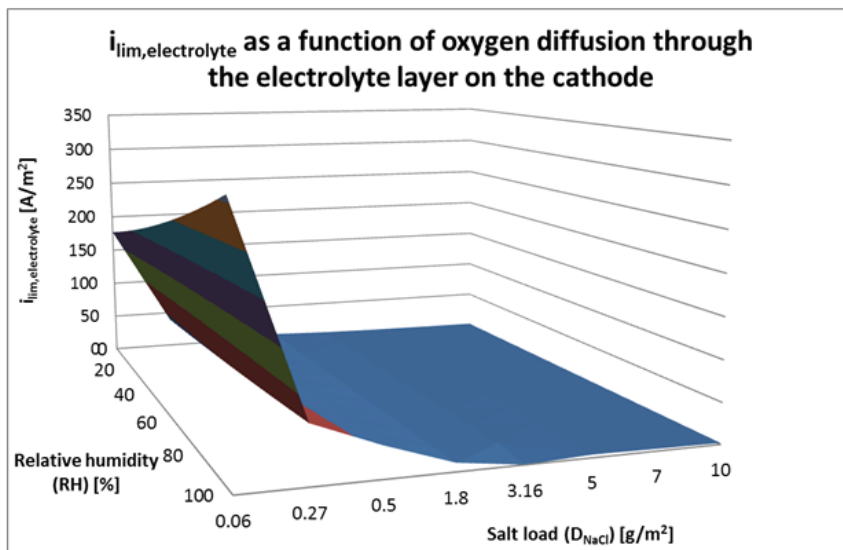


Figure 104: i_{lim} as a function of oxygen diffusion through the electrolyte layer on the cathode.

Comparing Figure 102 and Figure 104, we can conclude that the diffusion of oxygen will always be slower or dramatically slower through the electrolyte than through the air inside the conductor. We can therefore ignore the diffusion of oxygen through the gaps between the strands, and concentrate on the diffusion through the electrolyte layer as the rate limiting mechanism.

Expression (5.2.2-10) generates a value for i_{lim} that is approximately twice as high as compared to the function used in the Comsol tutorial (Chen, Cui et al. 2008), expression (5.2.2-10). The higher value is a result of a slightly thinner electrolyte layer and a slightly higher diffusion coefficient. Despite this deviation, the agreement can still be considered quite good. Equation (5.2.2-10) will be used in the modeling of atmospheric galvanic corrosion in chapter 7.

5.2.3 Salinity as a function of relative humidity

The conductivity of the electrolyte is an important parameter in galvanic corrosion. This section will discuss the conductivity's dependence on salt load density and relative humidity.

The conductivity of the electrolyte is a function of the salt concentration. Using data from the experiment discussed in the previous section, the concentration of NaCl in the electrolyte layer as a function of relative humidity is plotted in Figure 105. Because NaCl starts to deliquesce at 76 % RH, all values for salt concentration below 76 % have no practical meaning from a galvanic corrosion perspective. The salt will be solid with

some water absorbed in its crystal lattice. The values below 76 % RH (marked with a dotted line) will therefore be excluded from the following discussion.

The maximum solubility of NaCl in water is approximately 36 grams/100 ml at room temperature, which is equal to 26 mass %. If the calculated salt concentration is higher than 26 mass %, it means that there will be solid salt crystals in the electrolyte. The solubility limit of 26 mass % is also marked in Figure 105 with a dotted line. Any values exceeding 30 mass % were excluded from the subsequent analysis. Although the solubility limit is 26 %, a few values between 26 and 30 mass % were included to account for uncertainty in the mass measurement and to get a sufficiently large data set for the trendline fits.

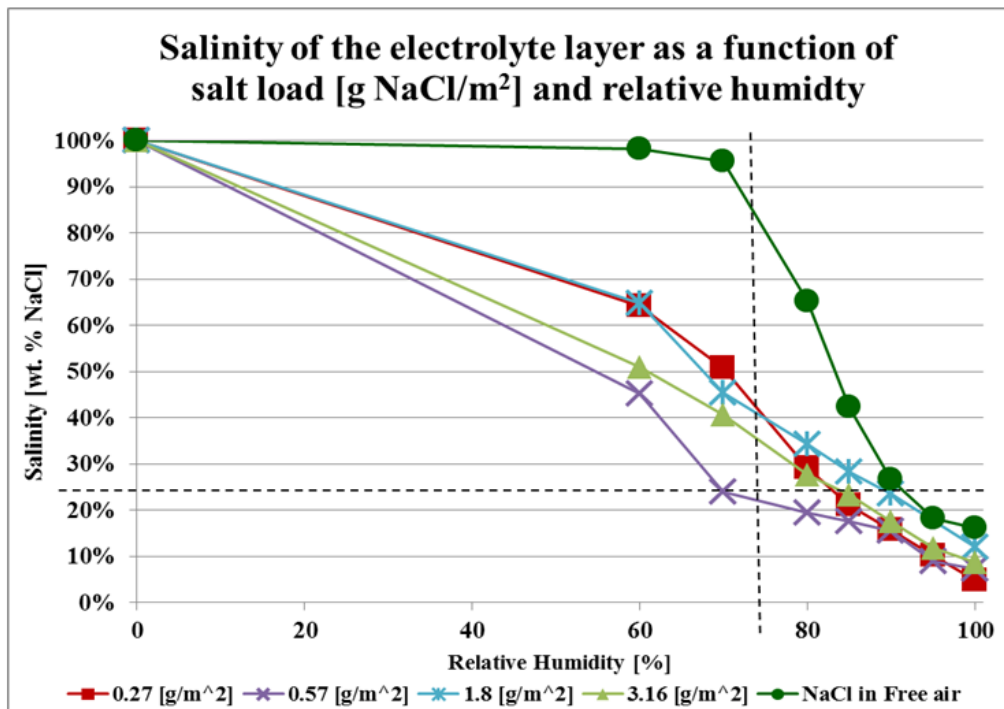


Figure 105: Salinity of the electrolyte as a function of salt load density and relative humidity.

Focusing on relative humidity levels of 85 % or higher and salinities below 30 mass %, we can fit linear functions to all the plots. As seen in Figure 106, the linear fits are quite good. With exception of one salt load density – 0.57 g/m^2 – the slope of the functions are all approximately -1.0 \%/\% . (The data set for 0.57 g/m^2 has in general quite a bit of irregularities in the values compared to the other samples, perhaps caused by large uncertainties due to the very low mass measured).

The salinity decreases approximately 1 % for each percentage point increase in relative humidity. There is no clear relation between salt load density and salinity, although the lowest salt load density (0.27 g/m^2) had the lowest salinity and the NaCl in free air had the highest salinity. The salinities stayed within 11 percentage points for all RH levels between 85 and 100 %. The salinity should be independent of salt load density, and the differences in Figure 106 can likely be attributed to measurement errors as measured masses are very small.

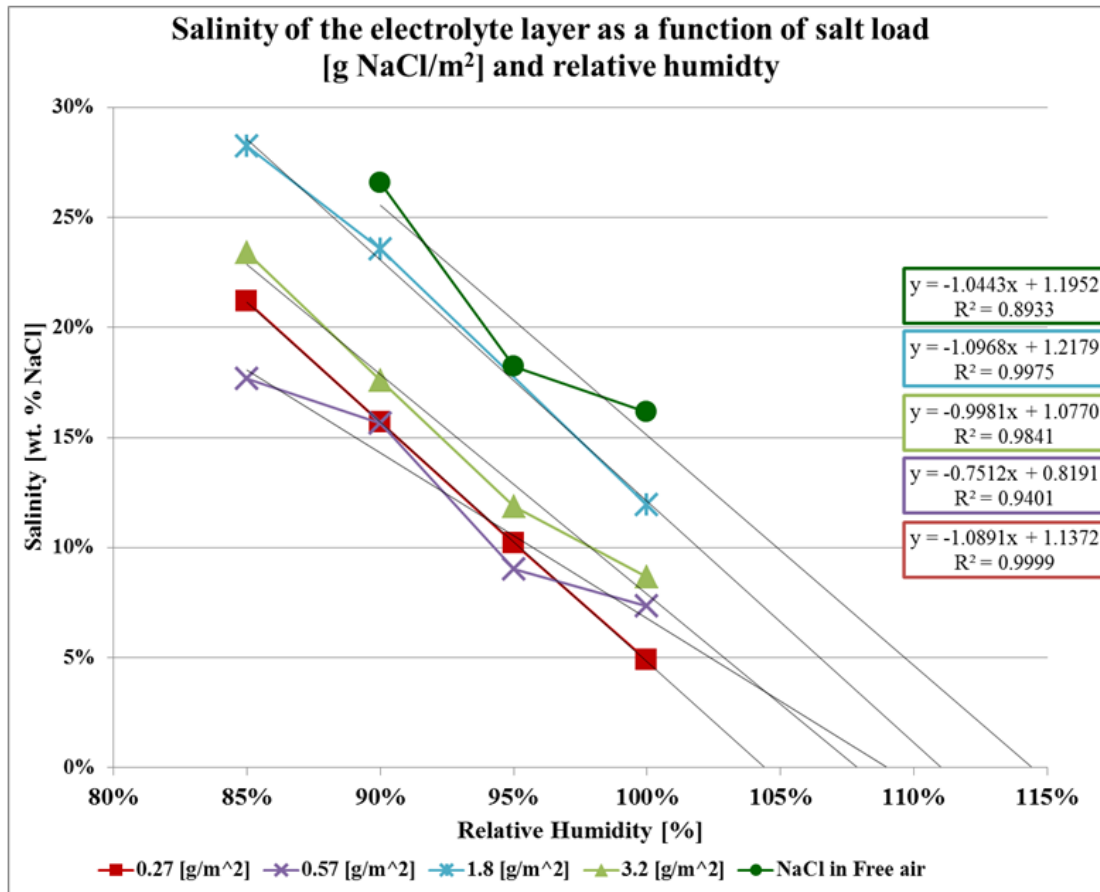


Figure 106: Salinity of the electrolyte as a function of salt load density and relative humidity.

Conductivity as a function of relative humidity

The conductivity of an electrolyte can be calculated using Kohlrausch's law, which was presented in section 2.3.2. Using an average of the relations presented in Figure 106 and the relations between relative humidity, salt load density, and electrolyte layer thickness presented above, the conductivity of the electrolyte as a function of humidity can be calculated. Figure 107 illustrates the results.

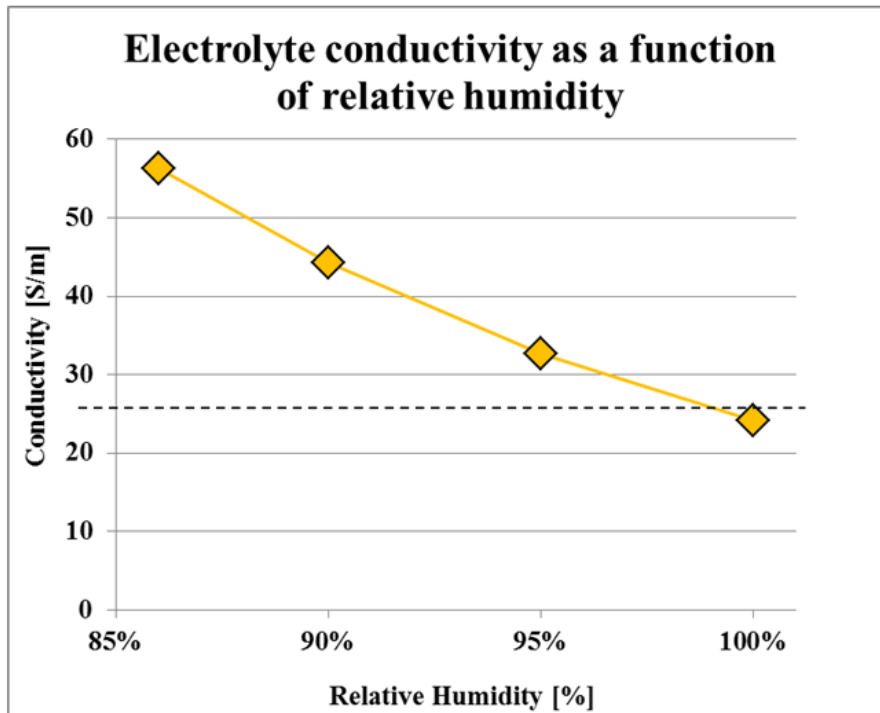


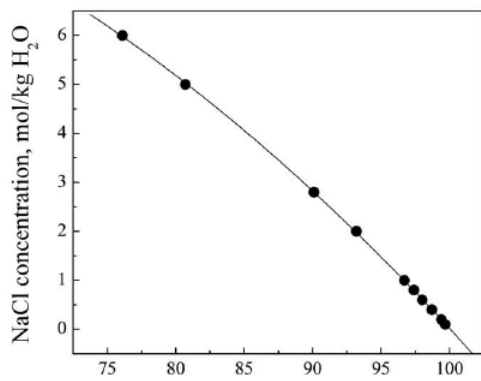
Figure 107: Conductivity as a function of RH for non-saturated electrolytes.

Figure 107 highlights a problem with Kohlrausch's; it generates conductivity levels higher than the conductivity of a saturated solution. The maximum conductivity of a NaCl solution is 24.4 S/m and it occurs in saturated state (Foxboro 1999) (marked with a dotted line in Figure 107). Only at relative humidity levels above 99.9 % would the conductivity be lower than the conductivity of a saturated solution. At 99.9 %, the conductivity would be 24.4 S/m, but at 70 % it would be 148 S/m and at 40 % it would be 902 S/m. The linear model used to generate this function clearly does not work on these high concentrations, which is a known problem with Kohlrausch's law. Nevertheless, we can conclude that if there is liquid electrolyte present, it will always have conductivity that is somewhere between that of seawater and that of a saturated electrolyte, which means that the conductivity is very high. Also, it was concluded in chapter 4 that the

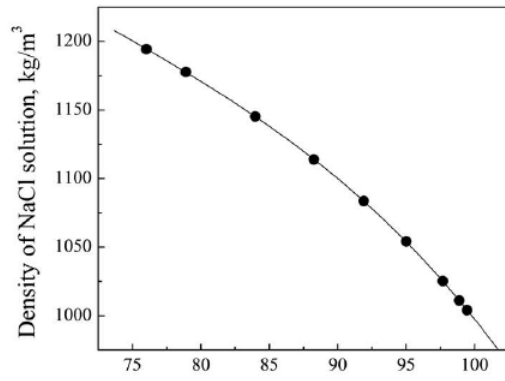
conductivity has a very weak effect on the galvanic corrosion rate as long as the conductivity is sufficiently high. In the conditions presented here, the electrolyte conductivity will always be sufficiently high.

Comparing with data used in Comsol tutorials:

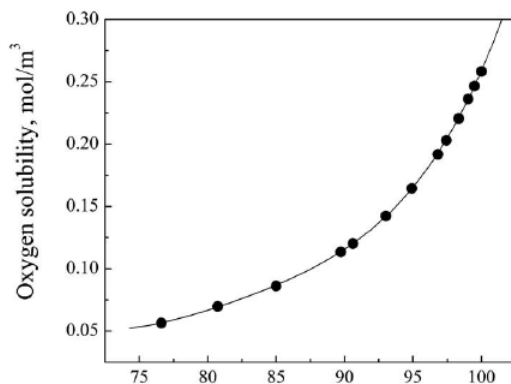
Reference (Chen, Cui et al. 2008), which is the source of data for the Comsol tutorials, shows a quite different conductivity function. It shows the conductivity and the NaCl concentration both approaching zero at 100 % RH, which does not agree at all with the measurements performed in this study. The Comsol tutorial gets around this problem by conveniently using the range 80 % 98 % for its examples. The procedure for obtaining the data in the literature is not specified and it does not agree with the measurements conducted in this study. Due to the large deviation between the literature values and the unreasonable claim that the salt concentration and conductivity is zero at 100 % RH, the fixed value of 24.4 S/m will be used for modeling atmospheric conditions in this study instead of references (COMSOL 2014), (Chen, Cui et al. 2008). The rationale for this decision was presented above.



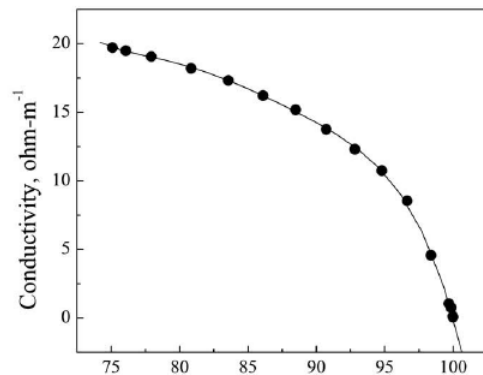
(a) Relative humidity, %



(b) Relative humidity, %



(c) Relative humidity, %



(d) Relative humidity, %

Figure 108: Data from the literature (Chen, Cui et al. 2008) for a) NaCl concentration, b) density, c) oxygen solubility, and d) conductivity.

CHAPTER SIX: NUMERICAL MODELING OF GALVANIC CORROSION – IMMERSED CONDITIONS

There are several numerical methods that can be used to model and predict galvanic corrosion. The non-linear electrode kinetics makes numerical modeling attractive and interest in these methods has existed for at least seven decades, with rapid development starting in the 1970s (Munn and Devereux 1991).

The literature reports several different numerical methods such as the *finite difference method*, the *boundary element method* (also called the *integral equation method*), and the *finite element (FE) modeling* (Munn and Devereux 1991), (Bardal, Johnsen et al. 1984). The FE modeling is often considered the most advantageous method and appears to be the most popular these days (Munn and Devereux 1991), (Turner 2012), (Munn 1986) perhaps due to the availability of commercial software such as the COMSOL® Multiphysics (from here on only referred to as “Comsol”) with modules for corrosion and electrochemistry.

The basic procedure for FE modeling of galvanic corrosion involves solving the *partial differential equations that describe the electric fields* in the conductive medium, and applying the *boundary conditions which describe the non-linear electrode kinetics* of the corroding materials (Munn and Devereux 1991). The dissolution (corrosion) rate may then be calculated using Faraday’s law. Although Comsol takes care of the computational

part, it still requires a significant amount of input data for the specific system being modeled that needs to be acquired either experimentally or from the literature.

This chapter will present the fundamental mathematical relations for numerical modeling of galvanic corrosion. It will also compare the different numerical approaches with physical validation models for immersed galvanic corrosion, while the next chapter will present numerical modeling of atmospheric galvanic corrosion.

6.1 Basic procedure for Finite Element Modeling of galvanic corrosion

The rate and distribution of the corrosion attack on the corroding electrode is correlated to the electrochemical potential distribution within the electrolyte and the reacting surfaces (Zhang 2011). The potential distribution is governed by the Fourier equation for a conductive medium (Munn and Devereux 1991).

6.1.1 Common assumptions

Several assumptions have to be made to perform FE modeling of corrosion. Here are some of the most common:

- The *properties of the metal-electrolyte system* must be known.
- The *chemical reactions* must be known (the most common reactions were presented in chapter 2).
- The process must be considered *quasi-steady state* (Munn and Devereux 1991).

- A function has to be fit to the electrode kinetics, which is typically non-linear (see chapters 2 and 5).
- The corrosion process is often assumed to not be mass-transport limited, but it will be shown later in this dissertation that this assumption is only valid under certain conditions.

6.1.2 Step-by-step procedure

The basic procedure for FE modeling of galvanic corrosion is the following:

Step 1) Input data

Obtaining input data.

Step 2) Electrical potential

Numerical prediction of the electrical potential distribution in the electrolyte. The potential is due to the presence of dissimilar metals (or other conductive materials) connected through an electrolyte and through metallic contact. The potential can also be caused by an externally applied current or potential, but that is outside the scope of this work.

Step 3) Current density

The net current density is calculated using the polarization curve (typically experimentally acquired) for that particular metal-electrolyte system.

Step 4) Corrosion rate

The metal dissolution rate can be calculated using Faraday's law.

6.2 Fundamental mathematical relations

Numerical modeling of galvanic corrosion is a boundary value problem governed by several different equations and boundary conditions.

6.2.1 Differential equation for conductivity of the electrolyte

The rate and distribution of the corrosion attack on the corroding electrode can be correlated to the electrochemical potential distribution within the corrosion system (Zhang 2011). To calculate the potential distribution in the electrolyte, the flow of electrical charge through the electrolyte first has to be calculated. The governing equation for any field problem in a conductive medium is the Fourier-Ohm law. The Fourier-Ohm law has the same base as the Fourier law for conductive heat transfer, and the flow of charge (Q) can be compared to the flow of energy in heat transfer (the two applications are compared in section 6.2.1.1) .

When the medium is linearly conductive, the flow of electrical charge can be written as a one-dimensional continuum expression of Ohm's law (Munn and Devereux 1991):

$$Q = -\sigma A \frac{\partial \phi}{\partial x} \Delta t \quad (6.2.1-1)$$

where

Q = amount of charge transferred across the medium boundary,

σ = electrical conductivity of the electrolyte (assumed to be uniform),

A = area of the boundary,

ϕ = electrical potential at a point,

x = linear dimension in the x -direction (orthogonal to the boundary), and
 t is time.

The electrical potential ϕ is the potential at the center of the infinitesimal element of the electrolyte shown below in Figure 109.

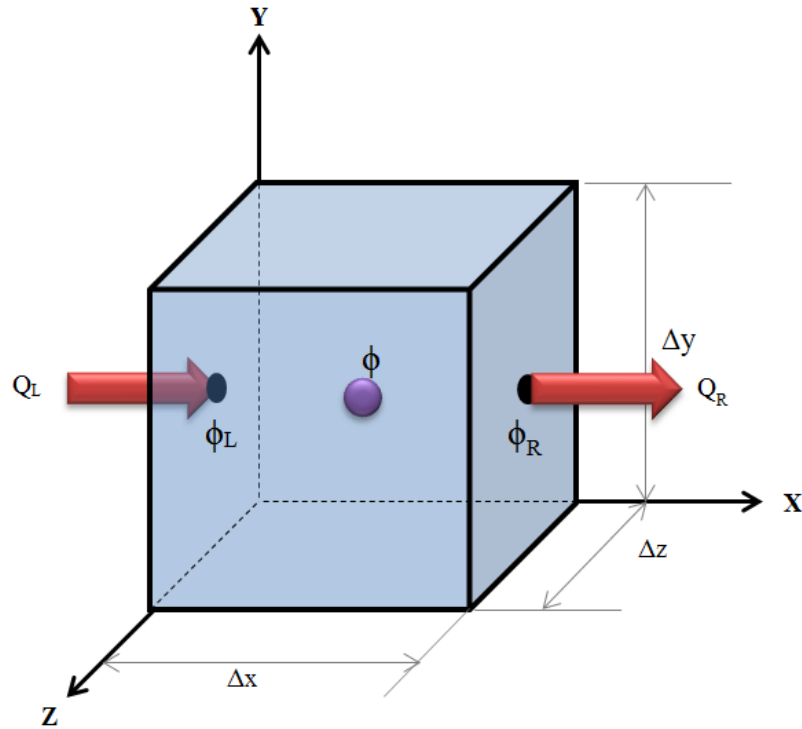


Figure 109: Infinitesimal element of the electrolyte.
 Based on (Munn and Devereux 1991).

The element can be divided into two halves, where the potential over the right-hand half-thickness of the element is (Munn and Devereux 1991):

$$\Delta\phi_R = \frac{\partial\phi}{\partial x} \left(\frac{1}{2} \Delta x \right) \quad (6.2.1-2)$$

Because ϕ is the potential at the center of the element, the potentials over the two half-thicknesses can be written as:

$$\phi_L = \phi - \frac{\partial \phi}{\partial x} \left(\frac{1}{2} \Delta x \right) \quad (6.2.1-3a)$$

$$\phi_R = \phi + \frac{\partial \phi}{\partial x} \left(\frac{1}{2} \Delta x \right) \quad (6.2.1-3b)$$

Using equations (6.2.1-1) and (6.2.1-3b), we can write the charge *entering* the left side of the element as (Munn and Devereux 1991):

$$Q_L = -\sigma A \frac{\partial}{\partial x} (\phi_L) \Delta t = -\sigma \Delta y \Delta z \frac{\partial}{\partial x} \left(\phi - \frac{1}{2} \frac{\partial \phi}{\partial x} \Delta x \right) \Delta t \quad (6.2.1-4)$$

We can similarly express the charge *leaving* the element on the right-hand side as (Munn and Devereux 1991):

$$Q_R = -\sigma \Delta y \Delta z \frac{\partial}{\partial x} \left(\phi + \frac{1}{2} \frac{\partial \phi}{\partial x} \Delta x \right) \Delta t \quad (6.2.1-5)$$

The net gain of charge in the element is then (Munn and Devereux 1991):

$$\begin{aligned} Q &= Q_L - Q_R \\ &= -\sigma \Delta y \Delta z \left[\frac{\partial}{\partial x} \left(\phi - \frac{1}{2} \frac{\partial \phi}{\partial x} \Delta x \right) - \frac{\partial}{\partial x} \left(\phi + \frac{1}{2} \frac{\partial \phi}{\partial x} \Delta x \right) \right] \Delta t \\ &= \sigma \Delta y \Delta z \frac{\partial^2 \phi}{\partial x^2} \Delta x \Delta t \end{aligned} \quad (6.2.1-6)$$

In three dimensions, the net gain of charge is (Munn and Devereux 1991):

$$Q = \sigma \left(\frac{\partial^2 \phi}{\partial x^2} + \frac{\partial^2 \phi}{\partial y^2} + \frac{\partial^2 \phi}{\partial z^2} \right) \Delta x \Delta y \Delta z \Delta t \quad (6.2.1-7)$$

If the charge is stored in the element, the potential of the element will change in the following way (Munn and Devereux 1991):

$$\Delta\phi = \frac{Q}{\rho c \Delta x \Delta y \Delta z} \quad (6.2.1-8)$$

where

ρ = density of the electrolyte, and

c = specific capacitance of the electrolyte.

Rearranging equation (6.2.1-8) gives an independent expression for charge:

$$Q = \rho c \Delta x \Delta y \Delta z \Delta\phi \quad (6.2.1-9)$$

If we equate the net gain of charge in (6.2.1-7) with the charged stored in (6.2.1-9), Δx , Δy , and Δz will cancel out, and we will get (Munn and Devereux 1991):

$$\sigma \left(\frac{\partial^2 \phi}{\partial x^2} + \frac{\partial^2 \phi}{\partial y^2} + \frac{\partial^2 \phi}{\partial z^2} \right) \Delta t = \rho c \Delta\phi \quad (6.2.1-10)$$

As $\Delta t \rightarrow 0$, equation (6.2.1-10) becomes:

$$\frac{\sigma}{\rho c} \left(\frac{\partial^2 \phi}{\partial x^2} + \frac{\partial^2 \phi}{\partial y^2} + \frac{\partial^2 \phi}{\partial z^2} \right) = \frac{\partial \phi}{\partial t} \quad (6.2.1-11)$$

To simplify the notation, we can replace $\frac{\partial^2 \phi}{\partial x^2} + \frac{\partial^2 \phi}{\partial y^2} + \frac{\partial^2 \phi}{\partial z^2}$ with the Laplacian operator ∇^2 . Equation (6.2.1-11) then becomes (Munn and Devereux 1991):

$$\frac{\sigma}{\rho c} \nabla^2 \phi = \frac{\partial \phi}{\partial t} \quad (6.2.1-12)$$

Equation (6.2.1-12) is the field equation, which is also known as the *Fourier equation*. It describes the electrical potential distribution in a conductive medium (Munn and Devereux 1991). Because most electrochemical problems are considered to be quasi-steady state ($\delta/\delta t = 0$), the governing equation becomes (Munn and Devereux 1991):

$$\nabla^2 \phi = 0 \quad (6.2.1-13)$$

6.2.1.1 Analogy with heat conduction

As mentioned in the introduction, Fourier's law also governs conductive heat transfer. Table 14 below illustrates the similarity between the Fourier's law for conductive heat transfer and the Fourier-Ohm law for ionic conduction. The comparison below assumes that both the thermal conductivity k and the electrolyte conductivity σ are constants, but both variables can be replaced with functions.

Table 14: Conductive heat transfer vs. Ionic conduction – the same mathematical base Sources: (Munn 1986), (Incropera, Dewitt et al. 2007).		
Phenomenon	<u>Conductive heat transfer</u>	<u>Ionic conduction</u>
Quantity being transferred [unit in SI system]	Energy [joule, J]	Charge (as positively or negatively charged ions) [coulomb, C]
Governing equation	Fourier's Law $q''_x = -k \frac{\partial T}{\partial x}$ where q''_x = heat flux [W/m ²] k = thermal conductivity [W/(m*K)] $T(x)$ = temperature distribution [K]	Fourier-Ohm's Law $q''_x = -\sigma \frac{\partial \phi}{\partial x}$ where q''_x = charge flux [C/(s*m ²)] σ = conductivity of the electrolyte [S/m] or [1/(Ω *m)] $\phi(x)$ = potential distribution [V]
Accumulation of energy or charge in a finite element	$\Delta T = \frac{Q}{\rho c_p \Delta x \Delta y \Delta z}$ where ΔT = change in temperature [K] Q = accumulation of energy in the element [J] ρ = density of the material [kg/m ³] c_p = specific heat capacity of the material [J/kg*K] $\Delta x \Delta y \Delta z$ = volume of the element [m ³]	$\Delta \phi = \frac{Q}{\rho c \Delta x \Delta y \Delta z}$ where $\Delta \phi$ = change in potential [V] Q = accumulation of charge in the element [C] ρ = density of the electrolyte [kg/m ³] c = specific capacitance of the electrolyte [F/kg] $\Delta x \Delta y \Delta z$ = volume of the element [m ³]

6.2.2 Boundary conditions

The next step in the numerical modeling is to select suitable boundary conditions. Munn and Devereux (Munn and Devereux 1991), and Kasper (Kasper 1940) have described five generic boundary conditions for modeling of corrosion and other electrochemical systems:

1) *First boundary-value problem (constant potential)*

A constant potential over a portion of the boundary is specified. In a corrosion system, this could be a suitable boundary condition for a non-polarizing metal electrode.

2) *Secondary boundary-value problem (constant current)*

A constant current flow – the so called Neumann boundary condition – characterizes this boundary condition. A constant-current cathodic protection system would be an example of a corrosion system that exhibits this behavior.

3) *Mixed boundary-value problem*

A combination of 1) and 2), as well as systems containing any combinations of these and the following types of boundary conditions.

4) *Third boundary-value problem (linear)*

A linear relation exists between the applied boundary current and the polarization potential. Real electrodes exhibit this polarization behavior only within a few tens of millivolts of the reversible corrosion potential.

5) *Fourth boundary-value problem (non-linear)*

The relation between the current through the boundary and the boundary

potential does not obey a linear relationship. This is the general case for polarization behavior and will be the focus of this chapter. There are two general types of non-linear boundary conditions: logarithmic (Tafel) and exponential (Volmer-Butler). Tafel boundary conditions will be used in the models presented in this dissertation.

6.3 Comsol Multiphysics Corrosion Module

The commercial software package Comsol has been used for the finite element models presented in this dissertation. The software is convenient and takes care of all the heavy computational work, but a relatively large amount of input data still has to be supplied by the user. This section will present the software and its features.

6.3.1 Comsol electrochemistry modules

Comsol has four different electrochemistry modules: *Batteries and Fuel Cells*, *Electrodeposition*, *Corrosion*, and *Electrochemistry* (Figure 110). All modules rest on the same physics, but the user interfaces are tailored for the particular applications. Only the *Corrosion* module was used in this study.

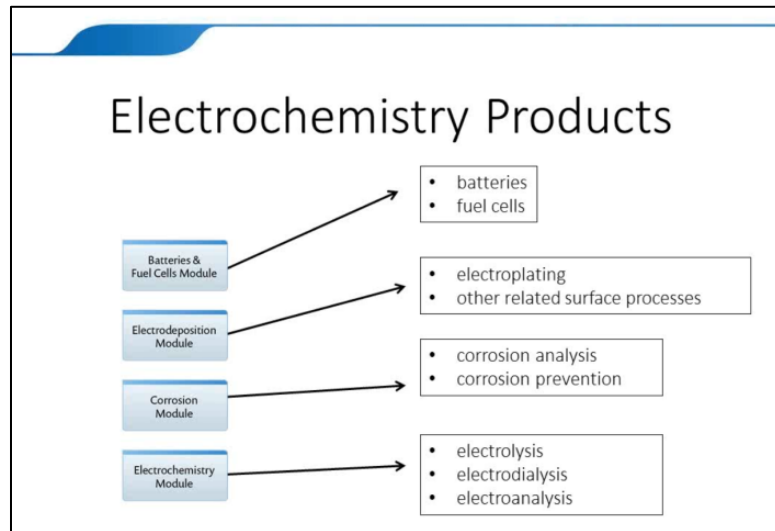
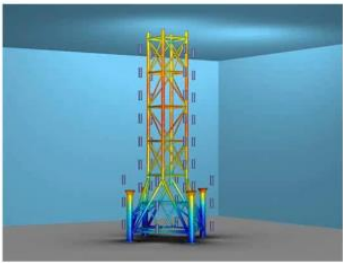


*Figure 110: The Comsol electrochemistry modules.
Source: (Comsol 2014).*


Comsol supplies a large selection of example problems and tutorials, many of them based on real cases. These fill two functions: they display the capability of the software package, and they help the user to get started with the software. Figure 111 through Figure 113 illustrate some of the capabilities of the Comsol Corrosion module.

Corrosion Module: Corrosion Prevention

- Easy modeling of common corrosion prevention processes:
 - Cathodic protection (most common).
 - Anodic protection.
 - Surface passivation.



“How effectively / efficiently can I mitigate corrosion in my system?”



*Figure 111: Comsol example problem: corrosion prevention.
Source: (Comsol 2014).*

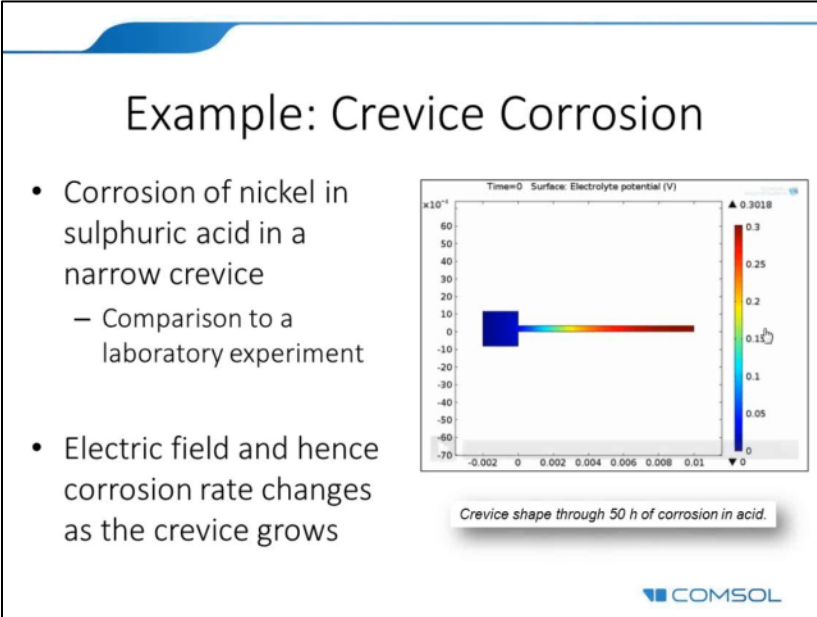


*Figure 112: Comsol example problem: crevice corrosion.
Source: (Comsol 2014).*

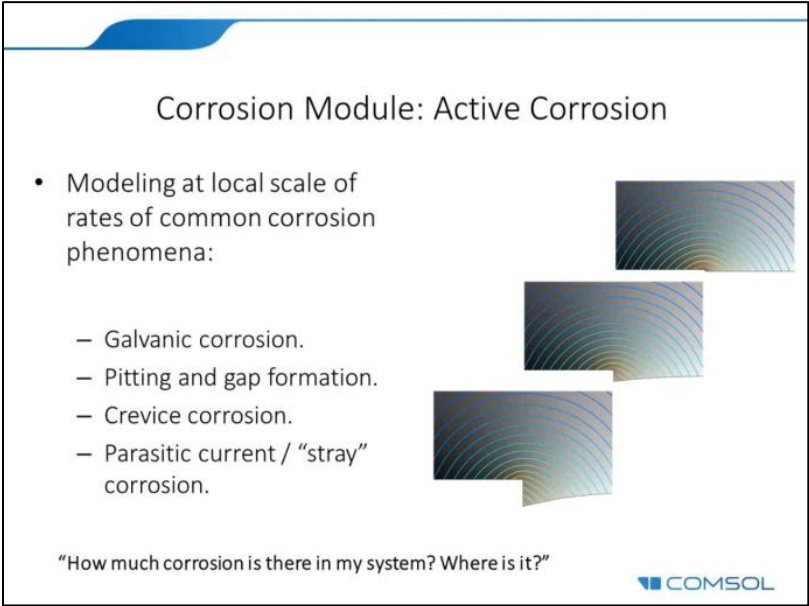


*Figure 113: Comsol example problem: corrosion with deformed geometry.
Source: (Comsol 2014).*

6.3.2 Current distribution

The main ‘physics’ type the user has to select in the Comsol corrosion modeling is the *current distribution*. It also has choices of *Electroanalysis*, *Shell electrode* and *Corrosion with deformed geometry*.

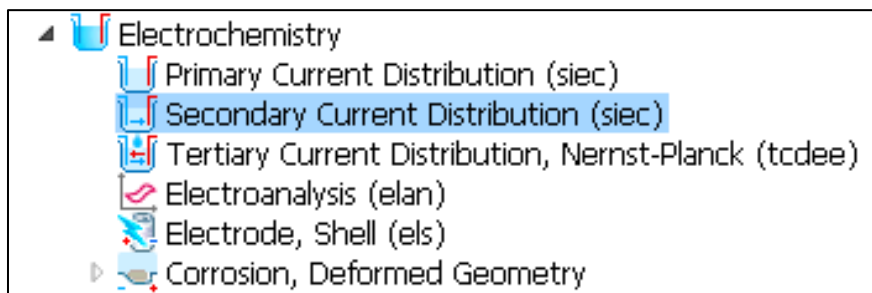


Figure 114: The available ‘physics’ types in the Comsol Corrosion module interface.
Source: Screenshot of the Comsol interface.

Primary current distribution

The primary current distribution is used to estimate the ohmic losses in simplified models of electrochemical cells. It defines the transport of ions in an electrolyte of uniform composition. It neglects over-potentials and reaction kinetics.

Secondary current distribution

Secondary current distribution is used for generic modeling of electrochemical cells. The relation between charge transfer and overpotential can be described using Butler-Volmer, Tafel, or other kinetic expressions. The conduction of currents in the electrodes and electrolytes are described by Ohm’s law in combination with a charge balance. Secondary current distribution has been used in the model presented in this section.

Tertiary current distribution (Nernst-Planck)

Individual transport of ions in the electrochemical cell is taken into account to describe the current and potential distribution in the Nernst-Planck interface in the tertiary current distribution alternative. This physics interface can be used to model significant concentration gradients of current-carrying species (ions).

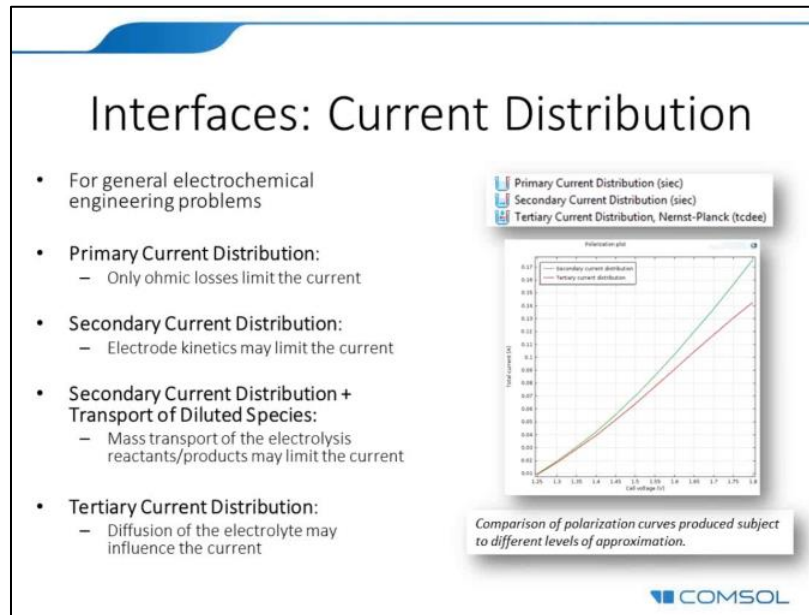


Figure 115: Applications for the different current distribution alternatives in the Comsol corrosion module. Source: (Comsol 2014).

6.3.3 Study type

Comsol has four different preset ‘study types’ in the corrosion module: *AC impedance stationary*, *AC impedance time dependent*, *Stationary*, and *Time dependent*.

There is also the option to create custom studies.

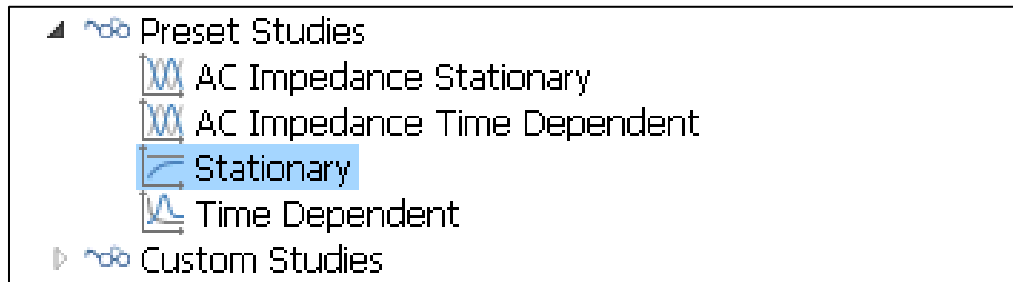


Figure 116: The available 'study' types in the Comsol Corrosion module interface.
Source: Screenshot of the Comsol interface.

AC impedance stationary

This study type is used to model stationary electrochemical impedance spectroscopy (EIS) in electrochemical cells.

AC impedance time dependent

This study type is used to model time dependent electrochemical impedance spectroscopy (EIS) in electrochemical cells.

Stationary

The stationary study type is used when field variables can be assumed to not change over time. This study type has been used in the Comsol models presented in this dissertation.

Time dependent

The time dependent study type is used when field variables change over time.

6.3.4 Step-by-step procedure

The basic procedure for finite element modeling of galvanic corrosion in Comsol is the following:

Step 1) Input data and model geometry

The software requires a minimum input of Tafel slopes, equilibrium potentials, exchange current density, and electrolyte conductivity. The geometry has to be built and meshed.

Step 2) Electrical potential

The software computes the electrical potential distribution in the electrolyte. The potential is due to the presence of dissimilar metals (or other conductive materials) connected through an electrolyte and through metallic contact. The potential distribution can also be calculated for externally applied currents, but this feature has not been used in this study.

Step 3) Current density

The net current density is calculated using the input specified above for the particular metal-electrolyte system.

Step 4) Corrosion rate

The metal dissolution rate can be calculated using Faraday's law.

The step-by-step procedure is illustrated in Figure 117 below.

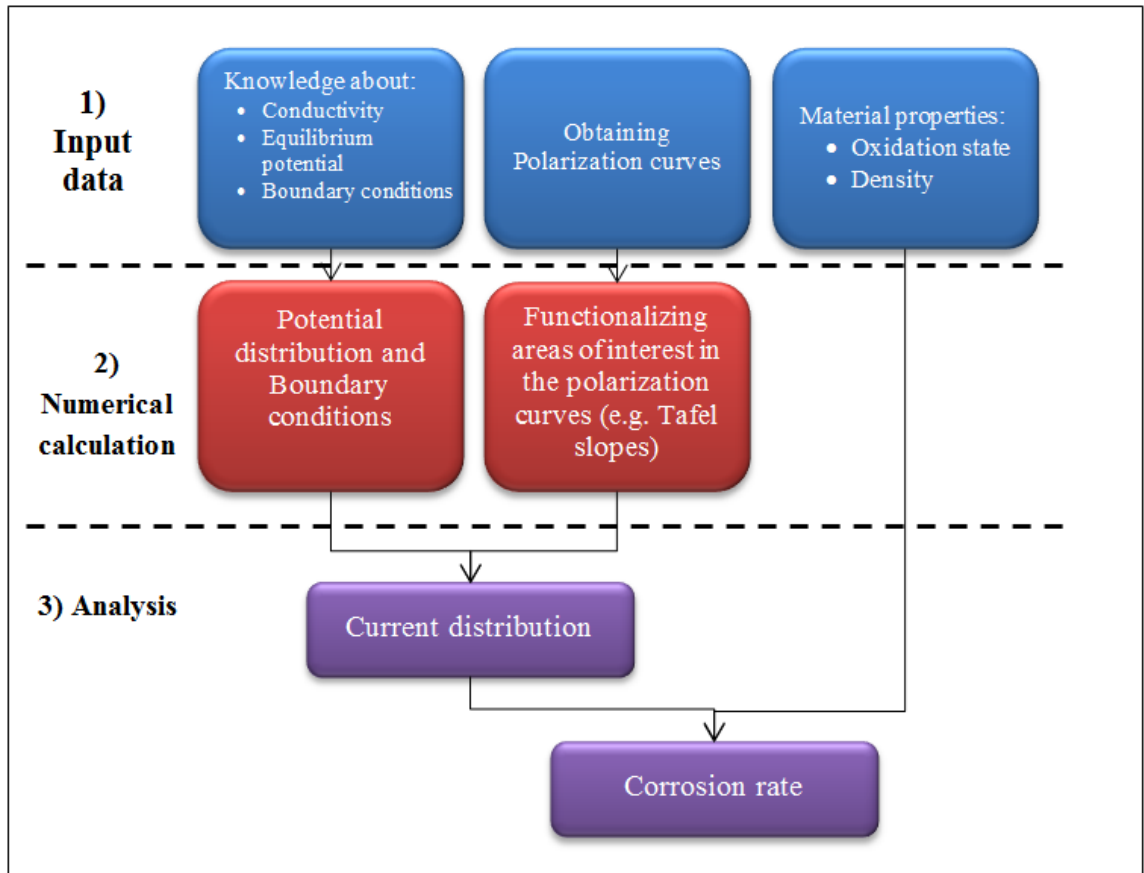


Figure 117: Step-by-step procedure for FE modeling of galvanic corrosion in Comsol.

Note that the basic process described above is based on the assumption that the process is not mass-transport limited. Mass-transport limitations will be discussed in later sections.

6.4 Immersed model: Parallel electrodes, resistance dominated

This section will describe a simple galvanic corrosion model consisting of two parallel electrodes with the space between filled with an electrolyte. The model is solved in this section using both an analytical approach and FE modeling. The simple geometry was chosen because analytical solutions are often only available for simplistic systems. The results from these two numerical models will be compared with experimental measurements. The galvanic corrosion rate is assumed to not be mass transport limited.

The FE model is two-dimensional with electrodes of aluminum (6061-T6 alloy) and solid graphite, see Figure 118. The analytical and physical model has planar electrodes that are 50 mm high and 6 mm wide (Figure 119). Solid graphite was chosen instead of CFRP because it allows for more accurate estimations of the exposed carbon surface. Four different distances between the electrodes were used: 25 mm, 50 mm, 100 mm, and 200 mm. Four different NaCl aqueous solutions were also used: 0.6 M (3.5 mass % NaCl), 0.17 M (1 mass % NaCl), 0.017 M (0.1 mass % NaCl), and 0.0017 M (0.01 mass % NaCl).

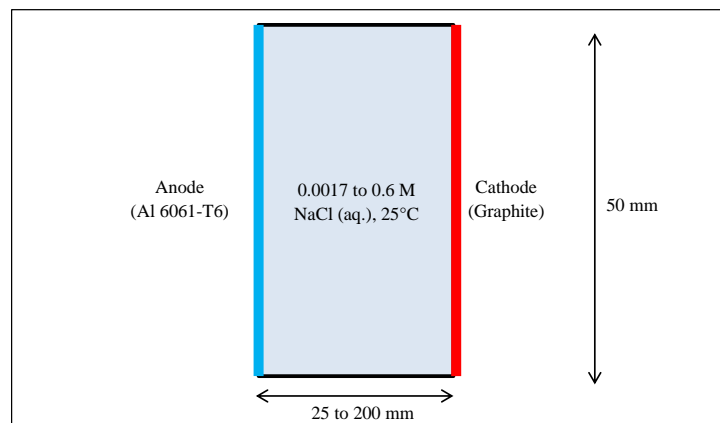


Figure 118: Illustration of the finite element model geometry.

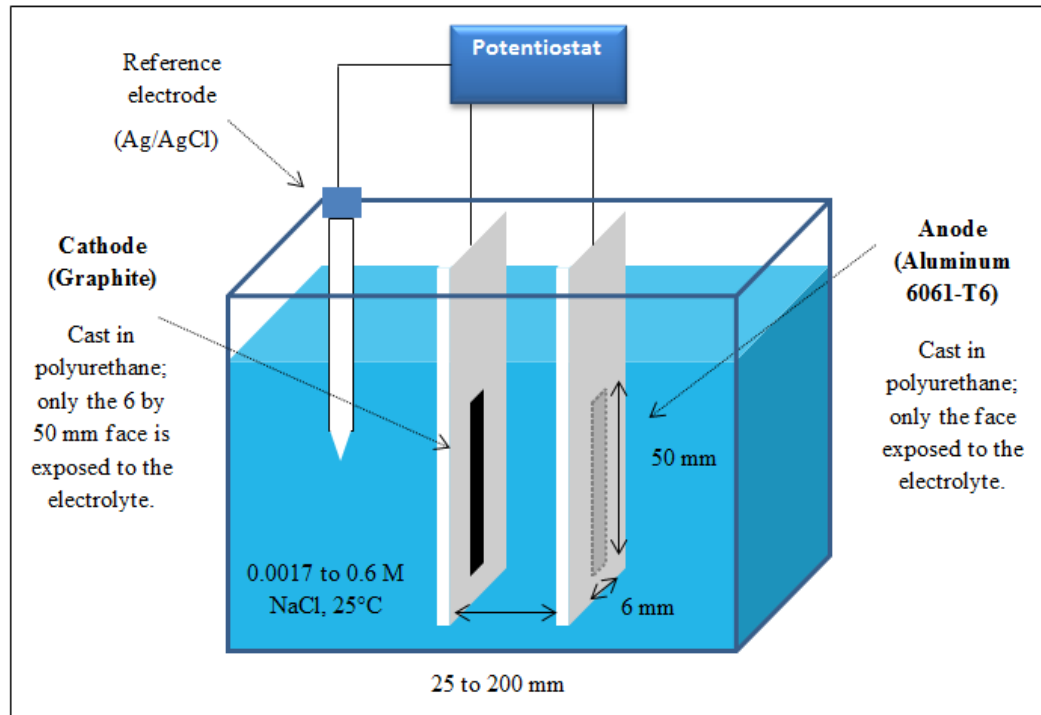


Figure 119: Validation experiment for parallel electrode model.

6.4.1 Input data

The data in Table 15 were used as input data for the numerical models presented in this chapter. The method for obtaining the input data was presented in chapter 4. The polarization curves used to obtain the data are repeated below.

Table 15: Input values for parallel electrode model in 0.6 M NaCl at RT (obtained experimentally)			
Variable name	Variable	Value	Unit
$E_{eq,Al}$	Equilibrium potential, aluminum 6061-T6	-0.690	V
$E_{eq,C}$	Equilibrium potential, graphite	-0.140	V
$A_{c,C}$	Tafel slope, graphite	-1.9558	V
$A_{a,Al}$	Tafel slope, aluminum 6061-T6	0.0153	V
$i_{0,Al}$	Exchange current density, Al 6061-T6	0.16681	A/m ²
$i_{0,C}$	Exchange current density, graphite	0.093521	A/m ²

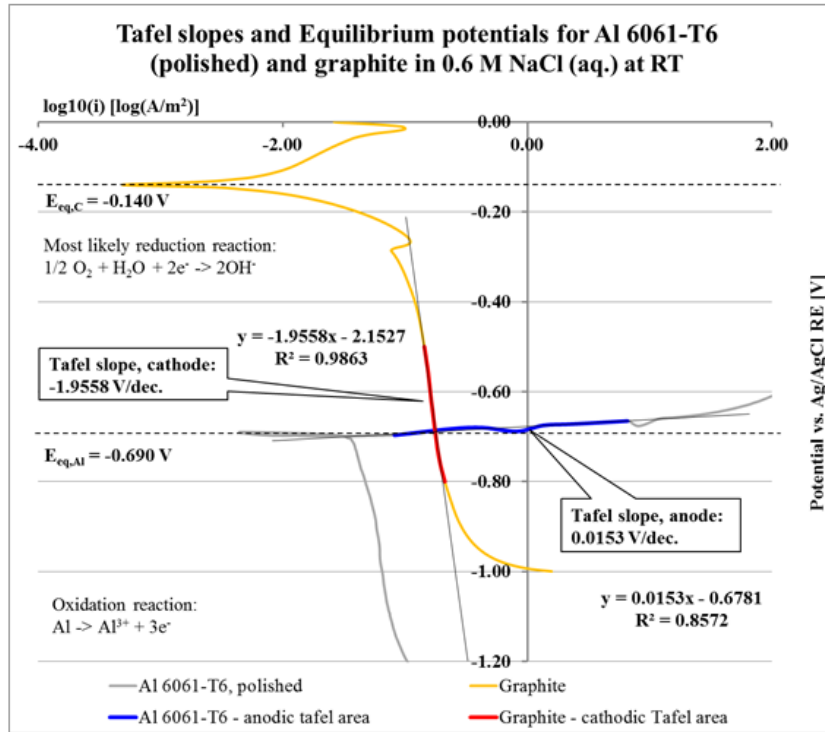


Figure 75 (repeated): Tafel slopes and equilibrium potential for aluminum and graphite.

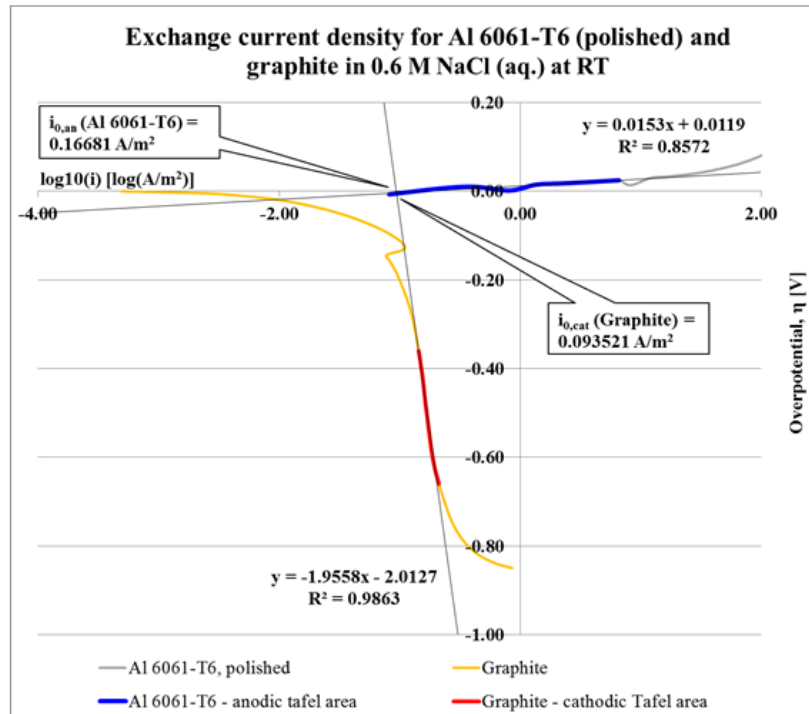


Figure 76 (repeated): Exchange current density for aluminum and graphite.

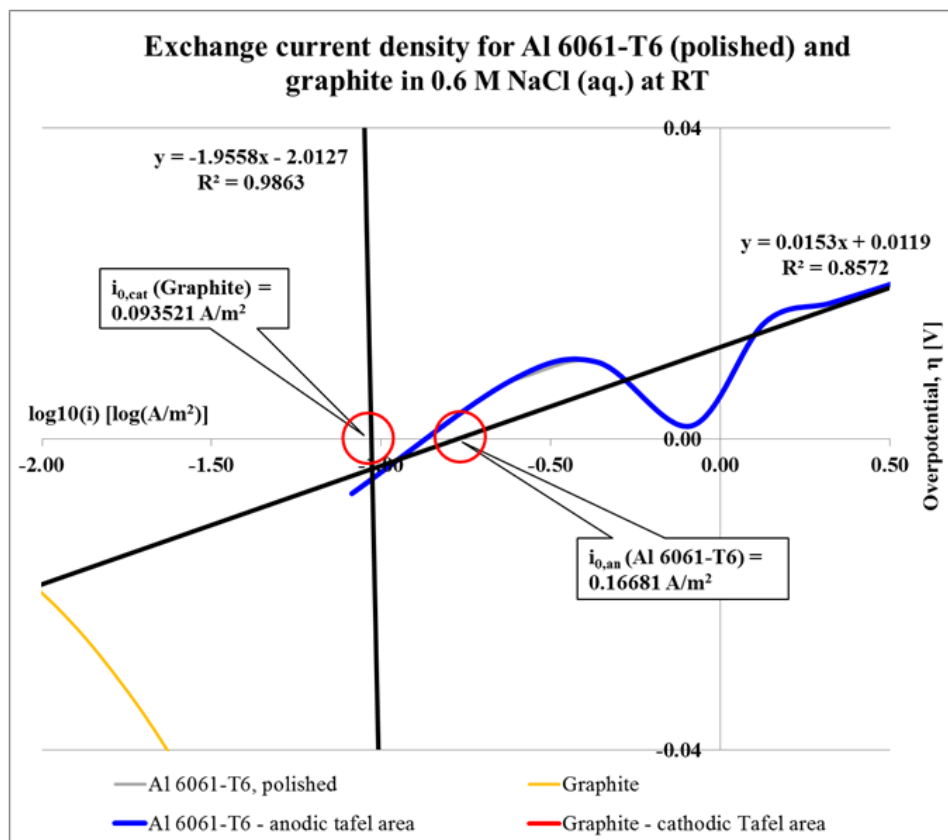


Figure 77 (repeated): Exchange current density for aluminum and graphite (zoomed in).

6.4.2 Analytical solution

The analytical solution assumes that the galvanic corrosion rate is solely controlled by the electrode kinetics and the resistance of the electrolyte.

Potential gradient

The potential gradient through the electrolyte is caused by the so called IR drop. In this case, the Fourier-Ohm's law (described in section 6.2.1) simplifies to Ohm's law where the voltage drop is a linear function of the resistance through the electrolyte and follows Ohm's law (Boyes 2009):

$$E_{IR} = I \cdot R \quad (6.4.2-1)$$

where

E_{IR} = potential drop through the electrolyte [V],

I = galvanic corrosion current through the electrolyte [A], and

R = resistance of the electrolyte [Ω].

The resistance of the electrolyte is a constant set by the conductivity of the electrolyte, the area of the electrodes, and the distance between the electrodes (this assumes that the composition of the electrolyte is uniform and does not change over time):

$$R [\Omega] = \frac{\rho_{el} [\Omega m] \cdot d [m]}{w [m] \cdot h [m]} \quad (6.4.2-2)$$

where

R = resistance [Ω],

ρ_{el} = resistivity of the electrolyte [$\Omega \cdot m$],

d = distance between the parallel electrodes [m],

w = width of the electrodes [m], and

h = height of the electrodes [m].

0.6 M NaCl (3.5 mass % NaCl) has a conductivity of 7.59 S/m, which is equal to a resistivity of 0.132 $\Omega \cdot m$. With this resistivity and electrode areas as described above, and a distance of 25 mm, the resistance of the electrolyte will be:

$$R = \frac{\rho_{el} [\Omega m] \cdot d [m]}{w [m] \cdot h [m]} = \frac{0.132 [\Omega m] \cdot 0.025 [m]}{0.006 [m] \cdot 0.05 [m]} = 11.0 \Omega \quad (6.4.2-3)$$

Table 16 below lists the calculated resistances for additional electrolyte concentrations and electrode distances used in the model (conductivity based on Kohlrausch's law, presented in section 2.3.2).

Table 16: Resistance of selected electrolytes			
NaCl concentration [mass %]	NaCl molarity [M]	Distance between electrodes [mm]	Resistance [Ω]
3.5	0.6	25 mm	11.0
3.5	0.6	50 mm	22.0
3.5	0.6	100 mm	43.9
3.5	0.6	200 mm	87.8
1.0	0.17	25 mm	38.4
1.0	0.17	50 mm	76.9
1.0	0.17	100 mm	154
1.0	0.17	200 mm	307
0.1	0.017	25 mm	384
0.1	0.017	50 mm	769
0.1	0.017	100 mm	1537
0.1	0.017	200 mm	3074
0.01	0.0017	25 mm	3843
0.01	0.0017	50 mm	7686
0.01	0.0017	100 mm	15371
0.01	0.0017	200 mm	30742

Galvanic corrosion current from overlaying polarization curves

Overlaying of the potentiodynamic polarization curves provides a rough estimate of the expected galvanic corrosion current, but it neglects the IR drop (more about that problem below) (Zhang 2011). A similar estimate can also be obtained by finding the intersection between the two linear curve fits that were used to generate the Tafel slopes (Figure 75, repeated above). This approach assumes that the IR drop through the electrolyte can be neglected. Setting the two equations extracted from the figure equal to each other yields the following result:

$$0.0153x - 0.6781 = -1.9558x - 2.1527 \quad \rightarrow \quad x = -0.748110192$$

$$i = 10^x = 10^{-0.748110192} = 0.1786 \left[\frac{A}{m^2} \right] = 178.6 \left[\frac{mA}{m^2} \right] \quad (6.4.2-4)$$

Because the two electrodes have the same exposed area, the galvanic corrosion current densities will be equal. The value calculated above will be compared to a solution also taking into account the IR drop through the electrolyte at the end of this section.

Over-potentials

The *over-potential* is the measurement of how far the corrosion potential of a material is shifted from its equilibrium potential (marked with a dotted line in Figure 75). The greater the over-potential, the further away from the equilibrium potential, and the more *polarized* the material is said to be. Assuming that the corrosion potential of the aluminum-graphite couple during galvanic coupling is represented by the intersection of the two Tafel slopes (first part of eq. 6.4.2-4), the corrosion potential of the galvanic couple with respect to the Ag/AgCl reference electrode is the following:

$$E_{corr} = y = -1.9558x - 2.1527 = -1.9558 \cdot (-0.74811) - 2.1527 = -0.689546 \text{ V} \quad (6.4.2-5)$$

Using the value above for the corrosion potential and the equilibrium potentials for both materials, the over-potentials for graphite and aluminum would be:

$$\Delta V_C = E_{corr} - E_{eq,C} = (-0.689546) - (-0.140) = -0.549546 \text{ V} \quad (6.4.2-6a)$$

$$\Delta V_{Al} = E_{corr} - E_{eq,Al} = (-0.689546) - (-0.690) = 0.000454 \text{ V} \quad (6.4.2-6b)$$

where

ΔV = over-potential [V],

E_{corr} = corrosion potential [V], and

E_{eq} = equilibrium potential [V].

The potential of the graphite is shifted to a much more negative level, while the potential of the aluminum is shifted to a more positive level. The large polarization of the cathode is common under immersed conditions.

Galvanic corrosion current from over-potential

The galvanic corrosion current can also be estimated from the over-potentials using the Tafel equation (Revie 2000):

$$\Delta V = A_T \cdot \log\left(\frac{i}{i_0}\right) \quad (6.4.2-7)$$

where

ΔV = over-potential [V],

A_T = Tafel slope [V],

i = current density [A/m^2], and

i_0 = exchange current density [A/m^2].

Solving for the current density gives:

$$i = i_0 \cdot e^{\left(\frac{\Delta V}{A_T}\right)} \quad (6.4.2-8)$$

Using the values from above:

$$i_C = i_{0,C} \cdot 10^{\left(\frac{\Delta V_C}{A_{T,C}}\right)} = 0.093521 \left[\frac{A}{m^2}\right] \cdot 10^{\left[\frac{-0.549546}{-1.9558}\right]} = 0.1786 \left[\frac{A}{m^2}\right] = 178.6 \left[\frac{mA}{m^2}\right]$$

(6.4.2-9a)

$$i_{Al} = i_{0,Al} \cdot 10^{\left(\frac{\Delta V_{Al}}{A_{T,Al}}\right)} = 0.16681 \left[\frac{A}{m^2}\right] \cdot 10^{\left[\frac{0.000454}{0.0153}\right]} = 0.1786 \left[\frac{A}{m^2}\right] = 178.6 \left[\frac{mA}{m^2}\right]$$

(6.4.2-9b)

This method gives the same results as the intersection of the functions used to generate the Tafel slopes, which is expected as they are mathematically equivalent.

Accounting for the IR drop

The calculations of galvanic corrosion current above were assuming a negligible IR drop through the electrolyte. This may be a reasonable assumption when the electrolyte conductivity is high and the distance between the electrodes is short. With lower conductivity or larger distance, or both, the IR drop cannot be neglected. The IR drop decreases the over-potential that drives the galvanic corrosion, resulting in a lower galvanic corrosion current (see Figure 120). Because the IR drop is a function of the galvanic corrosion current, the final solution has to be found through numerical iteration.

Let us use the already presented configuration as an example. With an electrode area of 300 mm², the total galvanic corrosion current is:

$$I = i \cdot A = 0.1786 \left[\frac{A}{m^2}\right] \cdot 0.006 [m] \cdot 0.05 [m] = 53.6 [\mu A] \quad (6.4.2-10)$$

At this current, the IR drop through the electrolyte with 11 Ω resistance (from Table 16, for 0.6 M NaCl and 25 mm distance) would be:

$$E_{IR} = I \cdot R = 53.6 [\mu A] \cdot 11[\Omega] = 0.5896 [mV] \quad (6.4.2-11)$$

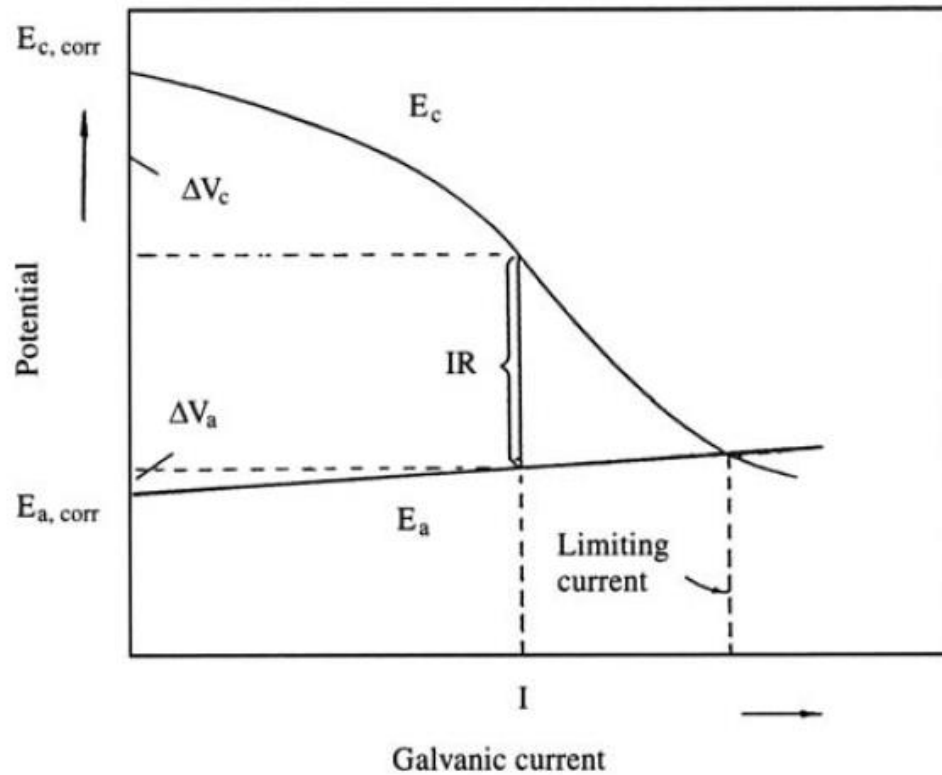


Figure 120: Illustration of the IR drop.
From (Zhang 2011).

This means that the galvanic corrosion current is not represented by the intersection of the two curves, but by the location to the left of the intersection where the distance between the two curves is 0.5896 mV.

Adding the IR drop of 0.5896 mV to equation (6.4.2-4) will result in the following galvanic corrosion current density:

$$0.0153x - 0.6781 + 0.0005896 = -1.9558x - 2.1527$$

$$\rightarrow x = -0.748409$$

$$i = 10^x = 10^{-0.748409} = 0.17848 \left[\frac{A}{m^2} \right] = 178.5 \left[\frac{mA}{m^2} \right] \quad (6.4.2-12)$$

By including the IR drop in the calculation, the calculated galvanic corrosion rate decreased from 178.6 mA/m² to 178.5 mA/m² because there was a slightly lower over-potential available to drive the galvanic corrosion reactions. Because the IR drop is a function of this current density, we need to re-calculate the IR drop again. Repeating this iteration will eventually make the solution converge, as can be seen in Table 17.

Table 17: Iterations to solve galvanic corrosion current, parallel electrode model in 0.6 M NaCl with 25 mm electrode distance						
Iteration	x	Galvanic current density [A/m²]	Galvanic current density [mA/m²]	Galvanic current [A]	Galvanic current [μA]	IR drop [V]
1	-0.748110192	0.1786	178.60	5.36E-05	53.58	5.883E-04
2	-0.747811737	0.1785	178.48	5.35E-05	53.54	5.879E-04
3	-0.747811942	0.1785	178.48	5.35E-05	53.54	5.879E-04

As illustrated in the table above, the galvanic corrosion current converges (to four significant figures) after the second iteration in this case. This is because the conductivity of the electrolyte is high and the distance short, which results in a very small IR drop. As it will be shown below, many more iterations will be needed if the conductivity is low and the distance large.

Final analytical solution

The final equation for the analytical solution for the galvanic corrosion current density in the parallel electrode model presented in this section is:

$$i = 10^{\left(\frac{-1.4746 - I \cdot R}{1.9711}\right)} = 10^{\left(\frac{-1.4746 - i \cdot A \cdot \rho \frac{d}{A}}{1.9711}\right)} = 10^{\left(\frac{-1.4746 - i \cdot \rho \cdot d}{1.9711}\right)} \quad (6.4.2-13)$$

where

i = galvanic corrosion current density [A/m^2],

I = galvanic corrosion current [A],

R = resistance of the electrolyte [Ω],

A = area of each electrode (assumes 1:1 area ratio) [m^2],

ρ = resistivity of the electrolyte [$\Omega \cdot m$], and

d = distance between electrodes [m].

Analytical results

Figure 121 illustrates the results for four different electrolytes and four different electrode distances solved through numerical iteration. The combination of the electrolyte with the highest conductivity (0.6 M NaCl) and the smallest distance (25 mm) converged after two iterations. The electrolyte with the lowest conductivity (0.0017 M NaCl) and the largest distance (200 mm) took 60 iterations to converge to the third decimal.

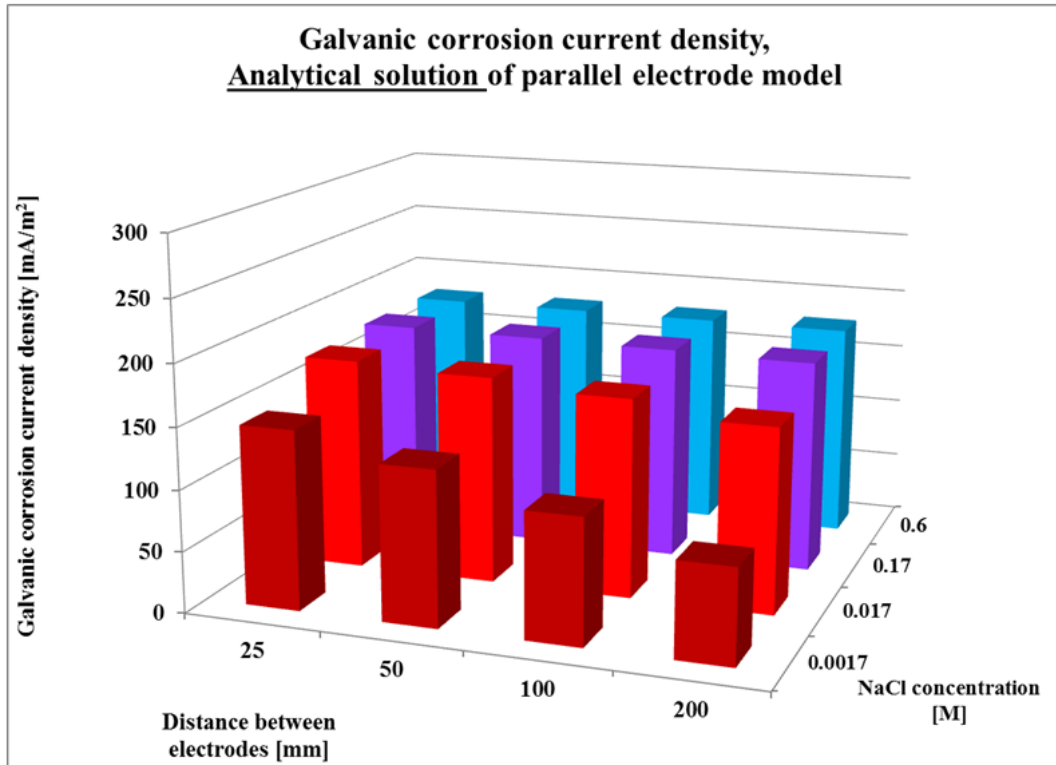


Figure 121: Analytical solution for parallel electrode model for four different electrolytes and four different electrode distances.

6.4.3 Finite Element model

A two-dimensional FE model was created in Comsol using the geometry in Figure 118 (repeated below) and the input values in Table 15 (repeated below).

The FE model is based on the following assumptions:

- The electrolyte is only defined by its conductivity which follows Kohlrausch's law (2.3.2-1).
- The electrolyte composition and conductivity is uniform.
- The current distribution is *secondary*, which assumes that the reaction rate is not limited by mass transport.
- The two half-cell reactions and their characteristics are defined in the electrode-electrolyte boundary interfaces. Both reactions are assumed to follow Tafel behavior.
- The upper and lower boundaries are insulated by applying a zero-flux boundary condition.
- A mapped meshing was used with a finer mesh closer to the electrodes and a coarser mesh towards the center.
- The electrodes are semi- infinitely wide.

Table 15 (repeated): Input values for parallel electrode model in 0.6 M NaCl at RT (obtained experimentally)			
Variable name	Variable	Value	Unit
$E_{eq,Al}$	Equilibrium potential, aluminum 6061-T6	-0.690	V
$E_{eq,C}$	Equilibrium potential, graphite	-0.140	V
$A_{c,C}$	Tafel slope, graphite	-1.9558	V
$A_{a,Al}$	Tafel slope, aluminum 6061-T6	0.0153	V
$i_{0,Al}$	Exchange current density, Al 6061-T6	0.16681	A/m ²
$i_{0,C}$	Exchange current density, graphite	0.093521	A/m ²

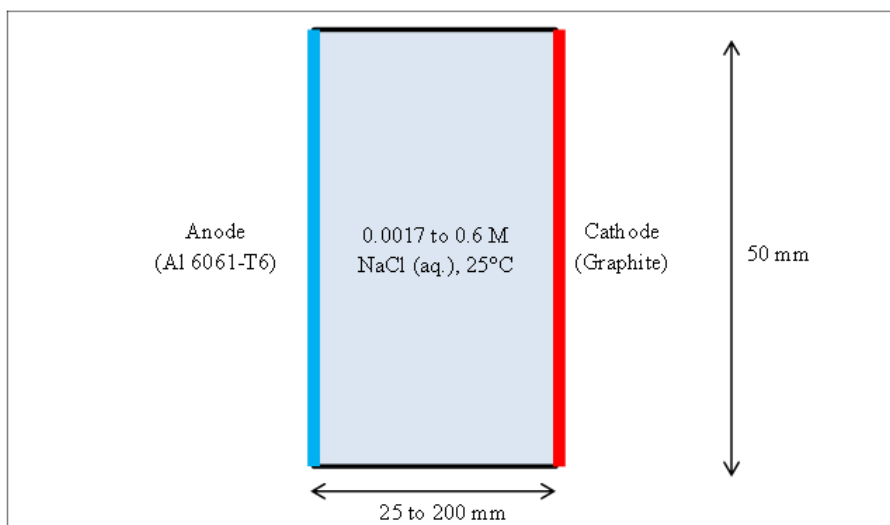


Figure 118 (repeated): Finite element model.

Parametric sweeps

The model was built with a fixed distance between the electrodes, and the study was performed through a parametric sweep of the four different electrolyte conductivities. The model was then re-built for each of the electrode distances (25, 50, 100, and 200 mm) and the parametric sweep was repeated.

Finite element results

Figure 122 illustrates the results from the sixteen different combinations of electrolytes and electrode distances. The trend is very similar to the analytical results shown in Figure 121, but the values are consistently a bit higher for the FE model.

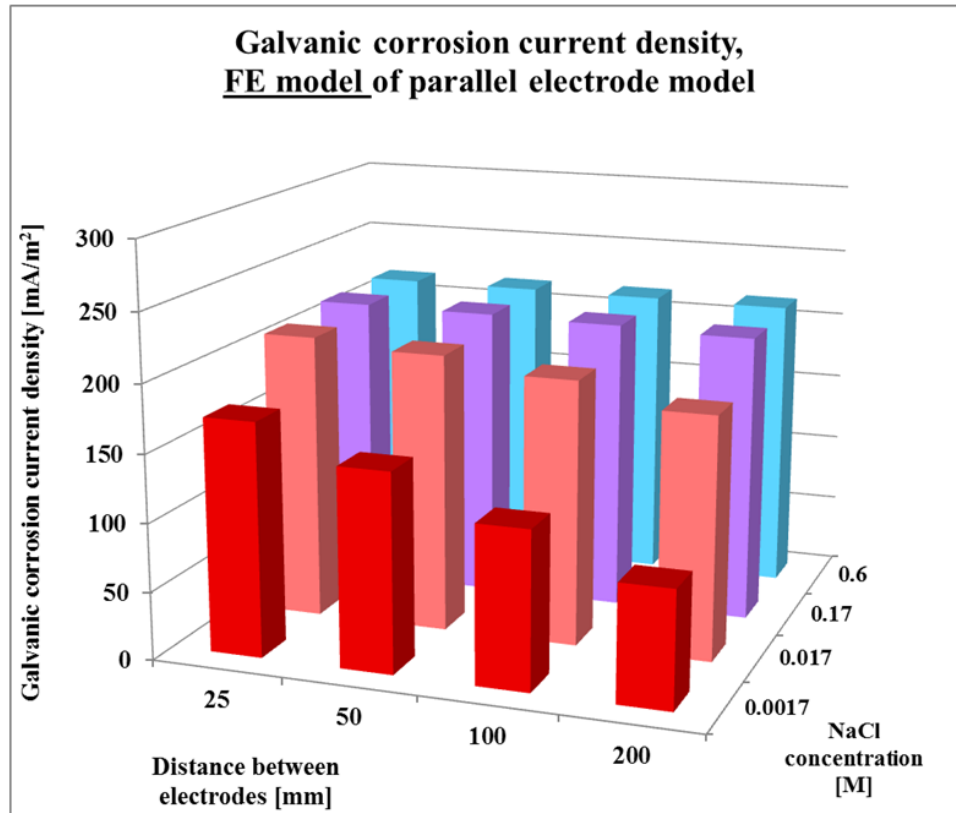


Figure 122: Finite element solution for parallel electrode model for four different electrolytes and four different electrode distances.

Figure 123 displays the potential gradient through the electrolyte for an electrode distance of 100 mm. The IR drop increases with decreased electrolyte conductivity due to the increased resistance. The figure clearly illustrates a linear gradient, supporting the assumption made in the analytical solution.

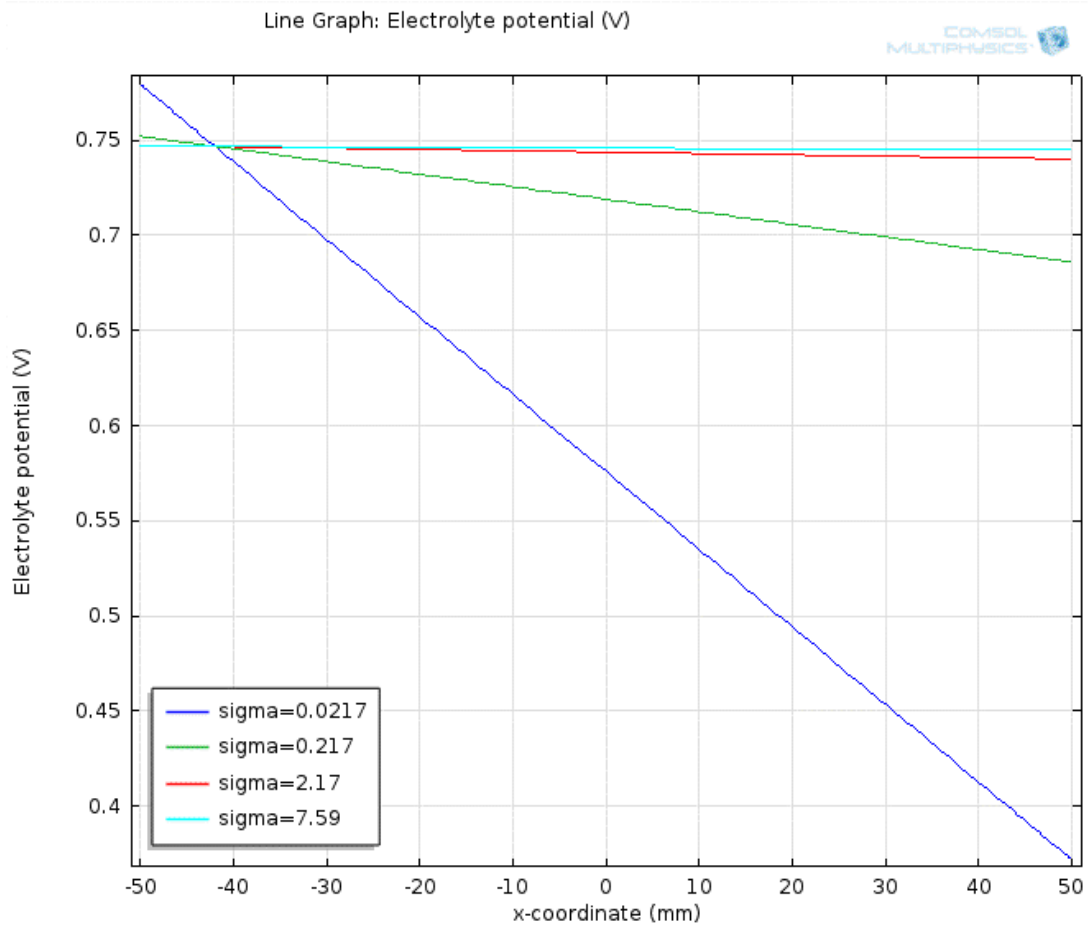


Figure 123: Potential gradient through the electrolyte for the parallel electrode model with 100 mm electrode distance. Sigma represents the conductivity of the electrolyte in S/m.

6.4.4 Experimental validation models

Two physical validation models were built as in Figure 119 (repeated below) and Figure 124. The second validation model was added after initial results indicated that the mass transport from the bulk electrolyte affected the results. Figure 125 shows the actual physical setup. The aluminum was washed and polished before each test series to avoid build-up of corrosion products and contamination between different electrolyte

compositions (this was particularly important while going from a strong electrolyte to a weak electrolyte).

The galvanic corrosion current was measured for the same conditions that were used in the numerical models: four different electrode distances (25, 50, 100, and 200 mm), and four different electrolytes (0.0017, 0.017, 0.17, and 0.6 M NaCl). The dissolved oxygen concentration in all electrolytes was 91% to 95 % of the saturation limit (Table 8, repeated below). All tests were performed at room temperature. The galvanic corrosion current was measured every 10 seconds during 30 minutes for each condition, and an average was calculated for the last 10 minutes. The measurements were repeated three times for each condition.

Table 8 (repeated): Conductivity, resistivity, and dissolved oxygen concentration of the electrolytes						
Molarity [M]	NaCl conc. [% mass fraction]	Conductivity [S/m]	Resistivity [Ω^*m]	Measured dissolved oxygen concentration (altitude and salinity corrected) [mg/liter]	Oxygen saturation limit (altitude and salinity corrected) [mg/liter] (Milwaukee 2010)	% of oxygen saturation limit
0.0017	0.01	0.0217	46.1	6.4	6.9	93 %
0.017	0.1	0.217	4.61	6.4	6.9	93 %
0.17	1.0	2.17	0.461	6.3	6.6	95 %
0.6	3.5	7.59	0.132	5.1	5.6	91 %

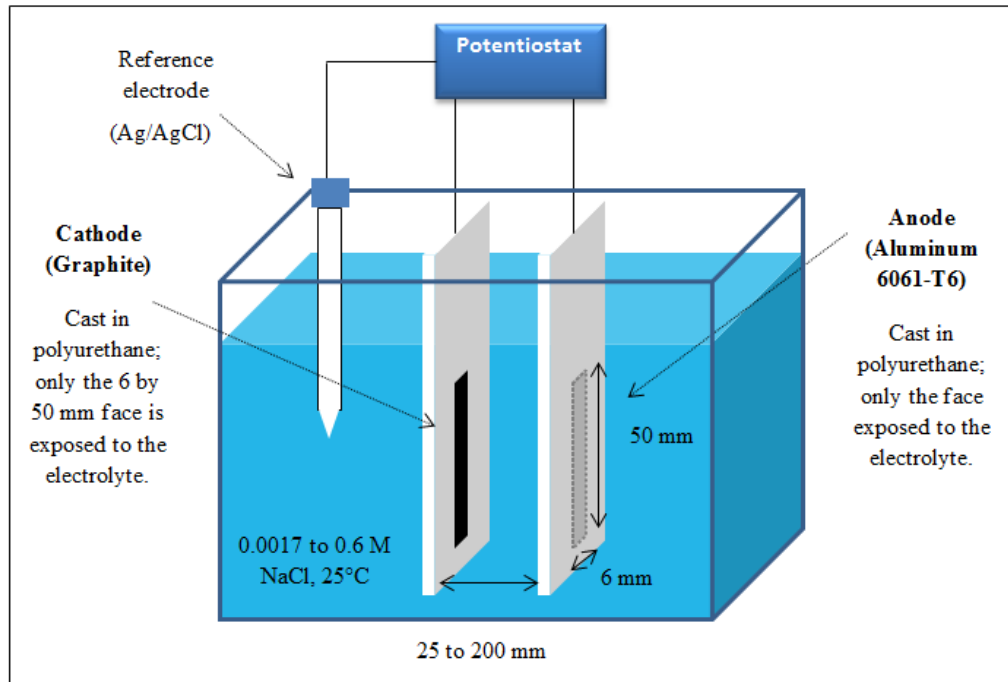


Figure 119 (repeated): Validation experiment for parallel electrode model with open electrolyte volume.

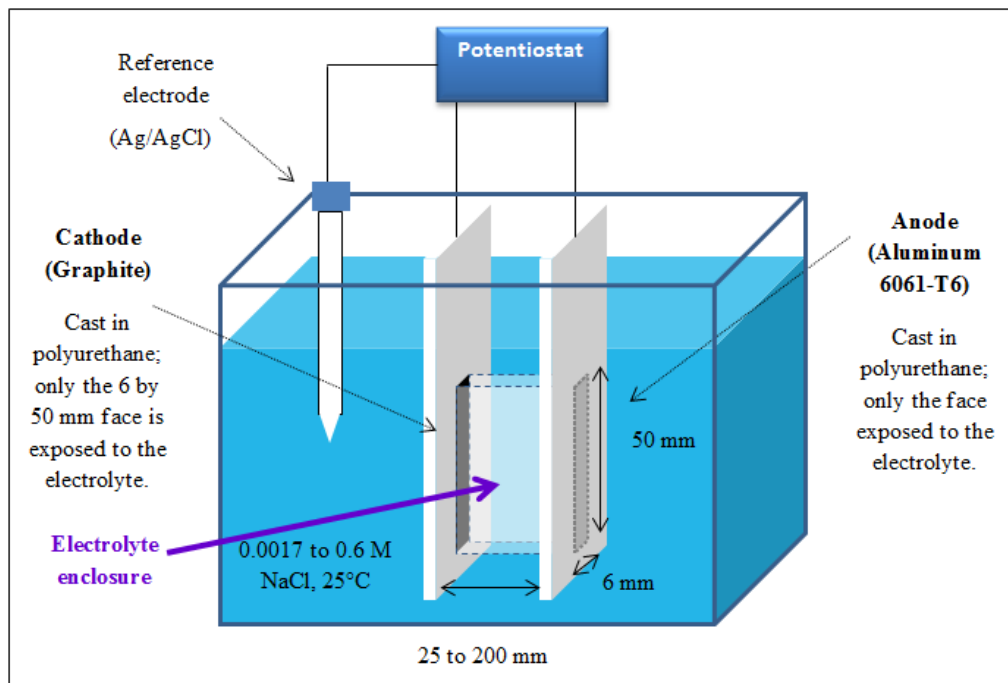


Figure 124: Validation experiment for parallel electrode model with enclosed electrolyte volume.

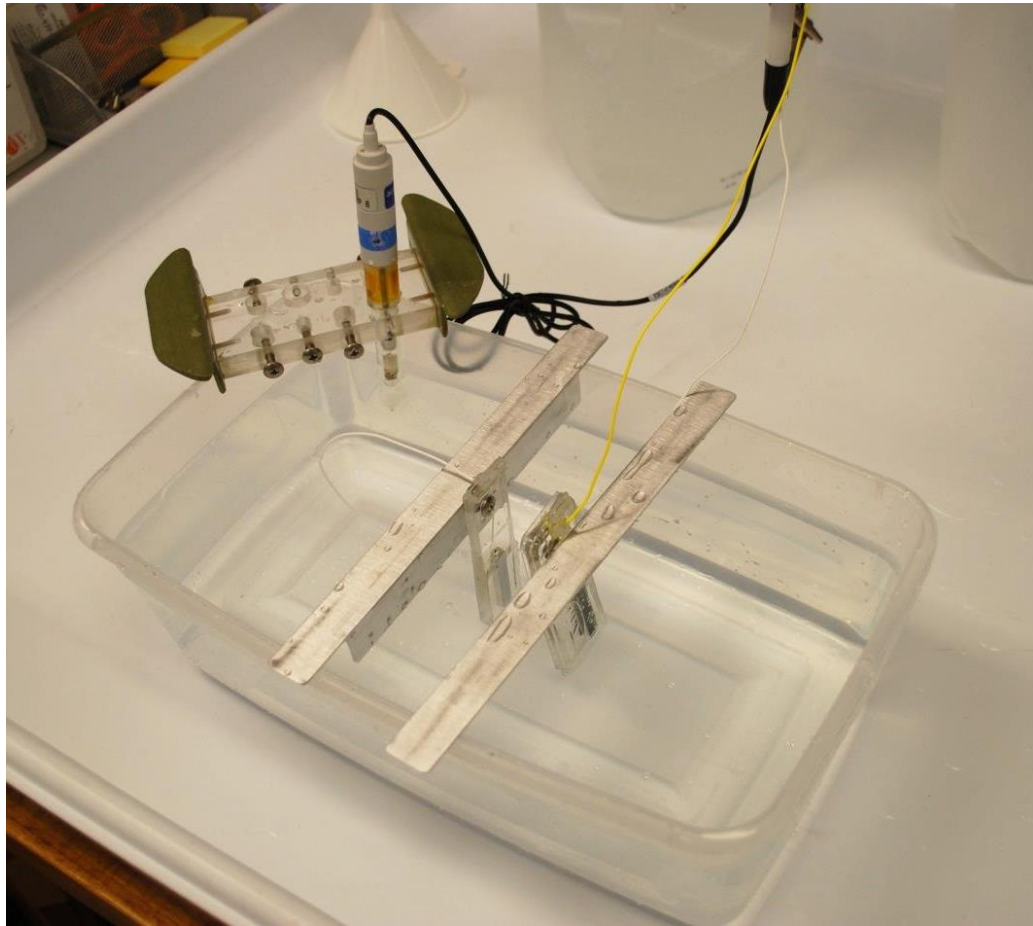


Figure 125: Setup for physical validation model (case A).

Figure 126 through Figure 128 show a comparison of galvanic corrosion current density from the analytical solution, the finite element model, and the two validation models for all sixteen different combinations of electrolyte composition and electrode distance.

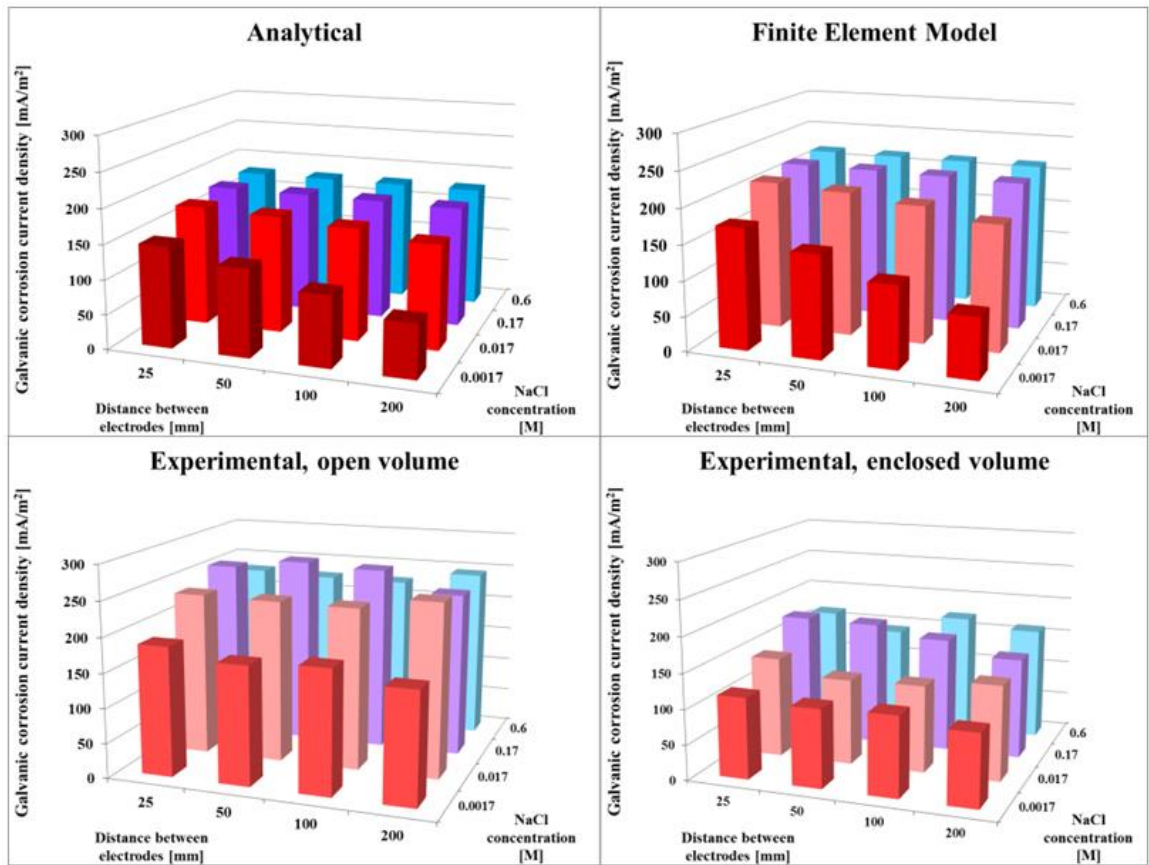


Figure 126: Comparison of analytical solution, finite element model, and experimental measurements.

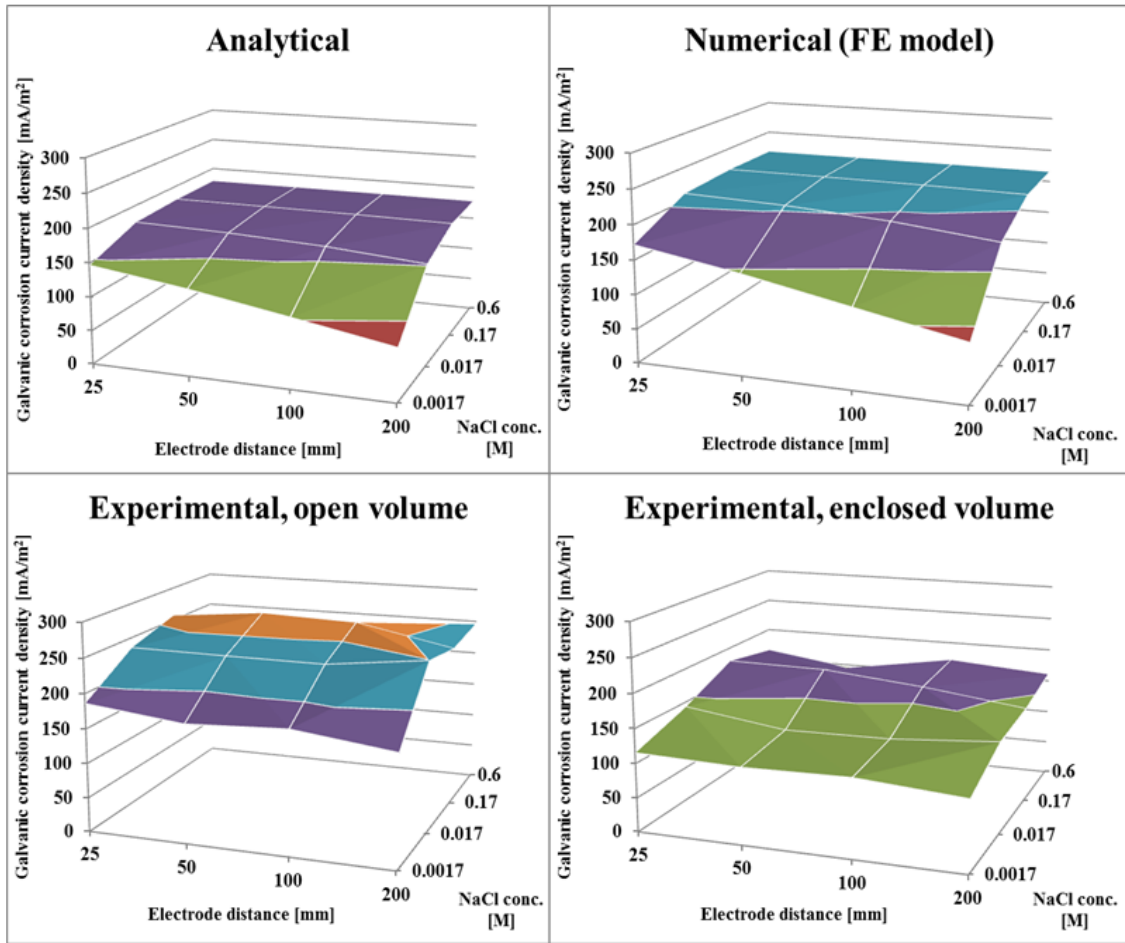


Figure 127: Comparison of analytical solution, finite element model, and experimental measurements.

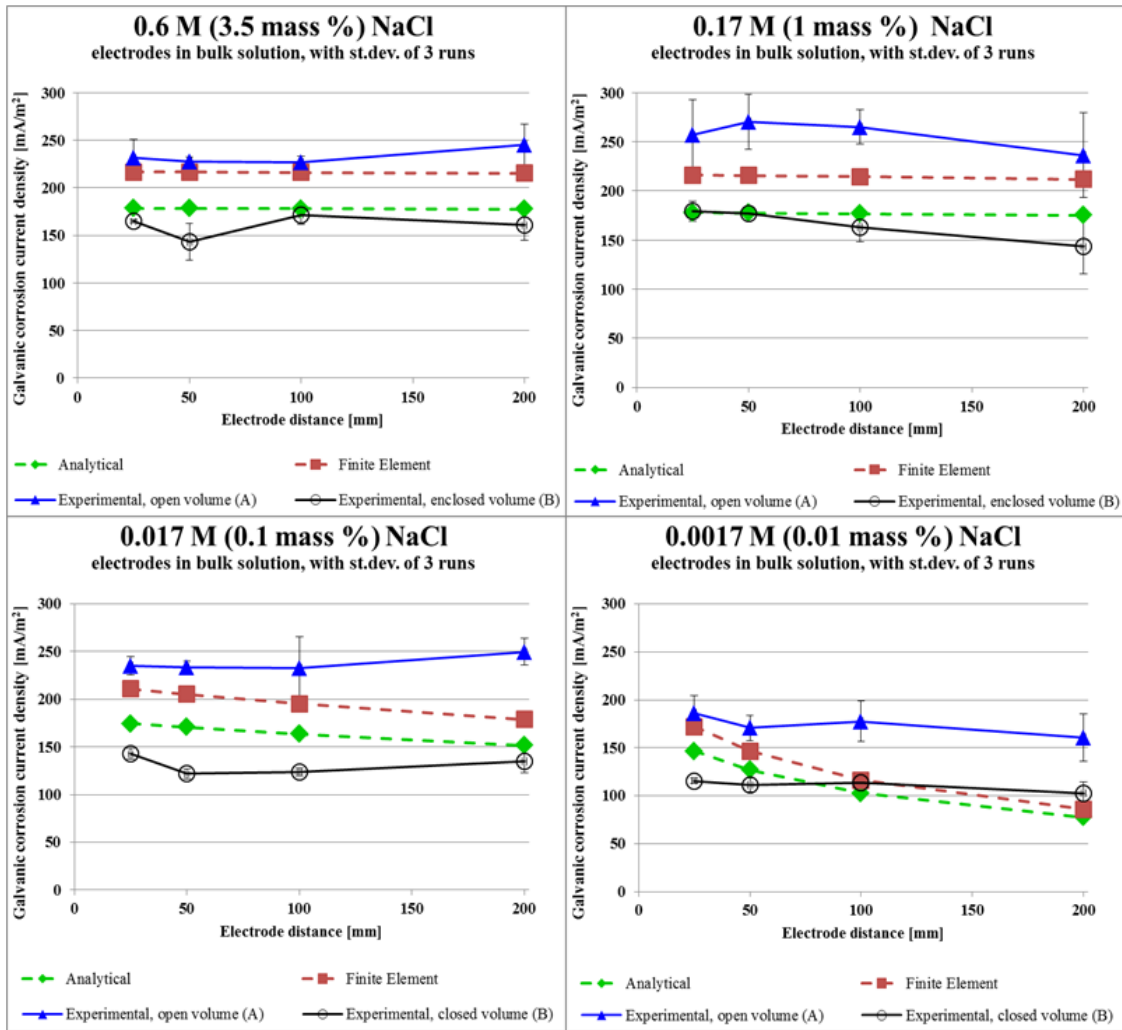


Figure 128: Comparison of analytical solution, finite element model, and experimental measurements for each NaCl concentration.

The sixteen charts above are all plotted on the same scale, and the agreement is quite good. The trends in the two numerical models are the same, but the values from the FE model are consistently higher than from the analytical solution. The difference is 11 to 21 %, with an average difference of 19 % and a median difference of 21 %. The two models are based on the same fundamental assumptions, but the FE model uses a more

sophisticated method of calculating the potential distribution and IR drop, which results in slightly higher values for the corrosion current density.

The experimental results straddle the results from the two numerical models. Validation model A with an open electrolyte volume generated generally higher corrosion current densities than the two numerical models, while validation model B with an enclosed electrolyte volume typically generated lower corrosion current densities. The results for the enclosed volume were on average 37 % lower than for the open electrolyte volume.

The general trend with lower corrosion rate in the enclosed volume indicates that ion mobility is important in the control mechanisms. Figure 129 contains representative measurements from both case A and B. The generally higher galvanic corrosion rates and more volatile nature of the corrosion current with the open electrolyte volume indicate that the open electrolyte volume affects the galvanic corrosion rate. The most likely way that the open electrolyte volume would affect the corrosion rate is by allowing for transfer of reactants or reaction products, or both, to the bulk electrolyte. This agrees with previous results that indicated that the galvanic corrosion reaction rate between aluminum and carbon in an immersed environment is highly dependent on the mass transport of reactants and reaction products. In both configurations, the highest experimental values can be found for the 0.17 M (1 mass %) NaCl electrolyte. This can likely be attributed to a combination of high conductivity and high level of dissolved oxygen. With mass transport appearing to be the most dominant control mechanism, a high level of dissolved oxygen (which is consumed in the cathodic reaction) should result in an increased

galvanic corrosion rate. This is confirmed in Figure 128 which shows consistently high galvanic corrosion rates for the 0.17 M NaCl electrolyte.

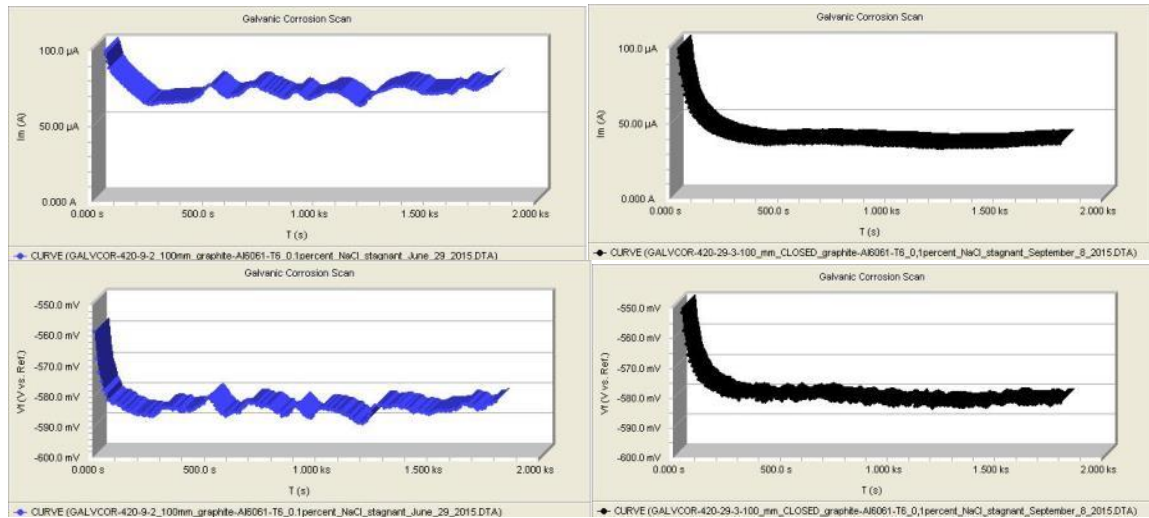


Figure 129: Open electrolyte volume vs. enclosed electrolyte volume. Representative experimental curves as a function of time for galvanic corrosion current and corrosion potential of the aluminum (versus Ag/AgCl reference electrode) for open electrolyte volume (left) and enclosed electrolyte volume (right). Electrode distance: 100 mm; electrolyte: 0.017 M (0.1 mass %) NaCl; exposed area: 300 mm²; duration: 30 minutes. Note that the data for the corrosion current is not normalized for the exposed area.

The main reason that the FE model and analytical model agree fairly well with the closed volume validation model can be found in the input data and assumptions for these models. The data for electrode kinetics was obtained in oxygen-rich, stagnant electrolyte, which is the same condition as for the validation model with the enclosed volume. With the electrolyte being enclosed and stagnant, the mass transport limitations are already accounted for in the electrode kinetics. However, these presented models are only representative for stagnant environments.

The importance of mass transport is also evident in Figure 130. The open or closed volume affects the corrosion current density to a much greater extent than the

electrolyte conductivity or the electrode distance. This suggests that the most important control mechanism in the immersed galvanic corrosion between aluminum and graphite is mass transport of reactants, reaction products, or both, but not resistance. Additional evidence for this hypothesis is that the test setup was very sensitive to agitation of the electrolyte. Any motion of the electrolyte caused an immediate increase in corrosion current. This type of control mechanism is known as *diffusion control*.

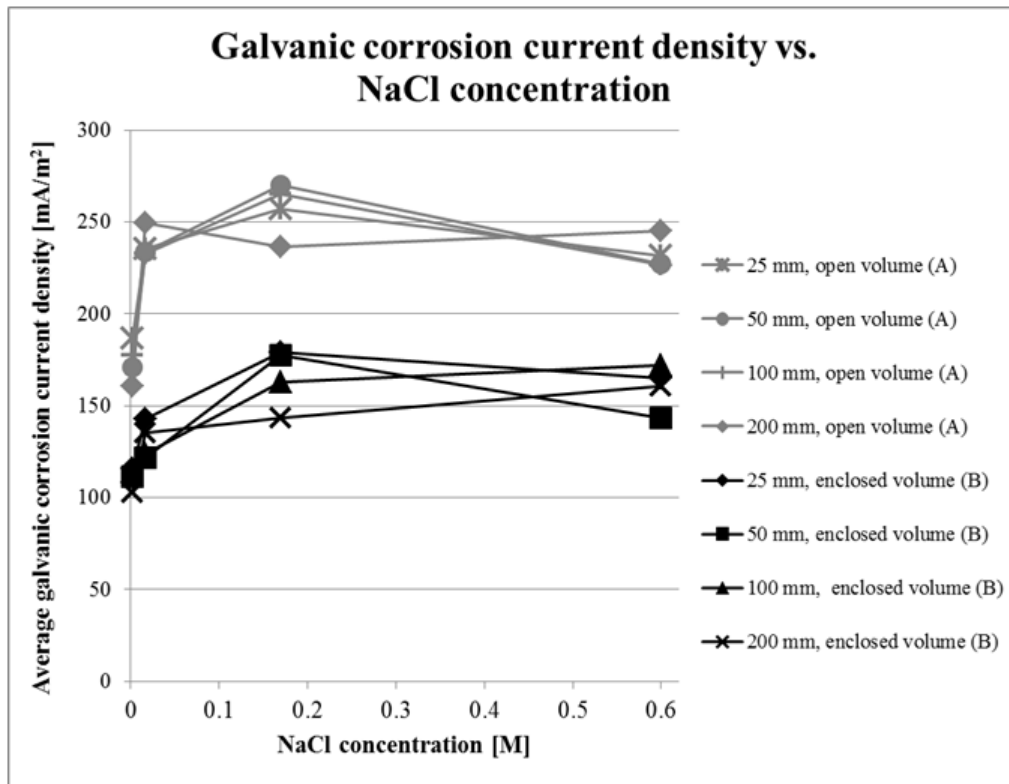


Figure 130: Comparison of analytical solution, finite element model, and experimental measurements for each NaCl concentration.

6.5 Chapter conclusions

This work has shown that a commercial software package can be used to quickly generate models with good agreement with experimental measurements. Simple geometries can also be solved manually through iteration. However, it is important to understand the mechanistic nature of models based on a few electrode kinetics input variables. The models may only be valid when the physical conditions are very close to the conditions used when the input data was obtained. It is also important to understand the control mechanisms because that will reveal which variables that highly affect the results and which will not. It was shown in the previous chapter that relatively small changes in the electrolyte agitation and in sample geometry can affect the galvanic corrosion rate with orders of magnitude due to changes in the oxygen transport. The parallel plate models showed that the electrolyte conductivity plays a much less important role than the oxygen transport. This agrees well with previous observations.

CHAPTER SEVEN: NUMERICAL MODELING OF ATMOSPHERIC GALVANIC CORROSION

The focus in this chapter is the ACCC transmission line conductor presented in chapter 1. It has a core of PMC that carries the mechanical load. The core is surrounded by helically wound aluminum strands, which carry the electrical current. The core has a center of unidirectional carbon fiber reinforced polymer (CFRP) and an outer layer of unidirectional fiberglass composite that serves as a galvanic corrosion barrier.

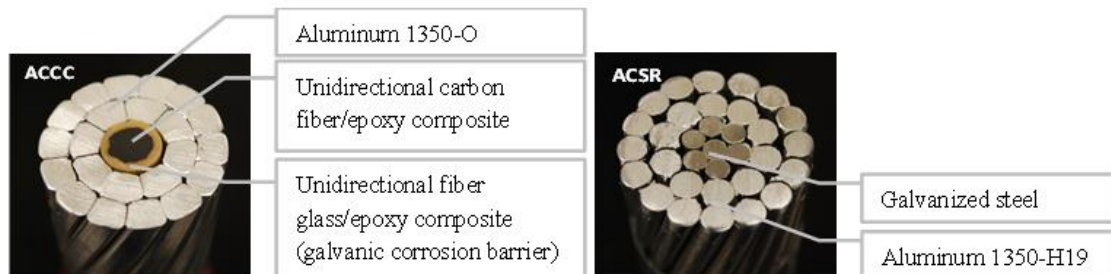


Figure 1 (repeated): ACCC vs. ACSR.

Left) ACCC conductor with a hybrid composite core with fully annealed aluminum strands.

Right) Conventional conductor with galvanized steel wires surrounded by hard drawn aluminum strands.

The fiberglass barrier can be damaged by, for example, over-bending, impact, fatigue (Burks, Armentrout et al. 2011), or aging (Hoffman, Middleton et al. 2015). If the conductor is bent to a too small radius, or subjected to severe low-velocity impact, the composite core may fail as in Figure 2 (repeated below). It is possible that an installation crew would simply trim off the damaged section and re-splice the conductor, not noticing

the crack along the centerline extending into the conductor core. The crack could potentially grow through Aeolian vibrations resulting in a large area of exposed CFRP. Fatigue may also be the source of a crack, as shown in Figure 3 (repeated below).



Figure 2 (repeated): Laboratory induced damage through low-velocity impact. The composite core fails in shear resulting in a long crack extending into the conductor. Photo courtesy of Daniel Waters.



Figure 3 (repeated): Cracks in the ACCC conductor corrosion barrier caused by Aeolian vibrations (high cycle fatigue) (Burks, Armentrout et al. 2011).

Numerical modeling is important for the understanding and prediction of galvanic corrosion. This chapter presents two numerical models that were developed in this study

for the quantitative prediction of the galvanic corrosion rate between aluminum and CFRP in the presence of an electrolyte under atmospheric conditions. The first model assumes a steady-state situation while the second model is time-dependent.

Both models have focused on one type of damage to the conductor: a split in the composite core along the centerline (Figure 79, repeated below), simulating potential damage caused by over-bending or low-velocity impact. This damage results in a large exposed area of the CFRP. The development of a physical sample design mimicking this type of damage was presented in chapter 3.

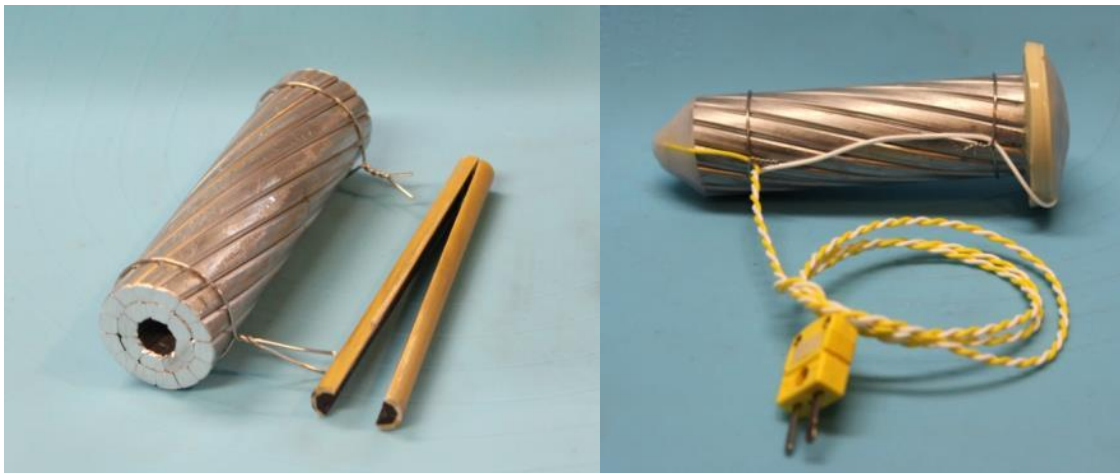


Figure 79 (repeated): Left) Damage introduced by splitting the composite core along the centerline. Right) Finished sample of ACCC with simulated damage.

7.1 Steady-state finite element modeling of atmospheric galvanic corrosion

7.1.1 Model geometry and reactions

In order to generate accurate results, the model geometry must be representative of the system being analyzed; although it typically needs to be simplified. This case is no exception. The relatively complex 3D geometry of the damaged conductor was simplified to a two-dimensional model (Figure 131). The model was simplified further by modelling only $\frac{1}{4}$ of the conductor; an approach that is common with symmetrical objects. This results in a two-dimensional geometry containing aluminium, the fiberglass barrier, and the exposed CFRP. The width of the modelled CFRP (3.5 mm) is half the diameter of the CFRP section of the core and the barrier width (1.5 mm) is the thickness of the fiberglass barrier.

The effective length of the aluminum was calculated in two different ways, as illustrated in Figure 131. Model a) is using the shortest possible path length through the strands, which gives an aluminum electrode length of 10 mm. It gives an area ratio of $\sim 1:3$ (CFRP:aluminum). In model b), the interfacial lengths (the red dotted lengths) are tied to $\frac{1}{4}$ of the exposed CFRP. With this approach, the aluminum electrode length would be 98 mm to reflect the 1:28 area ratio between the CFRP and the aluminum in the ACCC conductor with simulated impact damage. Because it is of great interest to understand the effect of the area ratios, both of these models will be used and the results will be compared.

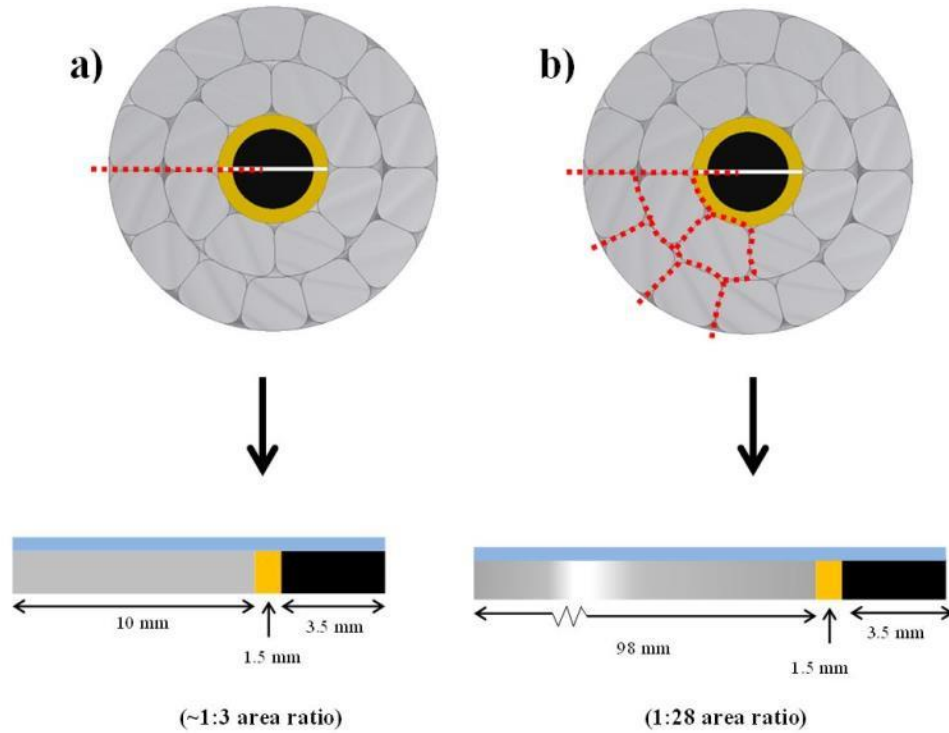


Figure 131: Two ways of creating a 2D model from a 3D structure.

A thin film of electrolyte will be modeled to span the three materials. The thickness of the electrolyte layer is a function of salt load density and the relative humidity (RH) of the surrounding air, using the expressions derived earlier in chapter 5. Figure 132 illustrates the model geometry. The chemical reactions will be modeled using the parameters discussed in chapter 4. The chemical reactions are illustrated in Figure 133.

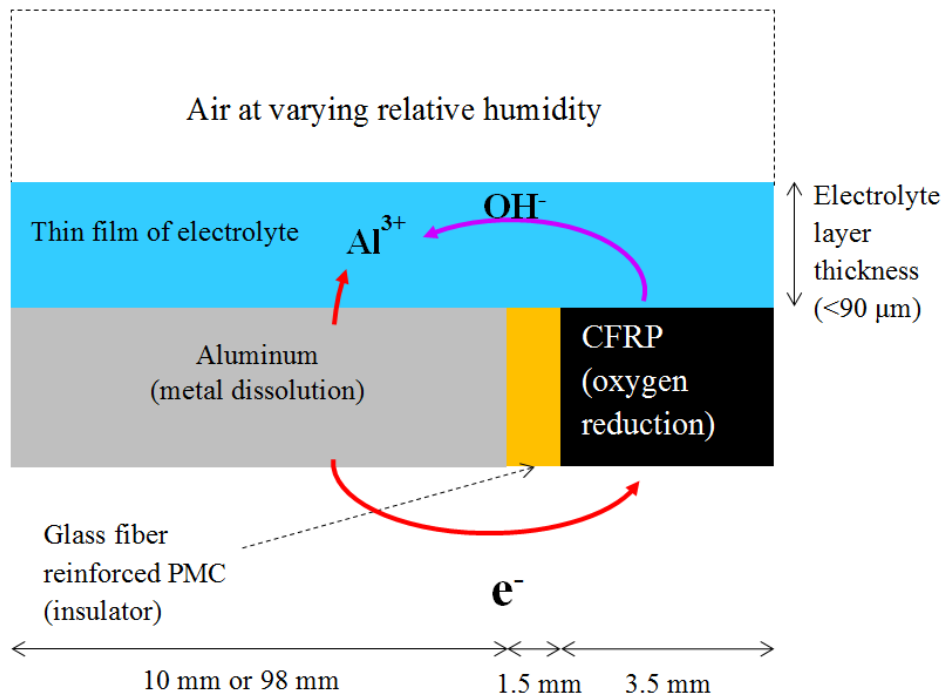


Figure 132: Model geometry.

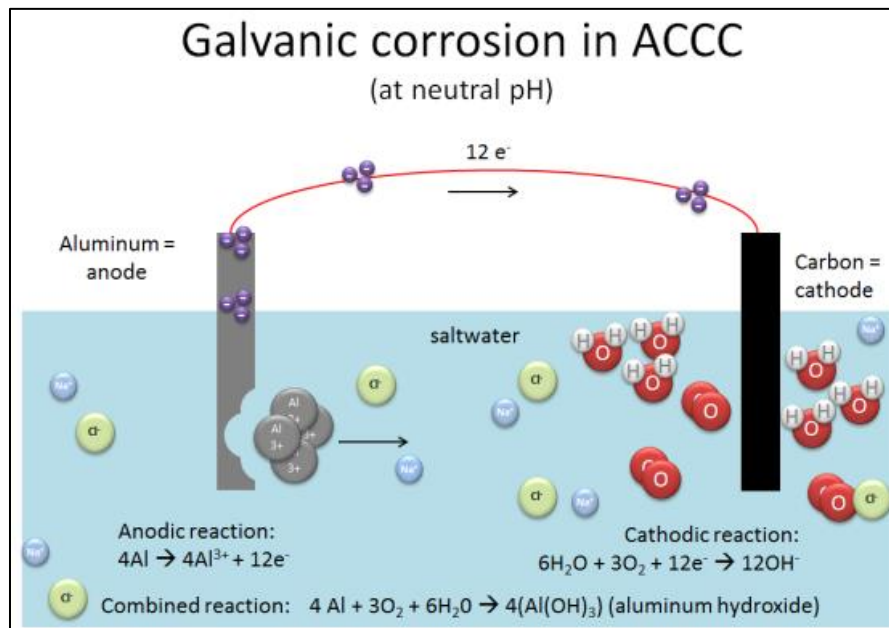


Figure 133: Illustrations of the chemical reactions taking place on anode and cathode.
 From (Håkansson 2013).

It was also assumed that:

- 1) The thin film of electrolyte is in equilibrium with the surrounding air.
- 2) The electrolyte film is uniform both in thickness and concentration.
- 3) The reactions are at steady-state.
- 4) The anodic reaction is metal oxidation ($\text{Al (s)} \rightarrow \text{Al}^{3+} + 3\text{e}^-$) and the cathodic reaction is oxygen reduction ($\text{O}_2 \text{(g)} + 2\text{H}_2\text{O (l)} + 4\text{e}^- \rightarrow 4\text{OH}^-$), resulting in the formation of aluminium hydroxide as the corrosion product ($4\text{Al (s)} + 3\text{O}_2 \text{(g)} + 6\text{H}_2\text{O (l)} \rightarrow 4\text{Al(OH)}_3 \text{(s)}$).

Secondary current distribution was chosen as the ‘study physics’, which assumes that the reaction rate is not limited by mass transport. However, the diffusion of oxygen is incorporated in the equation for the *theoretical maximum cathodic corrosion current* (i_{lim}), which makes the model indirectly incorporate a mass transport limitation.

7.1.2 Comsol model geometry and boundary conditions

The Comsol model was built as three rectangles representing the three *areas of electrolyte* spanning the three different materials (Al, CFRP, and the fiberglass barrier). The rectangles do not represent the materials themselves. Instead, the material properties and the reaction kinetics are represented by the electrode-electrolyte boundary interfaces. The two half-cell reactions and their characteristics are defined in by their equilibrium potentials, Tafel slopes and exchange current densities. The input data for Tafel slopes, exchange current density, and equilibrium potentials were obtained through potentiodynamic polarization scans of the individual conductor materials in 0.6 M NaCl aqueous solution at room temperature (RT). The experimental procedure for obtaining the input data was described in chapter 4, and the input values are found in table 1. Both half-cell reactions are assumed to follow Tafel behavior.

Figure 134 and Figure 135 show the finished geometry. Note that the aspect ratio could not be kept in the figures because the electrolyte layer is only a tiny fraction (a few micrometers) compared to the length of the geometry. Boundary 2 (blue) is the anode and represents the dissolution of metal from the aluminum surface. Boundary 8 (gray) is the cathode and represents the reduction of oxygen on the CFRP surface. Corrosion damage is only occurring on the aluminum surface. The fiberglass barrier is defined as an insulator and does not participate in the process. All outer boundaries of the geometry except 2 and 8 are assumed to be insulated by applying a zero-flux boundary condition.

The rate and distribution of the corrosion attack on the corroding electrode is correlated to the electrochemical potential distribution within the electrolyte and the

reacting surfaces (Zhang 2011). The potential distribution is governed by the Fourier equation for a conductive medium (Munn and Devereux 1991). The galvanic corrosion rate is limited by i_{lim} , which is a function of the oxygen diffusion through the electrolyte layer (described in chapter 5). The thickness of the electrolyte layer is in turn a function of salt-load density and relative humidity, which also was developed in chapter 5.

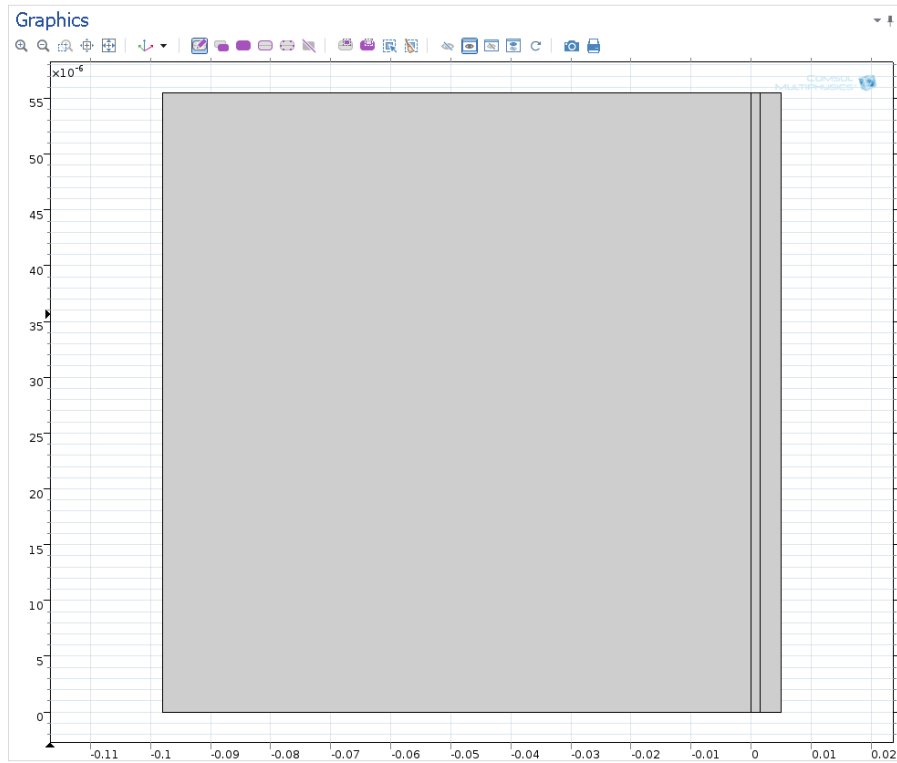


Figure 134: The finished geometry for the 1:28 area ratio (98 mm anode) as displayed in the Comsol user interface.

Units are in meters. Note that the figure is not to scale.

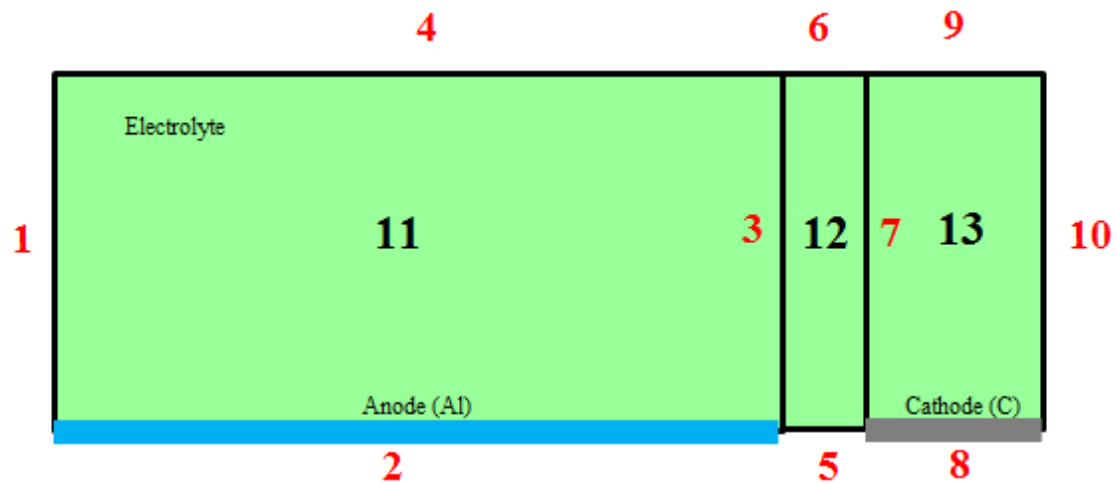


Figure 135: The finished geometry with boundaries (in red) and domains (in black). Electrolyte volume in green. Note that the figure is not to scale.

7.1.3 Electrolyte

The electrolyte is the same in all three domains. The electrolyte is only defined by its conductivity, which was set to a constant value of 24.4 S/m, as discussed in chapter 5. The electrolyte layer thickness is a function of relative humidity and salt load density. The expression for the electrolyte layer can be found in Table 18.

7.1.4 Current distribution

Secondary current distribution was chosen as ‘study physics’ (discussed in chapter 6). The secondary current distribution assumes that the reaction rate is not limited by mass transport rate. However, the diffusion of oxygen is incorporated in the i_{lim} equation, so there is a mass transport limitation integrated indirectly in this approach.

7.1.5 Global definitions and parameters

The parameters are used to define reactions, geometry, electrolyte properties etc. A summary of the parameters are found below.

**Table 18: Input values and functions for COMSOL
(formatted for Comsol)**

<u>Variable name</u>	<u>Variable</u>	<u>Function or value</u>	<u>Unit</u>
RH	Relative humidity	[varying from 0.8 to 1.0]	--
D_NaCl	Salt load density	[varying from 0.5 to 7.0]	g/m ²
E_cond	Electrolyte conductivity	24.4	S/m
d_film	Electrolyte layer thickness	D_NaCl*0.000000000215 *exp(0.000603*RH)	m
D_O2	Diffusion coeff. for O ₂ in the electrolyte at 20°C	1.97E-09	m ² /s
O2_solubility	Oxygen solubility in water	0.0003*exp(6.59*RH)	mol/m ³
Eeq_Al	Equilibrium potential, Al surface	-0.952	V
Eeq_C	Equilibrium potential, CFRP surface	-0.0605	V
ilim	Limiting current density based on oxygen diffusion through the electrolyte layer	D_O2*(O2_solubility)/(d_film * 0.00000259)	A/m ²
i0_Al	Exchange current density, Al surface	0.004232	A/m ²
i0_C	Exchange current density, CFRP surface	0.0547	A/m ²
Ac_C	Tafel slope, CFRP surface	-1.4949	V
Aa_C	Tafel slope, Al surface	0.1307	V

7.1.6 Average and maximum operators

The average and maximum corrosion currents can be displayed in the post-processing by using average and maximum operators. The operators are created using the function “Component couplings”. Average and maximum component couplings were added both to the anode and the cathode boundary.

7.1.7 Initial values

Initial values were added to shorten the number of iterative steps by the solver. The electrolyte potential in domains 12 and 13 were set to the negative equilibrium potential of the CFRP surface ($-E_{eq,C}$). The electrolyte in domain 11 was set to the negative equilibrium potential of the aluminum surface ($-E_{eq,Al}$).

7.1.8 Meshing

A so called *Mapped* meshing was used. Because the electrolyte layer thickness is so small compared to the length of the geometry, we can assume a negligible potential gradient through the thickness of the electrolyte. The meshing was therefore defined with only one element in the vertical direction. The mesh was defined so the element was very small close to the boundary interfaces and larger further away. Figure 144 shows the mesh zoomed in on the domain interfaces. The black area is where the mesh is so fine it cannot be seen at this zoom level.

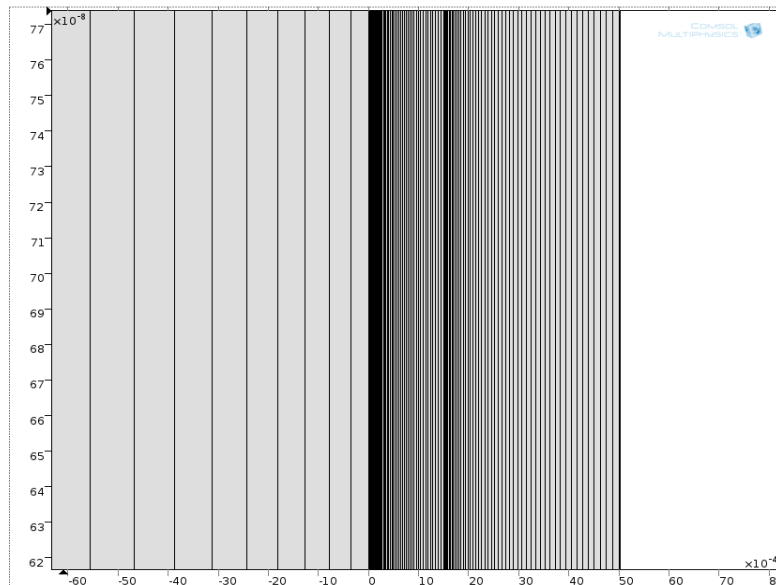


Figure 136: Mesh at the domain boundaries.

7.1.9 Parametric sweeps

The model was computed using two simultaneous parametric sweeps at RT. The salt load density was swept using the values 0.5, 1, 2, 3.1, and 7 g/m². The relative humidity was swept from 80 % to 98 % in 2 % increments.

7.1.10 Results: Comparison of 10 mm and 98 mm anode

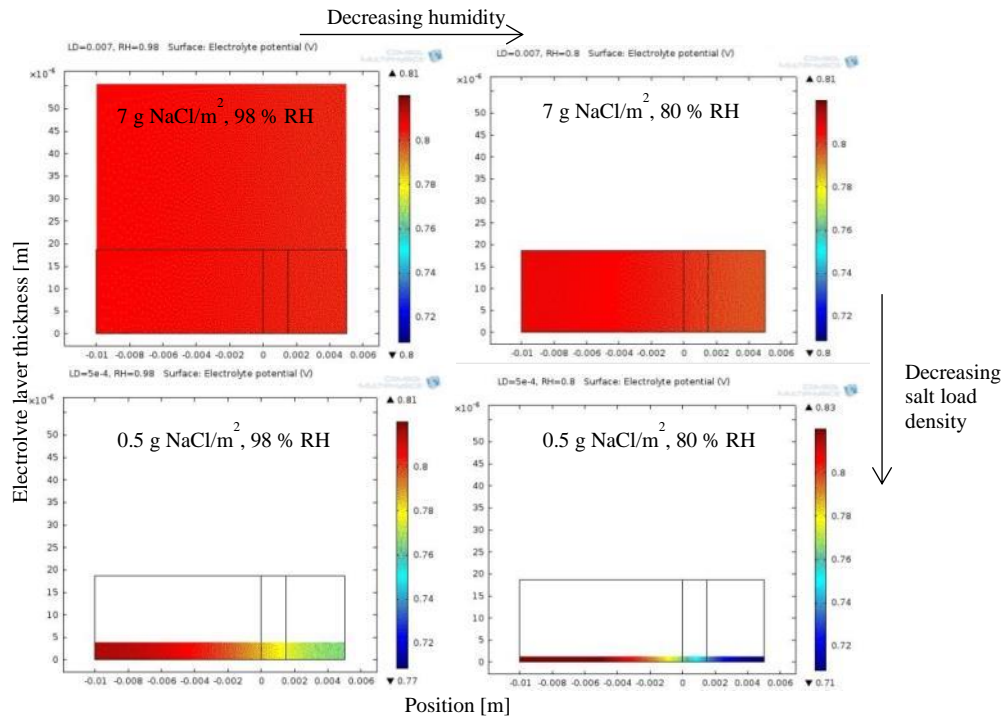
This section will present the results from the model and compare them to experimental measurements.

Potential distribution

One of the important questions in the development of the model was if the length of the aluminum electrode would affect the result. It is known that atmospheric galvanic corrosion acts locally due to the low conductivity of the electrolyte (Barton 1973), and it was suspected that the length of the aluminum electrode may have a minor influence on the results.

Figure 137 shows the potential distribution through the electrolyte for four different combinations of relative humidity (RH) and salt load density (LD): 7 g/m² and 98 % RH, 7 g/m² and 80 % RH, 0.5 g/m² and 98 % RH, and 0.5 g/m² and 80 % RH. The lowest salt load density and the lowest humidity result in the steepest potential gradient. This is expected because the thin electrolyte layer gives a high resistance and a high current limit, both resulting in a high potential drop. The potential drop over the length of the anode is larger with the 98 mm anode, which would be expected due to the longer distance, but the potential drop over the first 10 mm appears to be similar in Figure 137. Note that it appears that the electrolyte extends outside the domain, but this is only an artefact of changing the modeling parameters without re-building the model. It does not affect the results.

10 mm Al anode



98 mm Al anode

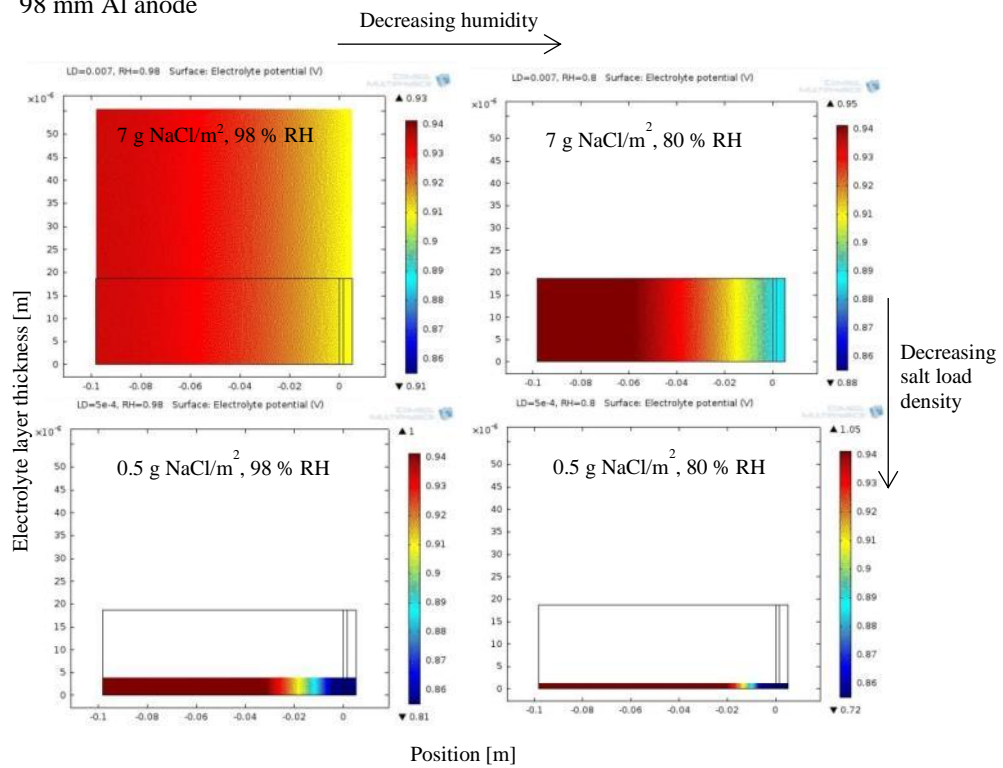


Figure 137: Potential distribution with different anode size, humidity, and salt load density.

Current density distribution

Inspection of the current density distribution supports the findings in previous section: the first 10 mm are very similar for both geometries (Figure 138). The highest anodic current density is just at the interface to the fiberglass barrier, and the difference between the two models is only approximately 30 %.

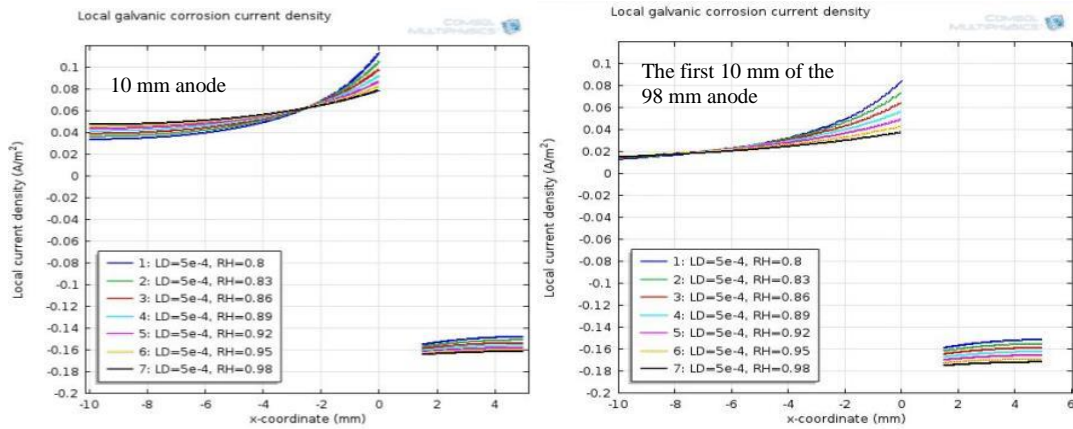


Figure 138: Local current density.
Left) 10 mm anode; Right) The first 10 mm of the 98 mm anode.

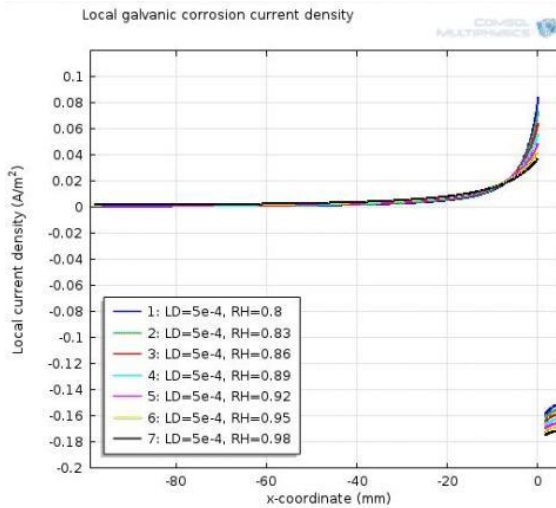


Figure 139: Current density with the 98 mm anode.

Maximum current density

The cathode areas in the two models are identical, and the maximum cathode current densities are within 12 % (Figure 140).

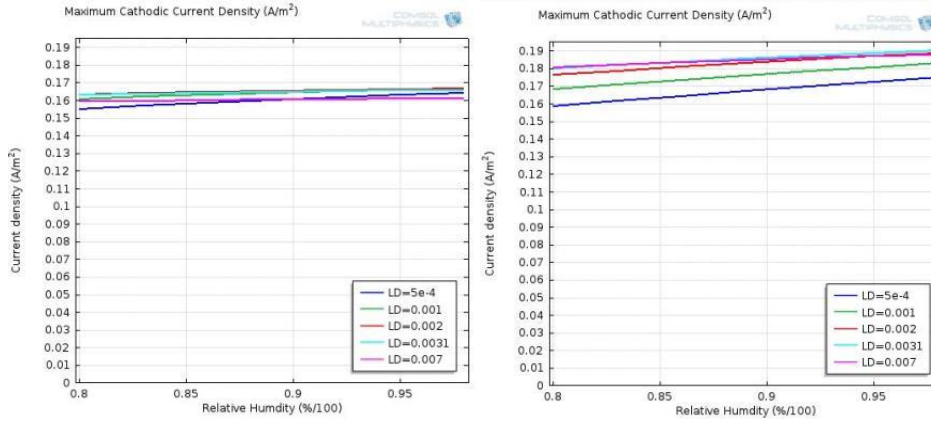


Figure 140: Maximum cathodic current density.
Left) 10 mm anode (model a); Right) 98 mm anode (model b).

Although the anode area in model b) is almost 10 times larger than in model a), the maximum local anode current densities were within 25 % (Figure 141). This supports the hypothesis that atmospheric galvanic corrosion is local and predominantly occurs close at the contact place between the two materials, mostly independent of the size of the anode.

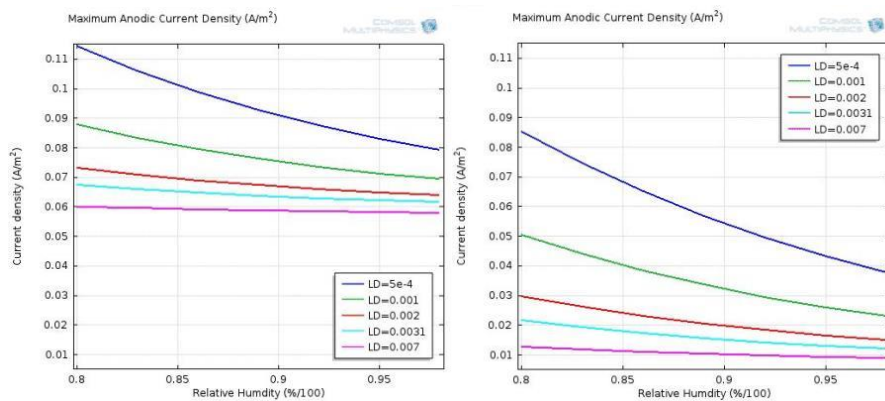


Figure 141: Maximum anodic current density.
Left) 10 mm anode (model a); Right) 98 mm anode (model b).

Average current densities

The average cathodic corrosion current densities show a very similar pattern to the maximum cathodic current densities (Figure 142). The similarities in the average cathodic corrosion current despite the 10-fold difference in anode size, supports the previous hypothesis that the corrosion process is under cathodic control. The limitation in the reaction rate for the cathode reaction limits the total galvanic corrosion rate. The variations in humidity and salt load density have a much greater effect on the total galvanic corrosion rate than the relative size of the anode, because the dominating control mechanism in the diffusion of oxygen through the electrolyte layer on the CFRP.

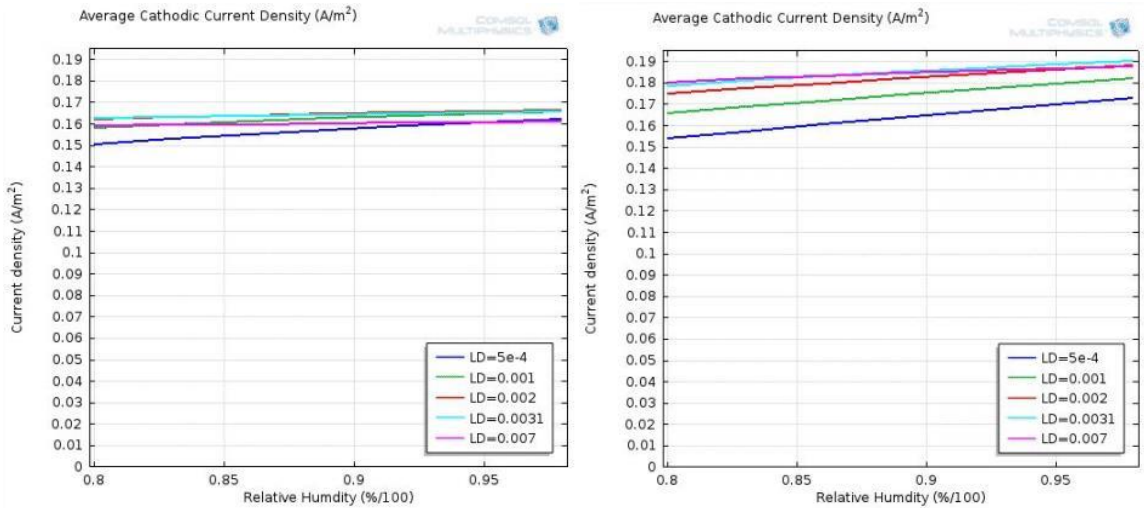


Figure 142: Average cathodic current density.
Left) 10 mm anode (model a); Right) 98 mm anode (model b).

The average anodic current density is a very different situation. The almost 10 times larger anode area in model b) results in an average anode current density that is only approximately 1/10th of model a). This points out an important feature of

atmospheric galvanic corrosion: the average current density may say very little about the local damage. The previous plots indicate that the local corrosion rate near the CFRP is approximately the same for both model a) and model b). The average anode current density would highly underestimate the local corrosion damage.

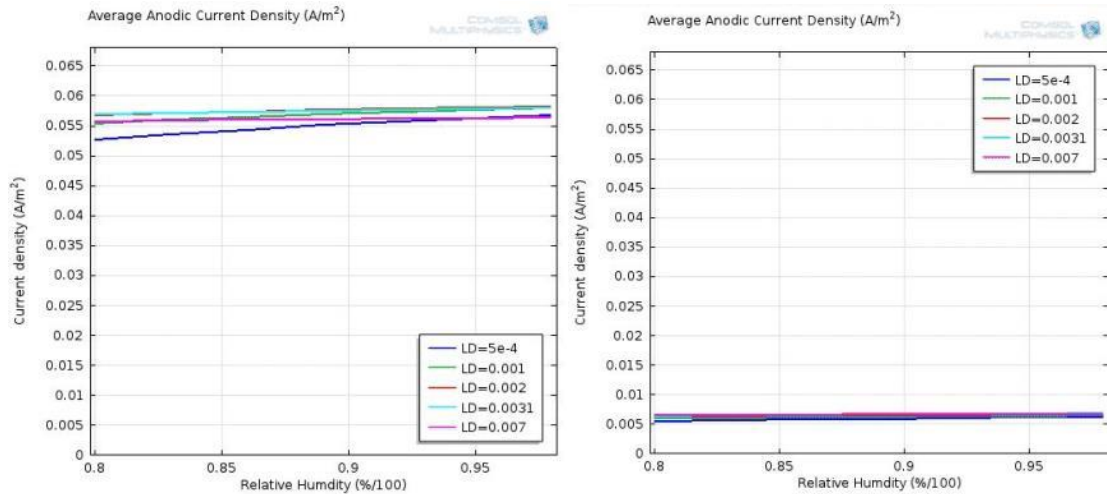


Figure 143: Average anodic current density.
 Left) 10 mm anode (model a); Right) 98 mm anode (model b).

The conclusion from the comparison of the 10 mm and 98 mm anode is that the results from the area close to the interface between Al and CFRP are similar, but the average anodic corrosion rates are widely different. This supports the earlier observations that the galvanic corrosion is under cathodic control. It also supports the existing knowledge that atmospheric galvanic corrosion is mainly localized close to the cathode (Barton 1973).

Although both the 10 mm and the 98 mm anode model can be considered fairly good representations of the damaged ACCC conductor, the 98 mm anode model was chosen for the remainder of this section.

7.1.11 Discussion

A further analysis of the data reveals that increased relative humidity results in reduced corrosion at the interface, but the more widespread corrosion increases the total corrosion rate. The increased local corrosion current density is most apparent with the lowest salt load density (0.5 g NaCl/m^2), which is shown in Figure 144.

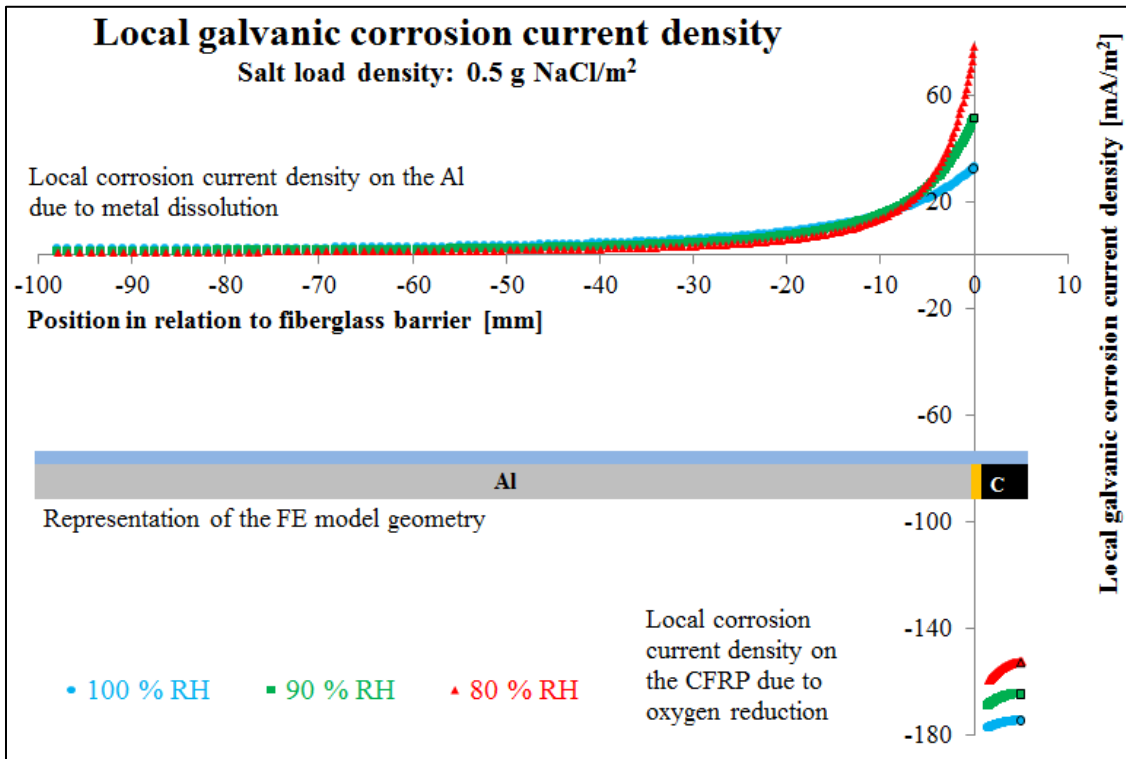


Figure 144: Local corrosion current density for a salt load density of 0.5 g NaCl/m^2

Figure 144 shows the general trend of increased total galvanic corrosion rate (best seen by comparing the local current density) with increased humidity and increased salt load density. This trend is present for all salt load densities in the parametric sweep except the highest (7 g NaCl/m^2). Figure 145 illustrates the relation for additional salt load densities.

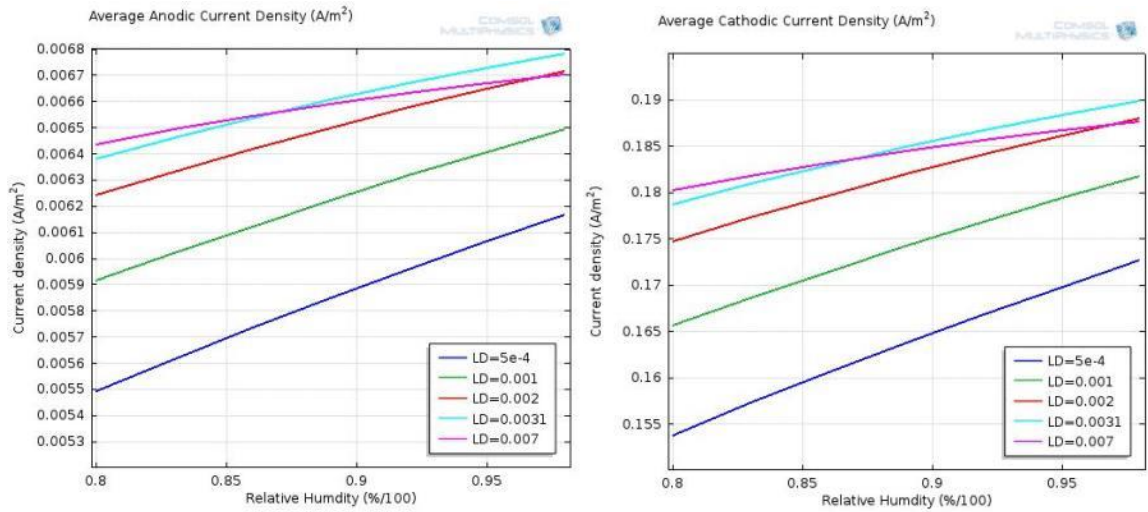


Figure 145: Average anodic and cathodic galvanic corrosion current densities (model b, 98 mm anode). Note that LD represents as D_{NaCl} (salt load density) in the Comsol interface.

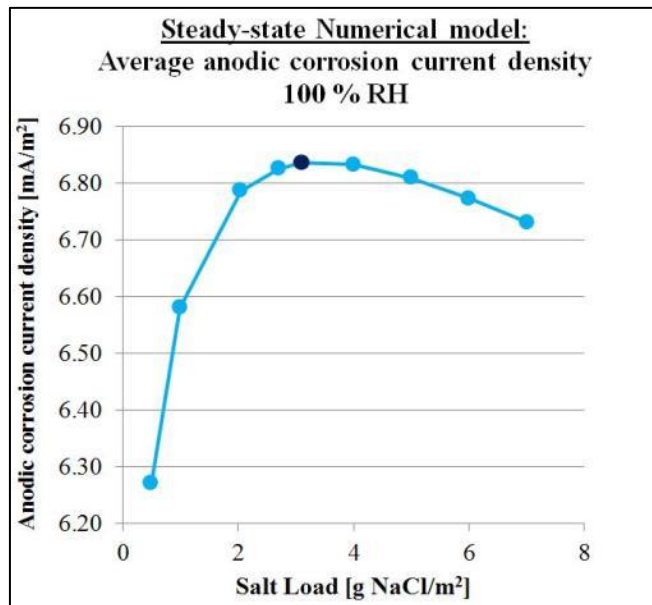


Figure 146: Average anodic corrosion current density as a function of salt load density at 100 % RH (model b, 98 mm anode). The dark marker illustrates the salt load density of 3.1 g/m^2 that is discussed further below.

The highest galvanic corrosion rate is predicted at approximately 3.1 g NaCl/m^2 .

This is also the salt load density in the experimental validation model that will be

presented in the next section. The trend indicates that there may be a shift in control mechanism at really high salt load densities. At low salt load density, the electrolyte layer is very thin and the main limiting mechanism is the high resistance of the electrolyte. At high salt load density, the electrolyte layer is thick and the main limiting mechanism is the diffusion of oxygen through the electrolyte layer. In the extreme case of immersion of the sample, the galvanic corrosion rate is lower than in atmospheric conditions, which has been shown in previous chapters and will be revisited in the next sections.

7.1.12 Comparison with experimental measurements

Experimental measurements were performed to validate the numerical model. Ten samples of ACCC with damaged corrosion barriers were prepared as described in chapter 3. For five of the samples, the aluminum strands were treated with the commercial aluminum cleaning product named AlumaPrep that contains phosphoric acid. This removed all scale, thick aluminum oxide, and grease from the aluminum strands before the sample was assembled again. These samples are called “Acid Prep” in subsequent sections. The aluminum strands for the other five samples were only cleaned with isopropyl alcohol. These samples are called “As Received”.

The ten samples were immersed in 0.6 M NaCl aqueous solution. A light vacuum was applied to ensure full penetration. This resulted in an average salt load density of 3.1 g NaCl/m². The samples were dried for 24 hours, and then subjected to 100 % RH at RT.



Figure 147: Validation samples in the humidity chamber.

The galvanic corrosion rates during the first day were excluded from the averages to allow sufficient time for the NaCl to deliquesce and for the corrosion to initiate (Figure 148). The average for days 2-5 was 10.1 mA/m^2 ($\sigma=1.7$) for the Acid Prep samples and 5.5 mA/m^2 ($\sigma=1.1$) for the As Received samples (expressed as anodic galvanic corrosion current density).

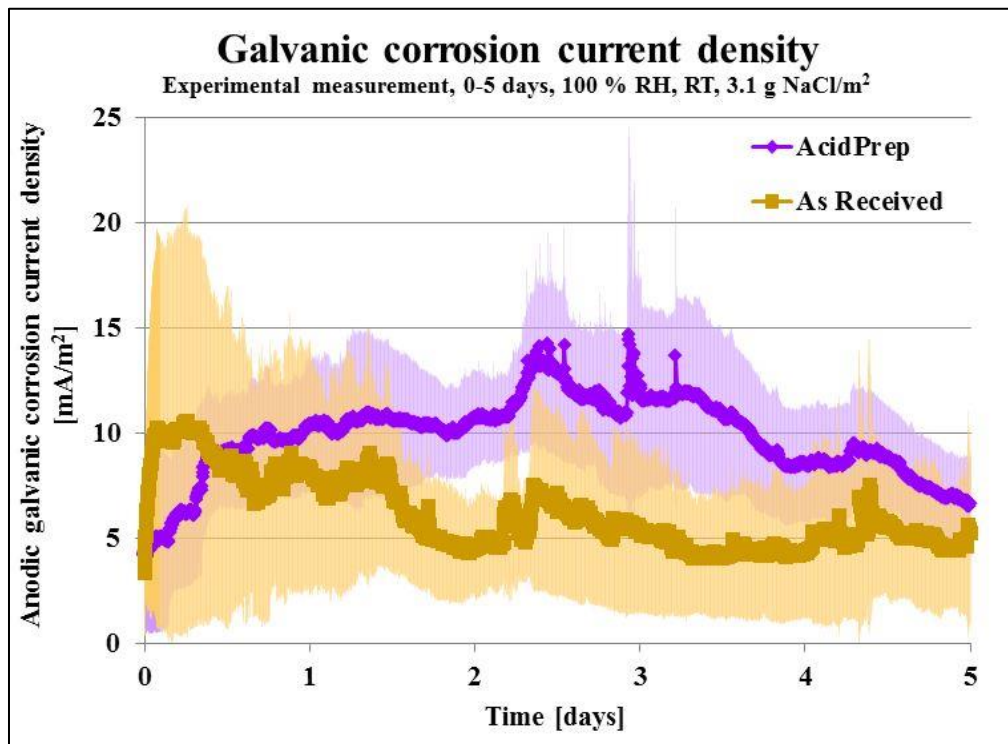


Figure 148: Averages for anodic galvanic corrosion current densities for days 0 to 5. The error bars represent one standard deviation.

The steady-state model generates an anodic galvanic corrosion current density of 6.8 mA/m^2 Figure 146 for the same conditions as used in the experimental measurements. Figure 149 shows that there is a fairly good agreement between the experimental measurements and the numerical model.

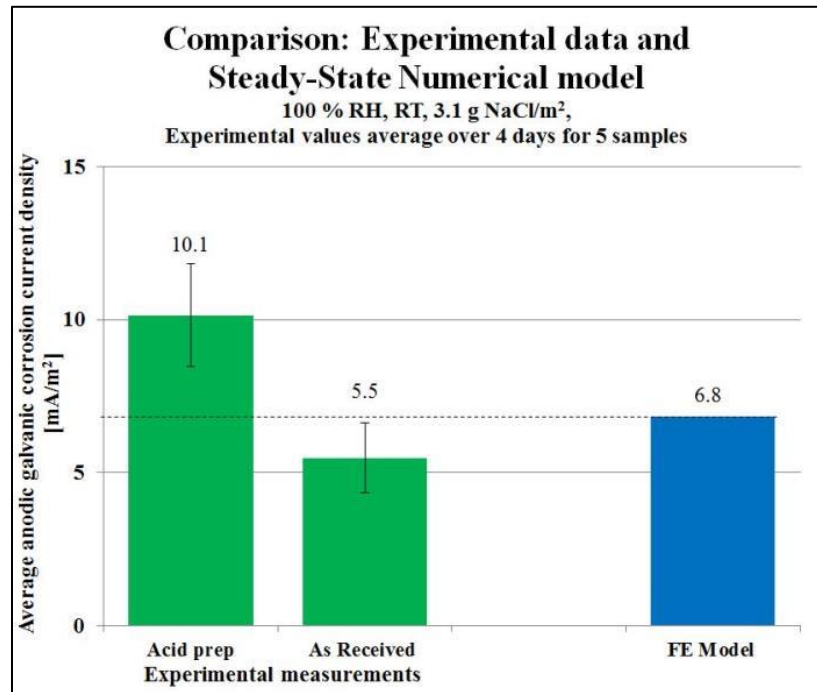


Figure 149: Comparison of experimental data and steady-state numerical model

The FE model described in this work is the first numerical model of galvanic corrosion in an ACCC conductor with a compromised galvanic corrosion barrier. The results from the model agree well with the laboratory measurements. The model shows that the galvanic corrosion in atmospheric conditions is localized near the interface of the two reacting materials. The galvanic corrosion is highly localized at low salt load densities, and becomes more evenly distributed over the aluminium surface at higher salt load densities and higher RH levels. The model has also shown that for higher salt load densities and higher humidity levels the total galvanic corrosion rate increases, but the effect is not linear. At very high salt load densities, the total galvanic corrosion rate decreases, which is believed to be due to the restricted oxygen diffusion through the electrolyte layer.

7.2 Time-dependent numerical model of atmospheric galvanic corrosion

While the numerical model presented in the previous section agrees with short-term validation measurements, it cannot explain the long-term decrease in galvanic corrosion current shown in Figure 150. The average from day 2 through 5 were used to validate the steady-state model presented in previous section, but beyond the first few days, the galvanic corrosion rates drops rapidly for both sample groups.

The average anodic galvanic corrosion current density for day 22 through 62 was 0.26 ($\sigma=0.09$) mA/m^2 for the As Received samples and 0.28 ($\sigma=0.11$) mA/m^2 for the Acid Prep samples. The values for day 22 through 62 are similar to the values measured for the same sample design in immersed environments: 0.63 mA/m^2 for stagnant electrolyte and 0.73 mA/m^2 in agitated electrolyte (see chapter 3).

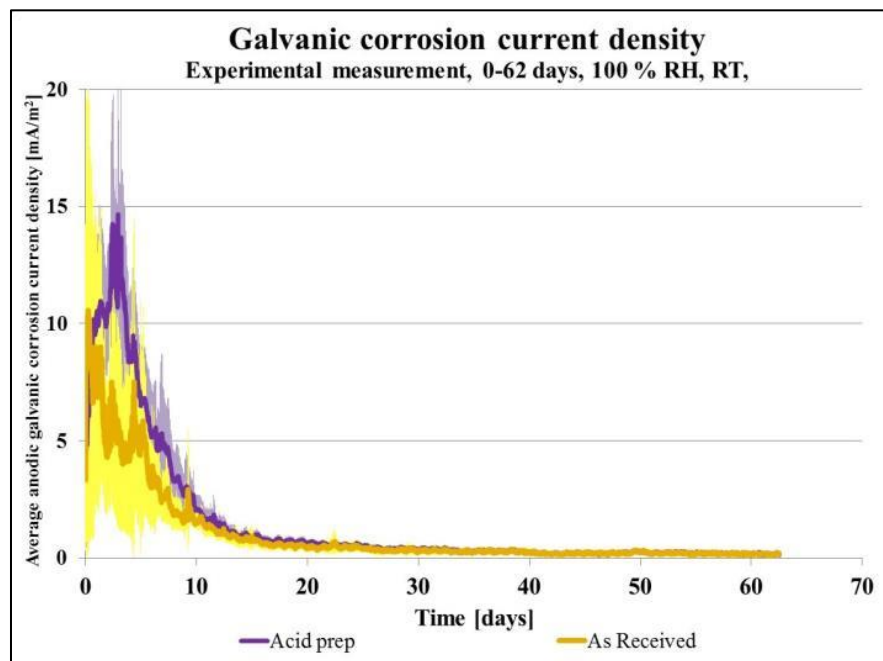


Figure 150: Average galvanic corrosion current for two sets of five samples in 100 % RH. The error bars show one standard deviation.

It was determined in chapter 4 and 5 that the galvanic corrosion in damaged ACCC samples appears to be mainly controlled by the transport of oxygen to the cathode (the exposed CFRP surface). The much faster diffusion of oxygen through air would explain why higher galvanic corrosion rates were measured in humid environments than in immersed environments. It would also explain why really high galvanic corrosion rates could occur for a short time during the drying of a sample when a continuous air path existed into the sample, but it was still wet enough for ion conduction between the cathode and anode. This was illustrated in Figure 87 (repeated below).

The build-up of corrosion products between the aluminum strands appears to cause an effect similar to immersion. The hypothesis that the buildup of $\text{Al}(\text{OH})_3$ gel will restrict the diffusion of oxygen to the cathode and thus limit the galvanic corrosion rate will be explored in this section.

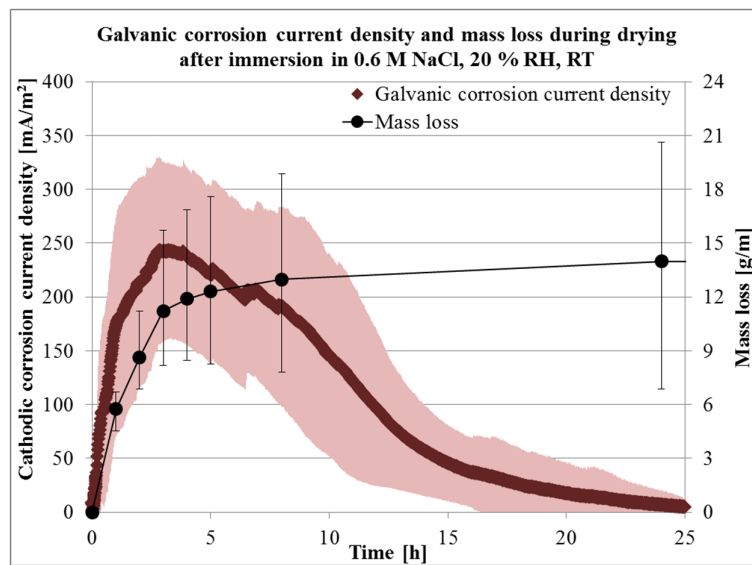


Figure 87 (repeated): Galvanic corrosion rate vs. mass loss during drying of an ACCC sample with compromised corrosion barrier after immersion in 0.6 M NaCl solution. Average for corrosion rate is for 18 samples and shaded region indicates one standard deviation. Average for mass loss is for five samples and error bars display the spread within the group.

7.2.1 Galvanic corrosion knee-point and formation of $\text{Al}(\text{OH})_3$ gel

Figure 151 shows both the average anodic galvanic corrosion current densities and the cumulative galvanic corrosion charge (expressed as mAh). There is a knee-point approximately at day 13 where the galvanic corrosion current levels out. At that point, the Acid Prep samples had an average cumulative galvanic corrosion charge of 539 mAh (1940 C) per meter of conductor and the As Received samples had an average of 342 mAh (1230 C) per meter of conductor.

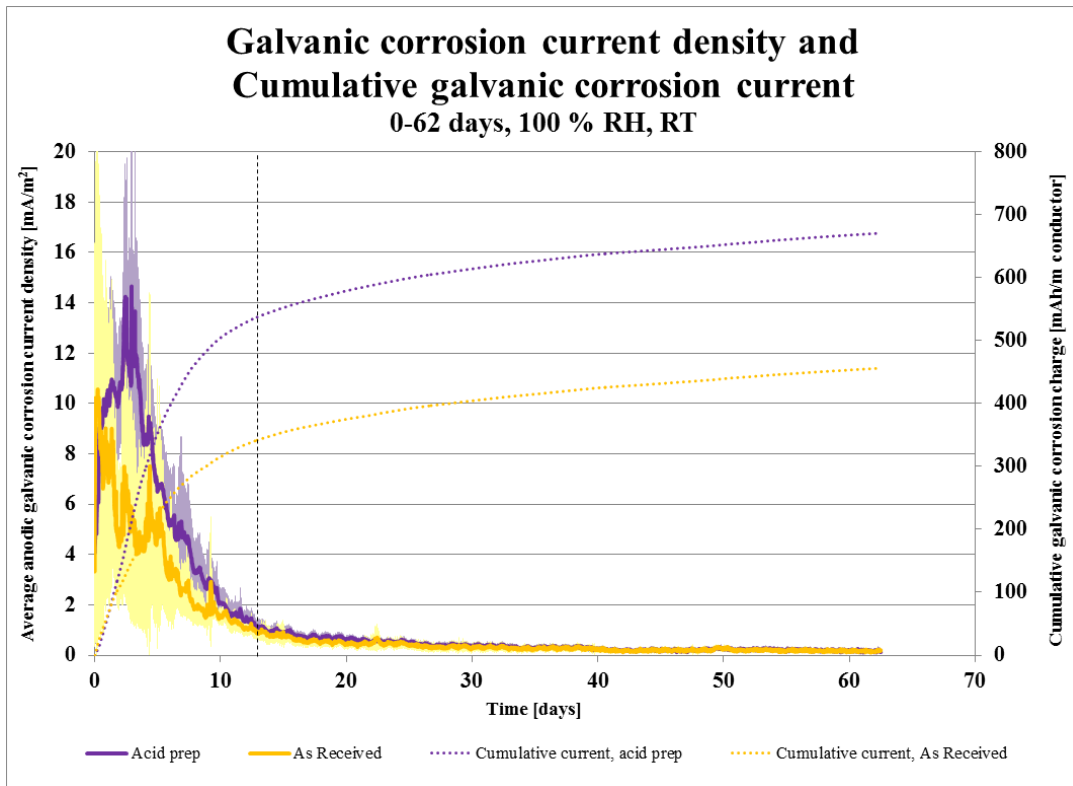


Figure 151: Average galvanic corrosion current for two sets of five samples in 100 % RH and the cumulative galvanic corrosion charge per meter of conductor. The shaded areas represent one standard deviation in the measurements.

Using Faraday's law (2.2.3-1, repeated below with values for aluminum), 0.180 g of aluminum per meter of conductor had to be lost to corrosion to generate the

cumulative galvanic corrosion charge of 539 mAh in the Acid Prep samples. 0.114 g was lost to generate the 342 mAh of cumulative charge in the As Received samples.

$$m_{Al} = C_{Ah} \cdot \frac{1}{F} \cdot \frac{A_{Al}}{n_{Al}} \cdot 3600 \quad (7.2-1)$$

where

m_{Al} = mass loss of aluminum [g],

C_{Ah} = accumulated corrosion charge [Ah],

F = Faraday constant (96 485 C/mol),

A_{Al} = atomic mass of aluminum (27 g/mol),

n_{Al} = valency of aluminum [e^- /ion] (3),

3600 = number of seconds in 1 hour.

Assuming that all aluminum was transformed to $Al(OH)_3$, it would form 0.52 g and 0.34 g respectively of $Al(OH)_3$. Newly formed $Al(OH)_3$ precipitates as a gelatinous substance on the surface of the corroding sample. It will over time crystallize and if the humidity is low enough the gel will dry to a white powder or solid mass. However, at 100 % RH the $Al(OH)_3$ will remain in gel form for a long time.

Some of the gel was removed and its mass was measured before and after drying. The presence of air bubbles and solid particles, as well as the small volume and viscous texture made it difficult to perform an exact density measurement, but it was determined to be approximately 1 g/cm³. The gel had a mass that was 47.8 times higher than the dry $Al(OH)_3$, which gives a mass ratio of solid aluminum to $Al(OH)_3$ gel of 1:138. Assuming that all of the 0.18 g aluminum lost to galvanic corrosion per meter of conductor of the

Acid Prep samples (as calculated above) was transformed into $\text{Al}(\text{OH})_3$ gel, it would form 24.8 cm^3 of gel. The volume would be 15.7 cm^3 for the As Received samples.



Figure 152: $\text{Al}(\text{OH})_3$ gel formation on a coplanar aluminum-graphite couple. Left) Start; Right) Gel has formed on the aluminum.

With an average volume of the crevices inside the samples of 27.7 cm^3 per meter of conductor, it can be calculated that the crevices in the Acid Prep samples will be close to completely filled with $\text{Al}(\text{OH})_3$ gel after 13 days based on the cumulative charge in Figure 151. This is also consistent with the visual observations of gel protruding from the crevices in Figure 153.

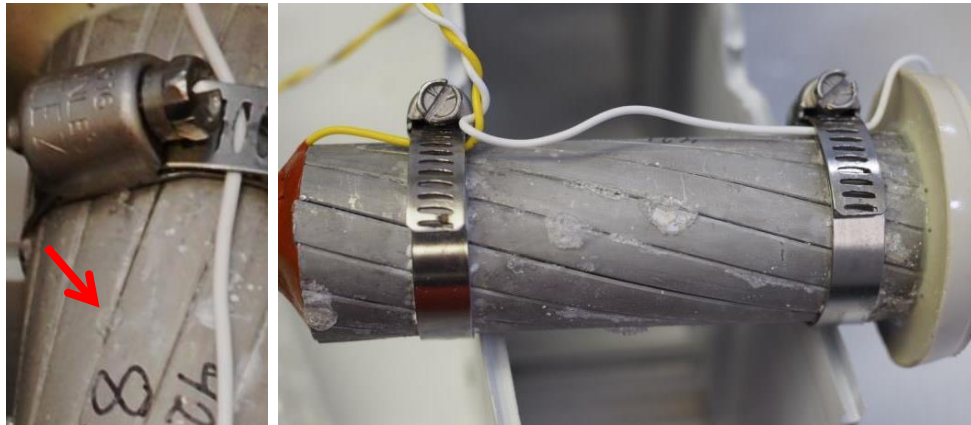


Figure 153: $\text{Al}(\text{OH})_3$ gel protruding from the crevices during corrosion testing. Left) Day 5, the first observation of $\text{Al}(\text{OH})_3$ protruding. Right) Day 62, just before the test was stopped. Large amounts of $\text{Al}(\text{OH})_3$ are visible on the outside of the sample, of which some has started to crystallize.

The gel volume formed in the As Received samples would not be large enough to fill the crevices. However, aluminum can also experience self-corrosion even when galvanic corrosion is present. The amount of self-corrosion could not be estimated in this test setup, but because the corrosion reactions and the corrosion products can be assumed to be the same as those of galvanic corrosion, the presence of self-corrosion would add to the deposition of $\text{Al}(\text{OH})_3$.

7.2.2 Assumptions for numerical model

The numerical model consists of two main components: the deposition of corrosion products generated from the galvanic corrosion and a mass transfer process. The two processes are directly linked to each other and therefore inseparable. The galvanic corrosion is generated by the mass transfer of oxygen from the air outside the sample to the CFRP. The galvanic corrosion in turn generates corrosion products, which deposit on the surface and limit the mass transfer of oxygen.

The fundamental assumptions are:

- 1) The galvanic corrosion rate is directly proportional to the mass transfer of oxygen to the CFRP from the surrounding environment.
- 2) There is only one cathodic reaction taking place: the reduction of oxygen.
$$\text{O}_2 (\text{gas}) + 2\text{H}_2\text{O} (\text{liquid}) + 4\text{e}^- \rightarrow 4\text{OH}^- \quad (7.2-2)$$
- 3) The cathodic reaction is taking place solely on the CFRP surface.

- 4) There is only one anodic reaction taking place: the dissolution of aluminum.



- 5) The only corrosion product is gelatinous Al(OH)_3 . The balanced reaction is: $4\text{Al} + 3\text{O}_2 + 6\text{H}_2\text{O} \rightarrow 4\text{Al(OH)}_3$ (7.2-4)

- 6) The self-corrosion rate is zero.
- 7) The diffusion coefficient for oxygen through the Al(OH)_3 gel is assumed to be the same as for water ($1.97\text{E-}9 \text{ m}^2/\text{s}$ (Giambattista, Richardson et al. 2004)) and does not change over time.
- 8) The oxygen does not react with anything else on the way to the CFRP surface.

7.2.3 Model geometry

The stranded geometry of the ACCC conductor with two layers of aluminum wires results in a fairly complex geometry. There are 14 strands in the outer layer and 8 in the inner layer, wound in an opposing helical pattern. Thus the oxygen diffuses through a maze of crevices where the effective cross sectional area gets smaller further towards the center of the conductor.

To simplify the complex geometry, the total volume of the crevices was combined into a rectangular block. The volume of the block is equal to the volume of all the crevices per meter of conductor (27.7 cm^3). The cross-sectional area of this simplified rectangular block is equal to the total opening of the crevices per meter of conductor. The

average crevice width was calculated to be 180 μm by measuring how much electrolyte was left inside the samples after immersion due to the capillary effect. With the 14 outer strands, an average crevice width of 180 μm , and a helical stranding, the total opening area is 0.0032 m^2 per meter of conductor. The length of the block would be 8.6 mm. This represents the maximum path length for the oxygen diffusion through the $\text{Al}(\text{OH})_3$ gel, which occurs when the crevices are completely full.

The formation of gelatinous $\text{Al}(\text{OH})_3$ due to the galvanic corrosion is assumed to take place at the aluminum edge closest to the CFRP cathode. It pushes outwards to fill up the crevice as the corrosion progresses. As the block grows, the diffusion path length gets longer. The diffusion path length is represented by Δx in Figure 154.

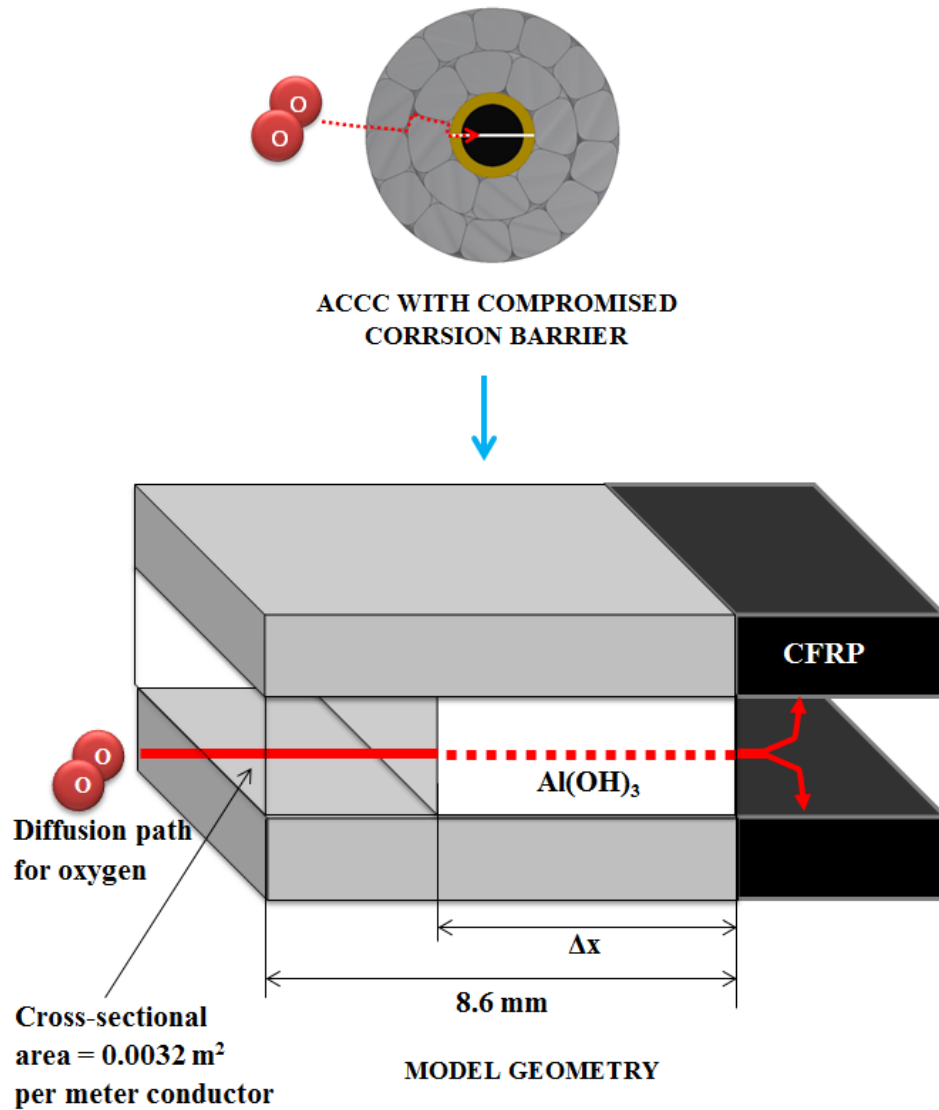


Figure 154: Model geometry.

7.2.4 Diffusion of oxygen through the corrosion products

The rate controlling mechanism in this model is solely the mass transport of oxygen through the gelatinous Al(OH)_3 to the CFRP surface, as illustrated in Figure 154. Because the gel consists mainly of water, the diffusion coefficient for oxygen through the Al(OH)_3 gel is assumed to be the same as for water ($1.97\text{E-}9 \text{ m}^2/\text{s}$) (Giambattista,

Richardson et al. 2004)). The concentration gradient of oxygen in the $\text{Al}(\text{OH})_3$ gel is assumed to be linear, and goes from 0.40 mol/m^3 (saturation level for water at sea level at 20°C (U.S.GeologicalSurvey 1998)) at the outer edge to zero at the inner edge.

Because the growth of the gel layer is so slow, the problem will be considered quasi-steady-state and Fick's 1st law will be applied.

7.3.5 Mathematical expression for galvanic corrosion rate

Based on the assumptions stated above, the oxygen flux, the diffusion path length, and the average galvanic corrosion current densities can be expressed as in (7.2-5)-(7.2-8).

For all the following equations:

i_{anode} = anodic galvanic corrosion current density [A/m^2],

i_{cathode} = cathodic galvanic corrosion current density [A/m^2],

J_{O_2} = flux of oxygen [$\text{mol}/(\text{s}\cdot\text{m}^2)$],

Ω_{O_2} = oxygen consumption per unit of galvanic corrosion charge [$\text{mol}/(\text{A}\cdot\text{s})$] ($2.59\text{E}-6 \text{ mol}/(\text{A}\cdot\text{s})$),

$D_{\text{O}_2, \text{Al}(\text{OH})_3, \text{gel}}$ = diffusion coefficient for oxygen through $\text{Al}(\text{OH})_3$ gel [m^2/s] ($1.97\text{E}-9 \text{ m}^2/\text{s}$),

Δc = the change in concentration of oxygen [mol/m^3] ($-0.40 \text{ mol}/\text{m}^3$),

Δx = diffusion path length [m],

$\rho_{\text{Al}(\text{OH})_3, \text{gel}}$ = density of the $\text{Al}(\text{OH})_3$ gel [kg/m^3] ($1000 \text{ kg}/\text{m}^3$),

138 = the mass increase from Al to $\text{Al}(\text{OH})_3$ gel,

W_{Al} = atomic mass of aluminum [g/mol] (27 g/mol),

F = Faraday's constant [C/mol] (96 485 C/mol),

n_{Al} = valency of aluminum [e^- /ion] (3),

$V_{Al(OH)_3, gel}$ = total volume of $Al(OH)_3$ deposited [m^3],

$A_{opening}$ = the cross-section of the $Al(OH)_3$ gel exposed to the surrounding air [m^2]

(0.0032 m^2), and

$A_{cathode}$ = the area of the exposed CFRP per meter conductor [m^2] (0.014 m^2).

Flux of oxygen through the deposited corrosion products:

$$J_{O_2} = -D_{O_2, Al(OH)_3} * \frac{\Delta c}{\Delta x} = -(1.97E(-9)) \left[\frac{m^2}{s} \right] \cdot \frac{-0.40 \left[\frac{mol}{m^3} \right]}{\Delta x [m]} = \frac{7.88E(-10)}{\Delta x} \left[\frac{mol}{s \cdot m^2} \right]$$

(7.2-5)

Average cathodic corrosion current density:

$$i_{cathode} \left[\frac{A}{m^2} \right] = \frac{J_{O_2}}{\Omega_{O_2}} \cdot \frac{A_{opening}}{A_{cathode}} = \frac{7.88E(-10) \frac{1}{\Delta x} \left[\frac{mol}{s \cdot m^2} \right]}{2.59E(-6) \left[\frac{mol}{A \cdot s} \right]} \cdot \frac{0.0032 [m^2]}{0.014 [m^2]} = \frac{6.95E(-5)}{\Delta x} \left[\frac{A}{m^2} \right]$$

(7.2-6)

Diffusion path length:

$$\Delta x [m] = \frac{V_{Al(OH)_3, gel}}{A_{opening}} = \frac{\left(\frac{138 \cdot W_{Al}}{F \cdot n_{Al} \cdot \rho_{Al(OH)_3, gel}} \right) \cdot \int_0^t (i_{cathode}) dt \cdot A_{cathode}}{A_{opening}} =$$

$$\frac{\left(\frac{138 \cdot 0.027 \left[\frac{kg}{mol} \right]}{96485 \left[\frac{C}{mol} \right] \cdot 3 \cdot 1000 \left[\frac{kg}{m^3} \right]} \right) \cdot 0.014 [m^2] \cdot \int_0^t (i_{cathode} \left[\frac{A}{m^2} \right]) dt}{0.0032 [m^2]} = 5.61E(-8) \cdot \int_0^t (i_{cathode}) dt [m]$$

(7.2-7)

Average anodic corrosion current density:

$$i_{anode} \left[\frac{A}{m^2} \right] = \frac{i_{cathode} \left[\frac{A}{m^2} \right]}{28} \quad (7.2-8)$$

7.2.6 Solving technique

The growth of the $Al(OH)_3$ gel layer is a function of the galvanic corrosion current density, while the galvanic corrosion current density is in turn a function of the gel layer thickness.

Substituting (6) into (7) and changing the variable of integration gives:

$$\Delta x(t) = 5.61E(-8) \cdot \int_{t_0}^t \left(\frac{6.95E(-5)}{\Delta x(u)} \right) du = 3.90E(-12) \cdot \int_{t_0}^t \left(\frac{1}{\Delta x(u)} \right) du$$

(7.3-9)

(Note that $1/\Delta x$ is undefined at $t=0$, which will be handled by a boundary condition later.)

Taking the derivative of both sides with respect to t , using the fundamental theorem of calculus, gives:

$$\frac{d(\Delta x)}{dt} = \frac{3.90E(-12)}{\Delta x(t)} \quad (7.2-10)$$

$$\Rightarrow \Delta x d(\Delta x) = 3.90E(-12) dt \quad (7.2-11)$$

$$\Rightarrow \frac{(\Delta x)^2}{2} = 3.90E(-12)t + K_0 \quad (K_0 \text{ is a constant}) \quad (7.2-12)$$

$$\Rightarrow \Delta x = \sqrt{7.80E(-12)t + K} \quad (K=2 K_0, \text{but still a constant}) \quad (7.2-13)$$

$$\Rightarrow i_{cathode} = \frac{6.95E(-5)}{\sqrt{7.80E(-12)t + K}} \quad (7.2-14)$$

$$\Rightarrow i_{anode} = \frac{i_{cathode}}{28} = \frac{2.48E(-6)}{\sqrt{7.80E(-12)t + K}} \quad (7.2-15)$$

7.2.7 Initial condition

An initial condition is needed for two reasons: 1) the numerical model is undefined at $t=0$, and 2) there are additional galvanic corrosion rate controlling mechanisms that are dominant when there is no deposited gel.

Two different initial conditions were used for the anodic galvanic corrosion current density: one experimental value and one value from a previous numerical model.

In the first case (A), the initial value for the anodic galvanic corrosion current density was taken as 10.1 mA/m^2 , which is the average for day 2 through 5 in the test series presented above (repeated in Figure 155 below).

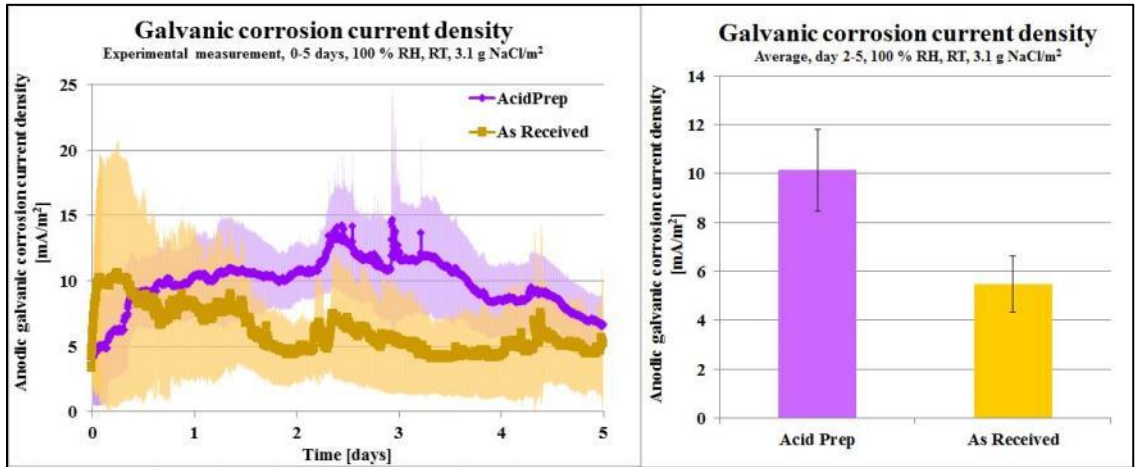


Figure 155: Experimentally measured galvanic corrosion rates. Left) Average corrosion rate for 10 samples. Right) Average corrosion rate for day 2-5.

In the second case (B), the initial value was calculated using the steady-state finite element model presented in section 7.1. That model predicted an average anodic galvanic corrosion current of 6.8 mA/m^2 . This is slightly lower than the three day average presented in this section, but within the range of the measurements presented in this dissertation.

These initial values establish the upper boundary for the anodic current density.

Using the boundary condition from case A, we solve for K at time $t=0$:

$$K = 6.03E(-8) \quad (7.3-16)$$

Thus:

$$i_{anode} = \frac{2.48E(-6)}{\sqrt{7.80E(-12)t + 6.03E(-8)}} \quad (7.3-17)$$

For case B, with the initial value for $i_{anode} = 6.8 \text{ mA/m}^2$, the corresponding equation is:

$$i_{anode} = \frac{2.48E(-6)}{\sqrt{7.80E(-12)t + 1.33E(-7)}} \quad (7.3-18)$$

7.2.8 Results and discussion

The numerical results are compared with experimental measurements in Figure 156 and Figure 157. Because it takes time for the NaCl to absorb water and form a continuous film, and because it takes time for the galvanic corrosion to initiate, the first days of experimental measurements showed erratic corrosion currents. The numerical model does not take into account these factors, so the first three days from the experimental measurements were removed from the comparison below.

Figure 156 shows a fairly nice agreement between the numerical model and the experimental data over 59 days. Figure 157 compares the numerical and experimental data for days 1-14. Although the predicted galvanic corrosion current is lower than the experimental values for the first 10 days, the agreement is very good beyond day 10. By day 13, the numerical models for both initial values predict an anodic current density of 0.83 mA/m^2 . The experimental measurement for day 13 in Figure 156 and Figure 157 (which corresponds to day 16 in Figure 151) was 0.73 mA/m^2 ($\sigma=0.18$). These are the same levels observed in the immersed tests presented in section 1. Although the slab model is a crude simplification of the conductor geometry, these results strongly suggest that the deposited gelatinous corrosion products in atmospheric conditions result in a similar oxygen mass transport limiting effect as the electrolyte in immersed conditions.

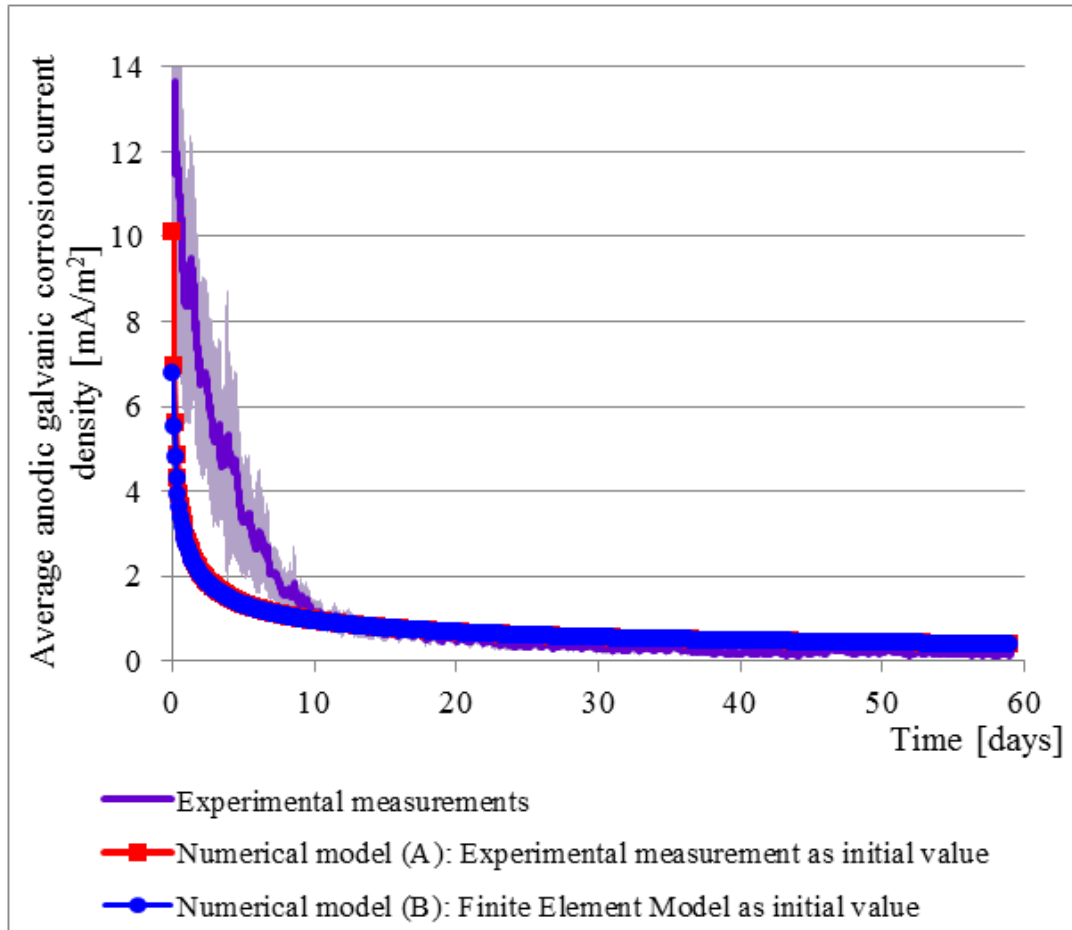


Figure 156: Average anodic galvanic corrosion current densities as a function of time. The shaded region represents one standard deviation of the experimental measurements

However, the calculated diffusion path length in Figure 157 shows that the crevices are less than half full by day 13 in the numerical model ($\Delta x = 2.7$ mm, compared to full crevices of 8.6 mm in the slab model). From the calculations of the gel formation based on measured galvanic corrosion currents, the sample should be close to full at this time. Because the first three days of the experimental data were removed in the comparison with the numerical model, Δx can be calculated in several different ways. Using the cumulative corrosion charge from the start of the test, Δx would be 7.8 mm by

day 13 (corresponds to day 10 in Figure 157). Using only the cumulative galvanic corrosion charge shown in Figure 157 and neglecting the first three days of the experimental test, Δx would be 4.9 mm.

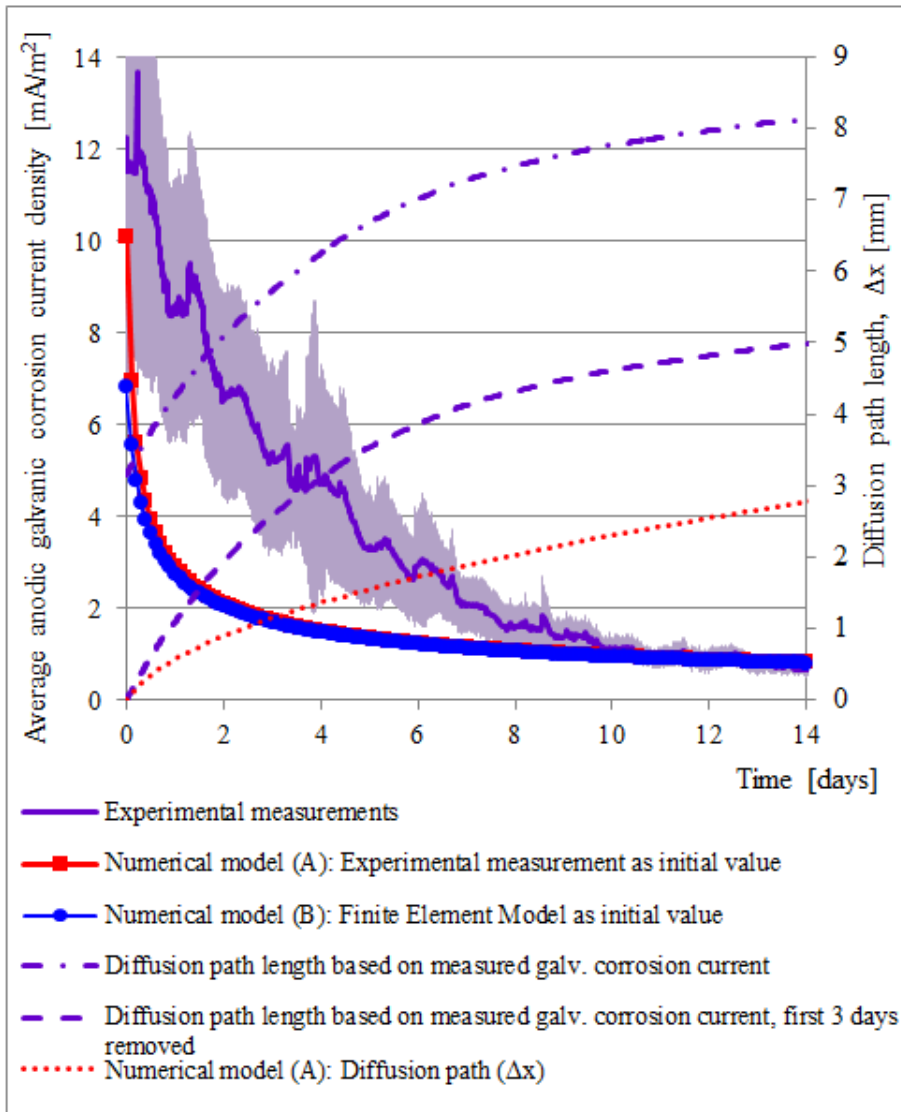


Figure 157: Average anodic galvanic corrosion current densities and thickness Δx for the first 14 days. The shaded region represents one standard deviation of the experimental measurements.

Although the value of Δx is smaller in the numerical model than estimated from the experimental data, these results still strongly support the hypothesis that the restriction of oxygen transport due to corrosion product deposition is the dominant control mechanism in this case.

7.2.9 Conclusions regarding this model

A new look at the role of corrosion product deposition in the galvanic corrosion between aluminum and CFRP has been presented in this paper. The focus was on an assembly consisting of a CFRP rod surrounded by tightly wound aluminum wires, namely a CFRP supported bare overhead high voltage transmission line conductor. The results from experimental measurements and numerical modeling suggest that the dominant rate controlling mechanism is the diffusion of oxygen to the CFRP surface. Strong evidence has been presented that the deposition of corrosion products in the form of gelatinous Al(OH)_3 restricts the diffusion of oxygen, which drastically reduces the galvanic corrosion rate.

The formation of Al(OH)_3 on samples initially immersed in 0.6 M NaCl and then subjected to 100 % RH at RT was observed to coincide with the decay in the galvanic corrosion current. The galvanic corrosion current decreased by one order of magnitude over a period of 13 days. The resulting galvanic corrosion rate after approximately two weeks was similar to the rate measured when the assembly was immersed in a NaCl containing electrolyte. The hypothesis was that the deposition of Al(OH)_3 gel restricted

the oxygen transport in a similar manner as the electrolyte would in the immersed environment.

A good correlation has been obtained between experimental measurements of galvanic corrosion current and a numerical model, where the deposition of $\text{Al}(\text{OH})_3$ and the diffusion of oxygen through the gelatinous $\text{Al}(\text{OH})_3$ were the only rate-limiting mechanisms.

The findings suggest that the deposition of corrosion products may be the most important rate controlling mechanisms in certain Al/CFRP assemblies where the CFRP is surrounded by the aluminum and where the path of diffusion for the oxygen is relatively long and narrow. The implications of these findings are that the galvanic corrosion rate in assemblies of this kind may be much lower than typically expected. To avoid a potentially severe over-estimation of the galvanic corrosion rate, the sample design and test conditions must represent the original geometry of the sample and the actual service environment as closely as possible. In addition, the results presented in this dissertation suggest that the test duration must be sufficiently long to allow for deposition of corrosion products.

7.3 Discussion and chapter conclusions

Several conclusions can be drawn from the two numerical models and the experimental validations presented in this chapter. First the results at 100 % RH will be compared, and second the results at varying relative humidity will be compared.

The steady-state Finite Element model described in section 7.1 predicted that the galvanic corrosion rate should be the highest near the cathode. This is known from

literature and could also be observed through microscopy of corroded samples. The predicted galvanic corrosion rates for one specific salt load density were compared to experimental measurements. The chosen salt density was 3.1 g/m^2 , which is the resulting salt load density when an ACCC conductor sample is immersed in 0.6 M NaCl (similar salinity to seawater) and then dried. The predicted galvanic corrosion rate at 100 % RH is within the range of measured values, as can be seen in Figure 158. However, the measured values vary dramatically depending on the exact testing conditions.

When the samples are brand new and initially treated with phosphoric acid to remove the oxide layer (“Acid Prep” in the above figure), the measured value is higher than the predicted. When the original oxide layer and scale is left intact, the value is lower than the predicted. The test series presented in Chapter 3 generated drastically lower values than the prediction. Those samples were from a conductor reel that had been stored outdoors for over 10 years and may have formed a thick passive layer. Figure 158 also includes values from conductors that had been exposed to 100 % RH for several weeks and were filled with Al(OH)_3 gel. These generated much lower galvanic corrosion rates than the numerical model.

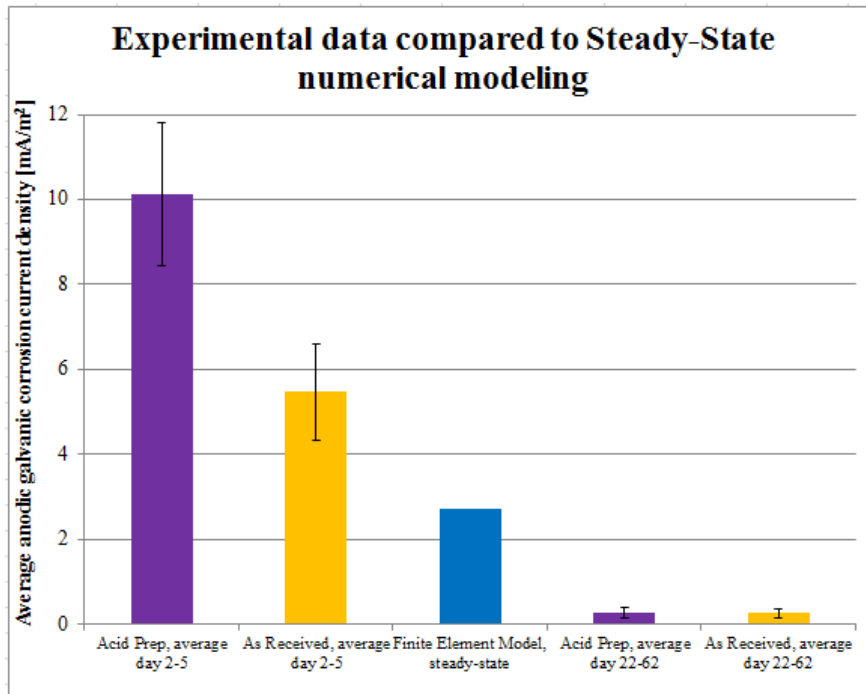


Figure 158: Comparison of the steady-state FE model with experimental values.

It can be concluded that the steady-state model provided a prediction that was within the range of the measured values at 100 % RH and 3.1 g/m². The predicted rate is good for a new sample with a very early stage of corrosion, but is not accurate for samples that have accumulated corrosion products or formed a stable oxide layer on the aluminum surface. This illustrates the active-passive behavior of aluminum and the difficulty to predict its corrosion rate. This model can only represent the ACCC conductor with a compromised galvanic corrosion barrier when it is brand new. Because the conductor is full of narrow crevices that will collect corrosion products, and pollutants, additional limiting mechanisms will soon appear. This will make the model inadequate beyond the first few days or perhaps weeks.

Comparing the shape of the curve for the finite element model results with the measured values indicates that there are additional control mechanisms that are not considered in the model. The experimental data exhibits an exponential trend with rapidly increasing galvanic corrosion with increased RH levels. The numerical data, on the other hand, increases with increasing RH, but the function has a slightly convex shape. This numerical model can clearly not fully explain the galvanic corrosion mechanism for these conditions. A likely cause for the discrepancy for values below 100 % RH could be the very thin electrolyte layer not being able to form a continuous electrolyte film between the CFRP and the aluminum, resulting in a much higher resistance than predicted, but this hypothesis has not been studied in any further detail.

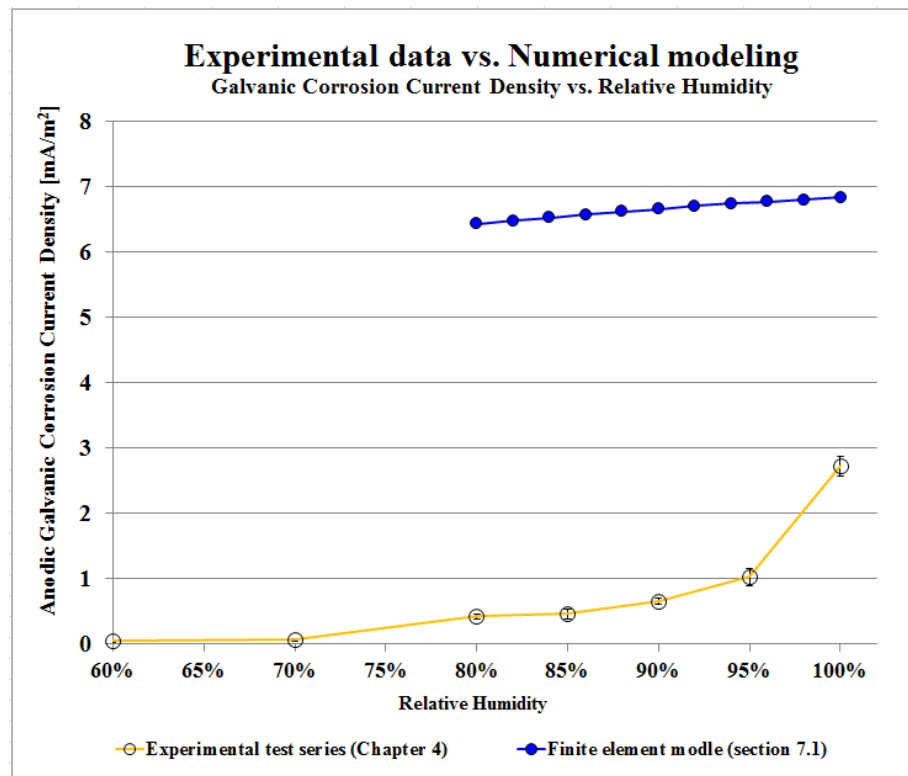


Figure 159: Comparison of the steady-state FE model with experimental values.

As mentioned several times before, the galvanic corrosion in the ACCC conductor with exposed CFRP appears to be mostly or completely dominated by the transport of oxygen to the cathode. Experimental measurements indicate that the accumulation of corrosion products in the form of $\text{Al}(\text{OH})_3$ gel appears to very effectively limit this transport. Within a short amount of time (10-14 days in 100 % RH at RT, with a salt load density of 3.1 g/m^2), the conductor was filled with gel and the galvanic corrosion rate decreased one order of magnitude from $6\text{-}10 \text{ mA/m}^2$ to approximately 1 mA/m^2 . This resulting galvanic corrosion rate is similar to the rate measured during immersion.

The galvanic corrosion in the ACCC conductor with exposed CFRP appears to be completely dominated by the transport of oxygen to the cathode. The accumulation of corrosion products in the form of $\text{Al}(\text{OH})_3$ gel very effectively limits this transport. Within a short amount of time (10-14 days in the conditions used here), the conductor will be filled with gel and the galvanic corrosion rate will have decreased one order of magnitude. The resulting galvanic corrosion rate is similar to the rate measured during immersion. While the agreement isn't perfect between the model and the experimental data in Figure 156 (repeated below), this time-dependent numerical model presented in section 7.2 provides support that the rapid decay in galvanic corrosion rate is mainly caused by the deposition of galvanic corrosion products in the form of gelatinous $\text{Al}(\text{OH})_3$.

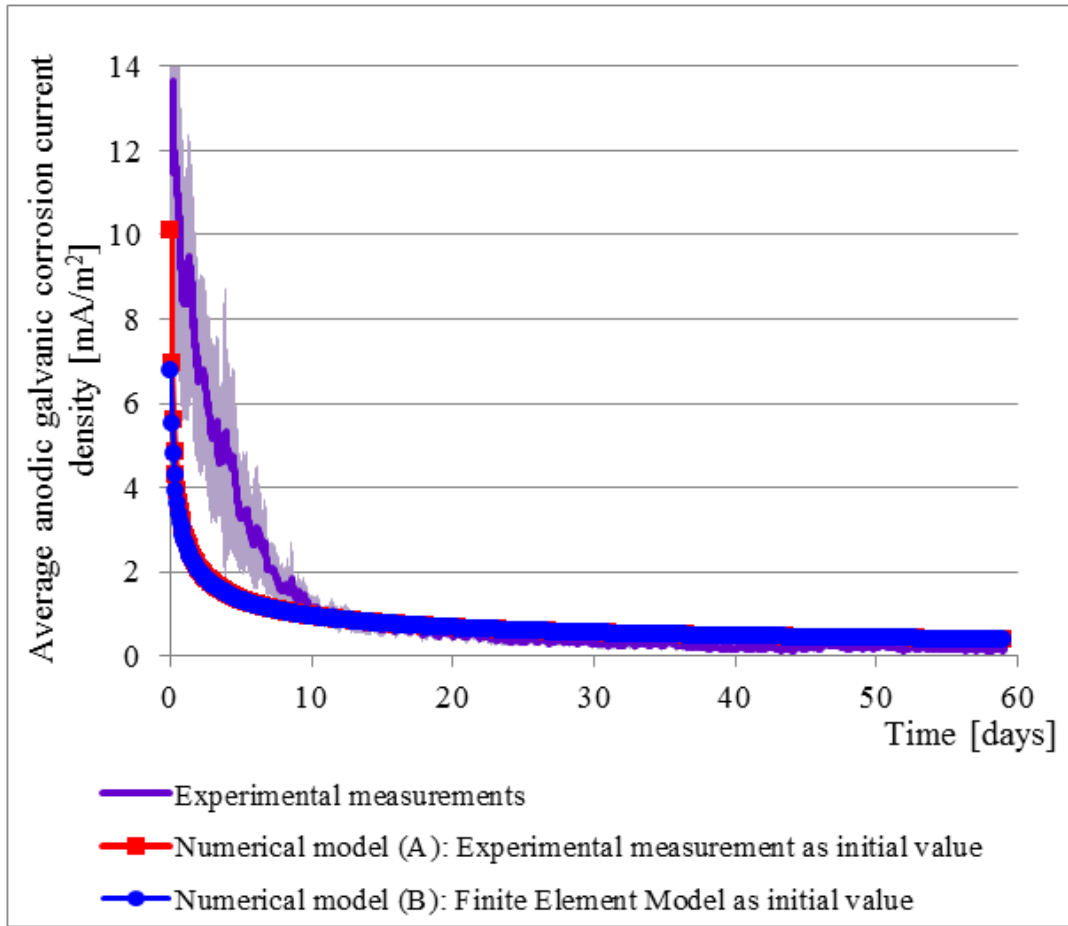


Figure 156 (repeated): Average anodic galvanic corrosion current densities as a function of time. The shaded region represents one standard deviation of the experimental measurements

CHAPTER EIGHT: MONITORING FOR GALVANIC CORROSION IN CARBON FIBER COMPOSITE CORE OVERHEAD CONDUCTORS USING TIME DOMAIN REFLECTOMETRY

A reliable inspection and monitoring method for evaluating the structural health of ACCC conductor is crucial for large-scale acceptance of this relatively new technology. Several different methods for structural health monitoring of composites have been attempted, including acoustic emissions (Barré and Benzeggagh 1994, Grosse and Ohtsu 2008), embedded fiber optics (Rao 1999, Ling, Lau et al. 2006), x-ray inspection (Aymerich and Meili 2000), eddy-current measurements (Valleau 1990, Mook, Lange et al. 2001), and ultrasonics (Aymerich and Meili 2000), (Cantwell and Morton 1985). All these methods suffer from weaknesses that so far have made them impractical in the service environment of power transmission conductors. Fiber optics sensors are invasive as they have to be embedded during the manufacturing of the composites. The required instrumentation is also complicated and expensive. Ultrasonic and acoustic emission methods are prone to high interference. X-ray inspection methods are unsuitable for in-service inspection due to the large size of the equipment. Inspections with ultrasonics, x-ray, and eddy-currents provide only *local* inspection, meaning that the equipment would have to be moved along the entire length of the conductor to inspect it. Time Domain Reflectometry (TDR), on the other hand, offers distributed sensing from a

single point of inspection. This chapter presents a new application of TDR for the inspection of ACCC bare overhead transmission line conductors.

The composite core in the ACCC transmission line conductor has an electrically conductive center consisting of a unidirectional carbon fiber reinforced polymer (CFRP), surrounded by an electrically insulating unidirectional glass fiber reinforced polymer. Together with the surrounding aluminum strands, the conductor geometry forms a coaxial cable: a conductor inside another conductor with an insulator in between. Although the CFRP never was intended to be used as a conductor, this study has shown that it is still sufficiently conductive that TDR can potentially be used to detect faults.

TDR was developed during the 1950s to locate and identify faults in cables in telecom and power distribution. These industries are still the major users of the TDR technology and cable testers are considered standard equipment by engineers and technicians. For coaxial cables, TDR enables non-invasive surveillance of a large cable with one single instrument from one single location and may replace many single-point measurement instruments (Riser-Bond 1997, O'Connor and Dowding 1999).

The telecom industry is the most frequent user of TDR, but it is far from the only user. TDR is used in geo-measurements, for example, to estimate the density and moisture content of soil, to monitor soil and rock deformation in mines, and to detect the water level in wells (O'Connor and Dowding 1999). TDR is also used for monitoring the hydration of cement (Hager and Domszy 2004). In the field of composites, TDR is, for example, used to monitor the curing of resin in laminates (Dominauskasa, Heider et al. 2007, Pandey, Deffor et al. 2013) for damage detection in laminates (Pandey,

Thorstenson et al. 2013, Todoroki, Ohara et al. 2015), and for automated measurement of crack propagation during testing of composites (Obaid, Yarlalagadda et al. 2006).

TDR for coaxial cables includes a broad range of remote sensing techniques to determine the location and nature of various reflectors. It is in principle similar to radar, but is confined to one dimension. For inspection of a coaxial cable, an ultra-fast rise time voltage step is launched into the cable (the voltage is applied between the inner and outer conductor). The electromagnetic pulse travels down the conductor at nearly the speed of light. When the pulse encounters a change in the characteristic impedance, a reflected pulse is returned back to the instrument. The time between the transmitted pulse and the reflection uniquely determines the fault location (O'Connor and Dowding 1999).

This chapter presents the theoretical foundation for use of TDR for structural integrity evaluation of ACCC, estimates of its viability, and the results of experiments performed to evaluate the potential of the method.

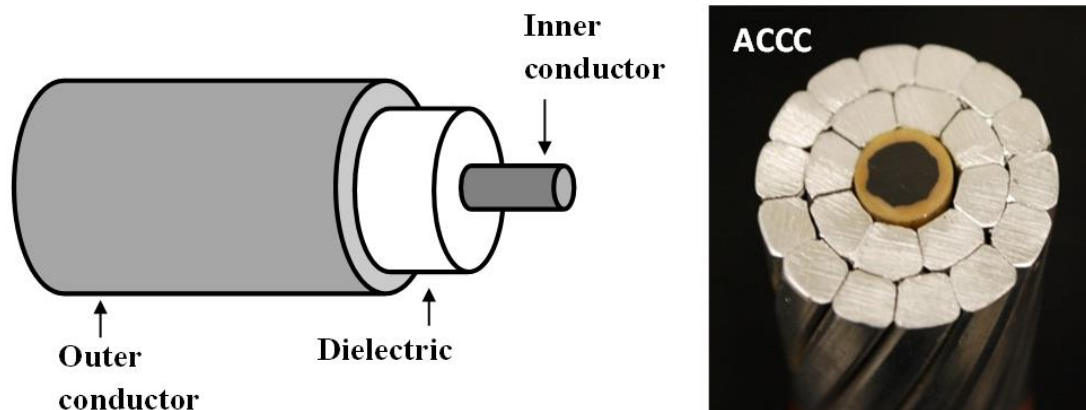


Figure 160: Typical coaxial cable vs. ACCC.

8.1 Circuit theory for TDR and application in ACCC

8.1.1 Transmission line theory

A coaxial cable, or any two insulated conductors placed close together such as a twisted pair of wires, forms a so called *transmission line* with a characteristic impedance (“transmission line” in this sense should not be confused with “high voltage transmission lines” which refers to the part of the electrical grid that transmits power over long distances at high voltage). The two conductors behave like a long continuous network of capacitors, inductors, and resistors which together make up the *characteristic impedance*. The inherent impedance of the coaxial cable is a function of the conductor diameter, the spacing between the conductors, and the dielectric constant of the insulation. If the conductor diameter, spacing, and dielectric constant are uniform, the impedance will be constant. Any sudden change in capacitance, inductance, resistance, dielectric constant, or conductance of the insulator will result a sudden change in impedance, which will cause a partial or total reflection of the wave. A larger change in impedance causes a larger reflection (Riser-Bond 1997).

Changes in impedance can have many causes: including a change in the conductor spacing caused by pinching or bird caging, local moisture absorption or aging of the polymer affecting the dielectric constant, or thinning of the insulation due to rubbing. Other potential causes are direct contact between carbon fibers and aluminum, partial fracture of one or both conductors, manufacturing flaws, and likely many other issues. Galvanic corrosion requires there to be an electrolytic contact in place between the CFRP and aluminum, and it is shown in this chapter that it too can be detected.

Figure 161 illustrates the reflection caused by a change in conductor spacing, using a twisted pair as an example (twisted pairs behave similar to coaxial cables). The upper waveform shows the constant impedance of the perfect twisted pairs. Only the open end changes the impedance and causes a reflection. The lower waveform shows the change in impedance caused by a separation of the conductors. The twisted pair can be compared to a network of capacitors where one of them has a greater separation of the plates. The change in impedance causes some of the energy to be reflected.

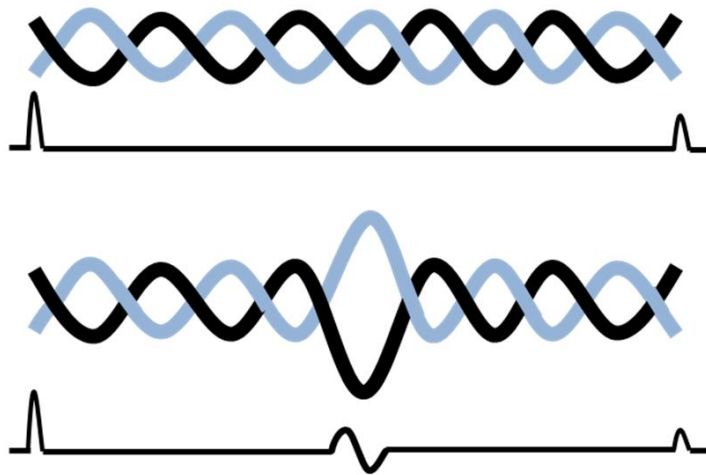
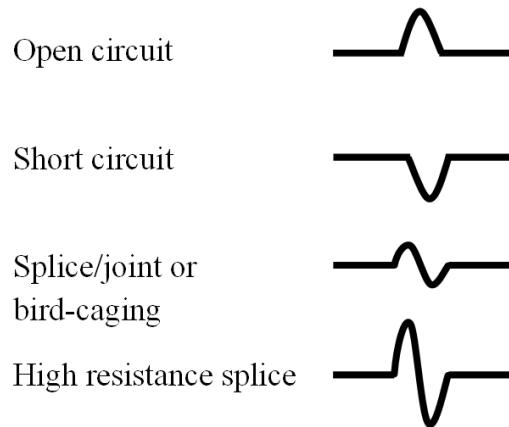


Figure 161: Reflection caused by change in conductor spacing.
Based on (Radiodetection 1997).

By analyzing the sign, length, and amplitude of the reflected pulse, additional information about the fault can be obtained (Radiodetection 1997). Figure 162 illustrates different TDR trace examples. *Open circuit* is the same as an open end of the conductor, which means that there is no electrical connection between the CFRP and aluminum, while a *short circuit* means that there is electrical contact between the CFRP and aluminum.



*Figure 162: Examples of common TDR reflections in coaxial cables.
Based on (Radiodetection 1997).*

The propagation of the pulse along the cable, as well as the characteristics and creation of the reflections, can be described using Maxwell's electromagnetic wave theory or circuit theory (O'Connor and Dowding 1999). Using circuit theory, the coaxial cable with its inner and outer conductor (Figure 163a) can be represented by an ideal, two-wire transmission line having forward and return conductors to represent the outer and inner conductor (Figure 163b).

As the launched voltage pulse propagates along the coaxial cable, the potential difference (V) creates a current (I). The propagation can be described using the following four parameters in the circuit network in Figure 163c-d (O'Connor and Dowding 1999):

- The potential between the inner and outer conductor represents the coaxial cable's capacity to store electric energy. This is expressed as capacitance, C [F/m].
- The current flowing in the conductors induces a magnetic field. The strength of the field is controlled by the coaxial cable's inductance, L [H/m].

- The dissipation of energy is caused by the resistance, R [Ω/m].
- The dielectric separating the two conductors has a small conductivity, G [S/m], which also causes some dissipation of energy.

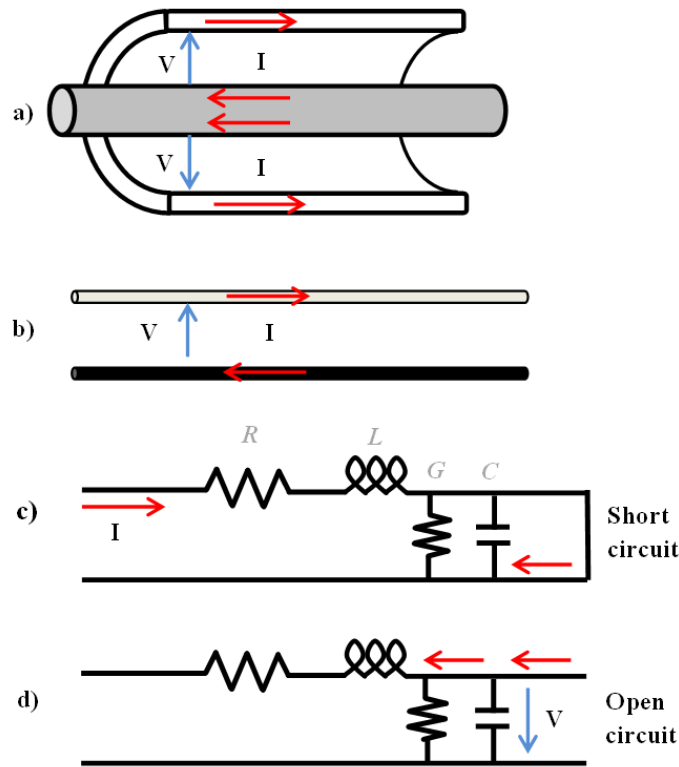


Figure 163: Lumped transmission line parameters: a) coaxial cable; b) parallel wire transmission line; c) lumped parameters with short circuit; d) lumped parameters with open circuit. (O'Connor and Dowding 1999)

By connecting many of these circuits together and using classical transmission line theory, a long piece of the conductor can be modeled. Lobry and Guery (Lobry and Guery 2012) used a similar approach to calculate the potential between the core and the strands in ACCC due to the resistance of the aluminum. They needed 30 to 100 circuits (depending on the initial assumptions) to get a correct answer compared.

A similar network could be used to calculate a fault's response to a pulse input, but according to TDR theory there is a much easier way. The circuit networks haven been analyzed and solved, and there are theories available, all proven through experience to work very well (Hewlett-Packard 1988).

Table 19: Data for the ACCC cable of the size “Drake”			
Parameter	Value	Unit	Comment/Reference:
d, outside diameter of inner conductor	6.65	mm	Average, varies between 6.2 and 7.1 mm along the conductor
D, inside diameter of outer conductor	9.5	mm	
ϵ_r , Relative dielectric constant of fiberglass epoxy composite	4.5	-	(Matweb.com 2015) For FR4 printed circuit material
ρ_{rd} , inner conductor material (unidirectional carbon fiber reinforced epoxy), resistivity relative to copper	1470	-	(Matweb.com 2015, Matweb.com 2015) Assuming 60 % volume fiber fraction, at room temp. Based on $1.5E-5 \Omega\text{-m}$ resistivity for the carbon fibers, and $1.7E-8 \Omega\text{-m}$ for copper.
ρ_{rD} , outer conductor material (Al) resistivity relative to copper	1.66	-	(Matweb.com 2015, Matweb.com 2015) At room temperature. Based on $2.83E-8 \Omega\text{-m}$ resistivity for Al.
δ , loss tangent	0.008 0.02	-	(Agilent.com 2013) Data for G10 (fiberglass composite) at 100 MHz (Technologies 2013) Data for FR4 (fiberglass composite), frequency not specified

8.1.2 Characteristic impedance

The characteristic impedance of coaxial cable is the value of impedance presented at its input of an infinite length of the cable. A finite length of the cable will present the same impedance if it is terminated with a load with the impedance equal of that of the characteristic impedance. When the cable is infinitely long, or terminated with the same impedance, all energy sent down the line is absorbed and no energy is reflected (Butler

1989). A continuous section of ACCC conductor installed in service can be up to 2000 m or longer, and will in the subsequent calculations be considered as having infinite length.

Assuming an infinitely long coaxial cable, the characteristic impedance is then (Hewlett-Packard 1988, Strickland 1997):

$$Z_0[\Omega] = \sqrt{\frac{R+j\omega L}{G+j\omega C}} \quad (8.1-1)$$

where

Z_0 = characteristic impedance [Ω],

R = resistance [Ω/m] (ohms/meter),

L = inductance [H] (henry),

G = conductance of the dielectric [S/m] (siemens/meter),

C = capacitance [F/m] (farads/meter), and

ω = frequency [Hz].

G can often be left out in equation (8.1-1) for normal coaxial cables (Strickland 1997). It is also common to only use the real parts of the inductance (L) and capacitance (C), and to ignore the resistance of the conductors (R). That gives the following simplified equation for the impedance (DigiKey 2013):

$$Z_0[\Omega] = \sqrt{\frac{L}{C}} = \frac{138}{\sqrt{\epsilon_r}} \cdot \log\left(\frac{D}{d}\right) \quad (8.1-2A)$$

where

Z_0 = characteristic impedance [Ω],

C = capacitance (F/m),

L = inductance (H/m),

d = outside diameter of inner conductor (m),

D = inside diameter of outer conductor (m), and

ϵ_r = Relative dielectric constant of fiberglass epoxy.

Applying equation (8.1-2A) on the ACCC using values from Table 19:

$$Z_{0,ACCC} = \frac{138}{\sqrt{4.5}} \cdot \log\left(\frac{9.5}{6.65}\right) = \mathbf{10.1 \Omega} \quad (8.1-2B)$$

8.1.3 Coefficient of reflection

Any abrupt change in the electrical impedance of the cable will cause a reflection of the pulse. The strength and sign of the reflection and can be calculated using the following equations.

The reflection coefficient, ρ , is defined as:

$$\rho = V_r/V_i \quad (8.1-3)$$

where

ρ = reflection coefficient (unitless),

V_i = voltage of the input pulse [V], and

V_r = voltage of the reflection [V].

The reflection coefficient (ρ) can have the value from -1 to 1. It is related to the characteristic impedance (Z_0) and the impedance of a fault (Z_L) by the following equation:

$$\rho = \frac{Z_L - Z_0}{Z_L + Z_0} \quad (8.1-4)$$

where

ρ = reflection coefficient (unitless),

Z_L = impedance of the fault [Ω], and

Z_0 = characteristic impedance [Ω].

The reflected pulse is identical to the initial pulse if the cable has open ends (an open end can be considered a fault with infinite impedance), and the coefficient of reflection will in that case be 1. If the cable has a hard short circuit either at the end or anywhere along its length, the impedance of the fault will be zero. Equation (8.1-4) shows that the coefficient of reflection will be -1, which means that the pulse will come back inverted (shown in Figure 162). For resistive faults that are in-between perfect shorts and perfect opens, the reflection will be a fraction of the initial wave. If the fault has complex impedance (it is inductive, reactive etc.), the reflection can have a different waveform than the initial pulse. It has been assumed in this work that faults in ACCC cables cannot have complex impedance, as this is most common where the TDR detects active equipment connected to the coaxial cable, such as tapping equipment (Hewlett-Packard 1988).

8.1.4 Velocity of propagation

The velocity of propagation (VOP) is necessary to be known in order to locate a fault. The VOP is expressed as percent of the speed of light in vacuum. The equation for VOP is (DigiKey 2013):

$$V_p = \frac{100}{\sqrt{\epsilon_r}} \quad [\%] \quad (8.1-5A)$$

where

V_p = velocity of propagation [% of speed of light in vacuum], and

ϵ_r = relative dielectric constant of the fiberglass epoxy (unitless).

Applying (8.1-5A) to ACCC using values from Table 19:

$$V_p = \frac{100}{\sqrt{4.5}} = 47.1 \quad \% \quad (8.1-5B)$$

8.1.4 Attenuation

To calculate the reflection that the actual measurement instrument will record, the attenuation (loss) of the pulse on the way to the fault and on the way back has to be taken into account. The cable attenuation is the sum of conductor losses and dielectric losses, and is a very strong and non-linear function of frequency. The “frequency” of the TDR can be seen as the inverse of the pulse length.

The equations for the loss of power in a coaxial cable are the following (Lobry and Guery 2012):

$$\alpha_{conductors} = \alpha_c = \frac{11.39}{z_0} \cdot \sqrt{f} \cdot \left[\frac{\sqrt{\rho_{rd}}}{d} + \frac{\sqrt{\rho_{rD}}}{D} \right] \quad \left[\frac{dB}{m} \right] \quad (8.1-6)$$

$$\alpha_{dielectric} = \alpha_{diel} = 90.96 \cdot f \cdot \sqrt{\epsilon_r} \cdot \tan(\delta) \quad \left[\frac{dB}{m} \right] \quad (8.1-7)$$

where

$\alpha_{\text{conductors}}$ = attenuation in the conductor [dB/m] (expressed as loss of power),

$\alpha_{\text{dielectric}}$ = attenuation in the dielectric [dB/m] (expressed as loss of power),

f = frequency [GHz],

Z_0 = characteristics impedance [Ω],

ρ_{rd} = resistivity of CFRP compared to copper (unitless),

ρ_{rD} = resistivity of aluminum compared to copper (unitless),

d = outer diameter of CFRP [m],

D = inner diameter for Al [m],

ϵ_r = relative dielectric constant of fiberglass reinforced epoxy matrix composite
(unitless),

δ = loss tangent of fiberglass reinforced epoxy matrix composite (unitless).

Note that (8.1-6) and (8.1-7) are expressed as power, which is common practice because one is typically concerned with power loss in radio frequency applications. The loss in voltage (in dB) is half of the loss of power (in dB). In this case, the loss of voltage is of greater interest because that is the measured reflection.

A high voltage transmission line can have a continuous conductor section of 2000 m or more. The conductor can be accessed from both ends, so the system has to be able to inspect a minimum of 1000 m of cable. During inspection of 1000 m cable, the pulse will travel a total length of 2000 m.

Table 20 and Figure 164 illustrate the result of applying (8.1-6) and (8.1-7) on a 2000 m section of ACCC, and shows that an increase in frequency (a decrease in pulse length) dramatically increases the attenuation. The high resistivity of the CFRP is the root cause of the high attenuation. The attenuation in the CFRP is responsible for 69 to 97 % of the total losses, depending on the pulse frequency (see Table 20). Because the ACCC conductor is designed to be operated at temperatures over 100°C, it is important to note that the calculated losses are based on values for resistivity and relative dielectric constant at room temperature. The resistivity of aluminum goes up with temperature while the resistivity of carbon goes down. Since the carbon dominates the attenuation, a higher temperature should mean lower attenuation. The temperature dependency for the relative dielectric constant of the specific fiberglass reinforced epoxy matrix composite used in the ACCC is currently not known, and would have to be measured in order to make a more accurate prediction of the attenuation at elevated operating temperatures.

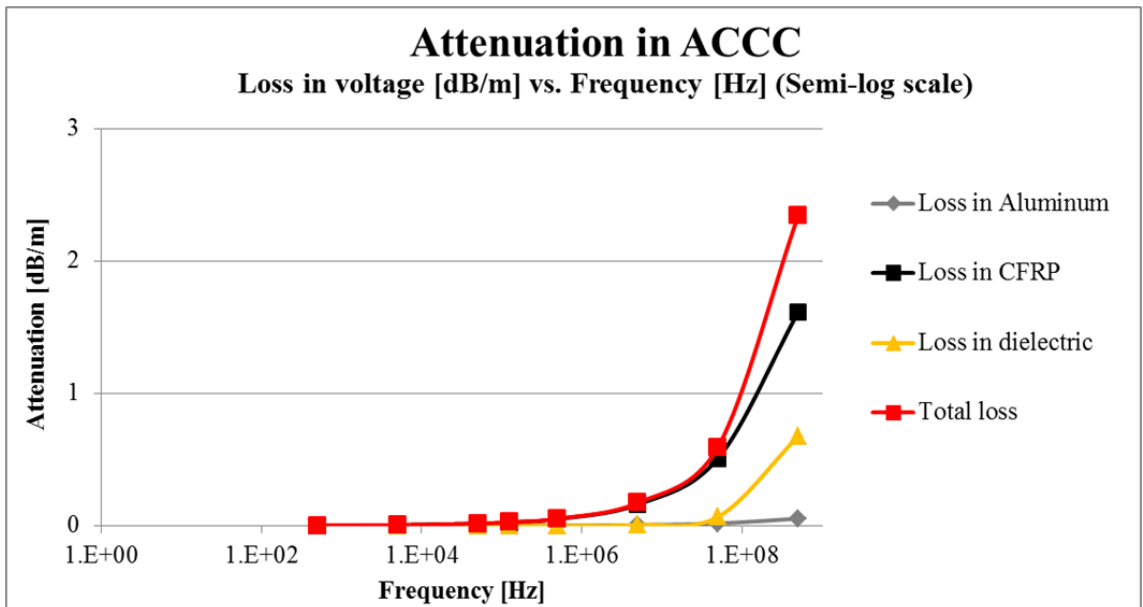


Figure 164: Attenuation in ACCC as a function of frequency

Pulse length	1 ms	100 μ s	10 μ s	4 μ s	1 μ s	100 ns	10 ns	1 ns
Frequency	500 Hz	5 kHz	50 kHz	125 kHz	500 kHz	5 MHz	50 MHz	500 MHz
Attenuation in Al [dB/m]	5.0E-5	1.7E-4	5.4E-4	8.6E-4	1.7E-3	5.4E-3	1.7E-2	5.4E-2
Attenuation in CFRP [dB/m]	1.6E-3	5.1E-3	1.6E-2	2.6E-2	5.1E-2	0.16	0.51	1.6
Attenuation in dielectric [dB/m]	7.0E-7	6.8E-6	6.8E-5	1.7E-4	6.8E-4	6.8E-3	6.8E-2	0.68
Total attenuation [dB/m]	1.7E-3	5.3E-3	1.7E-2	2.7E-2	5.3E-2	0.17	0.59	2.3
Total attenuation [dB/2000 m]	3.3	11	33	53	107	347	1190	4686
% of attenuation caused by CFRP	97 %	97 %	96 %	96 %	96 %	93 %	86 %	69 %

The largest difference between ACCC and typical coaxial cables is the high resistance inner conductor. While this does not change the direct nature of the conductor from a coaxial theory perspective, it will cause losses that can be problematic in a long structure such as a high voltage transmission line.

The way around the problem is to inject a higher voltage pulse, or use a longer pulse length, or both. The typical commercial TDR equipment has an output voltage of approximately 3 V. The big advantage of using a longer pulse is that the attenuation is significantly less because attenuation is a function of frequency. Increase in voltage does not decrease the attenuation; it only increases the amplitude of the reflected pulse in proportion to the increase in the initial pulse. However, both a higher voltage and longer pulse may be needed.

It is a common misunderstanding that a long pulse results in a less accurate measurement of the fault location than a short pulse. The TDR uses the rising edge of the pulse to locate the fault. The distance measurement is performed from the rising edge of the initial pulse to the leading edge of the reflected pulse, and the accuracy is not affected by the pulse length. However, a longer pulse can make it more difficult to locate separate faults that are close to each other. This still does not decrease the resolution or the

sensitivity; the only difference is that the two reflections might overlap each other to some extent (see Figure 165) (Radiodetection 1997).

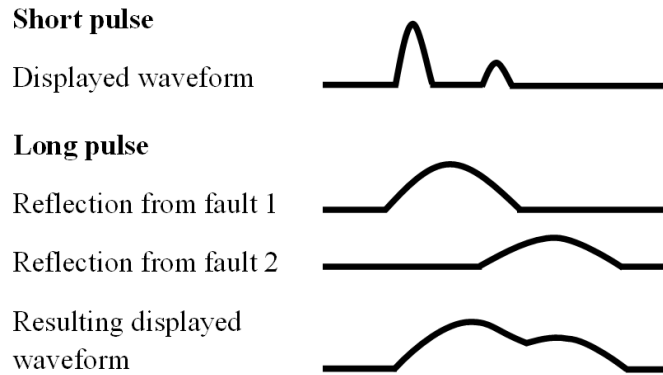


Figure 165: Reflections from a short pulse and a long pulse for the same two faults. Based on (Radiodetection 1997).

8.2 Experimental work

Experiments were performed to evaluate the viability of TDR for structural health inspection and monitoring of ACCC conductors, and to validate the calculations for characteristic impedance, VOP, and attenuation. The TDR used was a Riser-Bond model 1205 with WaveView software installed on a laptop computer. A Fluke ScopeMeter model 162 was used to confirm the voltage of the pulses and reflections.

All the experimental work was performed using a 22 m long section of ACCC. The pulse lengths used were 1 ns, 10 ns, and 100 ns. The available equipment can also generate pulse lengths between 1 μ s, and 4 μ s. The pulse takes a certain amount time – and thus distance – to launch. This distance is called the “blind spot”. It is much more difficult to locate a fault in the blind spot, as the reflection and the initial pulse will be combined in the final waveform. Therefore, the ACCC was connected to the

measurement equipment with a commercial metallic coaxial cable to overcome this blind spot. For pulse lengths of 100 ns and lower, a 15 m long impedance-matched metallic coaxial cable was used. For pulse lengths of 1-4 μs , an additional 250-1000 m of standard metallic coaxial cable would be needed between the instrument and the ACCC to accommodate the longer pulse length. At a pulse length of 4 μs , the blind spot is approximately 600 to 800 m.

The waveforms presented in this dissertation are single measurements from the TDR. The waveforms are not averaged, filtered, or conditioned in any other way. The repeatability is very high, as expected from a setup that is basically an electric circuit.



Figure 166: Connection between metallic coaxial cable and ACCC cable.

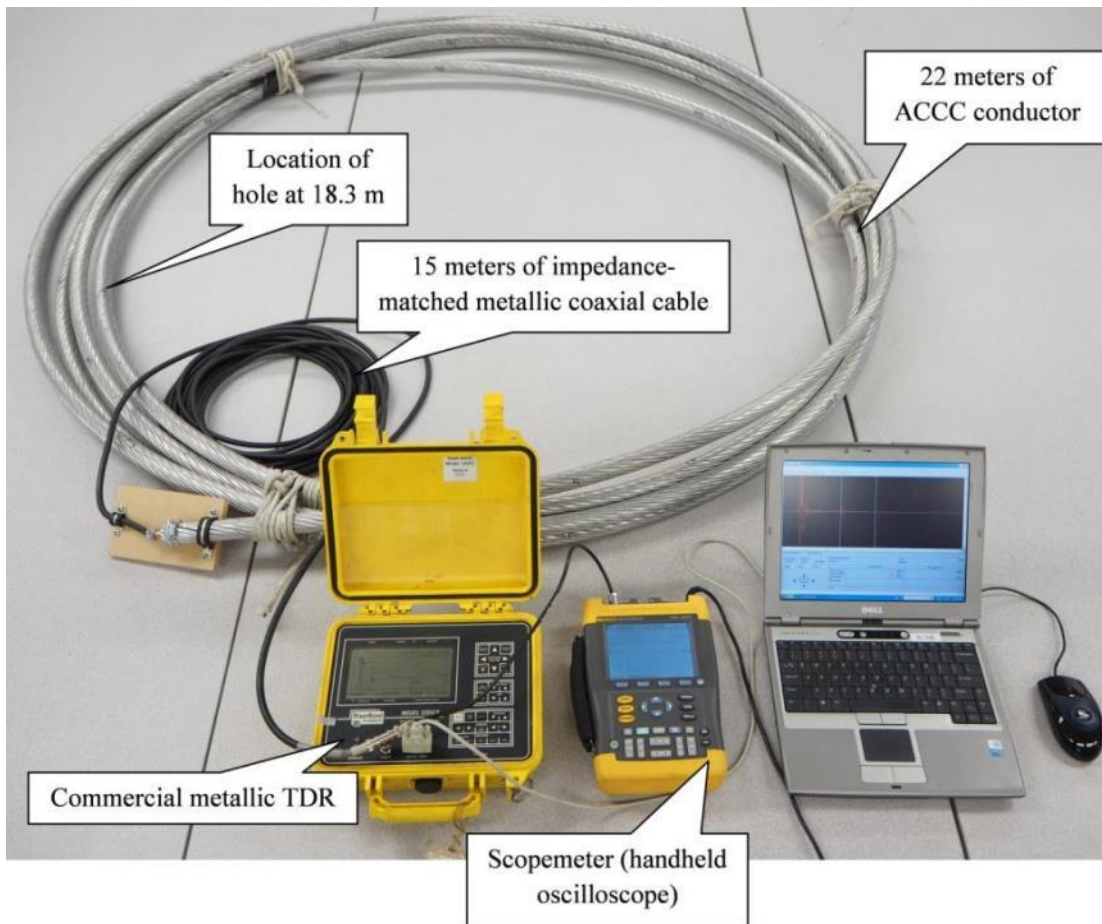


Figure 167: Experimental setup

8.2.1 Characteristic impedance

The characteristic impedance was measured using a commercial impedance analyzer. Table 21 lists the measured impedance as a function of frequency. The measured impedance of 13Ω at 70 Hz agrees well with the calculated value of 10.1Ω , which was calculated using 8.1-2A that ignores the frequency part on 8.1-1. The results from the higher frequencies indicate that the characteristic impedance may be affected by frequency. This will be discussed further in subsequent sections. It is important to note that the values presented in the table below are affected by the metallic coaxial cable

connecting the impedance analyzer to the ACCC, but it is unknown how and to what degree it has affected the measurements.

Frequency [Hz]	Impedance, Z [Ω]
71	13
143	21
287	46

8.2.2 VOP and attenuation

The reflections from the open end and the shorted end of the ACCC were used to validate the calculations for VOP and attenuation. The VOP in the ACCC conductor was estimated to be 47.1 % of the speed of light in section 8.1.4.

Figure 168 shows the waveforms from open and shorted ends at sub-nanosecond, 10 ns pulse length, and 100 ns pulse length. When VOP is set to 47.1 % in the software, the distance from the beginning to the end of the ACCC shows the correct length of 22 m. This confirms that the calculated VOP is correct.

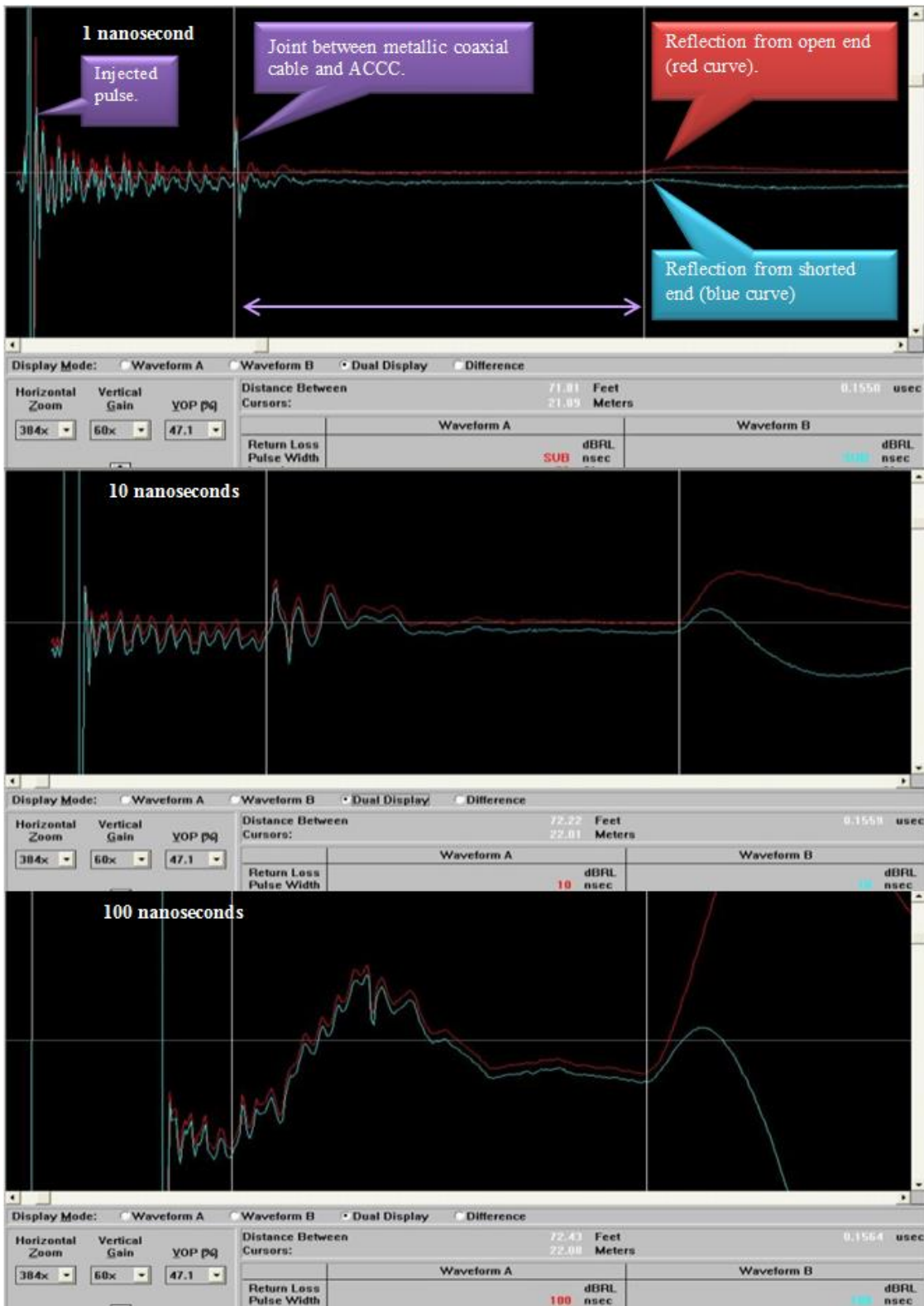


Figure 168: Waveforms for sub-nanosecond, 10 ns, and 100 ns pulse lengths.

The reflected pulse was also used to estimate the attenuation in the ACCC cable. The waveforms in Figure 168 are plotted on the same scale. With a similar amplitude of the initial pulse, the 10 ns (50 MHz) pulse generates a much larger reflection from the end of the ACCC conductor than the 1 ns (500 MHz) pulse, and the 100 ns (5 MHz) pulse generates an even larger reflection. This agrees with the assumption that the attenuation is strongly dependent on frequency.

Further analysis of the reflections from the open end gives a quantitative measurement of the attenuation. Figure 169 and Figure 170 compare the reflections from 1 ns, 10 ns and 100 ns pulse lengths. The reflection from the 1 ns pulse is so weak that it is only visible at large magnification (Figure 170). 99.8 % of the signal was lost with a pulse length of 1 ns, 95.3 % at 10 ns, and only 53.1 % at 100 ns. According to the calculations based on (8.1-6) and (8.1-7) that were presented in Table 2, the predicted loss of signal strength over 44 m (22 m times two as the signal has to travel both ways) is 2.0 to 3.8 times higher than the measured loss (Table 22).

The calculation discrepancy likely originates from the assumption that the characteristic impedance is independent of frequency. The measurement with a commercial impedance analyzer showed that this is an incorrect assumption; the characteristic impedance of ACCC is clearly a function of frequency. This is good news for the viability of the TDR as a method for structural health monitoring of composite core conductors; higher characteristic impedance means lower attenuation, as can be seen in (8.1-6) and (8.1-7).

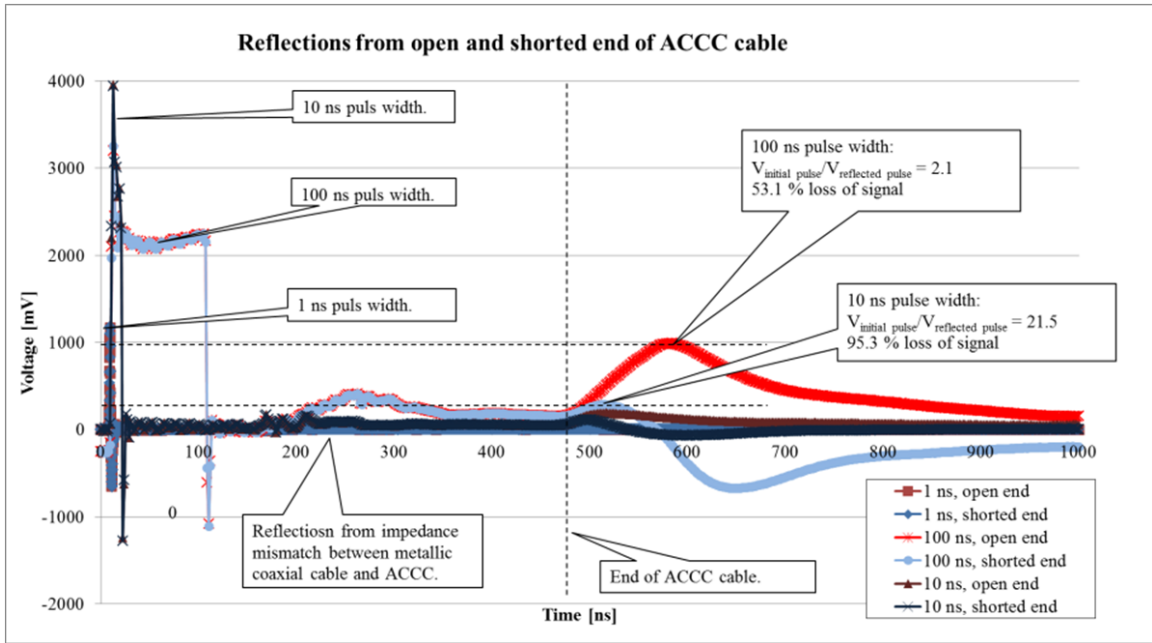


Figure 169: Reflections from open and shorted end of ACCC cable.

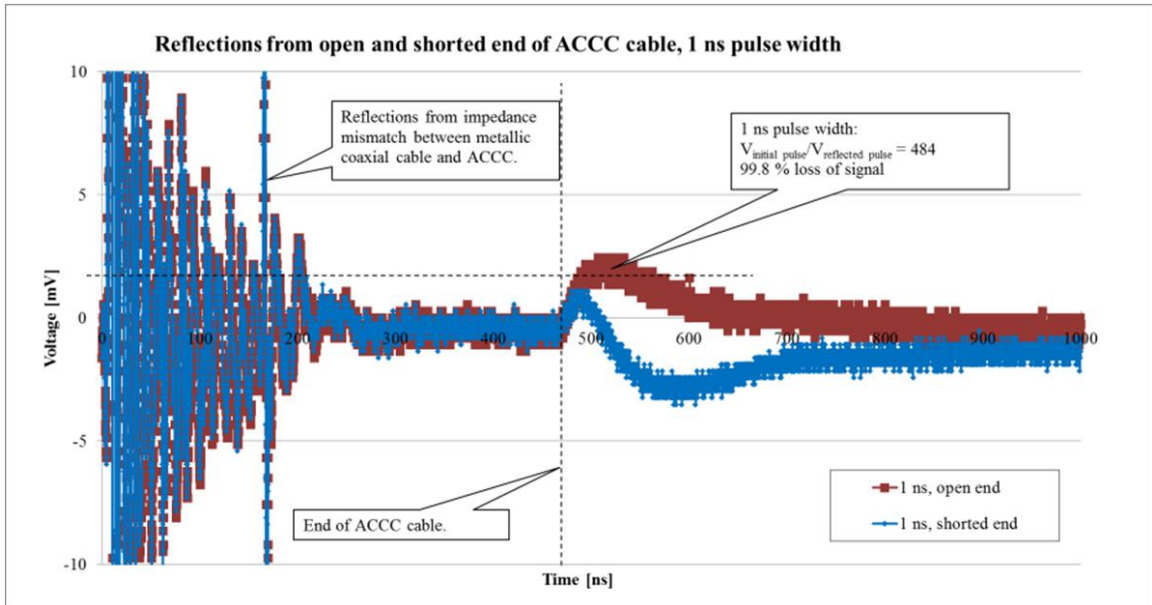


Figure 170: Reflection from open and shorted end of ACCC cable with 1 nanosecond pulse length.

Table 22: Measured vs. Predicted attenuation (expressed as loss in voltage)			
Pulse length	100 ns	10 ns	1 ns
Frequency	5 MHz	50 MHz	500 MHz
Ratio V_{in}/V_{refl}	2.13	21.5	484
Loss of signal	53.1 %	95.3 %	99.8 %
Attenuation:			
Experimental [dB/m]	0.075	0.30	0.61
Predicted [dB/m]	0.17	0.60	2.3
Attenuation over 200 m:			
Based on experimental data [dB]	150	606	1220
Predicted [dB]	347	1190	4686
Ratio Predicted/Experimental	2.3	2.0	3.8

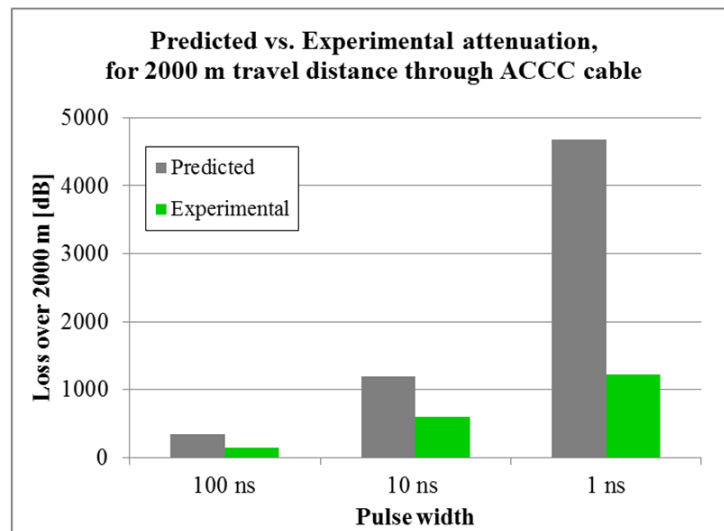


Figure 171: Predicted vs. Experimental attenuation, extrapolated to 2000 m of travel distance through an ACCC cable.

8.2.3 Detection of galvanic corrosion and other faults

The next experiment assesses the capability of the method to detect faults in the conductor. Small holes were drilled through the aluminum and the fiberglass barrier of the ACCC cable at two locations: 9.1 m (30 ft) and 18.3 m (60 ft), measured from the beginning of the ACCC cable. Three different materials were inserted in the holes to create short circuits between the CFRP and the aluminum: a metal probe (Figure 172), a paper rod soaked in 3.5 mass % NaCl aqueous solution (Figure 173), and a paper rod

soaked in saturated NaCl solution. The fault detection measurements were performed using 100 ns pulse length.



Figure 172: Metal probe inserted to make electrical contact between the Al and the CFRP.



Figure 173: Paper rod soaked in NaCl solution inserted to make electrical contact between the Al and the CFRP.

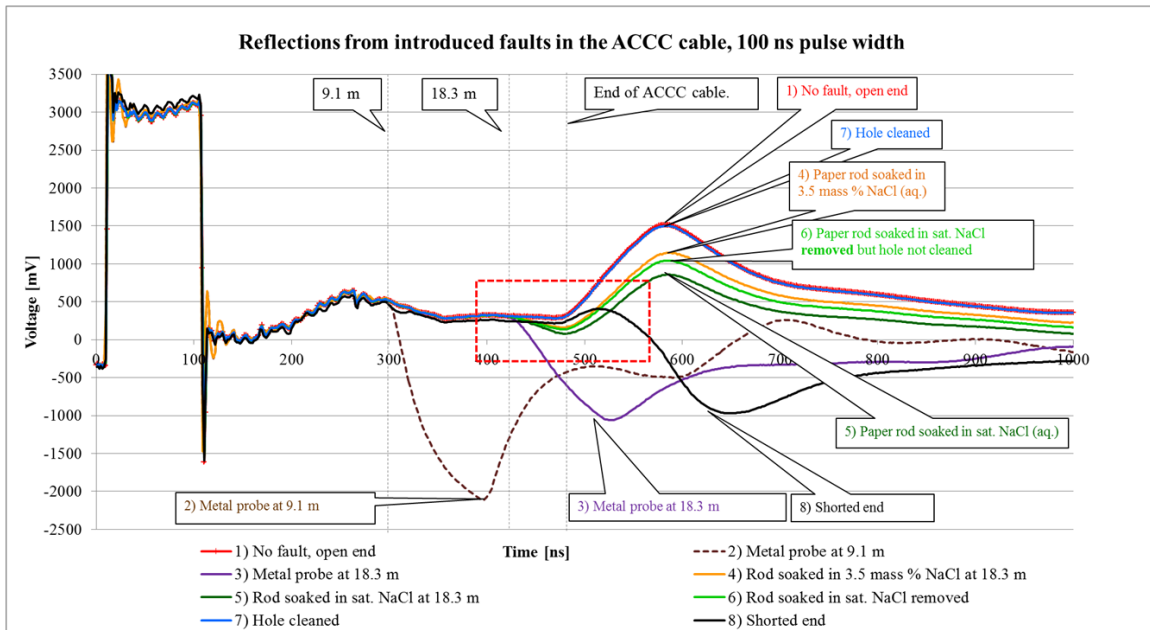


Figure 174: Reflections from different introduced faults.

Figure 174 shows the reflected waveforms from the introduced faults. The metal probes 2) and 3) give distinct reflections, very similar to a shorted end 8). The electrolyte bridges, created by making contact between the CFRP and aluminum with a paper rod soaked in aqueous NaCl solution, give much weaker reflections. This is expected as these bridges have much higher resistance than the metal probes. The area within the red box in figure 11 calls for a closer analysis, which is found in Figure 175.

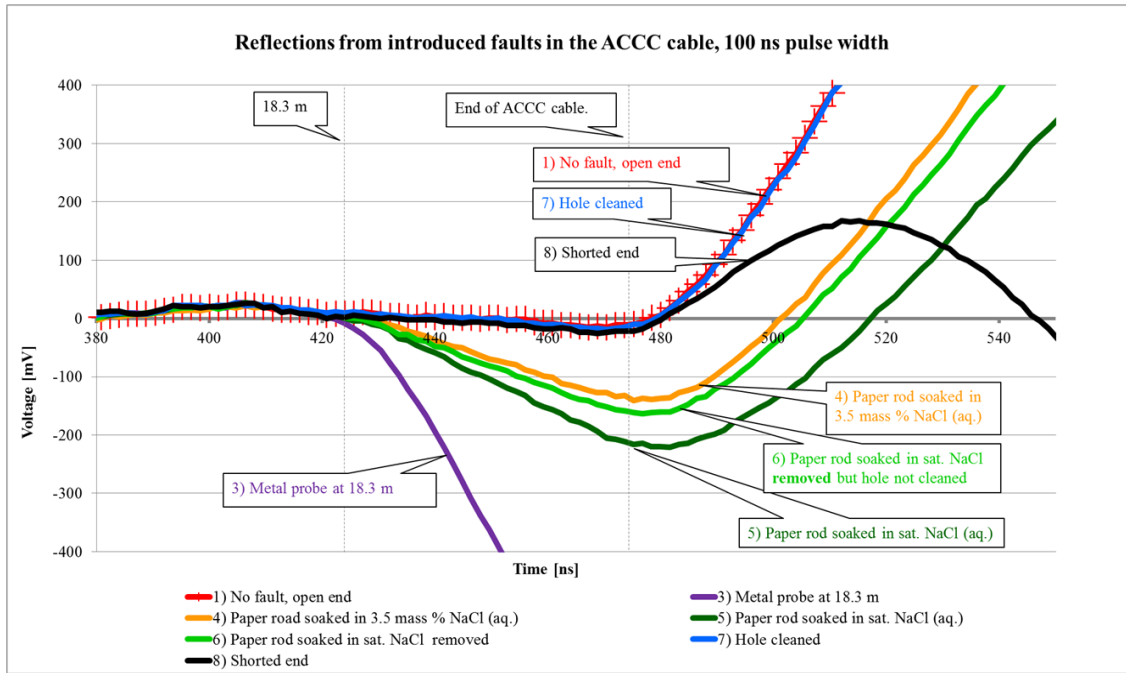


Figure 175: Reflections from different introduced faults.

The reflections from the electrolyte bridges are quite intriguing. Although much weaker than those from the metal probe, the reflections are distinct. The difference between 4) and 5) demonstrates that a higher NaCl concentration, and thus higher conductivity, gives a stronger reflection. In the case of the saturated NaCl solution 5), the solution left in the hole after the wet paper rod had been removed resulted in a very similar but slightly weaker reflection 6). After careful cleaning of the hole with distilled water, the reflection 7) is indistinguishable from the original state with no fault 1).

8.3. Discussion

ACCC is quite different from normal coaxial cables used for cable-TV and other radio frequency applications. Its inner conductor was never intended to be used as a conductor, and the complete cable has a much higher attenuation than coaxial cables with all-metal conductors. The high resistivity of the CFRP core is responsible for the very high attenuation. However, based on the data presented in this dissertation, inspection and monitoring of ACCC using TDR appears to still be possible.

The main solution to the attenuation is a longer pulse length. The trend in the experimental data is that the actual attenuation is approximately half of the mathematically predicted attenuation. Assuming that this relation holds for pulse lengths longer than 100 ns, the attenuation would be 26.5 dB over 2000 m for 4 μ s pulse length and 16.5 dB for 10 μ s pulse length. Because the coaxial cable connecting the TDR to the ACCC conductor has to be at least as long as the blind spot, 10 μ s is perhaps the longest practical pulse length. The pulse travels approximately 1500 meter in 10 μ s (exact value depends on the VOP of the specific cable used). Although there are coaxial cables that are lighter than normal cable-TV cables, 1500 m of coaxial cable will still be cumbersome to transport. However, there may be a better engineering solution other than an extension cable that will allow for a longer pulse length, but this is yet to be determined. 16.5 dB loss over 2000 m means that the amplitude of the return reflection from a hard short circuit such as a shorted end is $1/10^{1.65}$, or $1/45^{\text{th}}$ of the original voltage of the signal. This is of the same order of magnitude as the ratio of input voltage to

reflection voltage for the 10 ns pulse length in Figure 171, which was 1:21.5. This ratio was clearly measurable, and a ratio of 1:45 is most likely also measurable.

An additional challenge is that faults of interest such as galvanic corrosion may give a weaker reflection. However, it needs to be emphasized that the voltage used in the measurements in this study was only approximately 3 V. Electrolytes are non-linearly conductive, and a higher voltage will most likely result in a stronger reflection. Because this is a high-voltage power line system and does not contain sensitive equipment such as phones which are typically found in regular coaxial cable systems, the pulse amplitude for a TDR used in ACCC can be hundreds of volts or even higher. Other techniques such as filtering and averaging of multiple measurements can also be used to increase the sensitivity and reduce noise.

The ability to detect other faults that do not result in an electrical connection between the CFRP and aluminum needs to be further investigated. Such faults are for example partial fractures, loss of aluminum or fiberglass, water absorption of the fiberglass, gunshot damage, crushing or bird-caging. All these faults will cause a local change of the conductor impedance, and should theoretically be detectable. However, no firm conclusions about these kinds of faults can be drawn from the data presented here.

8.3.1 Applications of TDR on ACCC and similar cables

Figure 176 illustrates four potential uses of TDR in the evaluation and monitoring of ACCC transmission line conductors:

- In case a), the conductor is inspected on the reel as delivered from the manufacturer. The inspection only needs to be performed from one end of the conductor.
- In case b), the conductor is monitored in real-time as it is rolled off the reel and installed on the towers. The inspection needs to be done from the inner reel end of the conductor. The monitoring can be continuously recorded. The system can, for example, include an alarm that will sound if the device detects a new fault. Time and place of the fault can be recorded so it can be repaired.
- Inspection of the conductor after installation but before energizing is illustrated in case c), while case d) illustrates continuous monitoring during service.

Monitoring of energized transmission lines will require modifications and adaptations of the TDR such as protection from electromagnetic interference. The equipment must also be designed to protect the operator.

The TDR apparatus needs to have electrical access to the carbon core. This can easily be provided in future installations through the design of the so called “dead end” (the end sleeve where the conductor is crimped and then attached to the insulator which in turn is connected to the tower). In already installed conductors, the core can potentially be accessed without compromising the strength by making a hole through the dead end to access the conductor end. Alternatively contact can be made by drilling a tiny hole

through the dead end into the core and make a so called “vampire tap” by inserting a probe to the core that is insulated with the exception of the very tip.

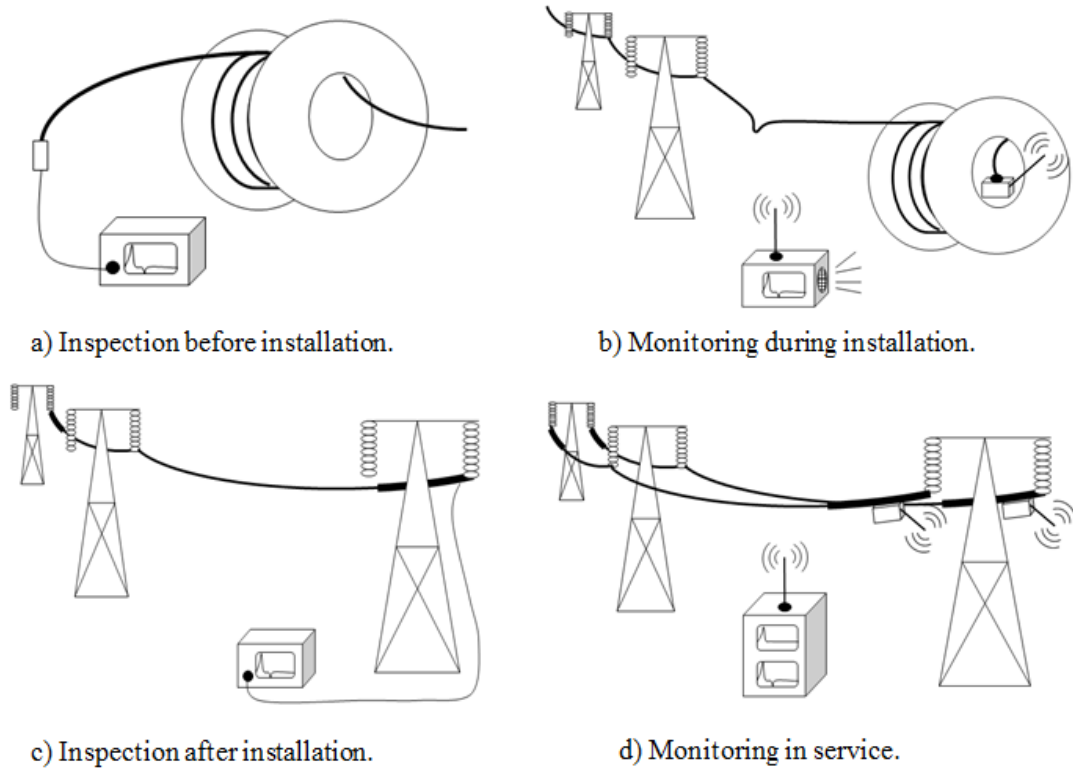


Figure 176: Potential applications of TDR on ACCC.

8.4 Chapter conclusions

It has been shown in this chapter that TDR can be used to find faults such as short circuits and electrolyte bridges between the CFRP and aluminum in a 22 m section of ACCC cable. Numerical modeling predicts that at least 1000 m of ACCC conductor can be inspected using a pulse length of approximately 10 μ s.

It is likely that TDR can be used to detect other faults of interest such as partial fractures, loss of aluminum or fiberglass, water absorption of the fiberglass, gunshot damage, crushing or bird-caging, but this has to be studied further.

Several potential future applications of TDR for structural health monitoring of overhead transmission lines with ACCC conductors have also been presented in this chapter:

- 1) Inspection of the conductor *before* installation to detect manufacturing faults or damage due to mishandling, and to determine the exact location of the fault on the reel. It can also be used to measure the length of the conductor on the reel.
- 2) Monitoring of the conductor *during* installation. If the conductor is for example over-bent and fractured, this can be detected in real time.
- 3) Inspection *after installation* but before energizing.
- 4) *Continuously* monitoring a conductor in service.

The method will likely also work for transmission line cables of other brands with similar geometry and electrical properties.

CHAPTER NINE: GENERAL DISCUSSION AND FINAL CONCLUSIONS

Components and structures containing both aluminum and CFRP can have outstanding mechanical properties, but can also be susceptible to galvanic corrosion causing accelerated corrosion of the aluminum. It is well known that aluminum and carbon (in the form of graphite, CFRP, or similar carbon containing, conductive non-metallic materials) form a strong galvanic couple, but it was observed early in this study that the measured galvanic corrosion rate was highly dependent on the testing conditions. It was determined later in the study that the dominating control mechanism was in most cases the transport of oxygen to the cathode (the carbon containing material), which is highly affected by area ratio, geometry, electrolyte agitation and oxygen content. This result, and the work leading up to this conclusion, will be discussed in this chapter.

The combination of aluminum and CFRP is used in many different applications. Two important examples are airplanes and the next generation high-voltage power transmission lines. In the case of the latter, a new design of a HTLS bare overhead transmission conductor has been of particular interest in this study. Due to the higher specific strength, relatively high operating temperature, and the low thermal expansion of the CFRP, the transmission line conductor ACCC utilizing a CFRP core for mechanical strength has greatly improved properties compared to the traditional designs. ACCC can

transmit up to twice the current through the same size and mass conductor, allowing for an increased power transfer without having to upgrade or add more towers.

General engineering practice is to avoid contact between aluminum and CFRP or similar materials in any application where moisture may be present. Although a typical solution is to insulate the CFRP from the aluminum with a layer of fiberglass composite or a polymer coating, it is of great importance to understand the consequences if the two materials accidentally become in contact.

Bare overhead transmission line conductors are exposed to the surrounding environmental conditions without any additional protective covers or coatings. Traditional bare overhead conductor designs such as the bi-metallic ACSR have a known inherent problem with galvanic corrosion between the galvanized steel and the aluminium. As opposed to ACSR, the ACCC conductor design has no inherent galvanic corrosion problem. The CFRP and aluminum in ACCC are separated with an insulating layer of fiberglass composite surrounding the CFRP. However, galvanic corrosion can develop in the ACCC conductor if the fiberglass barrier is compromised and CFRP-to-metal contact is present anywhere in the conductor. As shown by previous research at the University of Denver, the fiberglass barrier can be damaged by over-bending (Burks, Armentrout et al. 2009), impact, fatigue (Burks, Armentrout et al. 2011), or aging (Burks, Armentrout et al. 2011), (Hoffman, Middleton et al. 2015).

While it was suspected that the ACCC can develop galvanic corrosion if the fiberglass galvanic barrier is compromised, no systematic research had been performed in this area before this study was initiated. The rate controlling mechanisms in the corrosion

between aluminum and carbon were also not well understood. Neither was there a good method available to evaluate the problem of galvanic corrosion in bare overhead conductors. Thus, this dissertation set out to find methods to measure the galvanic corrosion performance and to understand the fundamental control mechanisms, which included both innovative experimental and numerical approaches. Additionally, it also set out to find a method of detecting galvanic corrosion in ACCC conductors.

This chapter will summary and discuss the findings in each of these areas, but will first describe the impact that this work has already had on the field of knowledge.

Impact of this work

Overall, this dissertation presents a broad array of innovative methods, numerical analyses, and experimental results that has led to an improved understanding of the galvanic corrosion of aluminum/carbon composite systems. The work has also provided much needed methods for the evaluation of galvanic corrosion in current and new transmission line conductor designs. It has also provided a promising proposal for the structural health monitoring of carbon fiber composite core conductors, for which a patent application is being prepared. The possibility of inspection and monitoring is crucial for the wider acceptance of the ACCC conductor and similar designs.

This comprehensive research has significantly contributed to the increased acceptance of composite core supported bare overhead transmission line conductors in both the United States and worldwide. The knowledge gained in this study is already aiding the evaluation and design of future conductor designs. It is also helping to predict

and prevent galvanic corrosion in many applications utilizing aluminum/carbon composite systems.

In-situ measurement of galvanic corrosion currents

The first part of this study was focused on developing a method for the in-situ galvanic corrosion testing of bare overhead transmission line conductors of various designs, but with particular focus on impact damaged ACCC conductors. The assessment method was originally developed during the author's master's work (Håkansson 2013), (Håkansson, Predecki et al. 2015), but was further improved in this dissertation work (Håkansson 2015), (Håkansson, Ricker et al. June 2016), (Håkansson, Hoffman et al. In preparation). This work was presented in Chapter 3. The outcome of the work was a method for real-time measurements of galvanic corrosion currents in conductor samples while retaining the original geometry of the conductors.

The damage to the fiberglass composite barrier was introduced by splitting the conductor core in the axial direction. This resulted in a large exposed area of CFRP (the area ratio of aluminum to CFRP was 1:28). The conductor sample was assembled to the original geometry (with the core being surrounded by the aluminum strands) and the galvanic corrosion current density rate was measured. A similar sample design was utilized for the traditional bi-metallic conductors ACSR and ACSS, but an insulating polyester mesh sleeve was inserted between the steel core and the surrounding aluminum strands to separate the materials while retaining the original geometry. The electric circuit was completed through an external measurement instrument.

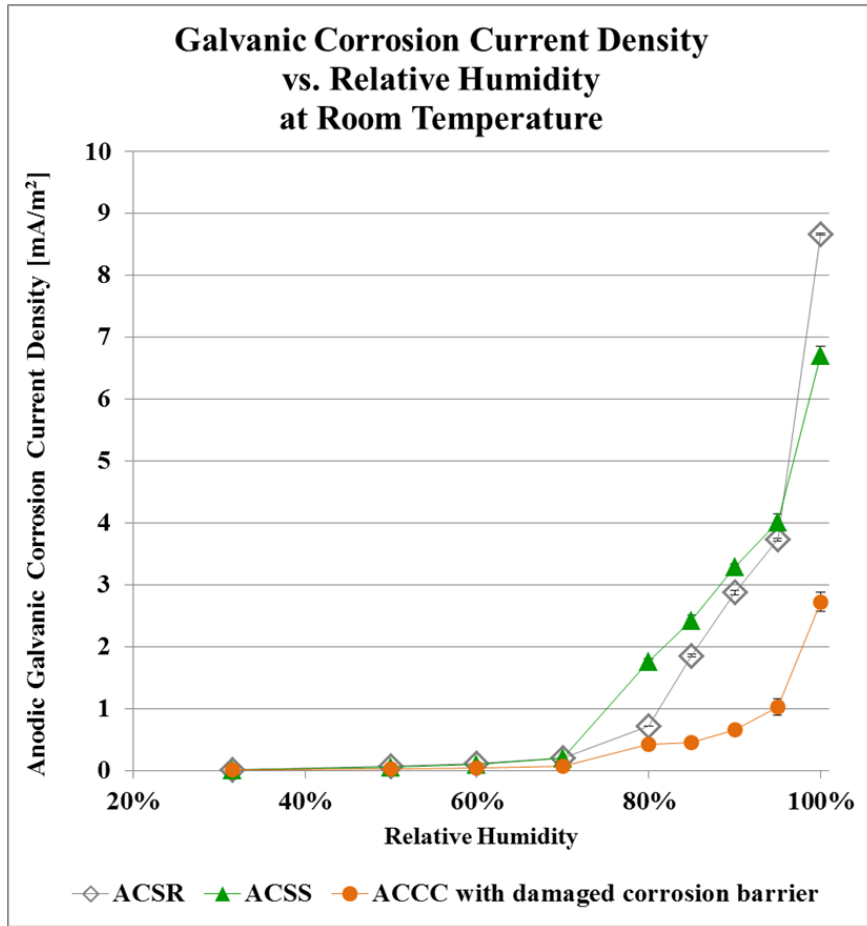


Figure 70 (repeated): Galvanic corrosion current density of corroding aluminum strands as a function of relative humidity for three different conductor designs.

Figure 70 above illustrates the galvanic corrosion current density of the corroding aluminum strands as a function of RH after exposure to 3.5 mass % NaCl aqueous solution and drying in room air. In general, the corrosion current displays an exponential dependency on the RH, a behavior that also has been reported in the literature. The results from the tested environments showed that even with a severely compromised galvanic corrosion barrier, the galvanic corrosion rate in ACCC was similar or lower than the inherent galvanic corrosion in ACSR. This is all good news for the ACCC conductor

from a corrosion perspective. With an intact corrosion barrier, the ACCC cannot develop galvanic corrosion because there cannot be an electrolytic contact between the CFRP and the aluminum.

It was also found that for the ACCC conductor with a compromised fiberglass barrier, humid corrosive environments may result in a higher galvanic corrosion rate than immersed conditions. This observation prompted intensified work to determine the rate controlling mechanisms in the galvanic corrosion process.

Experimental characterizations

Before starting the work to determine the rate controlling mechanisms, an experimental characterization was performed on the materials of interest for this study. The focus was on four different materials: CFRP from the ACCC conductor, Al 1350-O from the ACCC conductor, Al 6061-T6, and solid graphite. Materials from several other transmission line conductors were also included in the galvanic series (Figure 71, repeated below). The experimental characterization determined that CFRP and graphite were both more noble than all the tested metals.

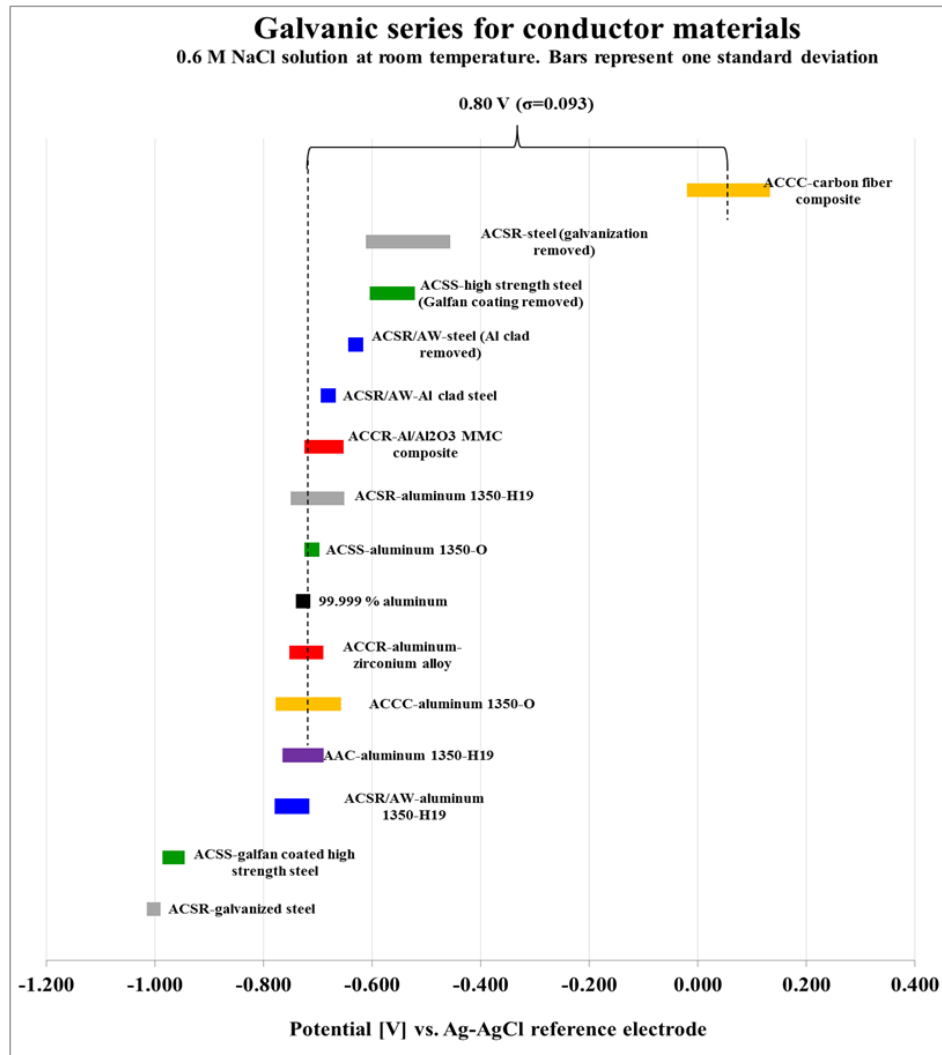


Figure 71(repeated): Galvanic series for materials of interest in this study in 0.6 M NaCl at room temperature, vs. Ag/AgCl reference electrode. Acronyms refer to common conductor types and are explained in Appendix A. The difference in corrosion potential between CRFP and aluminum from the ACCC conductor is highlighted.

Cathodic control

Through the extensive experimental work presented in Chapter 4, it was concluded that the galvanic corrosion of the aluminum/carbon couple (“carbon” represents both solid graphite and CFRP) is under *cathodic control*. This means that the total galvanic corrosion rate is controlled by the rate at which dissolved oxygen arrives at

the carbon surface. A large number of galvanic corrosion measurements were performed in 0.6 M NaCl aqueous solution. The lowest cathodic galvanic corrosion current density was measured in oxygen-starved electrolyte, while the highest was measured when a jet of electrolyte with a velocity of 1 m/s was directed onto the cathode surface. The lowest cathodic current density was 9 mA/m², while the highest was 10 662 mA/m². The difference is a factor of 1 184, or more than 3 orders of magnitude! This clearly illustrates the necessity of designing the test setup to closely simulate the real service environment. If the test setup does not represent the service environment for the component, the galvanic corrosion rate may be grossly over or under estimated.

Cathodic control also means that the total galvanic corrosion rate is determined by the exposed carbon area, and is independent of the exposed aluminum area. The implication of this discovery is that in order to prevent corrosion damage, the exposed carbon area should be minimized. *Decreasing* the carbon area will *decrease* the total galvanic corrosion rate, and thus decrease the loss of aluminum. If the aluminum area is *decreased* and the carbon area is *left unchanged*, the total galvanic corrosion rate will stay the same. The result would be an *increased corrosion penetration* rate of the aluminum because the same amount of mass loss will occur on a smaller aluminum surface. This is an important finding.

Effect of geometry, area ratios, and oxygen supply

A selection of galvanic corrosion rates measured in this work is summarized in Figure 177. The galvanic corrosion rates are expressed in average anodic galvanic

corrosion current density for area ratios, geometries, and electrolyte properties that were of particular interest.

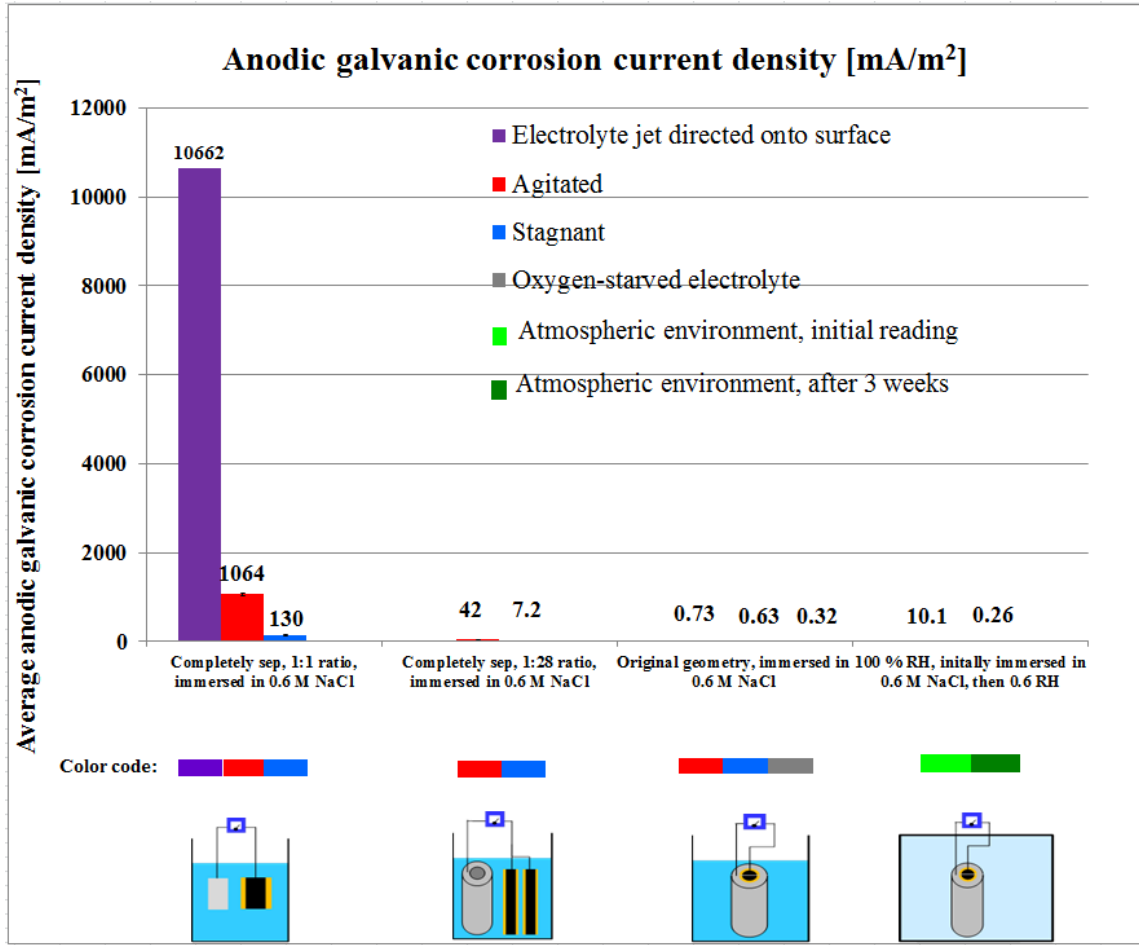


Figure 177: Summary of measured galvanic corrosion rates, mA/m².

In Figure 178, the galvanic corrosion rates are translated into average corrosion penetration rate of the aluminum. This assumes that the corrosion is uniform. Aluminum in neutral electrolytes develops pitting corrosion, which means that the corrosion is localized. The local corrosion penetration can therefore be much deeper than the plot indicates, but the average corrosion rates still represent the total mass loss of the aluminum.

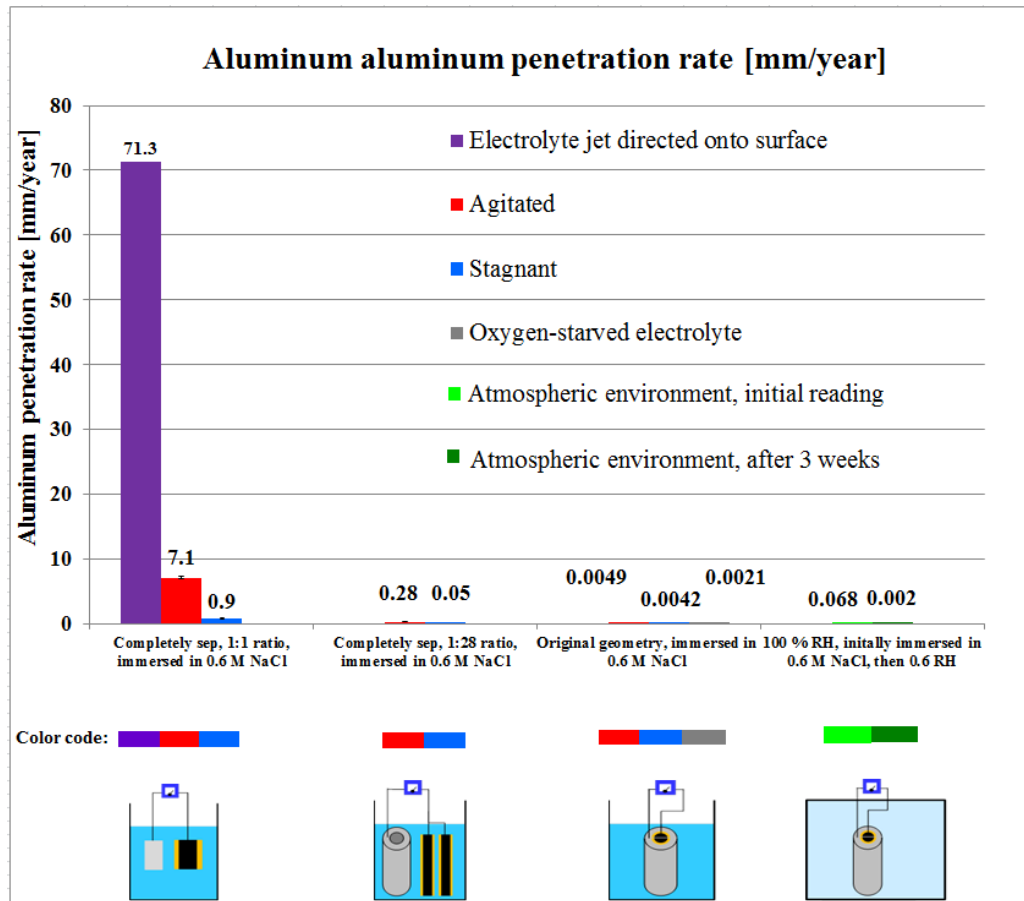


Figure 178: Summary of measured galvanic corrosion rates, mm/year.

It may be hard to comprehend what these rates would mean to a transmission line conductor. Using a failure criterion that assumes that a transmission line conductor is considered failed when it has lost 20 % of its aluminum cross-section, we can translate the above corrosion rates into time-to-failure. Figure 179 illustrates the time-to-failure using this criterion. The importance of a suitable testing method is obvious in the plot. Just by changing the area ratio, geometry, electrolyte agitation, surface preparation, and level of dissolved oxygen, the same materials immersed in the same electrolyte will have a predicted time-to-failure of 35 hours to 130 years. That is a difference of more than four

orders of magnitude! The difference in atmospheric conditions is also more than an order of magnitude depending on the surface preparation.

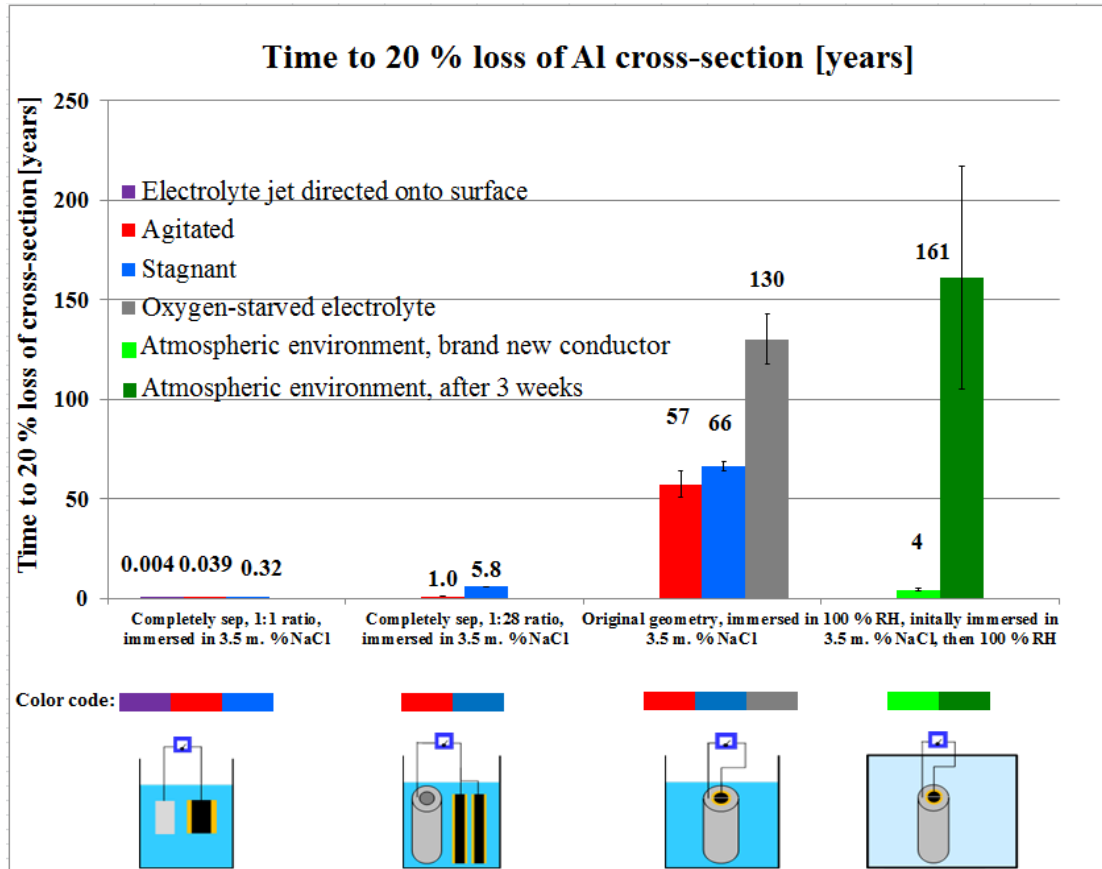


Figure 179: Summary of measured galvanic corrosion rates translated into time-to-failure for an overhead transmission line conductor.

Numerical modeling

Four different numerical models were developed to further investigate the rate-controlling mechanisms in aluminum/carbon couples. Two of the models were for immersed conditions and two were for atmospheric conditions.

Chapter 6 presented the two numerical models for immersed conditions along with two physical validation models. They all had an identical parallel plate configuration

and represented an immersed service environment such as an offshore oil drilling rig. There were two variables in both the numerical models and the physical validation models: 1) the distance between the electrodes that was varied from 25 mm to 200 mm, and 2) the NaCl concentration in the electrolyte that was varied from 0.0017 M (0.01 mass %) to 0.6 M (3.5 mass %) NaCl. The first numerical model was designed with an analytical approach, but had to be solved through numerical iteration because of the IR drop being a function of the galvanic corrosion current, which in turn is dependent on the IR drop. The second numerical model had the identical configuration and input values, but was a finite elements model solved with the commercial software package Comsol Multiphysics.

In the first validation model, the two electrodes were immersed in a bulk electrolyte. This allowed for possible mass transfer between the electrolyte volume separating the electrodes and the bulk electrolyte through direct and indirect paths. This is referred to in this section as the *open* electrolyte volume. In the second validation model, the electrolyte volume separating the electrodes was enclosed so that transfer could only occur in a direct path between the parallel electrodes. This is referred to as the *enclosed* volume. The two models are shown in Figure 119 and Figure 124, which are repeated below.

There was good agreement between the numerical models and the physical validation models. The galvanic corrosion rates measured in the physical validation models straddled the results from the two numerical models. The physical model with the *open* electrolyte volume resulted in galvanic corrosion rates that were higher than both

numerical models. The general trend for the physical model with the *enclosed* electrolyte was lower galvanic corrosion rates than both numerical models. The enclosed volume generated consistently lower galvanic corrosion rates than the open volume. This is believed to be due to the enclosure preventing self-convection of the electrolyte and thus eliminating the supply of oxygen-rich electrolyte from the bulk volume. This observation provides additional support that the oxygen transport is the dominant rate-limiting mechanism.

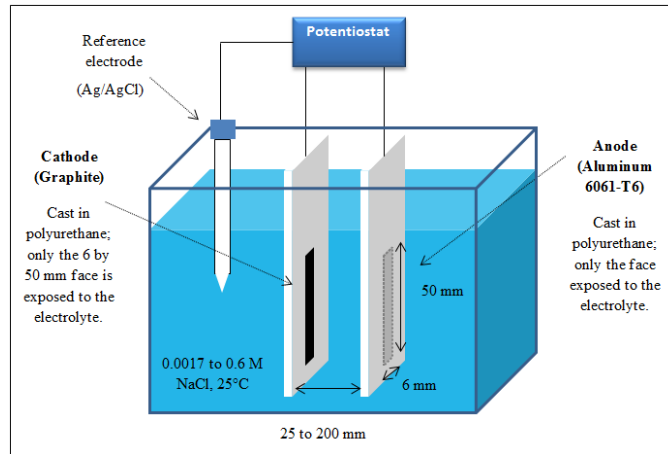


Figure 119 (repeated): Validation experiment for parallel electrode model.

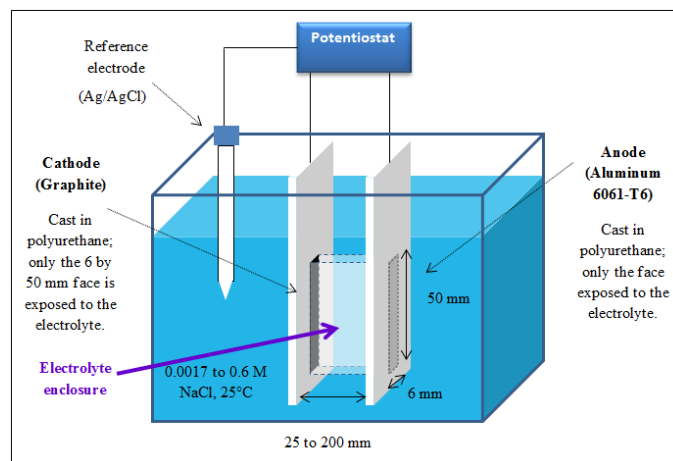


Figure 124 (repeated): Validation experiment for parallel electrode model with enclosed electrolyte volume.

Chapter 7 presented the two different numerical models for atmospheric conditions. While atmospheric galvanic corrosion follows the same fundamental principles as immersed galvanic corrosion, it is a special case where the reactions take place in a very thin electrolyte layer with a thickness on the order of a few μm . The first model was a static steady-state model with resistance and oxygen diffusion as the rate controlling mechanisms. The input values for the reaction kinetics were experimentally obtained. The second model was time-dependent with corrosion product formation increasing the oxygen diffusion path length as the rate controlling mechanism. The model used an experimentally obtained galvanic corrosion rate as its upper boundary condition, and experimentally obtained values for corrosion product generation.

The steady-state model predicted that the galvanic corrosion rate should be the highest near the cathode. This is known from literature and could also be observed through microscopy of corroded samples. The predicted galvanic corrosion rates for one specific salt load density were compared to experimental measurements. The chosen salt density was 3.1 g/m^2 , which is the resulting salt load density when an ACCC conductor sample is immersed in 0.6 M NaCl and then dried. The predicted galvanic corrosion rate at 100 % RH is within the range of measured values, as can be seen in Figure 158 (repeated below). However, the measured values vary dramatically depending on the exact testing conditions.

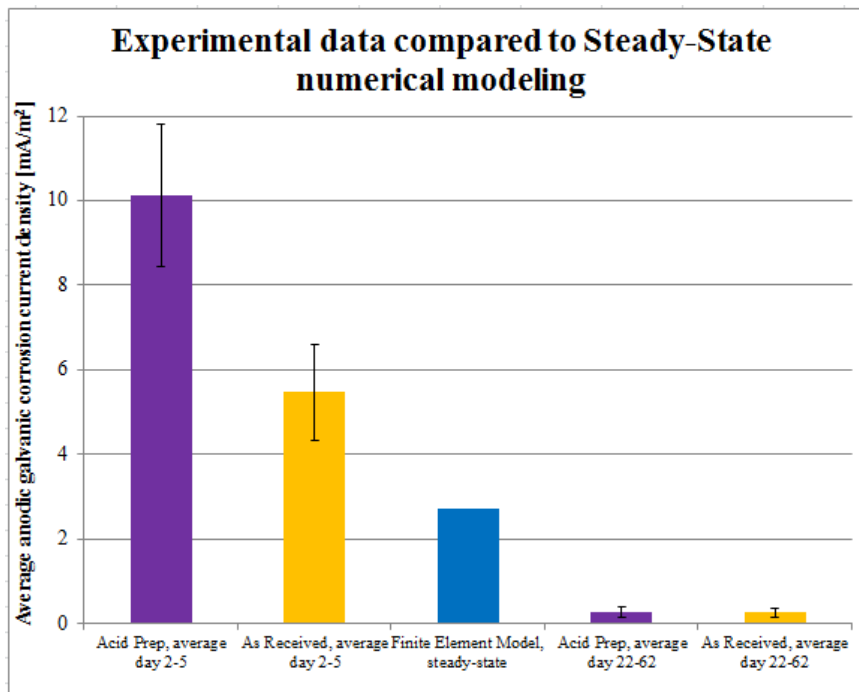


Figure 158 (repeated): Comparison of the steady-state FE model with experimental values.

When the samples are brand new and initially treated with phosphoric acid to remove the oxide layer (“Acid Prep” in the above figure), the measured value is higher than the predicted. When the original oxide layer and scale is left intact, the value is lower than the predicted. The test series presented in Chapter 3 generated drastically lower values than the prediction. These samples were from a conductor reel that had been stored outdoors for over 10 years and may have formed a thick passive layer. Figure 158 also includes values from conductors that had been exposed to 100 % RH for several weeks and were filled with Al(OH)₃ gel. These generated much lower galvanic corrosion rates than the numerical model.

It can be concluded that the steady-state model provided a prediction that was within range of the measured values at 100 % RH and 3.1 g/m². The predicted rate is

good for a new sample in a very early stage of corrosion, but is not accurate for samples that have accumulated corrosion products or formed a stable oxide layer on the aluminum surface. This illustrates the active-passive behavior of aluminum and the difficulty to predict its corrosion rate. This model can only represent the ACCC conductor with a compromised galvanic corrosion barrier when it is brand new. Because the conductor is full of narrow crevices that will collect corrosion products and pollutants, additional limiting mechanisms will soon appear. This will make the model inadequate beyond the first few days or perhaps weeks.

Comparing the shape of the curve for the finite element model results with the measured values indicates that there are additional control mechanisms that are not considered in the model. The experimental data exhibits an exponential trend with rapidly increasing galvanic corrosion with increased RH levels (see Figure 159, repeated below). The numerical data, on the other hand, increases with increasing RH, but the function has a slightly convex shape. This numerical model can clearly not fully explain the galvanic corrosion mechanism for these conditions. The discrepancy for values below 100 % RH could be caused by the very thin electrolyte layer not being able to form a continuous electrolyte film between the CFRP and the aluminum, resulting in a much higher resistance than predicted, but this hypothesis has not been studied in any further detail.

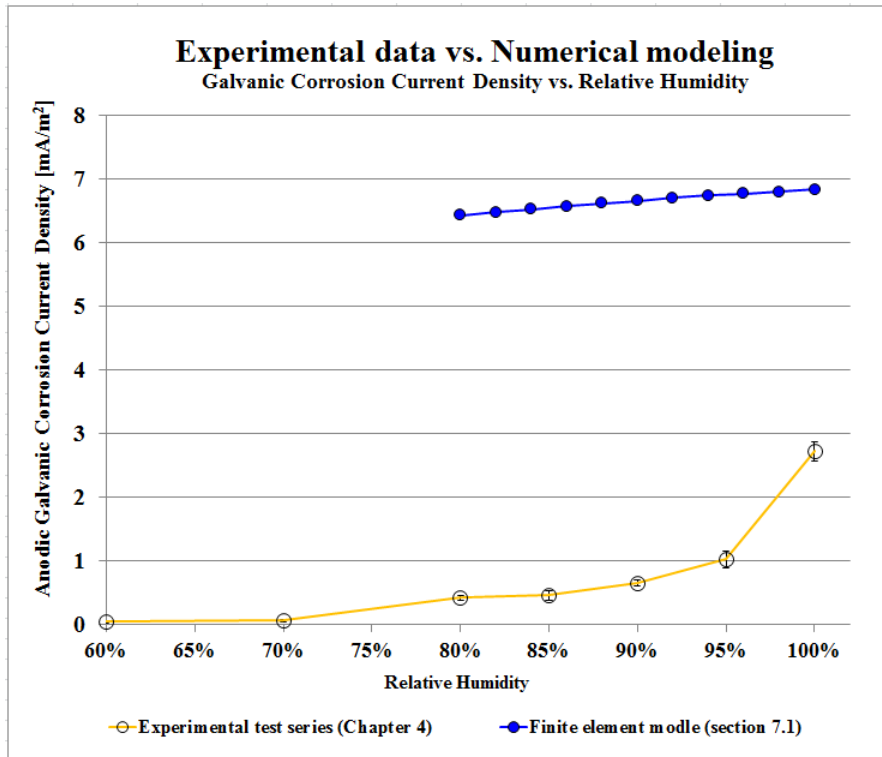


Figure 159 (repeated): Comparison of the steady-state FE model with experimental values.

As mentioned several times before, the galvanic corrosion in the ACCC conductor with exposed CFRP appears to be mostly or completely dominated by the transport of oxygen to the cathode. Experimental measurements indicate that the accumulation of corrosion products in the form of $\text{Al}(\text{OH})_3$ gel appears to very effectively limit this transport. Within a short amount of time (10-14 days in 100 % RH at RT, with a salt load density of 3.1 g/m^2), the conductor will be filled with gel and the galvanic corrosion rate will have decreased one order of magnitude from 6-10 mA/m^2 to approximately 1 mA/m^2 . The resulting galvanic corrosion rate is similar to the rate measured during immersion.

A numerical model was developed based on the hypothesis that the accumulation of corrosion products described above limits the oxygen transport. The predicted values beyond about 10 days agreed well with experimental measurements (see Figure 156, repeated below) and provided very strong support for the hypothesis.

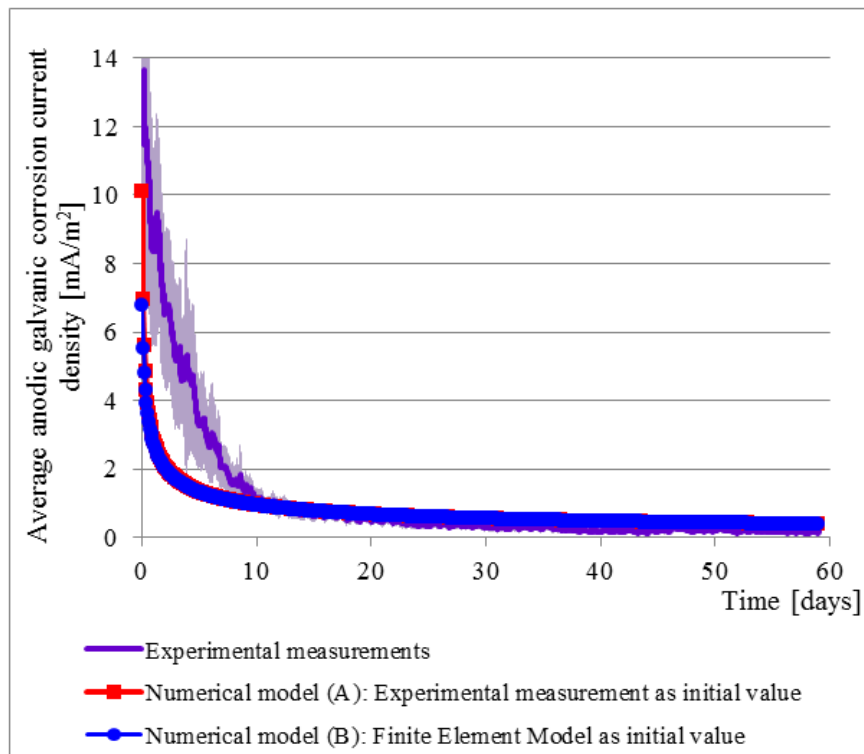


Figure 156 (repeated): Average anodic galvanic corrosion current densities as a function of time. The shaded region represents one standard deviation of the experimental measurements

The observation that the accumulation of corrosion products appears to limit the galvanic corrosion rate is quite interesting. For many metals, such as iron, the accumulation of corrosion products may accelerate or sustain the corrosion by holding moisture or by creating a concentration gradient, or both. In the ACCC case, however, the effect appears to be the opposite. The accumulation of corrosion products is slowing down the galvanic corrosion process. This is thanks to the cathode being located deep

inside a crevice. If the positions were switched – the anode was buried deep inside a crevice – the galvanic corrosion would be rapidly accelerated. This is, for example, the driving mechanism in crevice corrosion. The unique geometry of the ACCC conductor (with compromised corrosion barrier) appears to be very favorable from a galvanic corrosion perspective.

Monitoring for galvanic corrosion and other faults in ACCC conductors

This work has shown that the potential galvanic corrosion rate resulting from a compromised galvanic barrier in an ACCC conductor appears to be similar or less than the inherent galvanic corrosion rate in ACSR, and is probably not a threat to the ACCC's electrical properties. However, a damaged corrosion barrier is still an indication of a potentially serious structural problem. One of the fundamental conditions for galvanic corrosion to occur is that there exists an electrolyte bridge between the two participating materials, which in this case would be the CFRP core and the aluminum. This electrolytic contact between the two materials can be utilized in the structural health monitoring of the conductor, because it will locally change the electrical properties of the conductor.

The CFRP core with the fiberglass barrier and the surrounding aluminum strands form a coaxial geometry: a conductor surrounded by another conductor with an electrically insulating layer in-between. Although the CFRP was never intended to be used as a conductor, the high fiber fraction makes it sufficiently conductive for the use of electrical Time Domain Reflectometry (TDR) for inspection and monitoring. The principle of TDR is similar to radar, but is confined to one dimension. An ultra-fast rise

time voltage step is launched into the cable by applying a voltage between the inner and outer conductor. The electromagnetic pulse travels down the conductor at nearly the speed of light. When the pulse encounters a change in the characteristic impedance - which could be caused, for example, by an electrolyte bridge causing galvanic corrosion - a reflected pulse is returned back to the instrument. The time between the transmitted pulse and the reflection uniquely determines the fault location.

In the field of composites, TDR is, for example, used to monitor the curing of resin in laminates, for damage detection in laminates, and for automated measurement of crack propagation during testing of composites, it was not found that it had been used in the inspection of ACCC.

Experimental work using a 22 m long section of ACCC cable demonstrated that TDR can be used to find faults such as short circuits and electrolyte bridges between the CFRP and aluminum. Numerical modeling predicts that spans of at least 1000 m of conductor cable can be inspected using the method. It is likely that longer sections can be inspected utilizing a higher voltage (the test equipment utilized in this study had an output voltage of only 3 V) and signal processing such as filtering or integration.

It is likely that TDR can be used to also detect other faults of interest in the ACCC such as partial fractures, loss of aluminum or fiberglass, water absorption of the fiberglass, gunshot damage, crushing or bird-caging, but it is yet to be determined. There are several potential future applications of TDR for structural health monitoring of overhead transmission lines with ACCC conductors:

- 1) Inspection of the conductor *before* installation to detect manufacturing faults or damage due to mishandling, and to determine the exact location of the fault on the reel. It can also be used to measure the length of the conductor on the reel because the end of the cable gives a reflection similar to a fault.
- 2) Monitoring of the conductor *during installation*. If the conductor is, for example, over-bent and fractured, this may be detected in real time.
- 3) Inspection *after installation* but before energizing.
- 4) *Continuous monitoring* or intermittent inspection of an energized conductor in service (this would require the development of equipment that can withstand the high voltage environment).

The method will likely also work for non-ACCC transmission line cables with similar geometry and electrical properties.

Final conclusions

Based on the results presented in this dissertation, the following final conclusion can be drawn regarding the galvanic corrosion of aluminum/carbon composite systems in general and the ACCC conductor in particular.

Conclusions regarding the galvanic corrosion of aluminum/carbon couples in general:

- Aluminum and carbon (such as CFRP, graphite or other non-metallic carbon containing materials) form a *strong galvanic couple* in the presence of an electrolyte.

- The galvanic coupling can lead to severely accelerated corrosion of the *aluminum*.
- If possible, the contact between aluminum and carbon should be avoided. The two materials may be insulated from each other by fiberglass composites, polymers, polymer coatings or other non-conductive materials.
- The galvanic corrosion is under *cathodic control*.
- The galvanic corrosion process is also mainly under *diffusion control*, where the total galvanic corrosion rate is controlled by the rate at which oxygen arrive at the carbon surface.
- The total galvanic corrosion rate is determined by the exposed carbon area, and independent of the exposed aluminum area.
- Galvanic corrosion can occur even if no oxygen is present through the water splitting reaction, although the rate is much lower. This rate of galvanic corrosion can likely be considered negligible in many applications.
- The testing conditions and sample design can affect the results by orders of magnitude. The test setup must be designed to closely simulate the real service environment. If the test setup does not represent the service environment for the component, the galvanic corrosion rate may be grossly over or under estimated.

Conclusions regarding the ACCC conductor:

- The ACCC conductor *cannot* develop galvanic corrosion if the fiberglass galvanic corrosion barrier is *intact*.

- ACCC can *only* develop galvanic corrosion if the following three conditions are met *simultaneously*: 1) the fiberglass barrier is compromised in a way that results in exposed CFRP, 2) there is direct CFRP to aluminum contact somewhere in the conductor span, and 3) there is an electrolyte such as salt fog or polluted rain bridging the two materials.
- The formation of a stable layer of oxide on the aluminum surface decreases the galvanic corrosion rate in an ACCC conductor with a compromised corrosion barrier, and will also limit the pitting corrosion of ACCC conductors with an intact corrosion barrier.
- The measured galvanic corrosion rates in salt-loaded ACCC conductor samples with a compromised corrosion barrier in 100 % RH at room temperature were similar or lower than the galvanic corrosion rate in ACSR.
- The accumulation of corrosion products will limit the galvanic corrosion rate by restricting the diffusion of oxygen to the cathode (the CFRP) in an ACCC conductor with a compromised corrosion barrier.
- Thanks to the favorable geometry of an ACCC conductor (with a compromised corrosion barrier) with a much larger aluminum area than CFRP area and with the CFRP located in the center of the conductor, the galvanic corrosion rate is drastically limited due to the restricted transport of oxygen to the CFRP.
- Time Domain Reflectometry (TDR) can be used for detecting galvanic corrosion and short circuits between the aluminum and CFRP in a short

section of ACCC conductor. Numerical modeling predicts that the method can be used for inspection and monitoring of full conductor spans.

REFERENCES

Agilent.com (2013). "Loss Tangent." Retrieved Jan 22, 2013.

ASTM (2008). D1141-98, Standard Practice for the Preparation of Substitute Ocean Water, ASTM.

ASTM (2010). G116-99, Standard Practice for Conducting Wire-on-Bolt Test for Atmospheric Galvanic Corrosion. Annual Book of ASTM Standards. G01.04. West Conshohocken, PA, ASTM Intl. **03.02**.

ASTM (2011). B117-11, Standard Practice for Operating Salt Spray (Fog) Apparatus. Annual Book of ASTM Standards. G01.05. West Conshohocken, PA, ASTM Intl. **03.02**.

ASTM (2014). G71-81, Standard Guide for Conducting and Evaluating Galvanic Corrosion Tests in Electrolytes. Annual Book of ASTM Standards. G01.11. West Conshohocken, PA, ASTM Intl. **03.02**.

F. Aymerich and S. Meili (2000). "Ultrasonic evaluation of matrix damage in impacted composite laminates." Composites Part B: Engineering **31**: 6.

D. Banis, J. A. Marceau and M. Mohaghegh (1999). Design for corrosion control. Boeing Aeromagazine.

E. Bardal, R. Johnsen and P. O. Gartland (1984). "Prediction of Galvanic Corrosion Rates and Distribution by Means of Calculation and Experimental Models." Corrosion **Vol. 40**(No. 12): 628-633.

S. Barré and M. L. Benzeggagh (1994). "On the use of acoustic emission to investigate damage mechanisms in glass-fibre-reinforced polypropylene." Composites Sci. Technol. **52**: 7.

K. Barton (1973). Protection against atmospheric corrosion, Wiley.

W. Boyes (2009). Instrumentation Reference Book, 4th edition, Butterworth-Heinemann.

G. Brennan (2004). Refurbishment of Existing Overhead Transmission Lines. Integral Energy Australia, CIGRE Session 2004, B2-203.

B. Burks, D. Armentrout, J. Buckley, M. Baldwin and M. Kumosa (2009). "Hybrid composite rods subjected to excessive bending loads." Composites Science and Technology **69**, no. 15-16 (2009): 2625-32.

B. Burks, D. Armentrout and M. Kumosa (2011). "Characterization of the fatigue properties of a hybrid composite utilized in high voltage electrical transmission." Composites Part A **2011:42:1138-47**.

L. Butler (1989). Transmission Lines and Measurement of their Characteristics. Amateur Radio.

W. Cantwell and J. Morton (1985). "Detection of impact damage in CFRP laminates." Composite Structures **3**(241).

J. Chan, B. Clairmont, D. Rueger, D. Childs and S. Karki (2008). Demonstration of Advanced Conductors for Overhead Transmission Lines. Palo Alto, CA, EPRI: 112.

Z. Y. Chen, F. Cui and R. G. Kelly (2008). "Calculations of the Cathodic Current Delivery Capacity and Stability of Crevice Corrosion under Atmospheric Environments." Journal of The Electrochemical Society **155**(7): 9.

B. Clairmont (2008). High-Temperature Low-Sag Conductors. EPRI, Transmission Research Program Colloquium, Sacramento, CA.

I. S. Cole, W. D. Ganther, J. D. Sinclair, D. Lau and D. A. Patersona (2004). "A Study of the Wetting of Metal Surfaces in Order to Understand the Processes Controlling Atmospheric Corrosion." Journal of The Electrochemical Society **151**(12).

COMSOL (2014). Atmospheric corrosion, Tutorial, 2014

Comsol (2014). Webinar: Modeling Corrosion and Electrochemical Systems.

CorrosionDoctors (2014). "Corrosion Rate Conversion, Online tutorial." Retrieved Oct 10, 2014 from <http://www.corrosion-doctors.org/Principles/Conversion.htm>.

S. D. Cramer and J. B. S. Covino (2005). ASM Handbook Volume 13B Corrosion: Materials. Materials Park, OH, ASM Intl.

J. R. Davis (1999). Corrosion of Aluminum and Aluminum Alloys, ASM International.

J. Delmonte (1981). Technology of carbon fiber and graphite fibers composites, Van Nostrand Reinhold – Litton Educational Publishing Inc.

M. W. Denny (1993). Air and Water: The Biology and Physics of Life's Media, Princeton University Press.

DigiKey (2013). "Cable Design Equations – Coaxial Cable." Retrieved Jan 22, 2013.

A. Dominauskasa, D. Heider and J. W. G. Jr (2007). "Electric time-domain reflectometry distributed flow sensor.", Composites Part A Applied Science and Manufacturing **38**(1).

O. EncyclopediaBritannica (2014). Deliquescence. Encyclopedia Britannica Online.

O. EncyclopediaBritannica (2014). Hygroscopy. Encyclopedia Britannica Online.

EPRI (2000). Inspection & assessment of overhead line conductors: A state-of-the-science report, 1000258. Palo Alto, CA, EPRI.

EPRI (2002). High-Temperature, Low-Sag Transmission Conductors, 1001811. Palo Alto, CA, EPRI.

C. Foxboro (1999). Conductivity ordering guide.

R. Francis (2000). Galvanic Corrosion: A Practical Guide for Engineers. Houston, TX, NACE Intl.

O. S. U. Frankel G.S. (2003). Pitting Corrosion. Metals handbook Vol 13A, ASM International.

GamryInstruments (2011). Getting started with electrochemical corrosion measurement, Application note Rev 1.1, Gamry Instruments.

A. Giambattista, B. M. Richardson and R. C. Richardson (2004). College Physics, 1st edition, McGraw-Hill.

W. P. Goch (2013) Corrosion and Splices. Classic Connectors Inc.

C. U. Grosse and M. Ohtsu (2008). Acoustic Emission Testing, Springer Verlag.

A. Groysman (2010). Corrosion for everybody, Springer.

H. P. Hack (1993). Galvanic Corrosion Test Methods, NACE International.

H. P. Hack (2005). Galvanic. Corrosion tests and standards – application and interpretation, 2nd edition, R. Baboian, ASTM.

N. E. Hager and R. C. Domszy (2004). "Monitoring of cement hydration by broadband time-domain-reflectometry dielectric spectroscopy." J. Appl. Phys. **96**(5117).

E. Håkansson (2013). Galvanic Corrosion of High-Temperature Low-Sag (HTLS) High Voltage Conductors: New Materials – New Challenges. Thesis, Mechanical and Materials Engineering Department. Denver, CO, University of Denver. **MS**.

E. Håkansson (2015). Control mechanisms in the galvanic corrosion between a carbon fiber composite and aluminum SAMPE University Research Symposium. Dallas, TX, USA.

E. Håkansson, J. Hoffman, P. Predecki and M. Kumosa (In preparation). "New look at the role of corrosion product deposition in the galvanic corrosion between aluminum and carbon fiber composite " (In preparation).

E. Håkansson, P. Predecki and M. Kumosa (2015). "Galvanic Corrosion of High Temperature Low Sag Aluminum Conductor Composite Core and Conventional Aluminum Conductor Steel Reinforced Overhead High Voltage Conductors." Reliability, IEEE Transactions on **vol.64**(no.3): 928-934.

E. Håkansson, R. E. Ricker, P. Predecki and M. Kumosa (June 2016). "Electrochemical In-situ Assessment Method for Galvanic Corrosion in Bare Overhead Transmission Line Conductors." CIGRE Science & Engineering.

J. Hale (2006). Boeing 787 from the ground up. Boeing Aero Magazine.

Hewlett-Packard (1988). Time Domain Reflectometry Theory, Application Note 1304-2.

J. Hoffman, J. Middleton and M. Kumosa (2015). "Effect of a surface coating on flexural performance of thermally aged hybrid glass/carbon epoxy composite rods." Composites Science and Technology **106** 141–148.

F. P. Incropera, D. P. Dewitt, T. L. Bergman and A. S. Lavine (2007). Fundamentals of heat and mass transfer, 6th edition, Wiley.

C. Kasper (1940). "The Theory of the Potential and the Technical Practice of Electrodeposition: I. The General Problem and the Cases of Uniform Flow." Trans. Electrochem. Soc.(77(1)): 353-363;.

D. Landolt (1995). Chapter 1: Introduction to surface reactions: electrochemical basis of corrosion. Corrosion mechanisms in theory and practice. J. O. P. Marcus, Marcel Dekker.

L. Linares, Taborda, N., Zambrano, L., Perez, O. (2006). Failures Analysis by Corrosion in Power Conductors of Aluminum Alloys in Coastal-Lacustrian Environments. 2006 IEEE PES Transmission and Distribution Conference and Exposition Latin America, Venezuela.

H. Ling, K. Lau, L. Cheng and W. Jin (2006). "Viability of using an embedded FBG sensor in a composite structure for dynamic strain measurement." Measurement **39**: 16.

J. Lobry and D. Guery (2012). "Theoretical Study of Dielectric Breakdown in a New Composite Core HTLS Conductor." Power Delivery, IEEE Transactions on **vol.27**(no.4): 1862-1867.

Matweb (2013) Aluminum 1350-O. Matweb.com

Matweb.com (2015). Aluminum 1350-O. Matweb.com.

Matweb.com (2015). Copper, Cu, Annealed.

Matweb.com (2015). Elektro-Isola G-Etronax EP FR4 Epoxy, Glass Fabric Reinforcement, Light Yellow, Sheets

Matweb.com (2015). Zoltek Panex 35® Milled Carbon Fibers.

Milwaukee (2010). "User manual for portable dissolved oxygen meter model MW600."

P. M. S. Monk (2001). Fundamentals of electroanalytical chemistry, Wiley.

G. Mook, R. Lange and O. Koeser (2001). "Non-destructive characterization of carbon-fibre-reinforced plastics by means of eddy-currents." Composites Sci. Technol. **61**: 7.

P. L. Moreira, P., Lourenco, C., Sebrao, M., Sant'anna, I., Wavrik, J. (2008). "Internal Corrosion in Conductor Cables of Power Transmission Lines: Characterization of the Atmosphere and Techniques for Faults Detection."

R. S. Munn (1986). The modeling of galvanic corrosion systems using numerical methods with particular attention to boundary conditions of nonlinear polarization, University of Connecticut.

R. S. Munn and O. F. Devereux (1991). "Numerical Modeling and Solution of Galvanic Corrosion Systems: Part I. Governing Differential Equation and Electrode Boundary Conditions." Corrosion **Vol. 47**(No. 8): 612-618

NACE (2002). Corrosion costs and preventive strategies in the United States, NACE.

NACE/ASTM (2012). NACE/ASTM G193-12d Standard terminology and acronyms relating to corrosion, NACE/ASTM.

K. M. O'Connor and C. H. Dowding (1999). GeoMeasurements by Pulsing TDR Cables and Probes, CRC Press.

A. A. Obaid, S. Yarlagadda, M. K. Yoon, N. E. H. III and R. C. Domszy (2006). "A Time-domain Reflectometry Method for Automated Measurement of Crack Propagation in Composites during Mode I DCB Testing." Journal of Composite Materials **40**(22).

OmegaInstruments (2014). Equilibrium Relative Humidity Saturated Salt Solutions, Technical Note from OMEGA Instruments.

G. Pandey, H. Deffor, E. T. Thorstenson and D. Heider (2013). "Smart tooling with integrated time domain reflectometry sensing line for non-invasive flow and cure monitoring during composites manufacturing." Composites Part A: Applied Science and Manufacturing **47**: 6.

G. Pandey, E. T. Thorstenson and D. Heider (2013). "Electric time domain reflectometry sensors for non-invasive structural health monitoring of glass fiber composites." Progress in Electromagnetics Research **137**: 13.

M. Pourbaix (1974). Atlas of Electrochemical Equilibria in Aqueous Solutions. Houston, TX, NACE Intl.

QuantifoilInstruments (2014). Creating constant air humidity in closed vessels, Technical Note.

Radiodetection (1997). Radiodetection / BicoTest Time Domain Reflectometer (TDR), Electrical Industry Fault Locating Techniques, Application notes.
http://www.radiodetection.com/doclib/SPX_TDR_quick_Application_Ref_en.pdf

Radiodetection (1997). "Understanding TDRs." Retrieved Jan 22, 2013.

RadiometerAnalytical (2004). Conductivity: Theory and Practice, Technical notes D61M002.

- Y. J. Rao (1999). "Recent progress in applications on in-fibre Bragg grating sensors." Optics and Lasers in Engineering **31**: 27.
- A. Renton (2013). Transpower trials new corrosion inspection technologies for its high-voltage transmission network. Materials Performance, NACE: 4.
- R. W. Revie (2000). Uhlig's corrosion handbook, 2nd edition John Wiley & Sons.
- R. E. Ricker (1995). "Can Corrosion Testing Make the Transition from Comparison to Prediction?" Journal of Metals **47**(9): 32-35.
- R. E. Ricker (2008). "On Using Laboratory Measurements to Predict Corrosion Services Lives for Engineering Applications " Journal ASTM International **5**(7): 101350.
- R. E. Ricker and J. L. Fink (1997). Crevice Corrosion Metrology for Aging Aircraft. The First Joint DoD/FAA/NASA Convergence on Aging Aircraft. Ogden, UT, Universal Technology Corp., Dayton, OH: 489-503.
- Riser-Bond (1997). TDR Application Guide.
- P. R. Roberge (2008). Corrosion Engineering – Principles and Practice, McGraw-Hill.
- R. P. Roberge (2008). Corrosion Engineering: Principles and Practice. NY, McGraw-Hill.
- M. Schumacher (1979). Seawater corrosion handbook, William Andrew Publishing/Noyes.
- M. R. Stoudt, A. K. Vasudevan and R. E. Ricker (1992). Examination of the Influence of Lithium on the Repassivation Rate of Aluminum Alloys. Corrosion Testing of Aluminum Alloys. V. S. Agarwala and G. Ugiansky. San Francisco, CA, ASTM, Phila. PA. **STP-1134**: 196-213.
- J. A. Strickland (1997). Time Domain Reflectometry Measurements

S. Syed, Atomic Energy Research Institute (2006). "Atmospheric corrosion of materials." Saudi Arabia, Emirates Journal for Engineering Research: 11 (11), 11-24 (2006).

A. Technologies (2013). "PCB Layout Guidelines for Designing with Avago SFP+ Transceivers." Retrieved Jan 22, 2013.

F. Thébault, B. Vuillemin, R. Oltra, C. Allely and K. Ogle (2011). "Modeling bimetallic corrosion under thin electrolyte films." Corrosion Science **53**(1): 201-207.

A. Todoroki, K. Ohara, Y. Mizutani, Y. Suzuki and R. Matsuzaki (2015). "Self-Sensing TDR for Bearing Failure Detection of CFRP Laminate Fastener Hole with Particular Reference to the Effect of Fasteners." Open Journal of Composite Materials **5**: 60-69.

M. E. Turner (2012). Finite Element Modeling of Galvanic Corrosion of Metals in a Seawater Environment, Rensselaer Polytechnic Institute, Hartford, CT.

U.S. Geological Survey (1998). Solubility of oxygen in water, TWRI Book 9, 4/98, U.S. Geological Survey.

A. Valleau (1990). "Eddy-current nondestructive testing of graphite composite-materials." Mater. Eval. **48**: 9.

N. Van den Steen, H. Simillion, O. Dolgikh, H. Terryn and J. Deconinck (2016). "An integrated modeling approach for atmospheric corrosion in presence of a varying electrolyte film." Electrochimica Acta **187**: 714-723.

C. Vargel (2004). Corrosion of Aluminum, Elsevier.

R. Vera, D. Delgado and B. M. Rosales (2006). "Effect of atmospheric pollutants on the corrosion of high power electrical conductors: Part 1. Aluminium and AA6201 alloy." Corrosion Science **48**(10): 2882-2900.

X. G. Zhang (2011). Chapter 10: Galvanic corrosion. Uhlig's Corrosion Handbook, Third Edition. R. W. Revie, Wiley.

C. G. Zoski (2007). Handbook of Electrochemistry, Elsevier.

APPENDIX A: ACRONYMS, TERMINOLOGY AND SYMBOLS

A	Ampere
AAC	All-Aluminum Conductor
ACCC	Aluminum Conductor Composite Core
ACCR	Aluminum Conductor Composite Reinforced
ACCS	Aluminum Conductor Composite Supported (suggested generic name for ACCC)
ACSR	Aluminum Conductor Steel Reinforced
ACSS	Aluminum Conductor Steel Supported
ASTM	<i>American Society for Testing and Materials</i> , an international standards organization that develops and publishes technical standards
Ag	Silver
Ag/AgCl	Silver-Silver Chloride (a type of reference electrode)
Al	Aluminum
Al ³⁺	Aluminum Ion
Al(OH) ₃	Aluminum (tri) hydroxide
Al ₂ O ₃	Aluminum oxide, also known as Alumina
BPA	<i>Bonneville Power Administration</i>
CFRP	Carbon Fiber Reinforced Polymer matrix composite
Cl	Chlorine
Cl ⁻	Chloride ion
ΔG	Change in Gibb's Free Energy
e ⁻	electron
E	Potential [V]

F	Faraday's constant (96 485 C/mol)
GOALI	<i>Grant Opportunities for Academic Liaison with Industry</i>
HTLS	High Temperature Low Sag (Conductor)
H ⁺	Hydrogen ion
H ₂	Hydrogen gas
i	Current density [A/m ²]
I	Current [A]
KCl	Potassium Chloride
MMC	Metal Matrix Composite
NaCl	Sodium Chloride
O ₂	Oxygen gas
OH ⁻	Hydroxyl ion
PMC	Polymer Matrix Composite
RE	Reference Electrode
ROW	Right-of-way
RTV	Room Temperature Vulcanizing silicone rubber
SHE	Standard Hydrogen Electrode (a type of reference electrode)
TOW	Time of wetness – the number of hours per year that the relative humidity is over 80 % and the temperature is ≥0°C.
V	Volts
ZRA	Zero Resistance Ammeter

APPENDIX B: ERROR ANALYSIS

All experimental measurements contain errors. This section will discuss possible errors in the measurements presented in this dissertation, and how errors were minimized.

B.1 Effect of temperature and temperature control, and errors in temperature measurements

Budget restrictions excluded the purchase of NIST calibrated temperature sensors and temperature loggers. Since no NIST calibrated transfer standard was available, all temperature sensors and loggers were calibrated using a two-point calibration consisting of an ice-bath and boiling water prepared with distilled water. The offsets were assumed to be linear between 0°C and 100°C. Temperature data as well as temperature controllers were adjusted according to the calibration results.

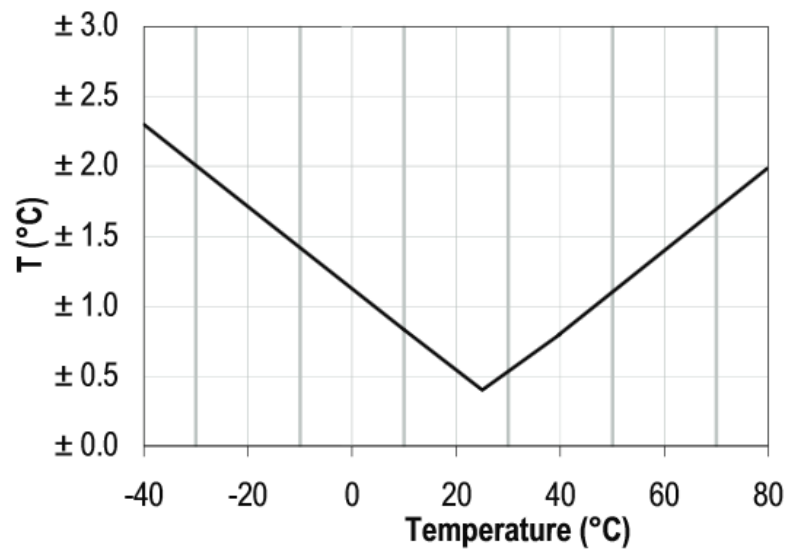


Figure 180: Specified accuracy in the temperature loggers.
Source: (LascarElectronics 2012)

Room temperature vs. Controlled (elevated) temperature

It is very common to perform tests at room temperature (RT). RT is a convenient choice since it excludes the need for temperature control. However, the test results can be affected if there are significant fluctuations in the temperature of the laboratory. The tests presented in this dissertation were all performed in Denver, Colorado, USA. Denver is located 1609 m above sea level and the semi-arid climate results in cold winters and hot summers. The high altitude causes also a large temperature difference between day and night. Many HVAC systems cannot keep up with these large temperature fluctuations, which was the case for the building where these tests were performed. The ambient conditions in the laboratory were logged continuously for most of this study. Analysis of the data from May 22, 2014 through January 3, 2015 revealed temperature fluctuations of up to 18°C (Figure 181). The lowest temperature registered was 15°C and the highest was 33°C, while the average temperature was 23.7°C ($\sigma=3.2^\circ\text{C}$). During the same period, the relative humidity fluctuated between 10 and 72.5 % with an average of 33.9 % ($\sigma=12.7$ %), but this did not affect the testing as it was performed in a humidity controlled chamber.

A comparison of the ambient temperature and the galvanic corrosion measurements in 100 % RH during that period showed clear oscillations following the change of the ambient temperature in 24 hour cycles (Figure 182). The highest temperatures inside the corrosion testing chamber were registered between 2 PM and 8 PM. The lowest temperatures occurred between 6 AM and 10 AM. The temperature inside the corrosion chamber followed closely the ambient temperature of the laboratory.

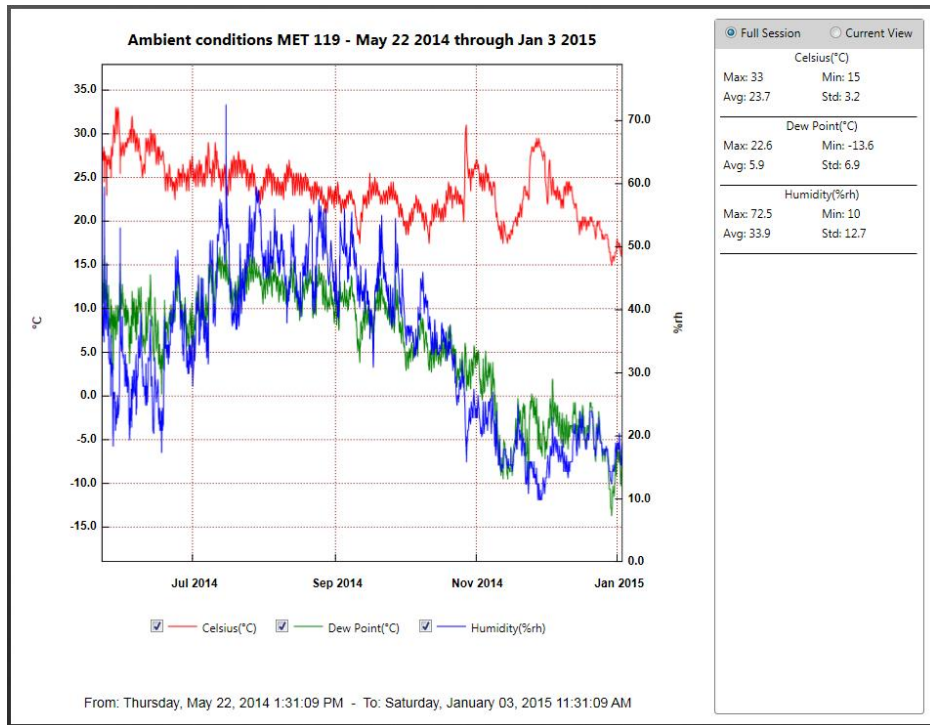


Figure 181: Temperature, relative humidity, and dew point fluctuations in the laboratory from May 22, 2014 to January 3, 2015.

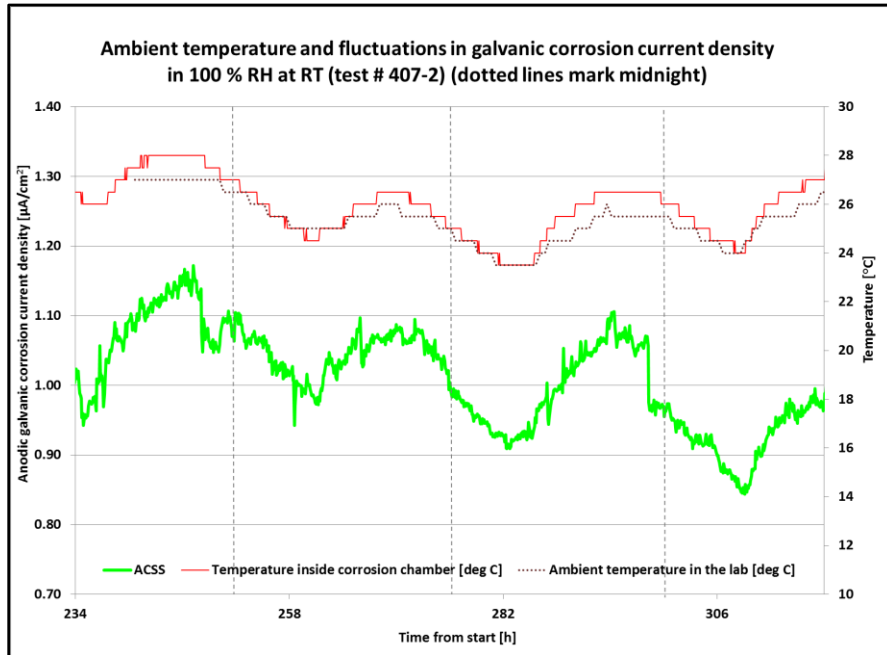


Figure 182: Example of ambient temperature and fluctuations in the galvanic corrosion current registered from July 11 to July 14 2014.

It is obvious that these fluctuations make the test results much more difficult to interpret and increases the uncertainties. The simplest solution to this problem is to temperature control the corrosion testing chamber itself. It is practically much easier to adjust the temperature to a level above room temperature than to below room temperature. Several standard tests such as the ASTM B117 are performed at a slightly elevated temperature (in the B117 case at 35°C). A temperature of 35°C can be accomplished with simple means. Our experiments have shown that even very inexpensive PID temperature controllers (<\$35) will stay within $\pm 2^\circ\text{C}$ (sometimes even $\pm 1^\circ\text{C}$) with proper tuning. Temperature controlled testing environments - provided that the controllers are properly tuned - could result in much smaller temperature fluctuations than if the tests are conducted at ambient temperature.

However, temperature control may cause interference with the galvanic corrosion current measurements due to electromagnetic noise. Figure 183 and

Figure 184 display electromagnetic noise affecting the galvanic corrosion measurements. The amplitude of the noise is low and does not pose a dramatic problem at high galvanic corrosion currents, as shown in Figure 183. The noise can be distinguished from the current signal by its distinct behavior and can be removed from the data.

At really low corrosion currents, the amplitude of the noise is large enough to shift the polarity of the measurement. The effect of the noise is obvious in

Figure 184.

After several failed attempts to keep the electromagnetic noise to an acceptable level, the decision was made to perform all tests at room temperature. As shown in Figure

182, the changes in corrosion rate due to temperature fluctuations are approximately 20 %. This is negligible compared to the changes of several orders of magnitude reported in section 5.2.

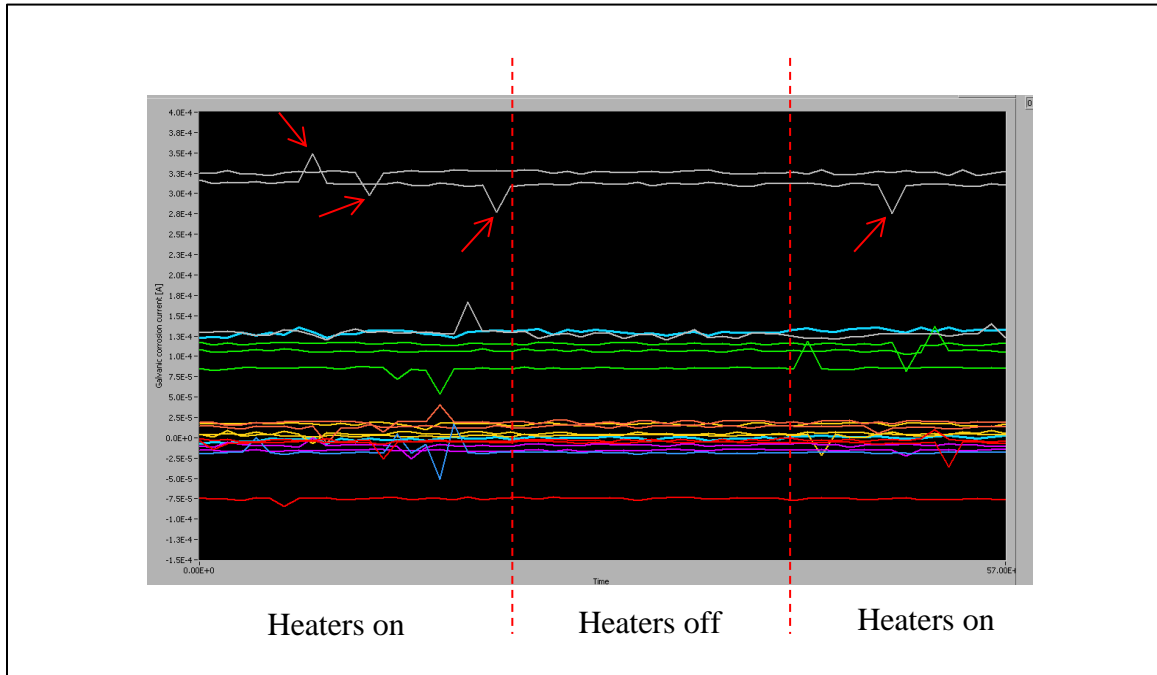


Figure 183: Noise from heaters in METC. The red arrows point out the noise in the upper two plots.

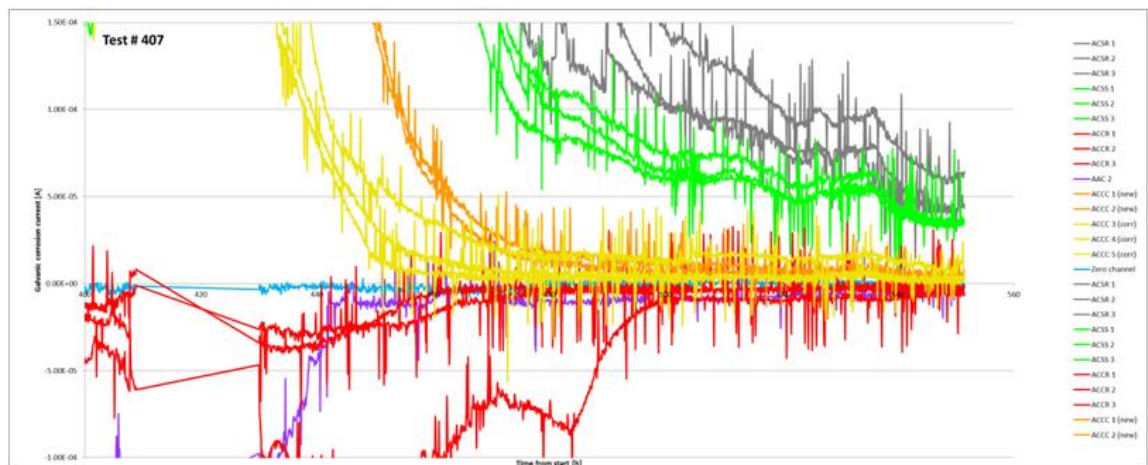


Figure 184: High degree of electrical noise in a test series with low corrosion currents.

B.2 Errors in humidity measurements

As with all sensors, humidity sensors also require calibration. Humidity is inherently difficult to measure. Even high-quality sensors (such as the Lascar EL-USB-2-LCD humidity loggers used in this study) have a specified typical overall error of $\pm 3\%$ and a maximum error of $\pm 5\%$ (LascarElectronics 2012).

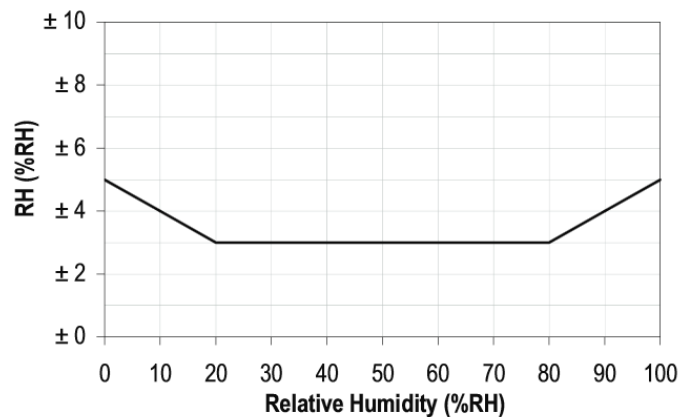


Figure 185: Specified accuracy in the humidity loggers
From: (LascarElectronics 2012)

The humidity sensors used in this study were subjected to a two-point calibration using saturated salt baths, and they were typically within the specified error of $\pm 3\%$ (in the few cases where they were not, they were not used). Figure 186 shows an ongoing calibration of a humidity control sensor. The controller should read 76 %, but reads 72 %. A 2-point calibration was performed, and the set-point was adjusted accordingly assuming a linear relation.

It was discovered that the humidity sensors for the humidity controllers used in this study could be damaged by long periods of high levels of humidity ($>90\%$ RH) and by direct exposure to condensate water. The problem was minimized by frequent

calibration using the saturated salt baths and by replacing the sensors whenever necessary. The humidity loggers were much less sensitive and did not need to be replaced.

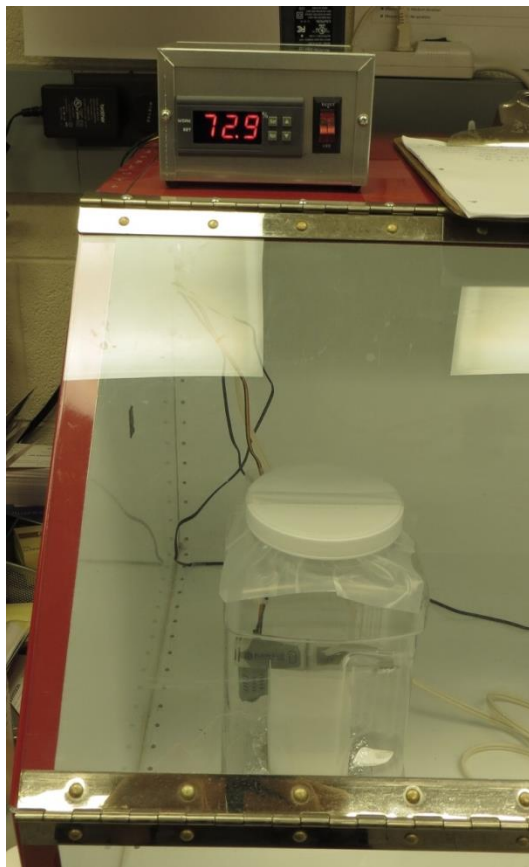


Figure 186: Calibration of humidity meter and humidity controller.

B.3 Errors caused by reference electrodes

Silver-silver chloride (Ag/AgCl) reference electrodes were chosen due to their ease of use and absence of toxic metals. The open circuit potential for a Ag/AgCl reference electrode at 25°C is +0.222 V compared to the standard hydrogen electrode (SHE) that is traditionally used for electrochemical measurements (Bates 1978). There is

a weak temperature effect in the open circuit potential, but because all measurements were made at room temperature, the temperature effect was assumed to be negligible.

The reference electrodes are filled with silver-saturated 4M KCl solution. The reference electrodes were flushed and filled with new KCl solution when crystal became visible in the electrode body, as shown in Figure 187. When not in use, the tips of the reference electrode were kept in silver-saturated KCl.

For long-term testing (weeks or longer), the reference electrode was placed in a silver-saturated KCl bath which was connected to the testing by a salt bridge. The use of a separate bath with KCl solution decreased the risk of foreign ions diffusing into the reference electrode.

Figure 188 shows the salt bridge used in this study.

A total of three reference electrodes were used throughout the study. The electrodes were periodically checked against each other by using the potentiostat to make sure the difference in the readings were no more than a few mV.

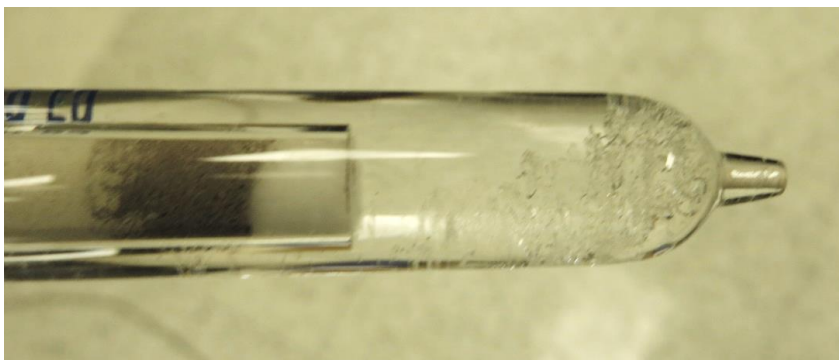


Figure 187: Crystals forming in the Ag/AgCl reference electrode.

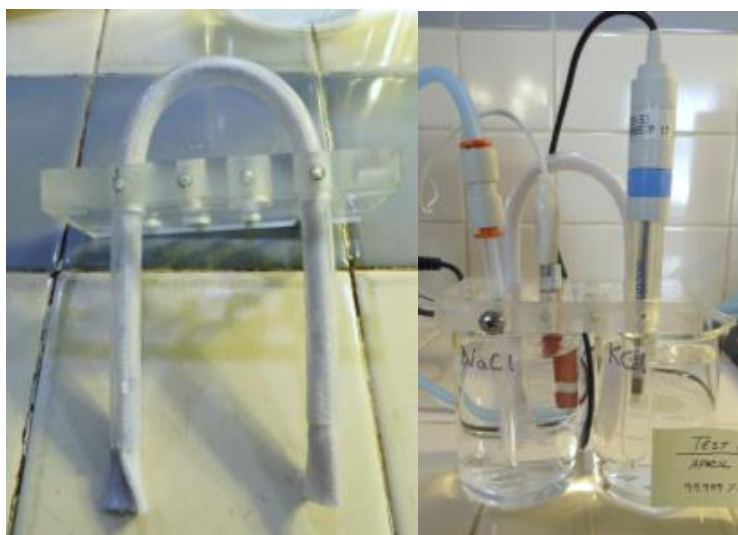


Figure 188: Salt bridge.

The salt bridge made of a cotton string in a plastic tube (left), the reference electrode in silver-saturated 4M KCl connected to the actual testing environment through a salt bridge (right).

B.4 Calibration of potentiostat

The potentiostat used in this study – a Gamry Series G 300 with the DC105 software suite – has a quite sophisticated built-in calibration procedure. This procedure was run when the potentiostat software requested it.

B.5 Errors in mass measurements

The mass losses and gains were measured using a high-quality digital scale with 0.0001 g resolution (Ohaus Voyager V12140 Digital Balance scale). The scale data sheet specifies a repeatability of 0.0001 g. With a typical sample mass of approximately 150 g, this means an error of $\pm 0.00007\%$, which can be considered negligible.

A larger source of error is the drying of wet or humid samples during the mass measurement process. The drying can be observed while the sample is sitting on the scale

as a decrease in mass. A typical sample can lose 0.0010 g or more during the time it takes to record the mass. A wet 100 mm long conductor sample contains approximately 3 grams of electrolyte. In this case, the drying during the mass measurement causes an error of approximately 0.03 %.

B.6 Errors in galvanic corrosion current measurements

The potentiostat used in this study has extremely high accuracy. The specified accuracy in both current and potential is 0.2 %. The multichannel precision shunt setup utilized for the larger test series uses 1 % precision resistors. The HP 34970A DASU used for the data logging has a specified accuracy of 0.004 %.

B.7 Conclusions about measurement errors

As shown in this section, the measurement errors are much smaller than the variations in corrosion rate of orders of magnitude caused by variations in geometry and environment presented in this dissertation. The errors caused by the measurement equipment and ambient conditions will therefore be considered negligible in this study.